Abstract

Ultra-fast laser ablation is the process of material removal from solid surfaces by pulsed sub-picosecond laser irradiation. In contrast to longer pulse durations, ultra-fast laser ablation shows the distinguishing feature of the timescale of excitation being below the timescale of consequent material heating. Excited charge carriers distribute the thermal energy over a larger volume than the optical penetration depth suggests, while the lattice remains in a cold state. Spatial energy distribution is followed by a fast carrier-lattice energy relaxation, which induces overheated and meta-stable states of matter. These meta-stable states are induced simultaneously in the laser-affected zone, forcing the material to relax in a variety of mechanisms, ranging from ultra-fast melting over hydrodynamic expansion to material ejection in a complex mixture of chunks, droplets or vapor.

While a multitude of publications successfully study the laser irradiation induced material dynamics of metals, we investigate laser ablation of covalent materials. In contrast to metals, covalent materials show a band gap, excitation-dependent carrier heat conduction and strong excitation-dependent interatomic bonding strengths, rendering the theoretical description of such materials a difficult task. However, it also gives rise to a number of unique dynamics like non-thermal melting, Coulomb explosions and altered carrier heat conduction due to charge carrier confinement.

In this work we choose silicon as our prototypical covalent material and perform molecular dynamics simulations of laser irradiated silicon, while applying an excitation-dependent interatomic potential. We present new parametrizations of the optical properties, as well as the extension of established charge carrier transport models for silicon, which are both tailored for the application on large scale massive multi-parallel high-performance computers. Finally we observe and characterize the novel and non-thermal ablation mechanics of laser irradiated silicon.

FMQ

University of Stuttgart
Germany

Dominic Klein

Laser Ablation of Covalent Materials

University of Stuttgart
Germany

Dominic Klein

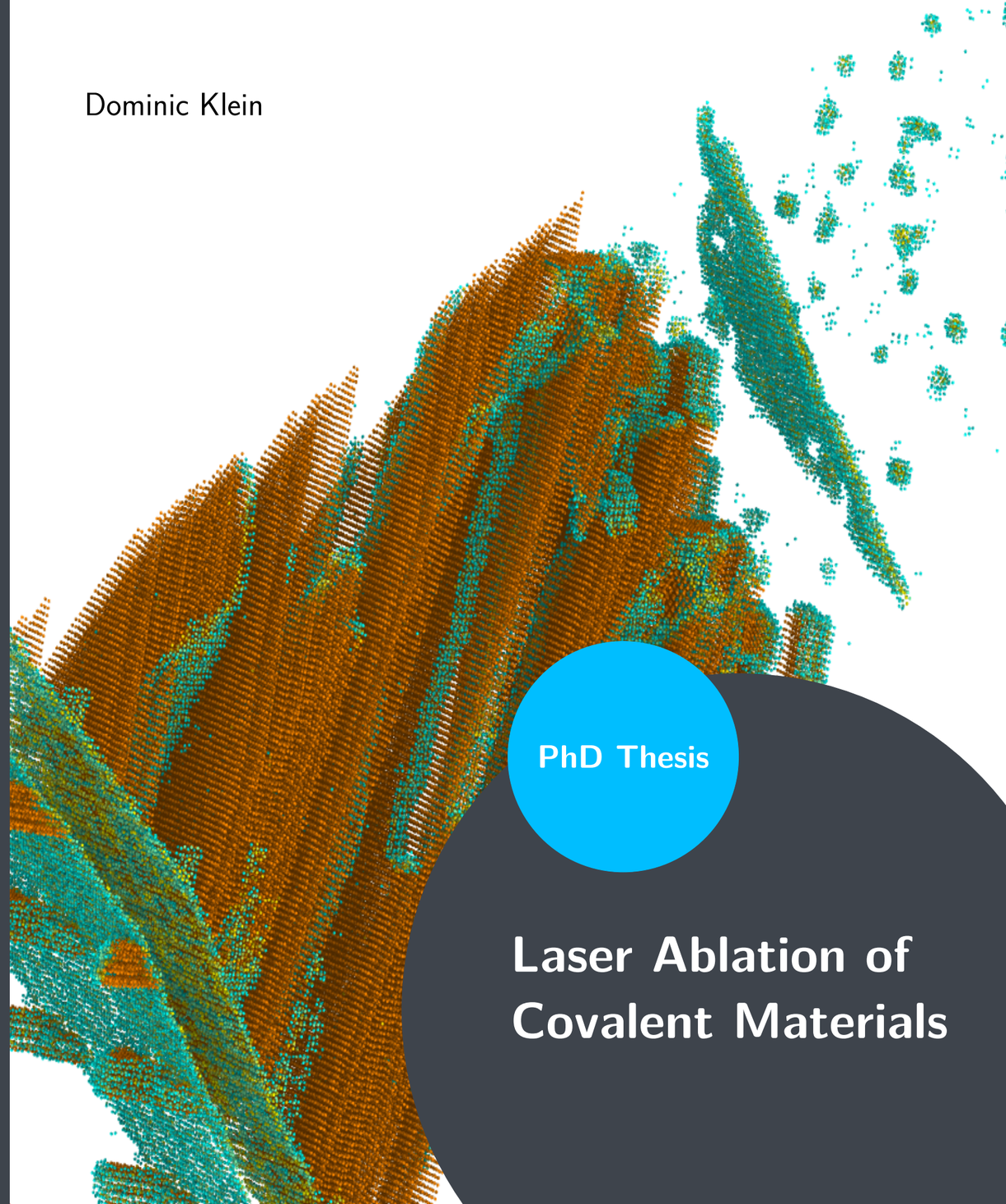

PhD Thesis

Laser Ablation of Covalent Materials

Laser Ablation of Covalent Materials

Laserablation kovalenter Materialien

Von der Fakultät Mathematik und Physik
der Universität Stuttgart zur Erlangung der
Würde eines Doktors der Naturwissenschaften (Dr. rer. nat)
genehmigte Abhandlung

Vorgelegt von
Dominic Alexander Klein
aus Nürtingen

Hauptberichter:	Apl. Prof. Dr. Johannes Roth
Mitberichter:	Prof. Dr. Christian Holm
Prüfungsausschussvorsitz:	Prof. Dr. Ronny Nawrodt
Tag der mündlichen Prüfung:	17.04.2023

Institut für funktionelle Materie und Quantentechnologien
der Universität Stuttgart
Pfaffenwaldring 57, 70550 Stuttgart

2023

pew pew pew!

- Leon Zwiener

Contents

Abbreviations

1D	One-dimensional
2D	Two-dimensional
3D	Three-dimensional
abl	Ablation
Al	Aluminium
BAA	Bond Angle Analysis
BETE	Boltzmann Energy Transport Equation
BOA	Bond Order Analysis
BTCS	Back in Time Centered in Space
CB	Conduction Band
CFD	Computational Fluid Dynamics
CFL	Courant-Friedrichs-Lewy
CNA	Common Neighbor Analysis
CPMD	Car-Parinello Molecular Dynamics
CPU	Central Processing Unit

CSP	Centro-Symmetric Parameter
CW	Continuous Wave
D	Drude-based Parameterization Set
DEQ	Differential Equation
DFT	Density Functional Theory
DOS	Density of States
e-e	Electron-Electron scattering
e-h	Electron-Hole scattering
e-i	Electron-Ion scattering
e-p	Electron-Phonon scattering
EAM	Embedded Atom Method
EDIP	Environment Dependent Interatomic Potential
exp	Experiment
FCA	Free Carrier Absorption
FD	Finite Differences
FTCS	Forward in Time Centered in Space
FTDFT	Finite Temperature Density Functional Theory
FWHM	Full Width at Half Maximum
HPC	High Performance Computing
I/O	Input/Output

ID	Identifier
IMD	ITAP Molecular Dynamics
ITAP	Institut für Theoretische und Angewandte Physik
LIPSS	Laser-induced Periodic Surface Structuring
MD	Molecular Dynamics
MEAM	Modified Embedding Atom Method
MIR	Mid Infrared
MOD	Modified Tersoff Potential
mod-CNA	Adaptive Common Neighbor Analysis
MOD*	Temperature-dependent Modified Tersoff Potential
MPI	Message Passing Interface
NDA	Neighbor distance analysis
NIR	Near Infrared
NPT	Isothermal–isobaric ensemble
nTTM	Density-dependent Two-Temperature Model
NVE	Microcanonical Ensemble
NVT	Canonical Ensemble
OVITO	Open Vizualization Tool
PBC	Periodic Boundary Conditions
PDE	Partial Differential Equation

PhD	Doctor of Philosophy
PLD	Pulsed Laser Deposition
RMSD	Root Mean Square Displacement
Si	Silicon
SLM	Selective Laser Melting
SPA	Single-Photon Absorption
SHE	Spherical Harmonics Expansion
SW	Stillinger-Webber Potential
T3	Tersoff Potential
TPA	Two-Photon Absorption
TSM	Thermal Spike Model
TTM	Two-Temperature Model
VASP	Vienna Ab initio Simulation Package
VB	Valence Band

Relations

$\stackrel{!}{=}$	Demanded by author
$\equiv$	Defined by author
$\approx$	Approximately equal
$\sim$	Approximately
$\leq$	Less or equal than
$<$	Less than
$\geq$	Greater or equal than
$>$	Greater than
$\gg$	Far greater than
$\ll$	Far smaller than
$\propto$	Proportional to

Abstract

Ultra-fast laser ablation is the process of material removal from solid surfaces by pulsed sub-picosecond laser irradiation. In contrast to longer pulse durations, ultra-fast laser ablation shows the distinguishing feature of the timescale of excitation being below the timescale of consequent material heating. Excited charge carriers distribute the thermal energy over a larger volume than the optical penetration depth suggests, while the lattice remains in a cold state. Spatial energy distribution is followed by a fast carrier-lattice energy relaxation, which induces overheated and meta-stable states of matter. These meta-stable states are induced simultaneously in the laser-affected zone, forcing the material to relax in a variety of mechanisms, ranging from ultra-fast melting over hydrodynamic expansion to material ejection in a complex mixture of chunks, droplets or vapor.

While a multitude of publications successfully study the laser irradiation induced material dynamics of metals, we investigate laser ablation of covalent materials. In contrast to metals, covalent materials show a band gap, excitation-dependent carrier heat conduction and strong excitation-dependent interatomic bonding strengths, rendering the theoretical description of such materials a difficult task. However, it also gives rise to a number of unique dynamics like non-thermal melting, Coulomb explosions and altered carrier heat conduction due to charge carrier confinement.

In this work we choose silicon as our prototypical covalent material and perform molecular dynamics simulations of laser irradiated silicon, while applying an excitation-dependent interatomic potential. We present new parametrizations of the optical properties, as well as the extension of established charge carrier transport models for silicon, which are both tailored for the application on large scale massive multi-parallel high-performance computers. Finally we observe and characterize the novel and non-thermal ablation mechanics of laser irradiated silicon.

1 Introduction

1.1 Ultra-fast Laser irradiated Solids

The invention of the laser was, without any doubt, one of the most disruptive innovation leaps of the 20th century. The ability to produce monochromatic coherent light allows laser light not only to be focused on a tight spot and to stay collimated over large distances, but also to be pulsed into pulse durations of a few femtoseconds [1], or in the case of X-ray pulses, even into the range of attoseconds [2]. The consequent ability to deposit defined amounts of photonic energy into areas in the nano scale, revolutionized the way humankind is able to interact with matter itself. The importance of this technical advance cannot be overstated, as six Nobel Prizes on the improvement of the laser light source itself [3–8] - the latest in 2018 [8] - underline.

The spectrum of applications in fundamental research range from the atomic scale, with applications such as laser cooling [9], laser trapping [10], inertial confinement fusion [11] over the molecular and nano scale with Raman spectroscopy and multiple microscopy techniques, to the probing of the atmosphere of remote planets. The vast number of applications in research is only outnumbered by the huge number of important industrial applications, such as photolithography in semiconductor manufacturing or material processing.

On first glance, one is tempted to view industrial laser material processing techniques, like laser drilling, laser cutting, laser welding or laser micro-structuring as primitive, or simple, when compared to the applications in fundamental research. However, this is far from being true. The highly non-linear material dynamics induced by rapid laser heating alone, gives rise to numerous highly complex effects and material behaviors which are far from being understood on a fundamental level.

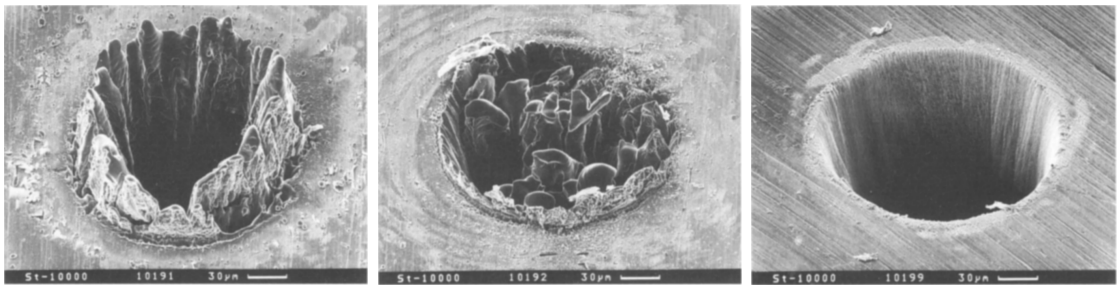

(a) $\tau_p = 3.3$ ns (b) $\tau_p = 80$ ps (c) $\tau_p = 200$ fs

Figure 1.1: SEM images of holes drilled in steel by pulsed laser ablation under different pulse durations τ_p, measured by Chicbkov[†] [13].

This can be observed in the relatively new field of additive manufacturing, where the precise origin of fusion-errors and sample-errors remains unclear [12]. Furthermore, the ability to produce sub-picosecond laser pulses added a new level of complexity and opportunities in the field of laser processing of materials.

Sub-picosecond, or ultra-fast, laser ablation comes with the distinct feature of the timescale of electronic excitation being below the timescale of material heating. When solids are treated with these intense ultra-fast laser pulses, one can observe that the ultra-fast heated material tends to ablate with increased precision and reduced damage of the surrounding material, leading to a more precisely defined ablation crater. In figure 1.1 we show steel machined by different pulse durations. In contrast to the treatment with longer pulse durations, the macroscopic material dynamics induced by ultra-fast laser treatment delicately depends on the electronic structure and therefore the quantum mechanical properties of the irradiated solid.

This dependence on the ultra-fast changing electronic structure does not only give rise to novel features and properties varying with the irradiated material and laser parameters, but also gives rise to a vast complexity for the description of such processes. In figure 1.2 we show SEM images of copper and silicon after being irradiated by p ultra-fast laser pulses of identical laser parameters. Here, we do not only observe differing ablation mechanics, but also we observe these ablation mechanics leading to novel surface morphologies, indicating the variability of the underlying processes when treating different materials. These surface morphologies

[†]Licensed by Springer Nature and Copyright Clearance Center (License Nr. 5440901375402)

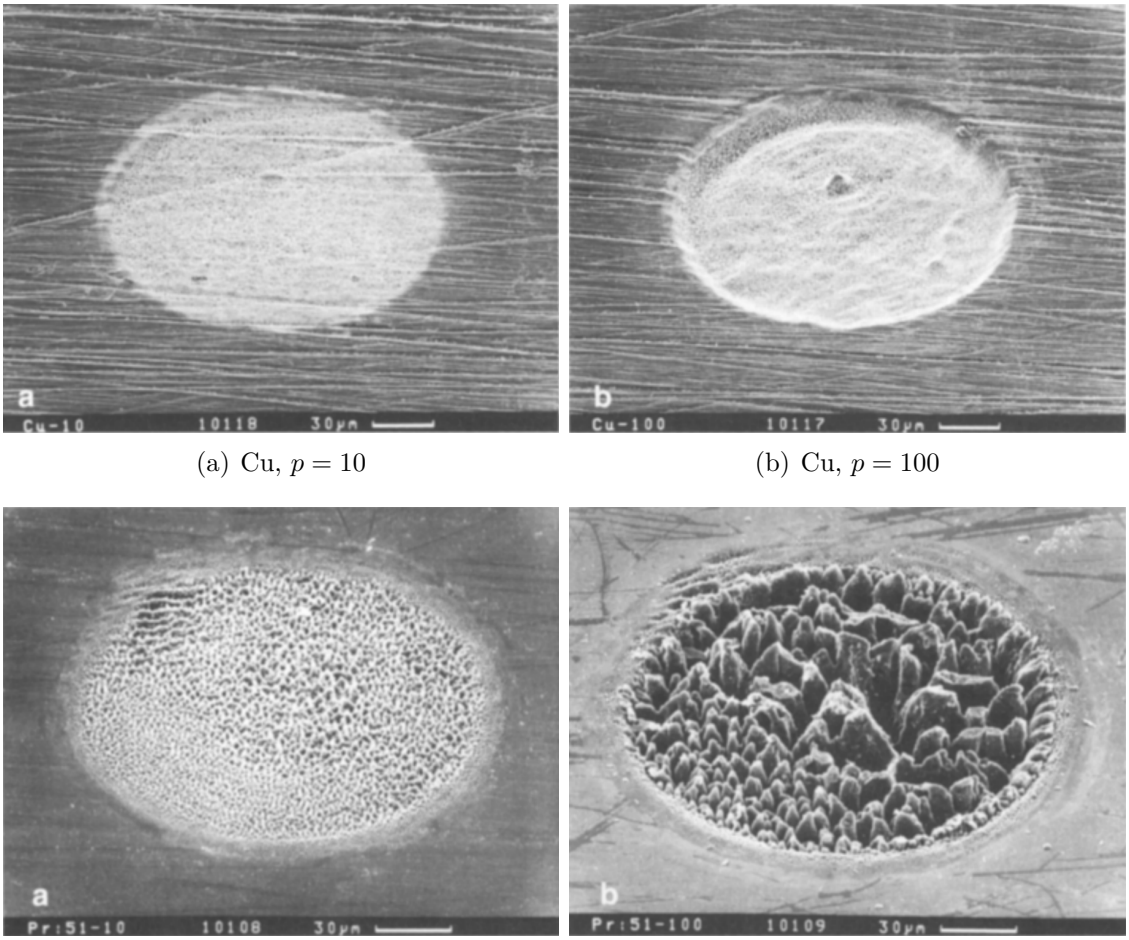

(a) Cu, $p = 10$ (b) Cu, $p = 100$

(c) Si, $p = 10$ (d) Si, $p = 100$

Figure 1.2: SEM images of holes laser-drilled in copper (Cu) and silicon (Si) by p number of laser pulses, measured by Chicbkov[†] [13].

also vary in laser parameters and give rise to a variety of applications that modify the mechanical, optical and chemical properties of material surfaces. In figure 1.3 we show SEM images of various structures induced on the surface of a titanium alloy by pulsed ultra-fast laser irradiation. Such functional surfaces can be machined to function as diffraction gratings [14–16], induce coloring [17] or the creation of holograms [18]. The immense increase in surface area of the sample can be utilized to increase absorption and reflectivity properties of materials [19, 20] and thus i.e.

[†]Licensed by Springer Nature and Copyright Clearance Center (License Nr. 5440901375402)

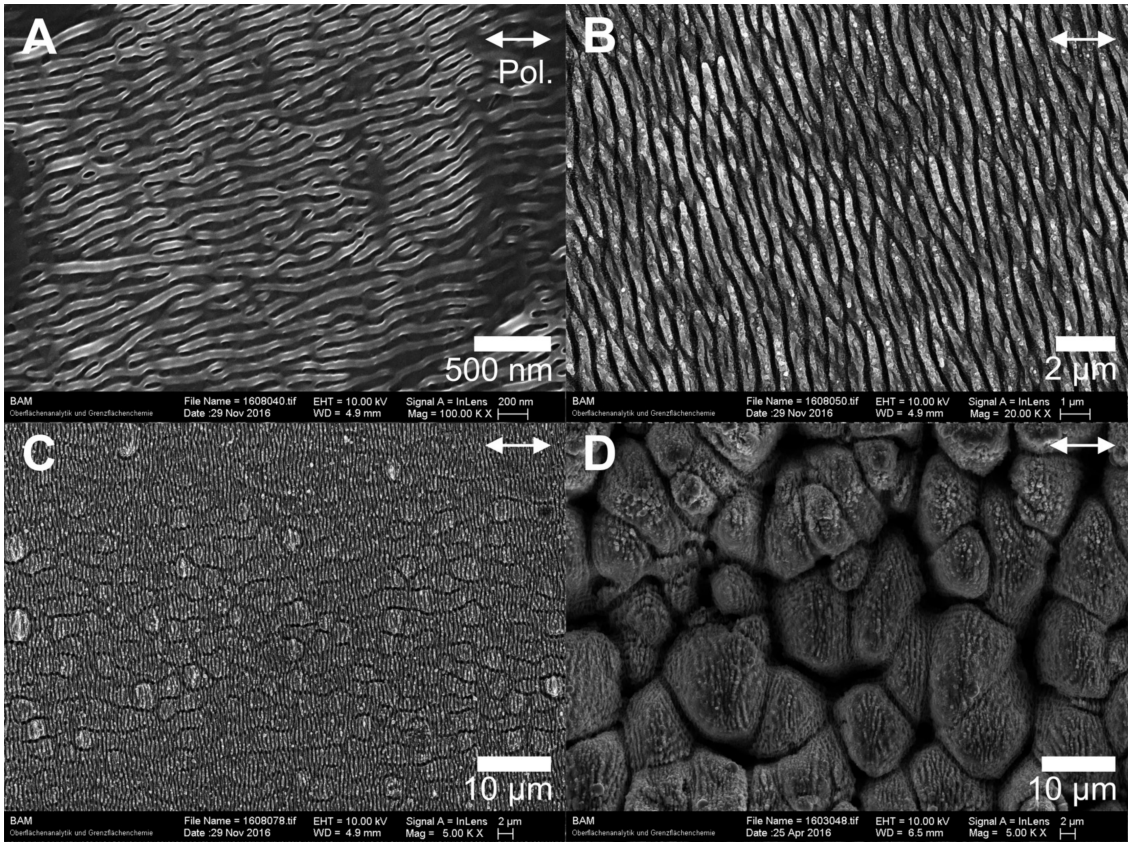

Figure 1.3: Top-view SEM images of high spatial frequency structures A, low spatial frequency structures B, grooves C and spikes D, found after ultra-fast pulsed laser irradiation of polished titanium alloy Ti-6Al-4V, measured by Camilo[‡] [32].

increase the efficiency of solar cells [21]. The control of surface roughness within the sub-wavelength regime also gives control over chemical properties starting at the creation of super hydrophobic surfaces [20, 22, 23] and anti-icing coatings [24, 25], up to directional flow control [20, 23, 26, 27] and anti-bacterial surface properties [28, 29]. Also it has been found that laser processed surfaces can reduce the coefficient of friction by 75% when compared to polished surfaces [26, 30, 31].

Apart from surface structuring, the ability to infuse huge amounts of energy on ultra-short timescales on very tight spots, allows to induce ultra-fast phase transitions and meta-stable phases [34–38], which force the heated matter to relax in complex dynamics and create unique features. This leads to the possibility to create

[‡]Reproduced from [32] with the permission of the Laser Institute of America

functional nano-features such as nano-bumps [39–46], nano-jets or spikes [41–43, 47]. In figure 1.4 we show a SEM image of a so-called microneedle, a structure induced by circular polarized single shot irradiation of silicon [33, 48–51].

For higher laser intensities, the dynamics of material removal and morphology of the remaining crater becomes of interest and shows an equally broad spectrum of physical effects that can be utilized. These effects span i.e. over electron ejection forming a plasma cloud in front of the sample, leading to plasma shielding effects for following laser pulses [52–55] to the accompanied ejection of the ablation plume. For varying irradiation and material parameters, the ablation plume shows distinct distributions of droplets and chunks [56, 57], which in turn can be utilized for coating applications [58]. In industrial applications, on the other hand, such as laser drilling, laser milling and cutting [59–61], peak efficiency is desired. For this, the plume composition is desired to be as homogeneous as possible to prevent product contamination by redepositing droplets.

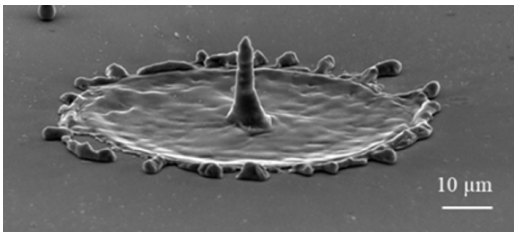

Figure 1.4: SEM images of Si microneedles fabricated by single pulse irradiation, measured by Ablez[§] [33].

However, while a variety of applications and experimental or empirical investigations exist, the underlying dynamics of laser-material interaction are still a topic of research. This is especially the case for band gap materials, due to the increased complexity of the electronic structure when compared to metals [62–65]. Excitation mechanisms, energy transport mechanisms, electron-lattice interaction and thus material heating, all depend on the complex interplay of the excited electron-hole plasma, carrier dynamics and carrier confinement effects. Further, in the case of covalent materials, interatomic bond manipulation by excitation has been observed, which can not only lead to ultra-fast non-thermal melting [66, 67] but also to achieve a state of purely repulsive bonds, thus inducing an extreme state of matter, with yet underexplored follow-up consequences on the material dynamics in laser ablation.

[§]Licensed under CC-BY-4.0

1.2 Processes in the Laser Ablation of covalent Semiconductors

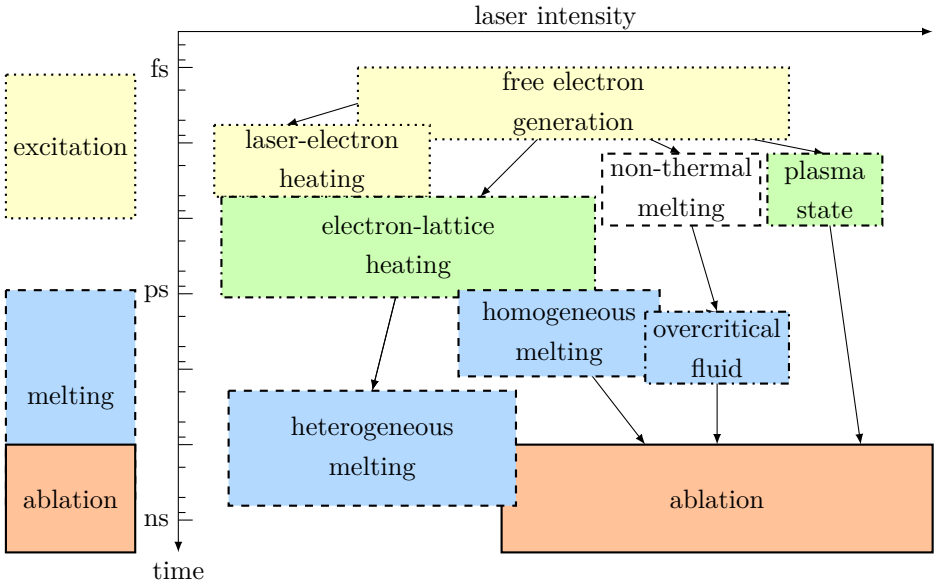

Figure 1.5: Flowchart of possible pathways from ultra-fast laser excitation towards ablation, roughly categorized into their timescale and required laser intensity.

The complexity of the material dynamics of laser irradiated semiconductors arises from the complexity of the numerous underlying highly non-linear processes, which are chained together over several length- and timescales. A temporal classification of the dominating processes, from laser pulse absorption to ablation is sketched in figure 1.5.

Ultra-fast laser pulses are absorbed by the electrons of the material and induce a highly non-equilibrium transient electronic state. During the laser pulse alone, properties of the material undergo ultra-fast changes as valence band (VB) electrons get excited into conduction band (CB) states and generating electron-hole pairs [68–71]. Simultaneously, excited CB charge carriers also absorb photon energy thus heating the electron-hole plasma. The ultra-fast changing electronic states change optical properties, cause spatial inhomogeneity and impose spatial gradients in carrier temperature, carrier density and energy. Carrier heat diffusion leads to

energy distribution within the carrier subsystem followed by heating of the macroscopic material by carrier-phonon relaxation [72]. The dynamics of this, again, is highly dependent on the band structure and the phonon spectrum of the respective material, which in turn is altered by the current local electronic excitation. Typically, the consequent lattice heating leads to lattice temperatures exceeding the melting temperature on a timescale of picoseconds and results in heterogeneous and homogeneous melting and often the formation of an overcritical fluid, which relaxes in a phase explosion. However, in the case of covalent semiconductors, electrons can get excited from bonding VB states into anti-bonding CB states. With sufficiently strong excitation, binding energies vanish and lead to the sudden collapse of the lattice [73–76]. This may occur on a timescale faster than carrier-phonon heating and is therefore called non-thermal melting [66, 67]. Ultimately, if a sufficient amount of energy is infused, the induced local highly non-equilibrium thermodynamic states, which result in extreme macroscopic thermodynamic conditions, can lead to material ejection of various forms.

Needless to say, the wide span of physical effects involved in laser ablation, their delicate dependency on material properties, the choice of studied material, laser wavelength and general boundary conditions make the formulation of a closed theoretical description of laser ablation an impossible task. Furthermore, the importance of physical phenomena on various space and timescales require knowledge from various fields of physics, such as optics, quantum mechanics, solid state physics, electromagnetics, atom and plasma physics, thermodynamics and hydrodynamics. Fortunately, decades of research managed to pinpoint the most relevant and fundamental processes involved in ultra-fast laser ablation and their interplay with each other. However, the non-thermal processes and their consequences on the ablation dynamics of laser ablation of covalent semiconductors are not yet understood. Many theoretical and computational investigations tackled separate effects like the material dynamics [77–79], laser light absorption [80–83], energy transport [84], melting kinematics [35, 74, 83, 85] and non-thermal effects [86–90]. Only few investigations [85, 91–93] tried to present a comprehensive simulation model, but failed to provide a description of the complete ablation process due to computational restrictions or the missing inclusion of non-thermal effects.

1.3 Structure and Goal of this Work

In this work we want to present a comprehensive simulation model for the simulation of laser ablation of covalent materials and investigate the implications of non-thermal melting on the material dynamics during laser ablation of covalent materials on the atomic scale. For this, we choose silicon as our prototypical covalent semiconductor and use the excitation-dependent interatomic interaction potential MOD*, developed by Kiselev [94, 95] as the method of a priori inclusion of non-thermal kinematics.

This renders the goal of this work twofold. The first goal is to first set up a continuum-atomistic model description that is capable of

1. offering a comprehensive dynamical depiction of the complete ablation process of laser irradiated silicon,

2. provide an a priori inclusion of the unknown phase behavior of highly excited silicon and

3. is performant enough to achieve experimental sample sizes within simulations in a high-performance computing environment.

The second goal is to analyze the simulation predictions and characterize the expected novel non-thermal ablation mechanics.

Modelling Ultra-fast Laser Ablation In chapter 2 we give a general overview of the main physical processes involved in laser ablation and present novel and established approaches on how to model them.

Numerics In chapter 3 we present the concepts of the numerical implementations we performed to solve the proposed continuum-atomistic models.

Results In chapters 4 to 7, we first present a compact synopsis of the parametrization details and proceed to fine-tune our continuum-atomistic model in terms of energy transportation and optical properties.

For this, we will construct a transition from the currently established parametrization based on fitting-laws towards our optical parametrization, which is solely derived from theory. We implement a Drude theory based description of free carrier absorption, as well as a two-photon absorption coefficient from theoretical calculations and validate their applicability by comparison against ultra-fast pump-probe experiments. We find both parametrizations are capable to reproduce the ultra-fast optical changes generated by the highly excited electron-hole plasma.

Following this, we extend our continuum-atomistic model to include the ultra-fast bond energy manipulation by excitation by implementation of an excitation-dependent interatomic potential, thus allowing the atomic system to reproduce non-thermal effects, like non-thermal melting. We validate the depicted material dynamics by comparison against finite-temperature density functional theory (FT-DFT) calculations and achieve a computationally performant description of the system.

We test and validate the predictions of the energy transport models, known as BETE, nTTM and TSM, against experimental data obtained by single shot laser ablation experiments under near identical conditions [96] and achieve a 1:1 match with the experimentally predicted ablation depths. As a result we obtain a combined continuum-atomistic model, capable of correct prediction of transport phenomena under varying electronic excitations. Further, we perform systematic laser ablation simulations and investigate and categorize novel non-thermal ablation mechanics.

Finally, we perform huge molecular dynamics simulations on samples with lateral extensions of several micrometers, thus being greater than the laser spot diameter. We irradiate the sample with Gaussian pulse shapes and investigate the complex mechanics involved in the formation of the ablation crater for varying fluences. Here we investigate and isolate effects based on lateral energy and material transport. Most notably, we compare our obtained crater morphology to recent single shot ablation experiments [76, 96, 97] and are able to offer detailed explanations on the often observed, but unexplained formation of amorphous structures around the laser crater.

2 Modelling Ultra-fast Laser Ablation

In this chapter we want to give a general overview on the main physical processes involved in laser ablation and how to model them. Although we aim to give a universal understanding of the occurring physical processes during laser ablation of metals and semiconductors, we emphasize on the phenomena occurring in silicon. Also the presented model descriptions aim to be as computational cheap as possible. Most often, more fundamental and more rigorous theoretical treatments exists, but however, are unsuitable to be combined together into a comprehensive description of the complete ablation process. Here, the finesse of modelling is to provide the most simplistic description of occurring phenomena that is still able to depict the nature of the most relevant underlying features of the respective dynamic.

The structure of this chapter follows the processes in figure 1.5 in ascending timescales. We begin with possible descriptions of the laser light absorption and accompanied laser-electron heating in section 2.1 and proceed to present the consequent carrier-lattice heating in section 2.2.

In section 2.3 we do not only present often applied models for the electron thermal conductivity, but also present new formulations to describe the energy fluxes that go along with inhomogeneous sample excitation.

The classification of melting kinematics is adressed briefly in section 2.4, as the modelling of those is incorporated in the description of the macroscopic material dynamic, presented in section 2.5. There we present concepts of hydrodynamic and atomistic approaches to depict the highly non-linear material dynamics induced by the ultra-fast heating during laser ablation.

2.1 Absorption of Laser Light

When a laser of intensity I irradiates the surface of a solid, the laser energy may be absorbed by electrons. The permitted absorption mechanisms involved strongly depend on photon energy, the band structure and electronic configuration of the irradiated solid.

In metals, absorption is typically dominated by free carrier absorption (FCA), where photons excite electrons below the Fermi edge to a higher energy state. In semiconductors, if the photon energy exceeds the band gap, VB electrons can be excited into empty CB states by single photon absorption (SPA). Further, it is observed that multi-photon absorption, like two-photon absorption (TPA), becomes a dominating process especially for lower laser intensities. Either way, the generated CB plasma allows for additional metal-like free carrier absorption.

There are several ways to model this behavior. The simplest way is to define an energy absorption rate α_k for all k-photon absorption processes. The general local intensity absorption along the laser axis x per unit volume and time can thus be written as a rate equation reading

$$\frac{dI}{dx} = -\sum \alpha_k I^k. \tag{2.1}$$

This simplification generates a compact description of absorption processes, but shifts the problem of accurate modelling to the determination and correct parametrization of all relevant α_k [98].

2.1.1 Absorption Processes in Metals

From the viewpoint of the Sommerfeld theory of metals, the electrons are initially distributed according to the Fermi-Dirac distribution f_{FD}. In figure 2.1, f_{FD} is sketched for an arbitrary electron temperature $T_c > 0$, as well as an arbitrary non-equilibrium distribution after the absorption of several photons of energy $E = \hbar\omega$. In metals a sufficient amount of free electrons are present in the CB, thus laser light absorption is heavily dominated by single photon free carrier absorption. Electrons of energy E' below the Fermi edge get excited into an empty state of energy $E'' =$

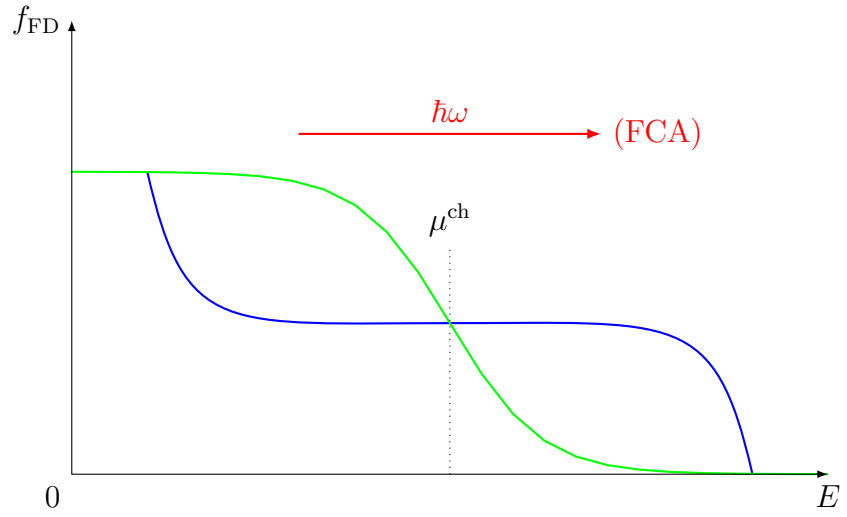

Figure 2.1: Sketch of the Fermi-Dirac distribution f_{FD} of electrons within a metal over electron energy E for an electron temperature $T_c > 0$ drawn in green. The new non-equilibrium distribution after the absorption of photons of energy $\hbar\omega$ is sketched in blue. μ^{ch} denotes the chemical potential.

$E' + \hbar\omega$ with a certain probability α_{FCA}. In the case of FCA, this absorption probability is surprisingly well modelled by the well-known Drude model. Although the Drude description and the Drude scattering rate $1/\tau_{\mathrm{D}}$ are phenomenological quantities [99] and do not necessarily have to reproduce the correct absorption rate, the Drude model offers mostly good agreement with experimental data on metals and semiconductors within the range of visible light [80, 92, 100–102]. Within this framework, the linear dielectric function $\hat{\varepsilon}(\omega)$

can be written as
$$\hat{\varepsilon}(\omega) = \varepsilon'(w) + \varepsilon''(\omega)i \tag{2.2}$$

with the real part
$$\hat{\varepsilon}'(\omega) = \varepsilon_r \left(1 - \frac{\omega_{\mathrm{p}}^2 \tau_{\mathrm{D}}^2}{1 + \omega^2 \tau_{\mathrm{D}}^2}\right) \tag{2.3}$$

and the imaginary part
$$\hat{\varepsilon}''(\omega) = \frac{\varepsilon_r}{2\omega\tau_{\mathrm{D}}} \left(\frac{\omega_{\mathrm{p}}^2 \tau_{\mathrm{D}}^2}{1 + \omega^2 \tau_{\mathrm{D}}^2}\right) \tag{2.4}$$

as a function of the plasma frequency $\omega_{\mathrm{p}} \propto \sqrt{n_c}$ and the collision frequency $1/\tau_{\mathrm{D}}$. From the dielectric function the complex refraction index $\hat{n} = \sqrt{\hat{\varepsilon}(w)}$ can be evaluated directly and the imaginary part determines the attenuation of the electromag-

netic wave. Said attenuation can be interpreted as the free carrier absorption rate, which leads to

$$\alpha_{\mathrm{FCA}}(\omega) = \frac{2\,\mathrm{Im}\,\hat{n}}{\lambda_{\mathrm{L}}}\,2\pi. \tag{2.5}$$

Therefore the FCA rate α_{FCA} is a function of the applied laser wavelength λ_{L} and the plasma frequency ω_{p}. On top of that, the Drude model offers to incorporate many scattering processes into the Drude scattering rate and allows to investigate the contributions of, for example electron-phonon or electron-hole collisions, which all are properties that change during laser irradiation. Supplementary, the Drude model allows to include these ultra-fast changes in the self-consistent description of reflectivity R by the Fresnel equation

$$R = \frac{|\hat{n}-1|^2}{|\hat{n}+1|^2}. \tag{2.6}$$

2.1.2 Absorption Processes in Semi-conductors

Analogously to our treatment of metals, the Fermi-Dirac distribution and dominating absorption mechanisms for semiconductors are sketched in figure 2.2. In contrast to metals, semiconductors show a band gap, separating the VB from the CB by an energy that is typically in the range of visible light. Also, at room temperature and in thermodynamic equilibrium the CB is typically very sparsely occupied. This gives rise to three categories of absorption processes. First, the so-called single photon interband absorption (SPA). Here, a single photon of energy $E_{\mathrm{ph}} > E_{\mathrm{gap}}$ excites an electron from the VB into the CB. Due to restricted states within the band gap, mainly electrons close to the edge of the VB get excited to states near the edge of the CB, thus generating an electron-hole pair. The excitation rate α_{SPA} therefore shows a strong dependence on the band gap of the material, which in turn depends on the density of the excited electron-hole plasma and material temperature. Due to this complex interplay α_{SPA} is most often described by phenomenological fitting-laws. Second, the now generated CB plasma induces a metallic absorption behavior that, again, can be described by the FCA Drude framework for metals. The probability to excite such an electron to a higher state within the CB depends on the

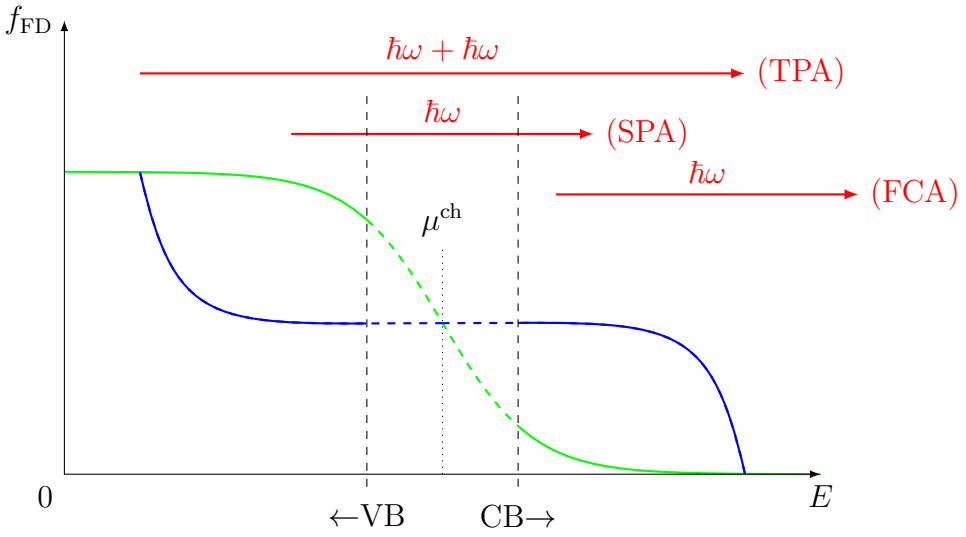

Figure 2.2: Sketch of the Fermi-Dirac distribution f_{FD} of electrons within a semiconductor over electron energy E for an electron temperature $T_c > 0$ drawn in green. The new non-equilibrium distribution after absorption of photons of energy $\hbar\omega > E_{\mathrm{gap}}$ is sketched in blue. μ^{ch} denotes the chemical potential and CB and VB mark the conduction- and VB edge.

number of excitable electrons. Therefore, intraband absorption strongly varies with the current electronic excitation during the laser ablation process [100]. Note that the plasma frequency ω_{p} now reflects the dependency of FCA on the CB carrier density. Third, the process of TPA is often very pronounced in band gap materials at certain wavelengths. TPA is the simultaneous absorption of two photons involving a virtual state within the band gap [103, 104] and allows electrons to surpass the band gap energy E_g. In specific situations, TPA can become the dominating absorption process. For example, silicon shows an indirect band gap. In visible light, the absorption of one photon is necessarily accompanied by a momentum change by phonon absorption, decreasing the absorption probability, while TPA allows for a direct absorption without any phonon absorption. Rigorous treatment of the origin of contributing non-linear effects lie outside the scope of the present work. In short, theoretical solid state band calculations [105–107] have shown that the two-photon absorption coefficient can be expressed as a general equation, which holds for most

parabolic and non-parabolic semiconductors [81] and reads

$$\beta_{\mathrm{TPA}} = K\frac{\sqrt{E_p}}{n_0^2 E_g^3}\cdot\psi(2\hbar\omega/E_g) \tag{2.7}$$

$$\text{with} \qquad \psi(2x) = \frac{(2x-1)^{3/2}}{(2x)^5} \tag{2.8}$$

$$\text{for} \qquad 2x > 1. \tag{2.9}$$

Here E_p is a result of approximations and is given by $E_p \approx 21\,\mathrm{eV}$ for most semiconductors [108] while K can be used as reasonable fitting parameter [81]. The combined attenuation rates therefore become

$$\frac{dI}{dx} = -(\alpha_{\mathrm{FCA}} + \alpha_{\mathrm{SPA}})I - \beta_{\mathrm{TPA}}I^2 \tag{2.10}$$

and are changing rapidly with the generation of the electron-hole plasma. This renders the simultaneous treatment of charge carrier generation essential for a correct laser light absorption description. For this, typically a rate equation of the form

$$\frac{dn_c}{dt} = \sum I^k \frac{\alpha_k}{k\hbar\omega} + \delta_{\mathrm{imp}} n_c - \gamma_{\mathrm{Aug}} n_c^3 \tag{2.11}$$

is applied [109]. Here, each term of the sum respectively accounts for k-photon absorption processes with identical absorption coefficients as in equation (2.10). Additionally, δ_{imp} is the impact ionization coefficient and accounts for the process where VB electrons with sufficient energy can excite a VB electron into a CB state creating an electron-hole pair. γ_{Aug} is the Auger recombination coefficient. Auger recombination is the process of a CB charge carrier, relaxing into the VB under photon emission, exciting another VB electron without moving into another band. Auger recombination is the dominating process of charge carrier recombination at high electron densities [110]. Note that the CB carrier generation equation (2.11) describes the temporal evolution of electron density without taking transport effects into account. These processes can simply be added in terms of a continuity equation.

2.2 Carrier-Phonon Relaxation

The charge carrier distribution does not only determine the optical properties of a solid, but also the subsequent energy fluxes following from spatial transport effects and the energy transfer to the lattice due to electron-phonon coupling. However, as already depicted in figure 2.1 and 2.2, photon absorption induces a strong non-equilibrium distribution in the carrier subsystem so that the concept of carrier temperature T_c as well as the Fermi-Dirac distribution no longer holds. Kinetic approaches allow for the study of the temporal evolution of such carrier-distributions. In ultra-fast excitation simulations this is typically modelled [111] by a system of coupled Boltzmann equations

$$\frac{\partial f(k)}{\partial t} = \left.\frac{\partial f(k)}{\partial t}\right|_{\text{e-p}} + \left.\frac{\partial f(k)}{\partial t}\right|_{\text{e-e}} + \left.\frac{\partial f(k)}{\partial t}\right|_{\text{S}} \qquad \text{and} \tag{2.12}$$

$$\frac{\partial g(q)}{\partial t} = \left.\frac{\partial g(q)}{\partial t}\right|_{\text{e-p}} \tag{2.13}$$

accounting for the change in electron $f(k)$ and phonon $g(k)$ energy distributions by excitation S. Here the scattering events of electron-electron e-e and electron-phonon e-p collisions enter the formalism without assumption on the energy distribution. Different groups performed this for various starting distributions, various materials and various formulations of scattering functions. The obtained result is a typical carrier thermalization time in the range of $1 - 80\,\text{fs}$ [112–115] for metals, semiconductors and dielectrics. It can be found that carrier thermalization time shows a dependence on pulse duration, decreasing with shorter pulses and higher fluences. After thermalization, the charge carrier distribution relaxes towards the Fermi-Dirac distribution and the concept of temperature is once again applicable. After thermalization the free electron density n_c, or in the case of semiconductors the CB carrier density n_c, are given by the energy integral

$$n_c = \int_{\text{CB}/0}^{\infty} f_{\text{FD}}(\varepsilon,\mu^{\text{ch}},T_c) D(\varepsilon) d\varepsilon \tag{2.14}$$

over the Fermi-Dirac distribution $f_{\text{FD}}(\varepsilon,\mu^{\text{ch}},T_c)$ times the density of states (DOS)

$D(\varepsilon)$ for all energies ε. Many authors point out that most transport models like i.e. the two-temperature model (TTM) assume an equilibrated electron system at all times, thus fail to accurately describe dynamics induced by low-excitation on ultra-short timescales but regain their validity after carrier thermalization.

Either way, carrier-carrier collisions will thermalize the carrier-system towards a carrier temperature T_c on a femtosecond timescale. T_c will be far greater than the lattice temperature T_l, thus induce a highly non-equilibrium state between the carrier and lattice subsystem. Due to electron-phonon collisions, the two subsystems will relax towards the same temperature within the so-called electron-phonon relaxation time. In analogous treatment within the Boltzmann equation framework, it can be found that the typical electron-phonon relaxation time for metals is in the order of picoseconds and up to hundreds of picoseconds for semiconductors and dielectrics, depending on the density of excited electrons. Electron-phonon collisions typically occur on a timescale of a few femtoseconds, but the transferred energy per collision is small due to the mass ratio of electrons to ions of about $m_e/m_i < 1/2000$, leading to the relaxation timescale being three orders of magnitude large than electron-phonon collision timescale. Nevertheless, electron-phonon relaxation time is always a function of electron-phonon coupling, which is a complex interplay between occupied electronic states and phonon spectra. However, modelling this coupling in a rate equation framework is a reasonable approximation if the coupling constant is parametrized sensibly.

The simplest model to describe this is the so-called simple two-temperature model. In this approximation, we neglect transport effects and assume a constant heat capacity c_i for the electron c and lattice l subsystem respectively. Also, we assume the energy coupling G being proportional to the temperature difference, reading

$$-c_c \frac{\partial T_c}{\partial t} = c_l \frac{\partial T_l}{\partial t} = G(T_c - T_l). \tag{2.15}$$

From this, we can identify an electron-phonon relaxation time of $\tau_c = \frac{c_c c_l}{G(c_l + c_c)}$. Unfortunately, the assumption of a constant specific electronic heat capacity, as well as the assumption of a constant electron-phonon collision parameter G, does not hold. For metals, a linear relation $c_c = \gamma T_c$ between carrier heat capacity and carrier temperature can directly be derived from Sommerfeld theory. Extending equation

(2.15) with this temperature-dependent heat capacity under the assumption $c_c \gg c_l$ will lead to linear decrease in electronic temperature

$$T_c(t) = -\frac{G}{\gamma}t + T_c(0). \tag{2.16}$$

Surprisingly, this very simplified model leads to good insights in the explanation of ultra-fast reflectivity measurements on homogeneously heated gold films [116] but fails at the description of more complex systems. More sophisticated descriptions of electron-lattice relaxation were developed by Kaganov, Lifshitz and Tantarov [117] to describe Cherenkov radiation, a process where ultra-fast free electrons propagate through an ion lattice, and were later adopted in the context of ultra-fast laser excitation by Anisimov [118, 119]. The derived electron-phonon coupling parameter reads

$$G = \frac{\pi^2}{6}\frac{m_e n_c c_s^2}{\tau_{\mathrm{fp}} T_c} \tag{2.17}$$

with the velocity of sound c_s within the material and τ_{fp} as the average inverse collision frequency. Allen [120] derived an expression for electron-phonon coupling based on Boltzmann collision integrals, thus dropping the assumption of free electrons. The derived coupling parameter reads

$$G = \frac{3\hbar\lambda\left\langle\omega^2\right\rangle}{\pi k_b T_c} \tag{2.18}$$

with $\lambda\left\langle\omega^2\right\rangle$ being the Eliashberg spectral function. In practice, $\lambda\left\langle\omega^2\right\rangle$ is calculated by DFT simulations [121] or taken from experimental data [122]. Furthermore Lin [121] derived another expression with the objective to incorporate possible T_c-dependencies based on the derivation of Allen resulting in

$$G = \frac{\pi\hbar k_b \lambda\left\langle\omega^2\right\rangle}{D(\epsilon_F)}\int_{-\infty}^{\infty} D(\epsilon)^2\left(-\frac{\partial f}{\partial \epsilon}\right)d\epsilon. \tag{2.19}$$

Based on this calculation, Lin also built up a database for metals [121, 123–125] based on experimentally determined Eliashberg spectral functions and density of states functions from ab initio DFT calculations.

However, all the presented approaches apply for metals but not for semiconductors. In case of semiconductors or dielectrics the density of generated electron-hole plasma alters not only the heat capacity of the plasma, but also changes the carrier-phonon collision probabilities drastically, leading towards a complex interplay of all involved parameters. First Boltzmann equation based approaches to determine the electron density-dependent electron-phonon coupling of SiO_2 were performed by Brouwer [126]. Nevertheless, the attained CB electron densities and electron temperatures differ hugely with inciting laser intensity and pulse duration, rendering it very difficult to develop a compact expression for the electron-phonon relaxation time. This is reflected in the variance of experimental data on the electron-phonon relaxation time in band gap materials [127–129]. This throws us back to the usage of carrier heat capacity based rate equation, analog to equation (2.15), where we assume a parametrized carrier-phonon relaxation time $\tau_c(n_c)$ and carrier density-dependent heat capacity derived from Sommerfeld theory. Thus we can write

$$G = \frac{c_c}{\tau_c} \tag{2.20}$$

$$\text{with} \qquad c_c = \frac{\partial U_c}{\partial T_c}. \tag{2.21}$$

2.3 Electron Thermal Conductivity

During laser irradiation, ultra-fast laser pulses do not only induce a highly non-equilibrium state between the carrier and ion subsystems, but also generate a spatial non-homogeneous temperature field within the carrier subsystem. Simultaneously to carrier-phonon relaxation, carrier-carrier collisions constitute a pathway for spatial heat conduction within the carrier subsystem, driving the spatial temperature distribution towards a state of vanishing temperature gradients. This is well-known as thermal conductivity. Thermal conductivity within the carrier subsystem occurs on the timescale of electron thermalization. As mentioned in section 2.2, electron-phonon relaxation takes place on a timescale roughly three orders of magnitude larger than carrier-carrier collisions. As a result, spatial equilibration of the carrier subsystem generates an energy flux deep into the sample, followed by energy dissipating into the ion subsystem. It is widely known that in metals, carrier-carrier

collisions are the dominant heat conduction mechanism. In semiconductors, the lack of CB carriers renders phononic heat transport the main equilibration pathway within the ground state. Excited semiconductors, however, show metallic carrier heat conduction if sufficient CB states are filled. Therefore, carrier heat conduction will dominate the spatial distribution of energy in both, metals and semiconductors, thus dominating macroscopic observables like ablation depth or damage threshold.

The thermal conductivity of the carrier subsystem is typically modelled with macroscopic continuum equations based on the classical Fourier law

$$\dot{\mathbf{q}} = -\kappa \nabla T_c \tag{2.22}$$

which assumes a heat flux $\dot{\mathbf{q}}$ proportional to the gradient of carrier temperature. The proportionality scalar κ is the so-called head conduction coefficient or thermal diffusivity. The Fourier law combined with the continuity equation, and therefore the assumption of energy conservation, leads to the well-known heat transport equation

$$c_c \partial_t T_c = \nabla(\kappa \nabla) T_c \tag{2.23}$$

and builds the basis of the often-applied and later described TTM 2.3.1 or, in the case of band gap materials the electron density-dependent two-temperature model (nTTM) 2.3.2. This approach holds its validity as long as the Fourier law holds. This restricts the approach temporally to timescales greater than the typical collision time of electrons and demands the characteristic feature of the temperature profile to be larger than the mean free path of charge carriers in order to achieve a valid description. Not only does the Fourier law implicitly demand equilibrium carrier distributions, an assumption that does not hold during ultra-short laser pulses, but it also assumes an instantaneously build-up heat flux, which is also not valid during ultra-short timescales. Further, the Fourier law does not account for ballistic electrons, which are reported to play a crucial role in the ablation mechanics of metals [116]. Despite this, implementations of the Fourier law generate great agreement with experimental data for ablation thresholds and depths in metals. On one side, this is due to the fact that the assumed thermal diffusivities κ are often phenomenologically measured quantities and are fine-tuned in order to reproduce

experimental data. On the other side however, kinetic approaches based on the Boltzmann transport equation [130] yield identical results in the context of laser ablation simulations. Also studies on the extension of the Fourier law

$$\tau_c \frac{\partial \dot{\mathbf{q}}}{\partial t} + \dot{\mathbf{q}} = -\kappa \nabla T_c \tag{2.24}$$

to account for the build-up time of the heat flux indicate that the finite propagation speed of the heat flux has minor to no effects on the temporal and spatial evolution of the lattice system but is numerically costly due to the hyberbolic nature of the resulting partial differential equation [131, 132]. Under consideration of the obtainable results, the application of the classical Fourier law seems to be appropriate for simulation timescales greater than the carrier-carrier collision time. This leaves us in search for a reasonable parametrization of κ.

For metals we can write the electron thermal diffusivity as

$$\kappa = \frac{1}{3} c_c \langle v^2 \rangle \tau_{col} \tag{2.25}$$

with the mean-square velocity $\langle v^2 \rangle$ of electrons and τ_{col} as the time of free flight. The time of free flight τ_{col} is determined by electron-electron and electron-phonon collisions and therefore shows a strong T_c and T_l dependency. For Fermi distributed electrons with temperatures below the Fermi temperature the expression [133]

$$\kappa(T_l,T_c) = \frac{1}{3} v_{\mathrm{F}} \gamma \frac{T_c}{A T_c^2 + B T_l}, \tag{2.26}$$

can be derived under the assumptions $c_c = \gamma T_c$, $v = v_{\mathrm{F}}$, τ_c and $1/\tau_{\mathrm{col}} = A T_c^2 + B T_l$. Here, the parameters A and B can be used as fitting parameters and arise from the assumptions $\tau_c \propto T_c^2$ and $\tau_{ep} \propto T_l$. For ultra-fast single pulse ablation simulations we can assume that $T_l \ll T_c$ and $A \ll B$ during the timescale of heat transport, reducing equation (2.26) to [134]

$$\kappa(T_c) = \underbrace{\frac{1}{3} \frac{v_{\mathrm{F}}^2 \gamma}{B T_l}}_{\equiv \kappa_0} T_c, \tag{2.27}$$

rendering κ_0 a often chosen as a fitting parameter. However, for electron temperatures far above the Fermi temperature, these descriptions lose their validity. This leads to the desire to construct approximated phenomenological wide-range models. The most popular being [134]

$$\kappa(T_c,T_l) = K\frac{(\theta^2+0.16)^{\frac{5}{4}}(\theta^2+0.44)\theta}{(\theta^2+0.092)^{\frac{1}{2}}(\theta^2+b\beta)} \tag{2.28}$$

with $\theta = \frac{k_\mathrm{B}T_c}{E_\mathrm{F}}$ and $\beta = \frac{k_\mathrm{B}T_l}{E_\mathrm{F}}$. K and β, again, are fitting parameters. The key feature of this model is that the low electron temperature limit $k_\mathrm{B}T_c \ll E_\mathrm{F}$ results again in

$$\kappa \propto T_c, \tag{2.29}$$

while the high temperature limit gives the well-known thermal diffusivity

$$\kappa \propto T^{\frac{5}{2}} \tag{2.30}$$

for low-density plasmas [135].

In the case of band gap materials, however, the density of the excited carrier plasma has to be taken into account. In the relaxation-time limit of the Boltzmann equation, heat conduction within the carrier system can be written as [109, 136]

$$\kappa = n_c\sigma_c\frac{F_0(\eta_c)}{F_{1/2}(\eta_c)}\frac{T_c}{q}\left[6F_2(\eta_c)F_0(\eta_c) - \frac{4F_1(\eta_c)^2}{F_0(\eta_c)^2}\right] \tag{2.31}$$

with σ_c being the mobility of charge carriers and

$$\eta_e = \frac{\mu_e^{\mathrm{ch}} - E_c}{k_B T_c} \tag{2.32}$$

being the reduced chemical potential. F_i denotes the Fermi-Dirac integral

$$F_i(\eta) = \frac{1}{\Gamma(i+1)}\int_0^\infty \frac{\eta^i}{\exp(t-\eta)+1}dt \tag{2.33}$$

$$\text{with} \qquad \Gamma(n) = \int_0^\infty x^{n-1}e^{-x}dx \tag{2.34}$$

being the gamma function. Note that for low excitations the assumption of Maxwell-Boltzmann distributed charge carriers becomes a reasonable approximation, which reduces (2.31) to

$$\kappa \propto n_c T_c. \tag{2.35}$$

and gives an analogue, but carrier density-dependent, expression to the low-temperature solution of metals (2.29).

2.3.1 Two-Temperature Model - TTM

The main idea of the TTM is that heat transport within the carrier and ion subsystem occur on distinct timescales, rendering it prudent to describe heat transport separately for both systems. The TTM was first introduced by Anisimov [119] under the assumption that the two subsystems exchange energy by electron-phonon collisions with a rate proportional to the temperature difference. For each system, the exchange of internal energy dU_i^{ex} can therefore be written as a rate equation of the form

$$dU_l^{\mathrm{ex}} = -dU_c^{\mathrm{ex}} = G\left(T_c - T_l\right), \tag{2.36}$$

with G as the electron-phonon coupling rate. By proposing that each temporal change of internal energy $\partial_t U_i$ only depends on temporal change in temperature $\partial_t T_i$, we can write

$$\partial_t U_i(T_i) = \frac{\partial U_i}{\partial T_i}\frac{\partial T_i}{\partial t} \tag{2.37}$$

and identify $c_i = \frac{\partial U_i}{\partial T_i}$ as the specific heat capacity for the respective system. Additionally, we assume that each subsystem with spatial temperature gradients shows heat conduction according to Fourier's law

$$\dot{\mathbf{q}} = -\kappa(\mathbf{r},T(\mathbf{r}))\nabla_{\mathbf{r}} T(\mathbf{r}) \tag{2.38}$$

with the spatial and temperature-dependent heat conduction coefficient κ. Now we apply the well-known continuity equation

$$\partial_t U_i = -\nabla \cdot \dot{\mathbf{q}}_\mathbf{i} + \Lambda \tag{2.39}$$

with Λ as an external source term and arrive at the general heat conduction equation

$$\partial_t U_i = \nabla \cdot [\kappa(\mathbf{r},T_i(\mathbf{r}))\, \nabla T_i] + \Lambda. \tag{2.40}$$

Doing this for each subsystem and identifying the external source term Λ as a superposition of the inter-subsystem exchange and the coupling to the laser field $S = dI/dx$, we arrive at the so-called TTM

$$c_c \frac{\partial T_c}{\partial t} = \nabla \cdot (\kappa_c \nabla T_c) - G\,(T_c - T_l) + S, \tag{2.41}$$

$$c_l \frac{\partial T_l}{\partial t} = \nabla \cdot (\kappa_l \nabla T_l) + G\,(T_c - T_l)\,. \tag{2.42}$$

The TTM is widely applied for theoretical predictions of experimentally observed phenomena in laser irradiated metals [13, 116, 137]. These effects mostly include heating rate and thermal conductivity, the determination of ablation and damage thresholds, or in combination with MD or hydrodynamic simulations, predictions of the melting depth and crater formation.

2.3.2 Density-dependent Two-Temperature Model - nTTM

The TTM presented in section 2.3.1 fails at the description of band gap materials such as semiconductors or dielectrics due to the varying transport properties with changing carrier excitations. At room temperature, band gap materials typically show a filled VB and a sparsely occupied CB. In the context of the modelling of laser ablation, this is a very crucial feature since CB electrons yield the major contribution to heat conduction at excited states, but show a vanishing contribution for the ground state.

Based on the broad success of the TTM, it was first expanded by Driel [109] to

include charge carrier effects and was adopted by several other groups [91, 92, 110, 138]. The derivation of the model can be done analogously to the TTM, while the main improvement lays in the description of the internal energy of charge carriers. From Sommerfeld theory, we know that we can write the internal energy of a non-degenerate electron subsystem with a band gap E_g and an electron density n_c as

$$U_c = n_c \left(E_g + 3k_b T_c\right). \tag{2.43}$$

Assuming and inserting

$$E_g = E_g(n_c, T_l) \tag{2.44}$$

alters the carrier heat capacity to

$$\frac{\partial U_c}{\partial T_c} = 3n_c k_b. \tag{2.45}$$

Inserting this into the general heat conduction equation, we arrive at the so-called nTTM, consisting of two coupled partial differential equations

$$\begin{aligned} 3n_c k_b \frac{\partial T_c}{\partial t} &= \nabla \cdot (\kappa_c \nabla T_c) - G\left(T_c - T_l\right) + S \\ &\quad - \frac{\partial n_c}{\partial_t}\left(E_g + 3k_b T_c\right) - n_c \left(\frac{\partial E_g}{\partial n_c}\frac{\partial n_c}{\partial t} + \frac{\partial E_g}{\partial T_l}\frac{\partial T_l}{\partial t}\right) \end{aligned} \tag{2.46}$$

and

$$c_l \frac{\partial T_l}{\partial t} = \nabla \cdot (\kappa_l \nabla T_c) + G\left(T_c - T_l\right). \tag{2.47}$$

To include the laser light induced generation of charge carriers in the CB the nTTM is mostly supplemented by a rate equation for charge carriers of the form

$$\frac{dn_c}{dt} = \sum_i \alpha_i I^i - \gamma_{\text{Aug}}\, n_c^3 + \delta_{\text{imp}}\, n_c, \tag{2.48}$$

already introduced in equation (2.11). Alternatively, some groups include these effects using a Monte-Carlo description of carrier dynamics [139].

At this point it is important to mention that the presented derivation of the nTTM

assumed a non-degenerate carrier system. For strong laser fields, and therefore for highly non-equilibrium carrier distributions, this seems like a crucial simplification. However, the Sommerfeld description of a degenerate electron-hole gas leads to an internal energy of

$$U_c = n_c E_g + \frac{3}{2} n_c k_B T_c \left[\frac{F_{3/2}(\eta_e)}{F_{1/2}(\eta_e)} + \frac{F_{3/2}(\eta_h)}{F_{1/2}(\eta_h)} \right] \tag{2.49}$$

with the introduction of the reduced chemical potentials

$$\eta_e = \frac{\mu_e^{\mathrm{ch}} - E_c}{k_B T_c} \qquad \text{and} \qquad \eta_h = \frac{\mu_h^{\mathrm{ch}} - E_c}{k_B T_h} \tag{2.50}$$

for electrons and holes. This definition leads to an altered version of (2.46) namely [91, 110]

$$\begin{aligned} 3 n_c k_b \frac{\partial T_c}{\partial t} = {} & \nabla \cdot (\kappa_c \nabla T_c) - G\,(T_c - T_l) + \Lambda \\ & - \frac{\partial n_c}{\partial_t} \left(E_g + 3 k_b T_c \left[\frac{F_{3/2}(\eta_e)}{F_{1/2}(\eta_e)} + \frac{F_{3/2}(\eta_h)}{F_{1/2}(\eta_h)} \right] \right) \\ & - n_c \left(\frac{\partial E_g}{\partial n_c} \frac{\partial n_c}{\partial t} + \frac{\partial E_g}{\partial T_l} \frac{\partial T_l}{\partial t} \right) \\ & - \frac{3}{2} k_B T_c n_c \frac{\partial n_c}{\partial_t} \frac{\partial \eta_e}{\partial n_c} \left(1 - \frac{F_{3/2}(\eta_e)}{F_{1/2}(\eta_e)} \frac{F_{-1/2}(\eta_e)}{F_{1/2}(\eta_e)} \right) \\ & - \frac{3}{2} k_B T_c n_c \frac{\partial n_c}{\partial_t} \frac{\partial \eta_e}{\partial n_h} \left(1 - \frac{F_{3/2}(\eta_h)}{F_{1/2}(\eta_h)} \frac{F_{-1/2}(\eta_h)}{F_{1/2}(\eta_h)} \right). \end{aligned} \tag{2.51}$$

2.3.3 Kinetic Transport Models

As mentioned in section 2.3.2, the nTTM is the most frequently applied model to simulate laser ablation of semiconductors. Although the extension from TTM to nTTM is the natural improvement, it also brings some massive downsides with it. In both cases, the general heat transport equation is assumed, thus heat conduction is purely driven by temperature gradients. This, however, does not correctly reflect spatial equilibration when vastly fluctuating local heat capacities due to inhomogeneous charge carrier excitations are considered. In the case of unexcited semiconductors, vanishing charge carrier densities in the CB lead to a vanishing

specific heat capacity $\frac{\partial U}{\partial T_c} \propto n_c$, generating immense carrier temperature gradients while showing vanishingly low energies. These immense charge carrier temperature gradients alone are mainly a numerical problem. The physical failure however is that energy transport is only allowed by heat transport, completely ignoring energy transport by advection. Advection by charge carrier transport does not only transport energy, but also equalizes the local heat capacities. Ignoring this equalization process does not only provoke artificial and unphysical energy fluxes but also overestimates carrier confinement due to local band gap narrowing [110]. Needless to say, the correct carrier dynamics shows to be of crucial importance for the resulting macroscopic dynamics of the sample.

A key part of this work is to improve the simulation models available for studying laser ablation of covalent materials. Due to the vast downsides of the nTTM approach, we are in search for more sophisticated transport models for charge carriers which account for energy transport apart from heat conduction. Naturally, we start with a kinematic description of charge carriers and derive everything further from statistical properties. However, energy transport properties in semiconductors are of great importance to the world since the invention of the diode. The description of these transport properties builds the basis of any semiconductor device ever produced. It is fairly safe to say that a considerable amount of research has already gone into the modelling of charge carrier dynamics in semiconductors. It is also safe to assume that not all of this knowledge has been fully utilized and transferred into the modelling of laser ablation.

From literature, we know the hierarchy of kinetic transport equations applicable for semiconductors and display them in figure 2.3. The hierarchy starts from n-coupled single particle Newtonian equations. From each equation, a subsequent equation can be derived under some reasonable assumptions. The main approximation for each transition is also denoted in figure 2.3. A rigorous derivation of each equation is outside the scope of this work, but detailed treatment of transport equations in semiconductors in general can be found in [140]. Anyway, we follow Jüngel [140] and step in at the semi-classical Boltzmann equation for an arbitrary

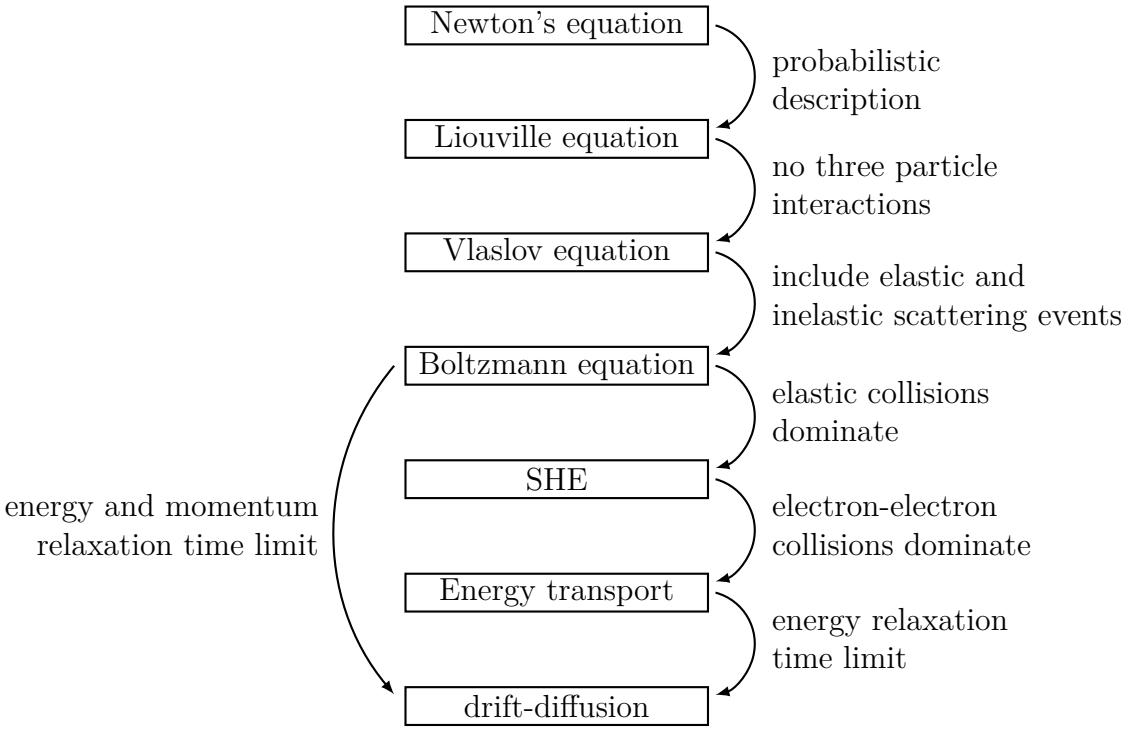

Figure 2.3: Schematic hierarchy of semiconductor transport models. The models respectively follow from the assumptions indicated by the arrows.

distribution function $f(\mathbf{r},\mathbf{k},t)$ reading

$$\partial_t f + \frac{1}{\hbar}\nabla_{\mathbf{k}} E(\mathbf{k}) \cdot \nabla_{\mathbf{r}} f + \frac{q}{\hbar}\nabla_{\mathbf{r}} V \cdot \nabla_{\mathbf{k}} f = Q(f). \tag{2.52}$$

Here, $\frac{1}{\hbar}\nabla_{\mathbf{k}} E(\mathbf{k})$ denotes the group velocity within the energy band $E(\mathbf{k})$ and V the effective electrical potential given by Poisson's equation

$$\nabla_{\mathbf{r}}^2 V = q(n_c(\mathbf{r}) - C(\mathbf{r})) \tag{2.53}$$

for charges q within the doping profile $C(\mathbf{r})$. $Q(f)$ is the collision operator accounting for arbitrary scattering mechanisms. In literature, this equation system is often denoted as Boltzmann-Poisson system. Although the Boltzmann-Poisson system offers all the transport effects we desire for the modelling of laser ablation, it is still a description based on the evolution of the local carrier distribution f. For our

use case of massive multi-parallel high-performance simulation of the macroscopic material dynamic, this is still a description that is computationally too expensive. In our search for a more compact description, we perform more approximations on the collision operator Q and arrive at the Boltzmann energy transport equation (BETE) presented in section 2.3.4. This description comes with the main advantage of being a solely energy gradient based description, thus eliminating the described problems accompanied by treating energy propagating separately in a temperature-based and carrier density based description. Alternatively, we perform the energy and momentum relaxation time approximation to derive the drift-diffusion limit of the Boltzmann equation shown in section 2.3.5.

2.3.4 Boltzmann Energy Transport Equation - BETE

The semi-classical Boltzmann equation (2.52) is still very costly to solve numerically due to the complex nature of the collision operator and the high number of independent variables. In the pursuit of a simpler model, we wish to simplify the Boltzmann equation by making the transition from a kinetic to a fluid dynamical model by performing hydrodynamic limits.

We follow [141] and impose the following assumptions:

- By applying the Matthiessian rule, the collision operator $Q(f)$ can be split into an elastic $Q(f)_{\text{el}}$ and an inelastic $Q(f)_{\text{inel}}$ operator and can therefore be written as

$$Q(f) = Q(f)_{\text{el}} + Q(f)_{\text{inel}}. \tag{2.54}$$

- The operator $Q(f)_{\text{inel}}$ is linear.

- The scattering rate is symmetric in $\mathbf{k}$.

To make the transition towards the hydrodynamic limit, we introduce the scaling

factors by defining the thermal velocity as reference velocity

$$v_{\text{ref}} = \sqrt{\frac{k_{\text{B}} T_c}{m_e^*}}. \tag{2.55}$$

The average timescales τ_{el} and τ_{inel} on which elastic and inelastic collisions occur respectively, lead to the mean free paths

$$\lambda_{\text{el}} = \tau_{\text{el}} v_{\text{ref}} \tag{2.56}$$

$$\text{and} \quad \lambda_{\text{inel}} = \tau_{\text{inel}} v_{\text{ref}}. \tag{2.57}$$

$$\text{We define a reference length} \quad \lambda_{\text{ref}} = \sqrt{\lambda_{\text{el}} \lambda_{\text{inel}}} \tag{2.58}$$

$$\text{and a reference time} \quad \tau_{\text{ref}} = \lambda_{\text{ref}} / v_{\text{ref}}. \tag{2.59}$$

$$\text{We scale position} \quad \mathbf{r} = \lambda_{\text{ref}} \mathbf{r}_{\text{sc}} \tag{2.60}$$

$$\text{and time} \quad t = \tau_{\text{inel}} t_{\text{sc}}. \tag{2.61}$$

Inserting these substitutions into the semi-classical Boltzmann equation leads to

$$\alpha^2 \partial_t f + \alpha \nabla_{\mathbf{k}} E(\mathbf{k}) \cdot \nabla_{\mathbf{r}} f + \alpha \nabla_{\mathbf{r}} V \cdot \nabla_k f = Q_{\text{el}}(f) + \alpha Q_{\text{inel}}(f) \tag{2.62}$$

and implicitly defines the scaling parameter

$$\alpha^2 = \frac{\lambda_{\text{el}}}{\lambda_{\text{inel}}}. \tag{2.63}$$

Now we impose physical assumptions. First, we demand that elastic collisions dominate the transport mechanics. We assume that the collision operator

$$Q(f) = Q(f)_{\text{c}} + Q(f)_{\text{ph}} \tag{2.64}$$

is given by a result of carrier-carrier $Q(f)_{\text{c}}$ and carrier-phonon $Q(f)_{\text{ph}}$ scattering. The carrier distribution function f can be approximated by the Fermi-Dirac distribution

$$f \overset{!}{=} f(\mu^{\mathrm{ch}},T_c,E) = \frac{1}{1+\exp\left(\frac{E-\mu^{\mathrm{ch}}}{T_c}\right)}. \tag{2.65}$$

We assume parabolic bands, giving us the energy surface

$$E(\mathbf{k}) = \frac{\hbar^2}{2m}\mathbf{k}^2. \tag{2.66}$$

These approximations, combined with the assumption that the scattering rate scales with $\sqrt{E}$ [142], are needed to perform the Fokker-Planck relaxation time approximation [143], yielding the energy transition rate

$$Q_{\mathrm{ph}}(\mu^{\mathrm{ch}},T_c,T_l) = \frac{3}{2}\frac{n_c(\mu^{\mathrm{ch}},T_c)k_b(T_c-T_{\mathrm{l}})}{\tau_{\mathrm{ph}}} \tag{2.67}$$

with $1/\tau_{\mathrm{ph}}$ as the mean carrier-phonon collision frequency. Now we insert all these assumptions into the semi-classical Boltzmann equation and perform the a Hilbert expansion in α for

$$f = f_0 + \alpha f_1 + \alpha^2 f_2 + \dots. \tag{2.68}$$

From our demand that elastic collisions dominate the transport mechanics, follows $\alpha \ll 1$, which motivates us to perform the Hilbert expansion up to first order. One can show [141] that the resulting equation system is only solvable if the equations

$$0 = \partial_t n_c - \frac{1}{q}\nabla\cdot\mathbf{J}_n, \tag{2.69}$$

$$\mathbf{W} = \partial_t U - \frac{1}{q}\nabla\cdot\mathbf{J}_U + \nabla V\cdot\mathbf{J}_n, \tag{2.70}$$

$$\mathbf{J}_n = D_{11}\nabla\left(\frac{q\sigma_e}{k_bT_c}\right) + D_{12}\nabla\left(\frac{-1}{k_bT_c}\right) - D_{11}\frac{q\nabla V}{k_bT_c}, \tag{2.71}$$

$$\text{and} \qquad \mathbf{J}_U = D_{21}\nabla\left(\frac{q\sigma_e}{k_bT_c}\right) + D_{22}\nabla\left(\frac{-1}{k_bT_c}\right) - D_{21}\frac{q\nabla V}{k_bT_c} \tag{2.72}$$

are fulfilled with

$$\mathbf{D} = \frac{q\hbar^3\tau_{\mathrm{ee}}}{6\sqrt{2}\pi}\begin{pmatrix} 1 & \frac{3}{2}k_bT_c \\ \frac{3}{2}k_bT_c & \frac{15}{4}(k_bT_c)^2 \end{pmatrix}. \tag{2.73}$$

The BETE describes energy transport in terms of internal energy coupled to charge carrier transportation, while charge carrier temperature becomes a value implicitly defined by the internal energy (2.49). Of course, for application of the BETE in laser ablation simulations the carrier continuity equation (2.69) and energy continuity equation (2.70) have to be supplemented by the laser and inter-system coupling term Λ. Anyway, the equations forming the BETE account for considerably more physical effects when compared to the nTTM. The carrier continuity equation (2.69) includes transport terms, which allow for charge carrier diffusion driven by entropic forces, charge carrier density gradients and internal and external electrical fields. Furthermore, the energy transported in advection of charge carriers enters the energy balance equation (2.70).

2.3.5 Density Dependent Thermal Spike Model - TSM

Starting from the BETE, we apply a second scaling

$$\beta = \tau_{\mathrm{ph}}/\tau_{\mathrm{ref}} \ll 1. \tag{2.74}$$

This second scaling corresponds to the limit where the energy relaxation time τ_{ph} is of the same order as the momentum relaxation time τ_{ee} and the thermal energy is high compared to the kinetic energy needed to surpass the distance λ_{ref}. In analogous treatment to section 2.3.4, we receive the drift-diffusion limit defined by the equations [141]

$$\frac{\partial n_c}{\partial t} = -\nabla\cdot\mathbf{J}_n + \frac{dn_c}{dt} \tag{2.75}$$

$$\text{and} \qquad \mathbf{J}_n = -q\sigma_n\left(\frac{k_bT_c}{q}\nabla n_c + n_c\nabla V\right). \tag{2.76}$$

In combination with the ambipolar approximation, Driel [109] showed that the total carrier flux **J** then can be written as

$$\mathbf{J} = -D_0 \left[\nabla n_c + \frac{2n_c}{k_\mathrm{b} T_\mathrm{c}} \nabla E_\mathrm{g} + \frac{n_c}{2T_\mathrm{c}} \nabla T_\mathrm{c} \right] \tag{2.77}$$

with the ambipolar diffusion coefficient

$$D_0 = \frac{1}{q} k_\mathrm{b} T_c \frac{\sigma_e \sigma_h}{\sigma_e + \sigma_h}, \tag{2.78}$$

including the electron σ_e and hole σ_h mobilities. This drift-diffusion limit of the Boltzmann equation combined with energy advection by carrier transportation and heat conduction will lead us towards the so-called Thermal-Spike model (TSM). To do this, we write the energy flux

$$\mathbf{W} = \left(E_\mathrm{g} + 3 n_c k_\mathrm{B} T_\mathrm{c} \right) \mathbf{J} - \kappa_\mathrm{c} \nabla T_\mathrm{c}. \tag{2.79}$$

as the combination of heat conduction by the well-known Fourier law and advection by the particle flux. The continuity equation for carrier density and energy then read

$$\frac{\partial n_c}{\partial t} = -\nabla \cdot \mathbf{J} + \frac{dn_c}{dt} \quad \text{and} \quad \frac{\partial U}{\partial t} = -\nabla \cdot \mathbf{W} + \frac{dU}{dt}. \tag{2.80}$$

Insertion of laser absorption and electron-phonon coupling analog to section 2.3.2 leads to the equation system

$$\begin{aligned} 3 n_c k_\mathrm{b} \frac{dT_c}{dt} = \quad & \nabla \cdot \left(\left[E_\mathrm{g} + 3 n_c k_\mathrm{B} T_\mathrm{c} \right] \mathbf{J} \right) \\ & + \nabla \cdot \left(\kappa_\mathrm{c} \nabla T_c \right) - G(T_c - T_\mathrm{ph}) + S \\ & - \frac{dn_c}{dt} (E_g + 3 k_\mathrm{B} T_c) - n_c \frac{\partial E_g}{\partial t} \end{aligned} \tag{2.81}$$

$$\text{and} \qquad \frac{\partial n_c}{\partial t} = \nabla \cdot \left(D_0 \left[\nabla n_c + \frac{2n_c}{k_\mathrm{b} T_\mathrm{c}} \nabla E_\mathrm{g} + \frac{n_c}{2T_\mathrm{c}} \nabla T_\mathrm{c} \right] \right) + \frac{dn_c}{dt} \tag{2.82}$$

where S and $\frac{dn_c}{dt}$ are given by the terms from section 2.1 describing laser light absorption or charge carrier generation. Note that for vanishing particle fluxes the

TSM reduces to the nTTM.

Analogous to the nTTM, the TSM can also be formulated for degenerate electron systems by inserting the degenerate particle flux

$$\mathbf{J} = -D\left[\nabla n_c + \frac{n_c}{k_\mathrm{b}T_\mathrm{c}}\left(\frac{F_{1/2}(\eta_e)}{F_{-1/2}(\eta_e)} + \frac{F_{1/2}(\eta_h)}{F_{-1/2}(\eta_h)}\right)\nabla E_\mathrm{g} + \frac{n_c}{T_\mathrm{c}}\left(2\frac{\frac{F_1(\eta_e)}{F_0(\eta_e)} + \frac{F_1(\eta_h)}{F_0(\eta_h)}}{\frac{F_{1/2}(\eta_e)}{F_{-1/2}(\eta_e)} + \frac{F_{1/2}(\eta_h)}{F_{-1/2}(\eta_h)}} - \frac{3}{2}\right)\nabla T_\mathrm{c}\right] \tag{2.83}$$

$$\text{with} \qquad D = \frac{1}{q}k_\mathrm{b}T_c\frac{\sigma_e\sigma_h}{\sigma_e+\sigma_h}\left[\frac{F_{1/2}(\eta_e)}{F_{-1/2}(\eta_e)} + \frac{F_{1/2}(\eta_h)}{F_{-1/2}(\eta_h)}\right] \tag{2.84}$$

derived in [109] into the energy continuity equations (2.80), assuming the the degenerate internal energy (2.49).

2.4 Ultra-fast Phase Transitions

During laser ablation, phase transitions occur as a result of sufficient laser energy absorption. These phase transitions can generally be divided into thermal or non-thermal processes.

Thermal Melting Processes Thermal melting processes follow thermodynamic pathways, driven by the second law of thermodynamics and the equipartition theorem. The main melting dynamics during laser ablation are homogeneous and heterogeneous melting. When the ion subsystem absorbs enough energy due to electron-phonon relaxation, the melting process starts at the surface of the sample. At the surface, the potential barrier for phase transition is the lowest due to the lack of dissipation into volume work. On top of that, the surface is typically the area of highest laser energy absorption, thus being the area of strongest electron-phonon heating. Depending on the applied fluence, the sample starts to melt or evaporate instantly, generating a liquid-solid or vapor-solid interface. This interface proceeds into the material limited by the speed of sound [144, 145]. This process is called heterogeneous melting. For higher fluences homogeneous melting can occur and was

observed in experiments [146] and computer simulations [35, 147]. Homogeneous melting is the process where the charge carrier subsystem is excited up to a considerable depth, again relaxing via electron-phonon relaxation, overheating the lattice and allowing nucleation processes to start simultaneously from several distributed critical nuclei. Rethfeld [35] studied the melting time of metals due to homogeneous melting in dependence of overheating T_l/T_m based on the probability

$$\omega = 2\left(\frac{16\sigma_{sl}^3\pi k_b^2 T_m^2}{3q^2}\right)^{\frac{1}{6}} n_s^2\sqrt{k_B T_l}\left(\frac{3k_B T_m^4}{16\pi q^4}\right)\eta\exp\left(-\frac{16\sigma_{sl}^3\pi k_b^2 T_m^2}{3q^2 k_b^3 T_l(T_l-T_m)^2}\right) \quad (2.85)$$

of the formation of one critical nucleus per time and volume derived in [148]. Here T_m describes the melting temperature, σ_{sl} the surface tension between the solid and liquid phase, η is a material specific parameter, n_s the density of the solid phase and q the latent heat for melting. It is found that the time for complete melting of overheated silver at $T_l/T_m = 1.35$ is about 100 ps, while silver overheated at $T_l/T_m = 1.45$ completely melts in roughly < 1 ps [35]. In contrast, with the speed of sound in silver being $v_s = 2200\,\mathrm{m/s}$, heterogeneous melting of a silver film of thickness $d = 100\,\mathrm{nm}$ would, roughly estimated, take

$$\frac{d}{v_s} \approx 45\,\mathrm{ps}. \quad (2.86)$$

Therefore, sub-picosecond melting-times can be reached with a sufficient laser fluence. However, the melting time is dominated by carrier-lattice equilibration rather than nucleation kinetics. Thus, melting times still show a lower limit in terms of electron-phonon relaxation time.

Non-thermal Melting Non-thermal melting on the other hand is based on the manipulation of interatomic bonding due to electronic excitation. After charge carrier thermalization but before electron-phonon relaxation, the electron subsystem is in an excited state with an extremely high charge carrier temperature, while the ion subsystem still remains at initial temperature. Metallic and covalent bonds are dependent on the electronic configuration of the respective atoms, thus showing a dependency on electronic excitation. DFT calculations for metals show that such

high temperature excitation tends to strengthen the effective electron-ion potential or, in case of simple metals like aluminium, show a neglectable effect on bonding strength [69, 149]. However, recent experiments suggest that bond softening in metals can occur due to surface effects [150]. Covalent materials like silicon on the other hand, show indisputable bond softening due to electronic excitation [69]. This bond softening originates from bonding VB electrons being excited into non-bonding CB states [68, 151], inducing drastic changes of the effective interatomic potential, resulting in weaker or even repulsive bonds. Strongly excited covalent materials undergo an ultra-fast change in interatomic bonding strength, allowing the lattice to restructure or disorder on a timescale of hundreds of femtoseconds. This process can be interpreted as melting but does not follow classic thermodynamical melting kinetics, hence the name non-thermal melting [152, 153].

2.5 Macroscopic Material Dynamic

2.5.1 The Complexity of the Long Time Material Dynamic

Carrier-phonon relaxation ultimately heats the lattice system. Sufficient laser heating will induce highly non-equilibrium states of the material, forcing the macroscopic system to equilibrate. The many possible relaxation pathways do not only depend on the studied material and infused laser energy, but also depend on the complex interplay of boundary conditions like external pressure or surrounding atmosphere [154]. However, this huge parameter space opens up an equally huge space of phenomena of ablation dynamic. Apart from ultra-fast phase transitions [34, 37, 155, 156] or slower heterogeneous and homogeneous melting [35–38], unusual material dynamics can be expected as a result of the inhomogeneous nature of the heating dynamic. Ultra-fast surface heating induces pressure or refraction waves propagating through the sample inducing spallation [37, 157–159]. For lower laser intensities, irradiated material is modified but not removed, recrystalizing in nano-structures [160–163] like nano-gratings, nano-wells [164], nano-bumps [39–46], nano-jets or spikes [41–43, 47]. Under certain conditions, these spikes can be precisely manipulated to form helix structures [33, 48–51]. For higher fluences the relaxation of near-surface pressure

causes the ejection of hot droplets and chunks [56, 57] in laser intensity-dependent distributions [55]. The composition of the removed material is relevant for the re-deposition on nearby surfaces [58] and can be utilized in many ways. The structure of the remaining crater is observed and shows self-organized patterns changing with pulse count, intensity and pulse duration [165, 166]. These remaining features can be utilized to form functional surfaces [167–171] for plasmonic devices, waveguides or super hydrophobic surfaces [32, 168–172]. The material dynamics also changes drastically during simpler industrial applications like laser drilling, cutting or welding [59–61], where for example the damage of the sourrounding material is of interest.

The broad range of effects renders modelling of the material dynamics a challenging task and not every modelling technique is able to reproduce every observable of interest. However, in this work we want to focus on the underlying mechanics of the generation of such features. In the following, we present the core concepts of modelling techniques applied to reproduce these highly non-linear material dynamics.

2.5.2 Phenomenological Description of the Ablation Depth

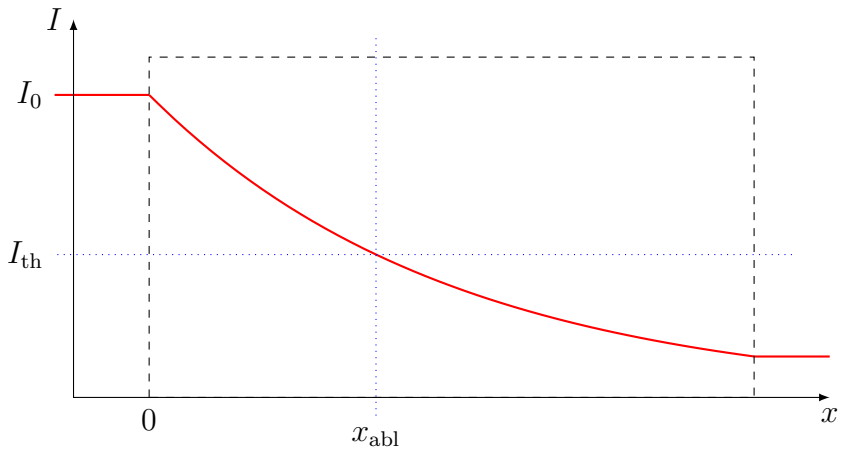

Figure 2.4: Sketch of local laser intensity $I(x)$ over sample length x. The sample is sketched by the dashed line. The estimated ablation depth x_{abl} and the threshold intensity I_{th} for ablation are denoted by the blue dotted lines.

The simplest estimation for the ablation depth x_{abl} follows directly from the assumption of neglectable heat transport and energy absorption by a constant SPA

entering the absorption law (2.1). The resulting laser intensity $I(x)$ within the sample is sketched in figure 2.4 and is directly proportional to the local energy deposition $\frac{dI}{dx}$. Such absorption behavior is described by the well-known Lambert-Beer law. When no energy transport is taken into account, we can define a threshold laser intensity I_{th} above which laser heating provides sufficient energy for material removal. Therefore, all material with $x < x_{\mathrm{abl}}$ gets ablated. The monotony of $I(x)$ directly demands

$$I_{\mathrm{th}}(x_{\mathrm{abl}}) \stackrel{!}{=} I_0 e^{-\alpha x_{\mathrm{abl}}} \quad \text{and thus implies} \quad x_{\mathrm{abl}} = \frac{1}{\alpha} \ln\left(\frac{I_0}{I_{\mathrm{th}}}\right). \tag{2.87}$$

Although the assumption of neglectable heat transport and Lambert-Beer absorption is of very disputable validity, the logarithmic dependency of ablation depth on laser intensity is often observed in metals. α is often adopted as a fitting parameter on experimental data, making it a phenomenological material parameter. Furthermore, under the assumptions introduced above, equation (2.87) can be written in terms of fluences, giving

$$x_{\mathrm{abl}} = \frac{1}{\alpha} \ln\left(\frac{\sigma}{\sigma_{\mathrm{th}}}\right). \tag{2.88}$$

This dependency is often applied in experiments to extrapolate the threshold fluence $\sigma_{\mathrm{th}}^{\mathrm{abl}}$ for material modification or ablation by fitting on ablation depth data. However, this oversimplification fails to describe the underlying ablation mechanisms in metals and completely fails for semiconductors where absorption coefficients undergo ultrafast changes during laser irradiation.

2.5.3 Hydrodynamic Material Dynamic Models

While phenomenological descriptions can determine the correct ablation depth, they lack insights into the dynamics of the ablation process. Analogously, heat-transport descriptions alone only offer insights into heat propagation and damage thresholds but not macroscopic material responses like the formation of a cupola, shock and rarefaction waves or general information about the sample surface. Such information is crucial, for example, for the explanation of the experimentally observed forma-

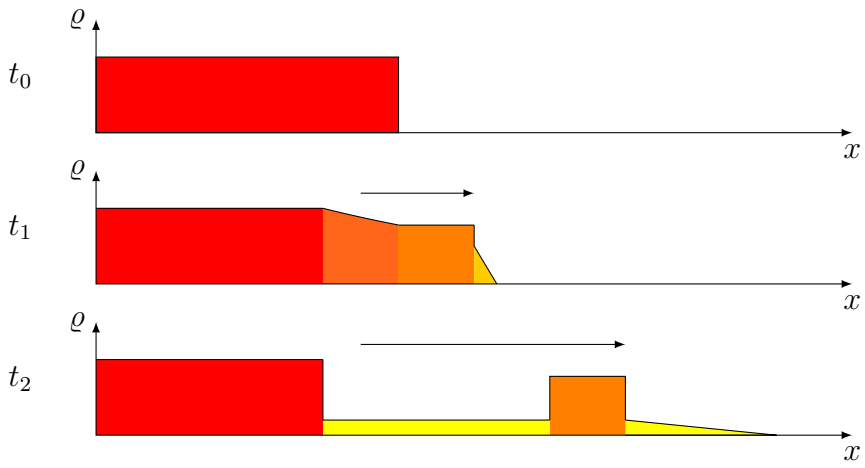

Figure 2.5: Sketch of typical laser ablation data obtained from hydrodynamical calculations on equation (2.91) at different times t_n. The colouring indicates the material density, where red is the density associated with a solid phase, orange associated with a molten phase and yellow associated with a vapour phase. The data shows an ejection of a layer of molten material.

tion of Newtonian rings [144]. Intrinsically, macroscopic effects are most efficiently modelled with macroscopic descriptions. On macroscopic timescales ultra-fast laser excitation can be viewed as an instantaneous heating process because carrier-lattice equilibration is typically faster than material expansion. This motivates a density field based model where a hydrodynamic description seems suitable.

The simplest of a variety of applied hydrodynamic models in the simulation of laser ablation is the so-called simple expansion model [173, 174]. The simple expansion model depicts the flow of expanding matter in terms of gas dynamics. In a one-dimensional formulation, the simple expansion model reads

$$\partial_t \varrho = -\partial_x(\varrho u), \tag{2.89}$$

$$\partial_t u = -\frac{1}{\varrho}\partial_x p - u\partial_x u \tag{2.90}$$

and describes the flow of density ϱ with velocity u in x-direction, depending on the local pressure p. In the simplest case this process can be viewed as an isentropic process, meaning constant entropy, implying a direct relation between pressure and density. This allows to calculate the density profile implicitly as the self similar

solution of [173]

$$\frac{x}{t}(\varrho) = -\sqrt{\frac{\partial p}{\partial \varrho}} + \int_{\varrho}^{\varrho_0} \frac{1}{\varrho'} \sqrt{\frac{\partial p}{\partial \varrho'}} d\varrho'. \tag{2.91}$$

Note that $\sqrt{\partial p/\partial \varrho} = c_s$ equals the local speed of sound. In figure 2.5, we display a typical one-dimensional solution of the presented hydrodynamic approach for different times. While the computational cost for this is rather low, we can clearly identify occurring ablation mechanics. However, this solution only maintains its validity under heterogeneous isentropic heating and therefore loses its validity for sub-picosecond laser pulses. To tackle this problem some groups extended the pure hydrodynamic approach with laser heating modelled by the TTM [159, 175, 176] and accomplished great accordance with experimental data for metals. The downside of this approach is that extensive assumptions have to be put into the material dynamics itself. For a hydrodynamic treatment of the material dynamic, detailed knowledge of the phase diagram as well as the thermodynamic pathways $p(\varrho)$ of the irritated material are needed as a parametrization. For example, nucleation kinetics, the nature of the thermal or non-thermal phase transition, instantaneous or delayed transition into a two-phase mixture, melting energies and vapor pressure have to be assumed [177].

2.5.4 Molecular Dynamics - MD

While hydrodynamic approaches allow for the computation of a large scale macroscopic material dynamics, the needed details of occurring phase transition are often unknown or the topic of interest itself. In contrast to hydrodynamic models where the phase behavior can be understood as an input parameter, molecular dynamics (MD) simulations offer an a priori inclusion of nucleation kinematics as well as the complete material behavior on an atomic scale. This renders the MD approach suitable for studying fast non-equilibrium phase transitions and atomistic features.

The basic idea behind this approach is to iteratively calculate the trajectory of each atom by integrating Newton's equation of motion for each atom separately for

a distinctive time step. The equation of motion for particle i reads

$$\mathbf{F}_i(\{\mathbf{r}\}) = m_i \ddot{\mathbf{r}}_i, \tag{2.92}$$

with m_i and $\mathbf{r}_i$ denoting the mass and position of particle i. Particle i interacts with every other particle of the ensemble, therefore the force $\mathbf{F}_i$ acting on particle i depends on the ensemble of positions of every atom of the ensemble $\{\mathbf{r}\}$. Consequently, we can write the force

$$\mathbf{F}_i = -\nabla_{\mathbf{r}_i} U(\{\mathbf{r}\}) = -\nabla_{\mathbf{r}_i} \underbrace{\left[U_1(\mathbf{r}_i) + \sum_{i \neq j} U_2(\mathbf{r}_i, \mathbf{r}_j) + \sum_{i \neq j} \sum_{i,j \neq k} U_3(\mathbf{r}_i, \mathbf{r}_j, \mathbf{r}_k) + \dots \right]}_{\equiv U(\{\mathbf{r}\})} \tag{2.93}$$

on particle i by a series of n-body potentials U_n. While the basic concept of MD is rather simple, the challenge lies within the choice or construction of $U(\{\mathbf{r}\})$. For a naive implementation the computational cost of N particles interacting with an n-body potential scales as N^n. This renders higher-order potentials useless for the simulation of macroscopic samples and yields the desire for simple fitting potentials, which can replicate the material property of interest. Such potentials are often phenomenological lower order potentials, fitted with various parameters to experimental data to reproduce desired macroscopic properties [178]. The macroscopic properties of interest are typically material specific observables like the bulk modulus, melting or evaporation temperature.

Nevertheless, with a well tailored interaction potential, the MD approach is able to describe all macroscopic phenomena involved during the ablation process on an atomic level. In the context of laser ablation, this unfolds the feasibility to observe formation of voids [179], material expansion [180] or the formation of crystal defects. Furthermore, the complete knowledge of the microstructure not only allows for the time resolved study of the propagation of cracks and other material defects but also for more complex effects like the generation of inter-metallic phases in multi material systems [181]. The greatest advantage of the MD approach is, however, the possibility of an atomistic description of the material far away from thermody-

namic equilibrium. This enables the possibility of a detailed investigation of the occurring ablation mechanisms under extreme conditions. With MD it is possible to distinguish between ablation based on evaporation [182] and ablation based on phase explosions [139, 179], Coulomb explosions [67, 88, 139] or spallation [158, 177]. Additionally, detailed statistics of the removed material can be obtained [57]. This includes information about how the removed material forms droplets after ablation, or how the removed material eventually redeposits on the sample surface and how this influences characteristics of the remaining crater.

The downside to this approach is the lack of accuracy in situations the potential was not designed to recreate, as well as the comparatively high computational cost for macroscopic samples. However, due to its advantages we choose the MD approach to be the main simulation technique applied which will be presented in detail in section 3.4.

2.5.5 Hybrid Simulation Techniques

MD simulations offer the required a priori inclusion of non-equilibrium phase and nucleation kinematics, thus seem to be the perfect model description for laser ablation. However, MD simulations alone are not able to model charge carrier dynamics due to their quantum nature. Even when treated as semi-classical particles, the sheer amount of particles needed to consider in a macroscopic sample would render this approach plainly unfeasible on todady's supercomputers. Since charge carrier dynamics play a major role in all ablation processes, their inclusion is essential. Multi-scale simulation approaches, as sketched in figure 3, solve this problem by simulating each subsystem on its respective timescale and couple each subsystem by an adequate description. In the context of laser ablation, this translates into the laser-affected zone being modelled within an MD approach. The charge carrier transport model is solved separately, while simultaneously being coupled to the MD system. To achieve huge macroscopic sizes, the sample can be extended by a hydrodynamic description. However, all further details and challenges of an hybrid setup are mainly of technical nature, with the major part consisting of the correct modelling of the respective interfaces. The implementation of the applied continuum-atomistic model and the respective coupling methods will be given in chapter 3.

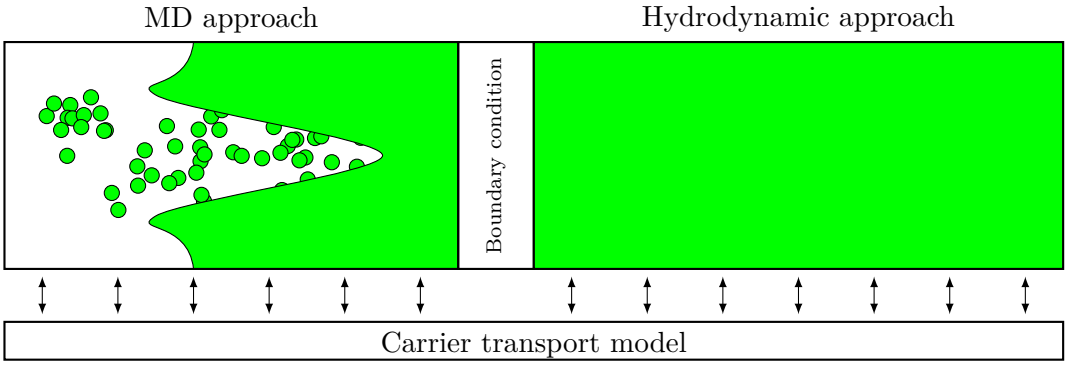

Figure 2.6: Sketch of a hybrid model approach. The sample material is shown in green. The carrier subsystem is modelled with a chosen transport model. The material dynamics within the laser-affected zone is modelled within the MD approach, while the depth of the sample is modelled within a hydrodynamic description. The transition from MD to hydrodynamics is accomplished by non-reflective boundaries.

3 Numerics

3.1 The Numerical Challenge

Our goal is to depict the highly non-linear material dynamics of laser irradiated bulk silicon by numerical simulation. The most prominent macroscopic result of the investigated material dynamics is the effect of laser ablation, which occurs on nanosecond time- and micrometer lengthscales. However, as emphasized in the previous chapters, the macroscopic material behavior is driven by a complex interplay of local non-linear electronic excitation and consequent non-linear transport effects. Local electronic excitation takes place on the femtosecond timescale, while the consequent transport effects distribute the infused energy over hundreds of nanometers within hundreds of picoseconds. Here, all addressed mechanics depend on each other and therefore have to be modelled and solved simultaneously.

In computational physics, a problem covering mechanics on several length- or timescales is always a complex problem. This is due to the fact that, in general, numerics is always a trade off between accuracy and computational cost. On one hand, increased temporal or spatial resolution always increases computational cost, while on the other hand, the typical length- or timescale of a physical phenomenon determines the lower bound of needed resolution. In principle, any physical simulation could be carried out on a quantum mechanical level considering ab initio methods. The resulting computational cost, however, would render macroscopic sample sizes unfeasible, even when computed on today's supercomputers.

To overcome this restriction, we use multiple simulation techniques for different time- and lengthscales combined into one simulation setup. Each simulation technique is tweaked to handle its respective physical phenomena most efficiently. The

models applied for energy transport effects are already derived within a continuum approximation, hence will be solved within the computationally cheap continuum approximation. To reproduce the non-equilibrium material dynamics induced by bond manipulation, we are in need of the benefits of the MD approach. The combination of both yields the so-called combined continuum-atomistic approach. However, MD simulations of samples on the micrometer scale require several hundreds of millions of atoms. To this day, a problem of this size can only be tackled on massive multi-parallel supercomputers[†]. It puts this work in the context of high-performance computing (HPC), which provides further challenges. In contrast to single node computing, large-scale massive multi-parallel simulations require sophisticated communication schemes among computation nodes, as the main performance bottleneck is shifted towards node to node communication.

In this chapter we will give an abstract overview of the applied numerics, the interplay of the simulation techniques considered in this work and how they are working together. The presented simulation techniques and numerics were implemented into our institutes in-house massive multi-parallel classical MD simulations code IMD (ITAP Molecular Dynamics) [183–185].

3.2 The Continuum-atomistic Approach on HPC Systems

Overview In figure 3.1, we show an abstracted overview of the interplay of the simulation techniques used in this work. Our sample lies within a simulation box. The simulation box is spatially divided into CPU cells, distributed over the number of physically available CPUs. Each CPU cell contains the local information of a finite difference (FD) grid which in turn contains a MD grid. For simplicity, only two- or one-dimensional grids are sketched here, while in practice all grids are three dimensional. Each FD cell is further separated into MD cells, which in turn contain the positions and velocities of their associated atoms.

[†]A single simulation in this work takes up to 240 hours of walltime on 131 072 CPU cores (AMD EPYC 7742), which translates into 31.5 million core hours. The simulations where performed on the High-Performance Computing Center of Stuttgart (HLRS).

A laser beam propagates though the sample and excites the charge carrier subsystem in terms of a source term within the transport models solved on the FD grid. On the FD grid, observables of the electronic subsystem, like local carrier temperature T_c or carrier density n_c are calculated within a continuum-mechanics approach. Depending on the applied transport model, this makes it necessary to solve coupled non-linear partial differential equations. The electron-phonon coupling is then modelled as an energy exchange between the respective FD cells and the atoms of the incorporated MD cells. In these MD cells the trajectory of each atom is calculated by solving Newton's equation of motion for each atom separately. The force acting on each atom is modelled as a classical interaction potential based on the atomic configuration and is parametrized from DFT calculations.

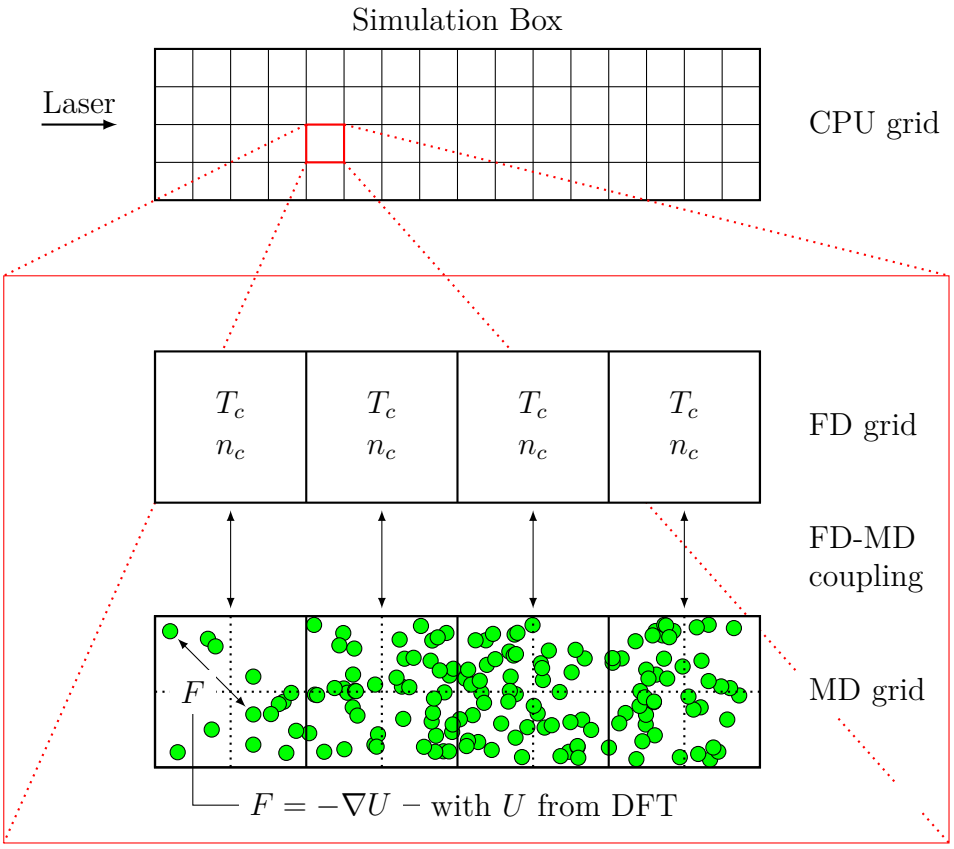

Figure 3.1: Schematic presentation of simulation composition in two dimensions. In practice, all grids are three-dimensional. Implementation of periodic boundary conditions and communication schemes are not shown.

Communication The presented decomposition contains the complete information of the investigated sample on an atomic level. However, each CPU alone only knows the information contained in its local FD and MD grid, thus not allowing any interaction among atoms of neighboring CPU cells. Obviously, this is not the intended behavior. For this reason, the FD grid within each CPU cell is extended with a so-called ghost-layer of FD cells. We sketch this in figure 3.2 as blue FD cells. In each FD communication the surface FD cells are copied and sent to the neighboring CPU cell, updating the associated local ghost cells. As a side note, periodic boundary conditions (PBC) are easily incorporated into this framework, as we only need to assign opposite surface CPU cells as neighboring CPU cells. Also, at this point it is important to note that in the FD communication only the continuum observables are communicated but no atomic information. For MD commutation we apply the analogous concept but only communicate the positions and velocities of surface MD cells in a separate routine. We disconnect MD and FD communication to be able to separately communicate only the necessary information and therefore speed up the communication process. From a physical standpoint, this is allowed since the MD and FD system each cover different timescales.

Flowchart In figure 3.3, we present a flowchart of the complete simulation program. Here we separately highlight the calculation loops of the MD and FD system as the MD or FD loop. The simulation runs from $t = 0$ to $t = t_{\text{end}}$, which is typically in the order of picoseconds for one simulation run. One MD step is typically chosen to be $\Delta t_{\text{MD}} = 1.018\,\text{fs}$, while an FD step is $\Delta t_{\text{FD}} = 1/1000 \cdot \Delta t_{\text{MD}}$ to achieve numerical stability.

An MD step is started by updating the MD ghost layers via MD commutation. Within the FD loop, the state of the electronic subsystem at $t = t_{\text{MD}} + \Delta t_{\text{MD}}$ is calculated by iterative solution of the transport equations. Once the new electronic state is calculated, we perform one MD step and calculate the observables of interest. This is repeated until the end of the simulation is reached. However, the true numerical finesse lays within the subroutines `MD step` and `FD step`, which will be explained in detail in section 3.3 and 3.4 respectively.

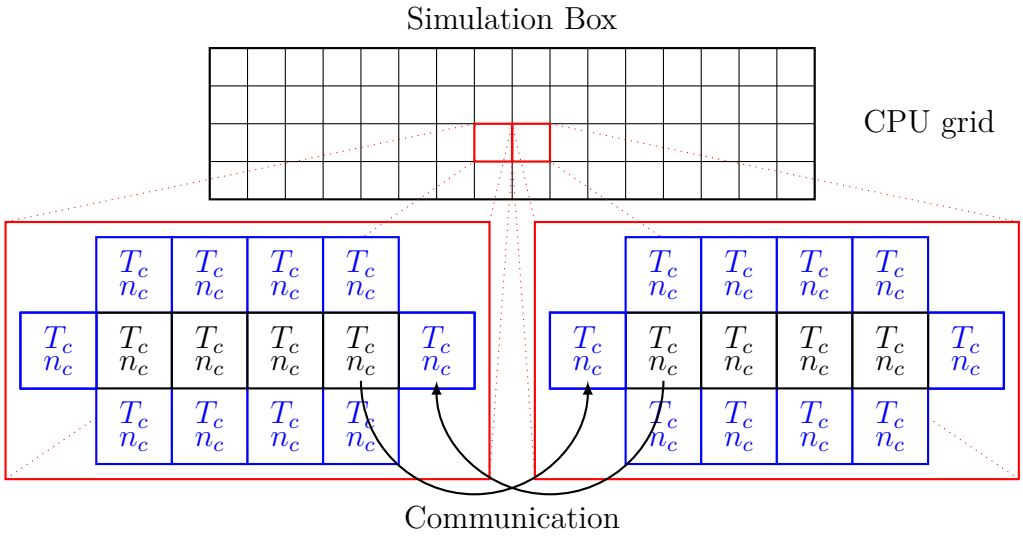

Figure 3.2: Concept of FD communication of adjoined CPU cells. Blue FD cells are ghost cells which contain the information of neighboring surface FD cells. The arrows indicate the sent and received data packages exchanged by two adjoining CPUs.

3.3 The FD System

3.3.1 Laser Pulse and Propagation

The absorption of laser light is not only the physical effect occuring on the shortest timescale, but it is also of electronic nature and therefore a problem to be solved on the FD grid.

Pulse Shape Assuming that the x-axis is the laser beam-direction, the power density I_0 of a laser pulse on the simulation box surface at $x = 0$ can be written as a Gaussian function

$$I_0(t,r) = (1-R)\sigma \cdot \underbrace{\sqrt{\frac{4\ln 2}{\pi t_p^2}} \exp\left(-4\ln 2 \frac{(t-t_0)^2}{t_p^2}\right)}_{\equiv I_0(t)} \cdot \underbrace{\frac{4\ln 2}{\pi b^2} \exp\left(-4\ln 2 \frac{r^2}{b^2}\right)}_{\equiv I_0(r)} \quad (3.1)$$

in the y-z-plane and simulation time t. Here R is the reflectivity, σ is the laser fluence, b is the laser pulse width, t_p is the laser pulse duration and t_0 is the time of

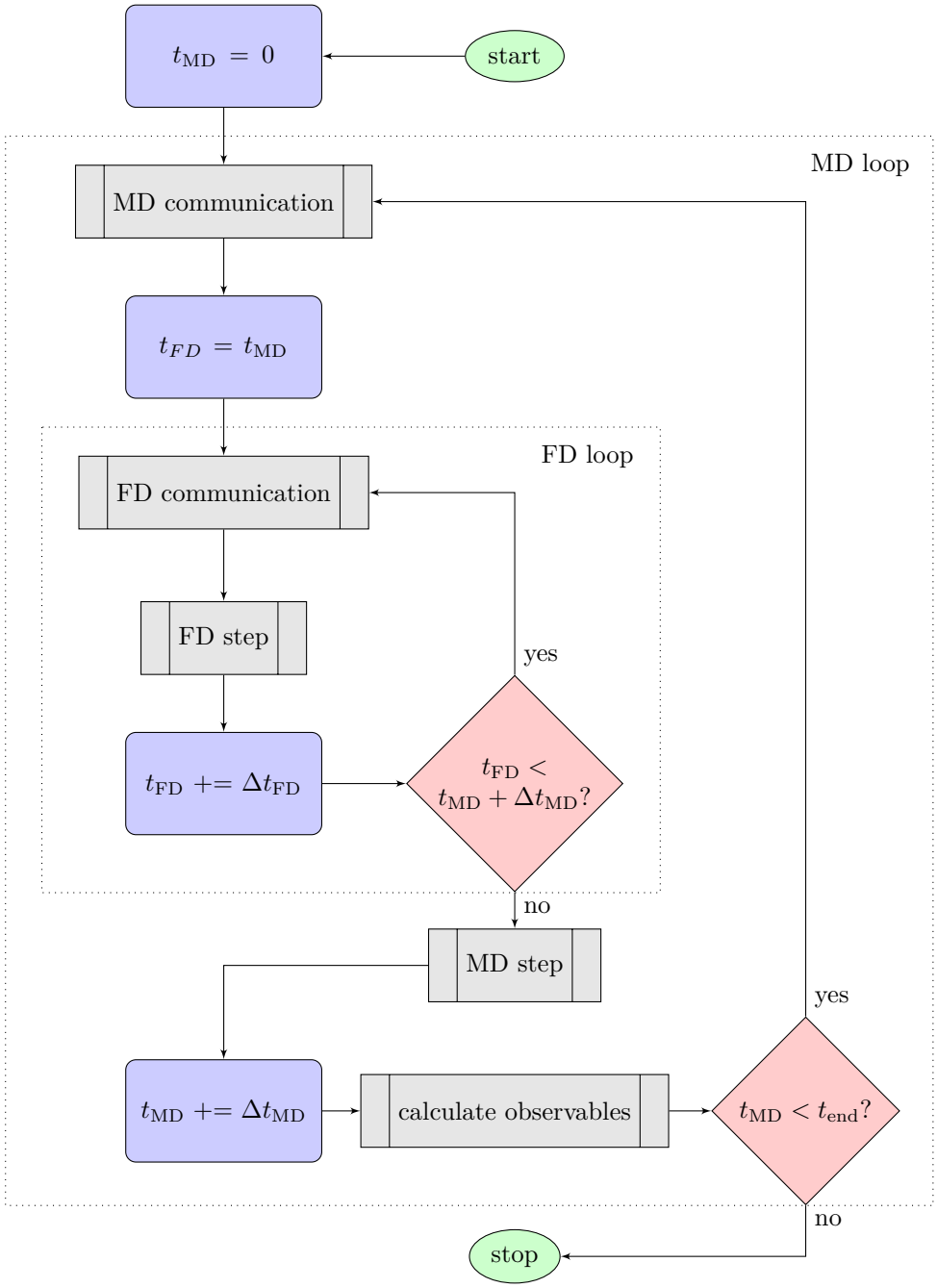

Figure 3.3: Flowchart of the simulation.

laser peak intensity. $r = |\mathbf{r}_0^{\mathrm{s}} - \mathbf{r}_{\mathrm{FD}}^{\mathrm{s}}|$ denotes the radial distance from the optical axis of laser light at the simulation box surface, discretized in FD cell coordinates. $\mathbf{r}_0^{\mathrm{s}}$ is

the chosen point of impact and

$$\mathbf{r}^{\mathrm{s}}_{\mathrm{FD}} = \begin{pmatrix} 0 \\ y_{\mathrm{FD}} \\ z_{\mathrm{FD}} \end{pmatrix} \tag{3.2}$$

the respective global FD cell surface position.

Pulse Propagation We assume that the laser power density is propagating into the sample in laser light-direction and each FD cell absorbs laser light according to their local electronic configuration. The decrease in laser power density dI_i when propagating through FD cell i with depth Δx_{FD} can therefore be written as the sum

$$\frac{dI_i}{\Delta x_{\mathrm{FD}}} = \sum_k^n A_k(\mathbf{x}_i, I_i) \tag{3.3}$$

over all local absorption mechanics $A_k(\mathbf{x}_i, I_i)$. From a physical standpoint, A_k depends on way more variables than position and local field intensity. However, for sake of simplicity, we chose not to list them all here, as the absorption terms vary with chosen absorption model. In practise A_k will always be calculated from the most recent data stored in FD cell i. In the production runs we use an MD time step of $\Delta t_{\mathrm{MD}} = 1.018\,\mathrm{fs}^{\dagger}$ and assume a constant energy imprint within that time step. As a consequence, we implicitly assume a propagation speed of sample length per Δt_{MD}. In reality, the refraction index of monocrystalline silicon ranges from $n = 3.44$ to $n = 3.688$ for wavelengths of $\lambda \in [800\,\mathrm{nm} : 2500\,\mathrm{nm}]$. A rough estimation gives a maximal and minimal propagation speed within the simulation of

$$\min(c_n) = c_s/n \approx 66620546\,\mathrm{m/s} \qquad \text{and} \tag{3.4}$$

$$\max(c_n) = c_s/n \approx 299792458\,\mathrm{m/s}, \tag{3.5}$$

$^{\dagger}1.018\,\mathrm{fs}$ equal 0.1 time units of the simulation program IMD.

which corresponds to a propagation speed range of $\sim 294\,\mathrm{nm}/\Delta\mathrm{t_{MD}}$ to $\sim 87.9\,\mathrm{nm}/\Delta\mathrm{t_{MD}}$. Consequently, we overestimate the light propagation speed in larger samples. However, given we use a pulse duration of $\tau_\mathrm{p} = 100\,\mathrm{fs} \approx 98\Delta t_\mathrm{MD}$ and the fastest occurring phenomenon of carrier thermalisation is typically in the order of $\sim 10^2\,\mathrm{fs}$ to $10^3\,\mathrm{fs}$, the energy imprint within one MD step is a valid approximation.

Ultimately, the problem to solve for the local power density reduces to the solution of a set of first order ordinary differential equations (3.3) with the boundary condition given by the local laser power density (3.1) for each time step. This is a standard problem solvable by numerical integration.

Ablation Specific Modification Before we solve the propagation equation, we first have to introduce an ablation simulation specific modification. During laser ablation simulation the atomic configuration will change drastically by boiling, spallation or material ejection, thus generating new surfaces and arbitrary sample geometries. Therefore, we alter the absorption rate of the i-th FD cell in x-direction to

$$\frac{dI_i}{\Delta x_\mathrm{FD}} \stackrel{!}{=} f(\mathbf{x_i}, I_i) = \begin{cases} \sum_k^n A_k(\mathbf{x_i}, I_i) & , N_i \geq N_\mathrm{crit} \text{ and } N_{i+1} \geq N_\mathrm{crit} \\ R\, I\, \Delta x_\mathrm{FD} & , N_i < N_\mathrm{crit} \text{ and } N_{i+1} \geq N_\mathrm{crit} \\ 0 & , N_i < N_\mathrm{crit} \text{ and } N_{i+1} < N_\mathrm{crit} \end{cases} \tag{3.6}$$

and introduce the parameters N_i and N_crit. N_i is the number of atoms within the FD cell i and N_crit the critical value under which the FD cell gets deactivated. R is the optical reflectivity of the surface generated by a deactivated FD cell. With this definition, we ensure that laser power density gets absorbed, when propagating through the sample, and decreases according when reflected at surfaces. Further, the laser beam propagates freely in vacuum.

Integration For the integration of the modified absorption equation we apply the well-known classic Runge-Kutta method [186]. In literature this method is often

referred to as RK4 and states that the differential equation of the form

$$\frac{dI}{dx} = f(x,I) \qquad \text{with the boundary condition} \qquad I(x_{\mathrm{FD}} = 0) = I(\mathbf{r}^{\mathrm{s}}_{\mathrm{FD}}) \tag{3.7}$$

has the solution on discrete coordinates x_n with spatial spacing Δx_{FD} given by

$$I(x_{n+1}) = I(x_n) + \frac{1}{6}(k_1 + 2k_2 + 2k_3 + k_4). \tag{3.8}$$

For all n, k_n is given by

$$k_1 = \Delta x_{\mathrm{FD}} f\left(x_n, I(x_n)\right), \tag{3.9}$$

$$k_2 = \Delta x_{\mathrm{FD}} f\left(x_n + \frac{1}{2}\Delta x_{\mathrm{FD}}, I(x_n) + \frac{1}{2}k_1\right), \tag{3.10}$$

$$k_3 = \Delta x_{\mathrm{FD}} f\left(x_n + \frac{1}{2}\Delta x_{\mathrm{FD}}, I(x_n) + \frac{1}{2}k_2\right) \text{ and} \tag{3.11}$$

$$k_4 = \Delta x_{\mathrm{FD}} f\left(x_n + \Delta x_{\mathrm{FD}}, I(x_n) + k_3\right). \tag{3.12}$$

3.3.2 Solving Continuum Transport Models

Independent of the applied transport model, the dynamics of the carrier system is given as the solution of two coupled parabolic partial differential equations (PDEs) of the form

$$\partial_t A(B) = \nabla_{\mathbf{r}}\left(K_A(A,B,M)\, \nabla A \right) + C_A(A,B,\mathbf{r},t,M) \qquad \text{and} \tag{3.13}$$

$$\partial_t B(A) = \nabla_{\mathbf{r}}\left(K_B(A,B,M)\, \nabla B \right) + C_B(A,B,\mathbf{r},t,M). \tag{3.14}$$

For simplicity, the dummy functions A and B are not given with all of their arguments and have to be understood as also explicitly dependent on the position $\mathbf{r}$ and time t. For example in the case of the TSM, A becomes the carrier temperature T_c, B becomes the carrier density n_c and C_* accounts respectively for coupling terms and laser light absorption. The function M is an $\mathbf{r}$-dependent dummy function, containing all the observables of the lattice system like the lattice temperature T_l. Since the characteristic timescales of the dynamics of the carrier and lattice system

differ in several orders of magnitude, we assume

$$\partial_t M = 0 \tag{3.15}$$

during one MD step.

Intrinsically, computers can't calculate or save continuous sets of data. Thus, every numerical solution, independent of solution scheme, is always an approximation of a function on a grid. For simplicity, we present the used algorithms on a one-dimensional spatial grid. In practice, we use three spatial dimensions. All grids in this work are equidistant euclidian grids, so every point position x or time t can be expressed as an integer multiple n of the respective grid spacing Δx_{FD} or Δt_{FD}. For the discretization on our FD grid we introduce the discrete

$$\text{position} \quad x = i\Delta x_{\mathrm{FD}} \equiv x_i \tag{3.16}$$

$$\text{and time} \quad t = j\Delta t_{\mathrm{FD}} \equiv t_j. \tag{3.17}$$

The notation of observable A at discrete arguments will be denoted as

$$A(x,t) \equiv A_i^j. \tag{3.18}$$

Using this notation, we will present solution schemes for our prototypical parabolic PDE (3.13). The left hand side of equation (3.13) accounts for time evolution, while the right hand side contains the information about the spatial configuration of observables at the current time. Consequently, we need to evaluate the time evolution of A at every position by integration of the right hand side with respect to its time dependency. For this, different numerical solution schemes are possible.

3.3.3 Explicit Solution Schemes

The explicit solution scheme is based on the approximation

$$A(x,t+\Delta t) \approx \int_t^{t+\Delta t} \partial_t A(x,t) dt \tag{3.19}$$

of temporal integration. The main advantage of this approximation is that $A(x,t+\Delta t)$ can be calculated solely based on the spatial configuration of A at time t. In our case, we use the forward in time centered in space (FTCS) Euler integration. Forward in times means that we approximate the time derivation by a Taylor series up to first order in t at time t_j. In our discrete notation this reads

$$\frac{d}{dt}A(x_i,t_j) = \frac{A_i^{j+1} - A_i^j}{\Delta t_{\mathrm{FD}}} + \mathcal{O}(\Delta t_{\mathrm{FD}}^2) \tag{3.20}$$

and expresses the time derivative by the current and next time step. For the spatial derivative, we proceed analogously but approximate the derivative at position x_i by both

$$\text{forward} \qquad \frac{d}{dx}A(x_i,t_j) = \frac{A_{i+1}^j - A_i^j}{\Delta x_{\mathrm{FD}}} + \mathcal{O}(\Delta x_{\mathrm{FD}}^2) \quad \text{and} \tag{3.21}$$

$$\text{backward} \qquad \frac{d}{dx}A(x_i,t_j) = \frac{A_i^j - A_{i-1}^j}{\Delta x_{\mathrm{FD}}} + \mathcal{O}(\Delta x_{\mathrm{FD}}^2) \tag{3.22}$$

differentiation. The average of both representations will give the space centered representation

$$\frac{d}{dx}A(x_i,t_j) = \frac{1}{2}\frac{d}{dx}A(x_i,t_j) + \frac{1}{2}\frac{d}{dx}A(x_i,t_j) \tag{3.23}$$

$$= \frac{A_{i+1}^j - A_{i-1}^j}{2\Delta x_{\mathrm{FD}}} + \mathcal{O}(\Delta x_{\mathrm{FD}}^3). \tag{3.24}$$

Note that this representation has a increased accuracy of $\mathcal{O}(\Delta x_{\mathrm{FD}}^2)$ because it can be derived in such a way that the second order errors cancel out. Now we apply these discrete differentiation representations to our prototypical PDE equation (3.13) and arrive at

$$
\begin{aligned}
A_i^{j+1} = A_i^j + K_i^j \frac{\Delta t_{\mathrm{FD}}}{\Delta x_{\mathrm{FD}}^2} \cdot \left[A_{i+1}^j - 2A_i^j + A_{i-1}^j\right] + \Delta t_{\mathrm{FD}} C_i^j \qquad (3.25)\\
+ \frac{\Delta t_{\mathrm{FD}}}{4\Delta x_{\mathrm{FD}}^2} \left[A_{i+1}^j - A_{i-1}^j\right] \Big\{ \qquad\qquad \Big\}\\
\qquad \frac{\partial K_i^j}{\partial A} \left[A_{i+1}^j - A_{i-1}^j\ \right] \qquad\qquad \Big\} \equiv \eta_i^j\\
\qquad + \frac{\partial K_i^j}{\partial B} \left[B_{i+1}^j - B_{i-1}^j\ \right] \qquad\qquad \Big\}\\
\qquad + \frac{\partial K_i^j}{\partial M} \left[M_{i+1}^j - M_{i-1}^j\right] \qquad\qquad \Big\}\\
\Big\}\\
+ \mathcal{O}(\Delta x_{\mathrm{FD}}^3) + \mathcal{O}(\Delta t_{\mathrm{FD}}^2), \qquad\qquad \Big\}
\end{aligned}
$$

with $\Delta t_{\mathrm{FD}} C_i^j + N_i^j$ being the non-linear contribution. A differentiation scheme like this is called FTCS, as the value A_i^{j+1} is obtained by the configuration of A at time t_j from surrounding x_i. Graphically, our FTCS scheme can be represented in a differential stencil shown in figure 3.4. Generally, more complex and more accurate

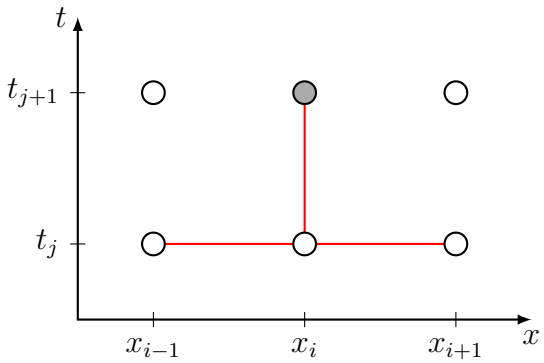

Figure 3.4: Differentiation stencil for an explicit forward in time centered in space (FTCS) differentiation scheme. The gray node is calculated with usage of all connected white nodes.

differentiation schemes can be derived by combinations of different Taylor series up to varying orders of error or Taylor series being evaluated at different points in time

and space. However, the core concept remains the same. See [186] for an overview of the most commonly applied schemes. Despite the promise of higher accuracy and stability of higher schemes, we choose to use first order Taylor series to derive our solution schemes. We choose this stencil because of performance reasons. The main advantage of the first order FTCS scheme is that the complete lattice $\{A_i^{j+1}\}_N$ known to CPU N can be calculated directly on CPU N with only one ghost-layer of neighboring FD cells. In our continuum-atomistic setup, this assures minimal communication overhead between CPUs, since only nearest neighbor CPUs need to communicate one ghost-layer. The presented scheme also uses minimal storage, since each CPU requires to store only two arrays of size $n_x n_y n_z$ for computation on an $n_x \times n_y \times n_z$ grid. This renders the presented FTCS scheme the most efficient but simplest solution scheme for PDEs on our combined continuum-atomistic simulation setup.

Stability The downside of simple and computationally cheap algorithms lies in their numerical stability. All numerical solution schemes have three main properties of interest: accuracy, stability and computational cost. Most often, one is a trade off of the other. In this section we choose the FTCS scheme due to its very low computational cost. However, the fastest scheme is of no use if the computed solutions are wrong. In case of the FTCS scheme, within N steps we accumulate errors in space in order of $N\Delta x_{\mathrm{FD}}^3$ and $N\Delta t_{\mathrm{FD}}^2$ in time. In practice, one chooses a sufficiently dense FD grid to accomplish $n\Delta x_{\mathrm{FD}}^3 \ll \hat{x}$ and $n\Delta t_{\mathrm{FD}}^2 \ll \hat{t}$ where $\hat{x}$ and $\hat{t}$ are the characteristic length- and timescales of the physical problem. However, in the typical use cases of parabolic PDEs, this error accumulation boundary is typically of lower interest since it is most often fulfilled when the stability criterion is satisfied [186]. The criterion for numerical stability can be derived by a von Neumann stability analysis. The von Neumann stability analysis assumes that the coefficients of the scheme vary slowly in space and time. In that case, independent solutions at a specific time step l can be solved within the plane wave ansatz

$$A_j^l = \xi(k)^l e^{ikj\Delta x_{\mathrm{FD}}} \tag{3.26}$$

where i is not an index but the imaginary unit, k is the spatial wave number and ξ a complex amplitude. These solutions are the so-called eigenmodes. The core idea is that within this framework, the time dependence of a single eigenmode is given by successive integer powers of ξ. A scheme can be called stable if its temporal evolution does not diverge and therefore fulfills

$$|\xi(k)| \leq 1 \tag{3.27}$$

for all k. Unfortunately, our complete prototypical PDE (3.25) is a non-linear PDE coupled to another non-linear PDE. A rigorous and precise mathematical stability analysis for such a system is a very complex and protracted task and will not be done within this work. However, such an analysis consists of linearization of all non-linear parts like $A^2 \approx A_0 + \delta A$, with A_0 being a solution to the linear part. The stability analysis then yields the stability regime of the eigenmodes of δA. Stability analysis of the linear part alone thus gives a first insight of the stability regime of the PDE since stability of the linear part is a necessary condition for stability of the complete PDE. Performing a von Neumann analysis of the linear part of our FTCS scheme equation (3.25) gives

$$\xi(k) = 1 - K_i^j \frac{\Delta t_{\mathrm{FD}}}{\Delta x_{\mathrm{FD}}^2} 4 \sin^2\left(\frac{k \Delta x_{\mathrm{FD}}}{2}\right), \tag{3.28}$$

which fulfills the stability criterion (3.27) when

$$\underbrace{2|K_i^j| \frac{\Delta t_{\mathrm{FD}}}{\Delta x_{\mathrm{FD}}^2}}_{\mathrm{CFL}} \leq 1 \tag{3.29}$$

holds. On a side note, all linear parabolic PDEs, like heat transport and diffusion type equations, discretized on a uniform grid reduce to this stability condition. This was pointed out and derived by Courant, Friedrichs and Lewy [187], which is why this stability criterion is often called Courant-Friedrichs-Lewy criterion, or simply the Courant condition. In literature, the left hand side of the criterion (3.29) is often called CFL number.

The stability criterion is an abstract formulation, which is why we now want to

give an example on the numerical restrictions in our use case. If we choose the nTTM in the simplest presented parametrization, shown in table 4.3, we arrive at the condition

$$\frac{2}{3}\frac{|\alpha+\beta T_c|}{n_c k_\mathrm{b}}\frac{\Delta t_\mathrm{FD}}{\Delta x_\mathrm{FD}^2} \leq 1 \tag{3.30}$$

for numerical stability. The necessary time step Δt_FD is inversely proportional to the carrier density n_c. For simulations on semiconductors this is a problem. In the case of silicon, the stability criterion within the IMD unit system at equilibrium conditions and grid spacing of $\Delta x_\mathrm{FD} = 1\,\mathrm{nm}$ reads

$$\Delta t_\mathrm{FD} \leq 4.7 \cdot 10^{-13}. \tag{3.31}$$

Translated back into SI-units this requires for FD time steps of $4.78 \cdot 10^{-27}\,\mathrm{s}$ or less. For a simulation time of 1 fs alone, we would require roughly $2.2 \cdot 10^{12}$ FD steps. This is not suitable for the combined continuum-atomistic approach.

3.3.4 Implicit Solution Schemes

In the previous section 3.3.3, we argued that the explicit solution schemes require an unattainable amount of FD time steps when implemented in our simulation setup. Implicit solution schemes counter this problem by replacing the introduced spatial derivatives evaluated at time t_j with its counterparts evaluated at future time t_{j+1} leading to

$$\frac{d}{dx}A(x_i,t_j) = \frac{A_{i+1}^{j+1} - A_i^{j+1}}{\Delta x_\mathrm{FD}} + \mathcal{O}(\Delta x_\mathrm{FD}^2) \tag{3.32}$$

$$\text{or respectivly} \qquad \frac{d}{dx}A(x_i,t_j) = \frac{A_i^{j+1} - A_{i-1}^{j+1}}{\Delta x_\mathrm{FD}} + \mathcal{O}(\Delta x_\mathrm{FD}^2). \tag{3.33}$$

As an example, the linear part of the PDE consequently becomes

$$A_i^{j+1} = A_i^j + \underbrace{K_i^j \frac{\Delta t_\mathrm{FD}}{\Delta x_\mathrm{FD}^2}}_{\equiv \alpha_i^j} \cdot \left[A_{i+1}^{j+1} - 2A_i^{j+1} + A_{i-1}^{j+1}\right] + \Delta t_\mathrm{FD} C_i^j, \tag{3.34}$$

where the right hand side is also dependent on the time t_{j+1}, leading to the differential stencil shown in figure 3.5(a). This scheme calculates the time evolution at position x_i under the usage of the observables at neighboring positions at the following time step t_{j+1}. No knowledge of neighboring nodes at time t_j are needed. Schemes like this are called fully implicit. Analogous to the FTCS scheme, this scheme is called backwards in time centered in space (BTCS). Unfortunately, the values at nodes in the future are unknown, rendering implicit schemes more like a set of conditions than an explicit calculation. However, the solution of the set of N conditions can simply be obtained as a solution of a linear equation system. In our example case, the system takes the form

$$\begin{pmatrix} 1 & -1 & & & & & & \\ 0 & 0 & & & \dots & 1 & -1 & \\ \alpha_0^j & \alpha_0^j & \alpha_0^j & & & & & \\ & \alpha_1^j & \alpha_1^j & \alpha_1^j & & & & \\ & & \alpha_2^j & \alpha_2^j & \alpha_2^j & & & \\ & & & \alpha_3^j & \alpha_3^j & \alpha_3^j & & \\ & & & & \ddots & \ddots & \ddots & \\ & & & & & \alpha_{N-1}^j & \alpha_{N-1}^j & \alpha_{N-1}^j \end{pmatrix} \begin{pmatrix} A_0^{j+1} \\ A_1^{j+1} \\ A_2^{j+1} \\ A_3^{j+1} \\ A_4^{j+1} \\ A_5^{j+1} \\ \vdots \\ A_{N-1}^{j+1} \end{pmatrix} = \begin{pmatrix} 0 \\ 0 \\ A_0^j + \Delta t_{\mathrm{FD}} C_0^j \\ A_1^j + \Delta t_{\mathrm{FD}} C_1^j \\ A_2^j + \Delta t_{\mathrm{FD}} C_2^j \\ A_3^j + \Delta t_{\mathrm{FD}} C_3^j \\ \vdots \\ A_{N-1}^j + dt C_{N-1}^j \end{pmatrix}, \tag{3.35}$$

which is tridiagonal and supported by two arbitrary boundary conditions in the first two rows. In our example, these requirements correspond to vanishing fluxes

$$\frac{d}{dx} A(x_0, t_{j+1}) \quad \stackrel{!}{=} \quad \frac{d}{dx} A(x_N, t_{j+1}) \quad \stackrel{!}{=} \quad 0 \tag{3.36}$$

at the box boundaries. Arbitrary boundary conditions are possible and simply have to be formulated as differential equations within the first two rows of α. For every

extra dimension we need two extra diagonals and two additional boundary conditions to keep the system solvable. Even when doing this, α will remain sparsely occupied. Unfortunately, we need to solve a linear equation system for every FD step, which is numerically very expensive, especially compared to explicit schemes. However, the great advantage of fully implicit schemes is that they are extremely stable. Performing a von Neumann stability analysis on the scheme equation (3.34) gives

$$\xi(k) = \frac{1}{1 + \alpha_i^j 4 \sin^2\left(\frac{k\Delta x_{\mathrm{FD}}}{2}\right)}, \tag{3.37}$$

which is unconditionally stable for any time step Δt_{FD}. Unfortunately, despite the stability, the error of this scheme is still of order $\mathcal{O}(\Delta t_{\mathrm{FD}}^2)$. The unconditional stability paired with the accumulation of numerical errors is possible due to the property of implicit solution schemes to reproduce the equilibrium solution for unreasonably big time steps. This can be seen when we regroup the linear PDE equation (3.34) and perform the limit $\Delta t_{\mathrm{FD}} \to \infty$. Equation (3.34) then simply becomes

$$\frac{K_i^j}{\Delta x_{\mathrm{FD}}^2} \cdot \left[A_{i+1}^{j+1} - 2A_i^{j+1} + A_{i-1}^{j+1}\right] = -C_i^j \tag{3.38}$$

$$\text{which translates back to} \qquad K\nabla^2 A(x) = -C \tag{3.39}$$

and is the steady state formulation of our problem. Consequently, fully implicit schemes obtain the correct equilibrium solution at big time steps Δt_{FD} at the cost of huge errors in the dynamics of small scale features. In contrast to this, fully explicit algorithms tend to sustain small scale features while being in danger of amplifying those to the point where the scheme becomes unstable. We now want to use the positive qualities of both worlds. The combination of both, fully implicit and fully explicit schemes leads to so-called semi-implicit schemes. In this work we use the semi-implicit Crank-Nicolson scheme [188] whose differential stencil is shown in figure 3.5(b). The basic idea is averaging FTCS and BTCS schemes by a mixing

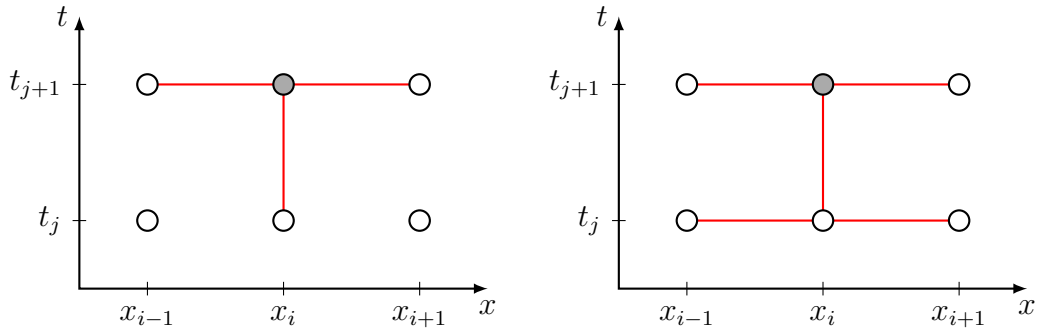

(a) Fully implicit scheme (b) Semi-implicit scheme

Figure 3.5: Differentiation stencil for an implicit and semi-implicit differentiation scheme. The gray node is calculated with usage of all connected white nodes.

parameter $\chi_m \in [0:1]$. The linear part of the PDE becomes

$$\begin{aligned} A_i^{j+1} = A_i^j &+ \chi_m \left(K_i^j \frac{\Delta t_{\mathrm{FD}}}{\Delta x_{\mathrm{FD}}^2} \cdot \left[A_{i+1}^{j+1} - 2A_i^{j+1} + A_{i-1}^{j+1} \right] \right) \\ &+ (1-\chi_m) \left(K_i^j \frac{\Delta t_{\mathrm{FD}}}{\Delta x_{\mathrm{FD}}^2} \cdot \left[A_{i+1}^{j} - 2A_i^{j} \quad + A_{i-1}^{j} \right] \right) \\ &+ \Delta t_{\mathrm{FD}} C_i^j + \mathcal{O}(\Delta x_{\mathrm{FD}}^2) + \mathcal{O}(\Delta t_{\mathrm{FD}}^2). \end{aligned} \tag{3.40}$$

Therefore, for $\chi_m = 0$ we obtain the fully explicit scheme and for $\chi_m = 1$ the fully implicit scheme. This allows us to dynamically adjust the main emphasis on small or global scale features, while still benefiting from the stability of implicit schemes. A von Neumann stability analysis yields

$$\xi(k) = \frac{1 - \alpha_i^j 2 \sin^2\left(\frac{k\Delta x_{\mathrm{FD}}}{2}\right)}{1 + \alpha_i^j 2 \sin^2\left(\frac{k\Delta x_{\mathrm{FD}}}{2}\right)}, \tag{3.41}$$

which is unconditionally stable for any Δt_{FD}. In practice, we obviously solve the non-linear transport equation instead of only the linear part of it. The actually solved linear equation system is obtained simply by writing the presented Crank-

Nicolson scheme (3.42) with all non-linear contributions as

$$\begin{aligned} A_i^{j+1} = A_i^j &+ \chi_m \left(K_i^j \frac{\Delta t_{\mathrm{FD}}}{\Delta x_{\mathrm{FD}}^2} \cdot \left[A_{i+1}^{j+1} - 2A_i^{j+1} + A_{i-1}^{j+1} \right] + N_i^{j+1} + \Delta t_{\mathrm{FD}} C_i^j \right) \\ &+ (1-\chi_m) \left(K_i^j \frac{\Delta t_{\mathrm{FD}}}{\Delta x_{\mathrm{FD}}^2} \cdot \left[A_{i+1}^{j} - 2A_i^{j} + A_{i-1}^{j} \right] + N_i^{j} + \Delta t_{\mathrm{FD}} C_i^j \right) \\ &+ \mathcal{O}(\Delta x_{\mathrm{FD}}^2) + \mathcal{O}(\Delta t_{\mathrm{FD}}^2). \end{aligned} \tag{3.42}$$

and set up a linear equation system analogous to the equation system (3.35). When doing so, the non-linear part of the fully implicit scheme η_i^{j+1} will enters into the coefficients α, while the non-linear part of the explicit scheme η_i^j enter on the right hand side.

3.4 The MD System

The basic idea of the MD approach is to calculate the particle trajectory by iterative integration of Newton's equation of motion for a finite time step Δt_{MD}.

The system is simplified by not treating ions and electrons separately, but together as a classical particle with no inner degrees of freedom. Consequently, classical MD neglects the electronic subsystem which re-enters our simulation by the combined continuum-atomistic extension. However, from an isolated numerical perspective the particles within an MD simulation are still treated as classical particles interacting with each other. Therefore, the dynamics of particle i follows Newton's equation of motion

$$\mathbf{F}_i(\{\mathbf{r}\}) = m_i \ddot{\mathbf{r}}_i, \tag{3.43}$$

with m_i and $\mathbf{r}_i$ denoting the mass and position of particle i. The force $\mathbf{F}_i(\{\mathbf{r}\})$ acting on particle i is a result of the interaction of particle i with its surrounding particles and/or external potentials. Therefore, the force acting on particle i can be written as the gradient

$$\mathbf{F}_i = -\nabla_{\mathbf{r}_i} U(\{\mathbf{r}\}) \tag{3.44}$$

of a classical interaction potential U with respect to the particle position $\mathbf{r}_i$. In this formulation, the interaction potential $U\{\mathbf{r}\}$ can be interpreted as the accumulated potential energy of the system, parametrized by the ensemble $\{\mathbf{r}\}$ of positions of every particle. For a system of N particles, this results in a set of N coupled differential equations, reading

$$\ddot{\mathbf{r}}_i = -\frac{1}{m_i} \cdot \nabla_{\mathbf{r}_i} U(\{\mathbf{r}\}). \tag{3.45}$$

For $N > 2$, no analytically general closed form solution of this problem exists, which is why an iterative solution is needed. Now, the MD approach is to approximate the solution of equations (3.45) by iterative numerical integration of the coupled DEQ system (3.45) in finite time steps Δt_{MD}. In each MD step, the system state at $t' = t + \Delta t_{\mathrm{MD}}$ is calculated from the system state at the current time t. Figure 3.6 shows an example of an MD simulation of a point mass in an external gravitational potential. The exact analytic solution, a simple parabola, is sketched in red. The dashed arrows and circles indicate the discrete MD trajectory at simulation times $t = n \cdot \Delta t_{\mathrm{MD}}$ for $n \in \{0,1,2,3,4\}$.

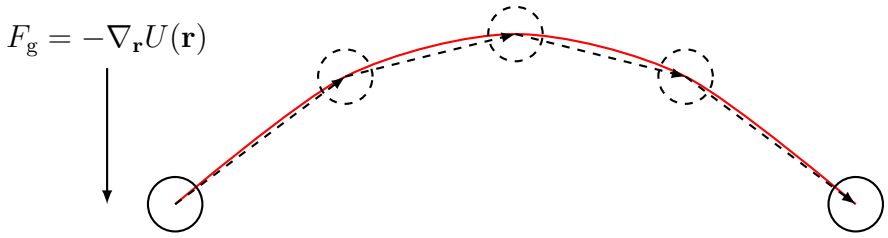

Figure 3.6: Basic example of an MD simulation of a point mass in an external gravitational potential $U(\mathbf{r})$. The solid circles indicate the positions of the point mass at the beginning and end of the trajectory. The red line indicates the analytical solution of Newton's equation of motion, while the dashed arrows and circles show the discrete solution obtained by the MD approach.

The accuracy of the numerically obtained trajectory is mainly determined by the size of the time step Δt_{MD} in connection with the applied integration scheme. The choice of initial particle positions and velocities can be viewed as a defined point in phase space, from where the dynamics of the system evolves. The underlying physics of the system enters the simulation by the choice of interaction potential U

and the choice of integration scheme. The physical influence of chosen integration scheme will be discussed in more detail in section 3.4.1. However, independent of the physical system that is aimed to reproduce, the general algorithm stays the same and can be easily summed up in the following block of pseudo code.

```
## Pseudo code of a simple MD simulation

initiate_simulation()          # Initialize

t = 0

while ( t < tend ):            # MD main loop
  calculate_forces()           # Calculate forces acting on each atom
  move_atoms()                 # Integrate Newton's equation of motion
  calculate_properties()       # Calculate desired and/or needed properties
  t = t + dt                   # Increment time
  do_additional_tasks()        # do arbritary evaluations
  do_output()                  # I/O
end
```

First, the simulation is initialized in `initiate_simulation()` outside of the MD main loop. This means all the simulation parameters are read, as well as the complete state of the system at time $t = 0$ in terms of position and velocity of each particle. For HPC applications this is also the moment to evaluate the composition of the sample and distribute all relevant sample fragments and global variables on the respective computing nodes. After initiation, the main loop is repeated for each time step until the end of the simulation is reached. Within the main loop, at each time step, the forces acting on each particle are calculated in `calculate_forces()` from the configuration of the sample and applied interaction potential. In `move_atoms()` the result is integrated with a chosen integrator, from which the new positions and velocities at time $t + \Delta t_{\mathrm{MD}}$ are obtained. Each particle then gets moved to its new position. Afterwards, the results are written out in `do_output()`. While this is the most basic MD loop, the MD loop can easily be extended with further constraints or functions at arbitrary MD steps. With simplicity as its strong suit, the MD approach shines with modularity. Additional tasks, like calculating observables or FD calculations, can be added in `do_additional_tasks()`.

3.4.1 Integrators

Algorithms for numerical integration are called integrators. In the context of MD simulations, this integration is commonly expanded to include modifications to the differential equation of motion. This modification of the differential equation of motion is utilized to impose major thermodynamical restrains to the particle dynamic. In the terminology of MD simulations the choice of integrator therefore includes the choice of thermodynamical ensemble.

Microcanonical Ensemble In the basic example of a parabolic throw, the particle moves in a conservative potential $U(\mathbf{r})$ with no energy dissipation. Therefore, the integrator in this example has to reproduce energy conservation by showing invariance in time reversal. An integrator fulfilling this restraint is called symplectic.

The symplectic integrator in this work, is the well-known leap-frog algorithm. In its full integer-step formulation, the updated positions $\mathbf{r}_i(t + \Delta t_{\mathrm{MD}})$ and velocities $\dot{\mathbf{r}}_i(t + \Delta t_{\mathrm{MD}})$ are given by

$$\mathbf{r}_i(t + \Delta t_{\mathrm{MD}}) = \dot{\mathbf{r}}_i(t)\,\Delta t_{\mathrm{MD}} + \frac{1}{m}\ddot{\mathbf{r}}_i(t)\,\Delta t_{\mathrm{MD}}^2 \tag{3.46}$$

and

$$\dot{\mathbf{r}}_i(t + \Delta t_{\mathrm{MD}}) = \dot{\mathbf{r}}_i(t) + \frac{1}{2}\left[\ddot{\mathbf{r}}_i(t) + \ddot{\mathbf{r}}_i(t + \Delta t_{\mathrm{MD}})\right]\Delta t_{\mathrm{MD}}. \tag{3.47}$$

It can easily be derived by Taylor expansion of the position and velocity at times $t \pm \Delta t_{\mathrm{MD}}$ up to third order and therefore shows a numerical accuracy of $\mathcal{O}(\Delta t_{\mathrm{MD}}^4)$. $\mathbf{r}_i$ and $\dot{\mathbf{r}}_i$ are given by the state of the system and $\ddot{\mathbf{r}}_i$ is calculated from $U(\{\mathbf{r}\})$ via equation (3.45). While gaining computational efficiency from its simplicity, this integrator shows a very robust stability behavior in long time MD simulations [189] due to its symplectic nature. This renders the leap-frog algorithm one of the go-to integrators for MD simulations. From the viewpoint of statistical mechanics, a system whose dynamics reflects time-inverse variance is intrinsically conserving the number of particles N, the volume V of the simulation box and the total energy E of the system. In other words, the leap-frog algorithm reproduces the microcanonical ensemble.

Canonical Ensemble Most often, MD simulations within the canonical ensemble are of interest, for example when the system is needed to be driven to a specific region in phase space or the system dynamics under specific thermodynamical gradients is studied. This can be the case when controlled energy exchange with an external heat bath is part of the situation of interest, like observing particle diffusion within a medium which is showing a temperature gradient. In our use case, the canonical ensemble is utilized to generate a specific initial state of the sample. In the framework of MD simulations, such canonical dynamics are accomplished by adding artificial terms to the Hamiltonian of the system. In this work, we use the Nosé-Hoover thermostat [190] which follows the Hamiltonian

$$\mathcal{H} = \sum_{i=1}^{N} \frac{1}{2m_i} \left(\frac{m_i \dot{\mathbf{r}}_i}{s^2} \right)^2 + U(\{\mathbf{r}\}) + \frac{1}{2Q} p_s^2 + L k_\mathrm{B} T \ln s. \tag{3.48}$$

Here L is the number of independent momentum degrees of freedom of the system, p_s is a virtual momentum of the new coordinate s, representing the properties of the external heat bath consisting of a particle with mass Q and temperature T. From this Hamiltonian, new equations of motion can be derived which follow the dynamics at a constant temperature T, namely

$$\dot{\mathbf{r}}_i = -\frac{\mathbf{p}_i}{m_i s^2}, \tag{3.49}$$

$$\dot{\mathbf{p}}_i = -\nabla_{\mathbf{r}_i} U(\{\mathbf{r}\}), \tag{3.50}$$

$$\dot{s} = \frac{p_s}{Q} \tag{3.51}$$

$$\text{and} \qquad \dot{p}_s = \frac{1}{s} \left(\sum_{i=1}^{N} \frac{\mathbf{p}_i}{m_i s^2} - L k_\mathrm{B} T \right). \tag{3.52}$$

The first two equations represent the dynamics of the simulated particles and the last two equations represent the dynamics within the heat bath. All equations together can be integrated by the leap-frog algorithm.

FD-MD coupling The Nosé-Hoover thermostat imposes a virtual friction on the particle dynamics to drive the system towards a specified temperature T_0. The

imposed friction can be interpreted as a function of temperature difference $|T_l - T_0|$ between the goal temperature T_0 and the systems temperature T_l and basically yields a controlled energy coupling towards a heat bath. We now apply the identical concept of coupling of the MD system to the FD system, where the FD system can be viewed as a heat bath. However, instead of driving the system to a defined kinetic energy via a dissipative dynamic, we demand energy conservation within the energy exchange between the MD system $\mathcal{H}_{\mathrm{MD}}$ and the FD system $\mathcal{H}_{\mathrm{FD}}$. Thus, we demand

$$\frac{d}{dt}\left(\mathcal{H}_{\mathrm{MD}} - \mathcal{H}_{\mathrm{FD}}\right) \stackrel{!}{=} 0. \tag{3.53}$$

The energy drained or exchanged from the FD system can be written as an analytical condition

$$\frac{d}{dt}\mathcal{H}_{\mathrm{FD}} = \pm C_\alpha, \tag{3.54}$$

where C_α is an arbitrary function depending on both FD and MD system variables. For example, in the classical TTM, presented in section 2.3.1, the rate

$$C_\alpha = G\left(T_c - T_l\right) \tag{3.55}$$

is chosen to represent the carrier-phonon coupling as a linearized rate equation. Of course, other parametrizations within the FD system are possible. Within MD, however, thermal energy is always varied by manipulation of particle velocity by a friction

$$F_i^{\mathrm{Fric}} = \xi m_i \dot{\mathbf{r}}_i. \tag{3.56}$$

We consider N particles that exchange energy with the FD system inside a volume V. ξ is identical for all particles i, thus we can write the demand

$$\frac{d}{dt}\mathcal{H}_{\mathrm{MD}} \stackrel{!}{=} \xi \sum_{i=1}^{N} m_i \dot{\mathbf{r}}_i^T, \tag{3.57}$$

from which

$$\xi = -\frac{\int_V C_\alpha dV}{\sum_{i=1}^{N} m_i \dot{\mathbf{r}}_i^T} \tag{3.58}$$

can be derived when energy conservation is considered. Here the index T indicates the thermal velocity, which is obtained after a coordinate transformation into the center-of-momentum frame of the particles. Translating this friction coefficient into our numeric framework, with the restraint of performing $n = \frac{\Delta t_{\mathrm{FD}}}{\Delta t_{\mathrm{MD}}}$ FD iterations per MD iteration, we get

$$\xi = -\frac{V_{\mathrm{FD}}}{n} \frac{\sum_{k=0}^{n} C_\alpha^k}{\sum_{i=1}^{N} m_i, \dot{\mathbf{r}}_i^T} \tag{3.59}$$

with V_{FD} being the volume of the coupled FD cell, N the number of particles in the MD system within the FD cell and $\sum_{k=0}^{n}$ summing over all discrete times of the FD iteration. The friction term is evaluated for each FD cell separately and added to the equations of motion of all particles i within the respective FD cell. Again, all resulting equations combined can be integrated by the Leap-Frog algorithm.

3.4.2 Effective Potentials

While thermodynamic constraints enter the simulation by choice of integration scheme, all material properties enter the simulation by choice of the effective interatomic potential $U(\{\mathbf{r}\})$ and particle mass m_i. From this choice follows the deterministic dynamics of the system, from which all macroscopic material properties, like phase behavior or elastic constants can be obtained. This again makes the choice of $U(\{\mathbf{r}\})$ crucial to the outcome of the simulation.

In general, each classical interaction potential can be written as a series of n-body

interaction potentials U_n. Therefore, the force

$$\mathbf{F}_i = -\nabla_{\mathbf{r}_i} U(\{\mathbf{r}\}) = -\nabla_{\mathbf{r}_i} \underbrace{\left[U_1(\mathbf{r}_i) + \sum_{i \neq j} U_2(\mathbf{r}_i, \mathbf{r}_j) + \sum_{i \neq j} \sum_{i,j \neq k} U_3(\mathbf{r}_i, \mathbf{r}_j, \mathbf{r}_k) + \dots \right]}_{\equiv U(\{\mathbf{r}\})}. \tag{3.60}$$

acting on particle i becomes a superposition of these contributions. Unfortunately, the computational cost of n-body interactions scales poorly with increasing n and therefore determines the computational cost of force calculation. In a primitive implementation, taking n-body interactions into account, the computational cost of force calculation of N particles will scale with $\mathcal{O}(N^n)$. As a result, the force calculation is typically by far the most computationally expensive part of a multi million particle MD simulation and therefore limits feasible simulation size. As always in numerics, poor scaling behavior gives rise to the trade-off between accuracy and efficiency. The need for a more efficient parametrization of U leads to a development where interatomic effective potentials are tailored to reproduce specific material properties better than others while keeping computational cost as low as possible by only taking into account the most dominant features. In case of silicon, a significant number of interatomic potentials have been developed and widely adopted in MD simulations within the last decades. These include for example

- the Modified Embedding Atom Method (MEAM) [191],
- the Stillinger-Weber Potential (SW) [192],
- the Tersoff Potential (T3) [193],
- the Modified Tersoff Potential (MOD) [194] and
- the Environment-Dependent Interatomic Potential (EDIP) [195].

The macroscopic physical properties for each potential are summarized in table 3.1. Also, a comparison to experimental data is presented. In the context of laser ablation, the dominating effects require for an emphasis on the modelling of melting temperature T_m, bulk modulus and elastic constants at the same time. We therefore

use the MOD and its derivations throughout this work. In addition, a classical carrier temperature-dependent potential, the MOD*, was developed at our institute by extending the MOD to include effects of electronic excitation [95]. In this following sections, we will give a short summary of the original and modified Tersoff potential and its extensions.

property	exp	MEAM	SW	T3	MOD	EDIP
C_{11} [GPa]	166	**167**	**162**	143	**166**	175
C_{12} [GPa]	64	**65**	82	75	**65**	**62**
C_{44} relaxed [GPa]	80	**80**	60	69	**77**	71
B [GPa]	99	**99**	108	**98**	**99**	**100**
T_m [K]	1683	2990	**1691**	2547	**1681**	**1520**

Table 3.1: Elastic constants C_{ij}, bulk modulus B and melting temperatures T_m of silicon for different interatomic potentials compared to experimental data (exp)[196]. Bold font numbers indicate an approximate accordance to experimental data.

The original Tersoff Potential The original Tersoff potential (T3) [193, 197] belongs to the most widely adopted empirical interatomic interaction potentials for silicon. One of the main features of the T3 is that directional dependence of bond strength in covalently bonded materials enters the potential via an environment-dependent term. This renders the T3 a pair potential

$$U = \frac{1}{2}\sum_{i\neq j}\phi_{ij} = \frac{1}{2}\sum_{i\neq j} f_c(r_{ij})\left[V_R(r_{ij}) - b_{ij}V_A(r_{ij})\right] \tag{3.61}$$

modelled as pair-like repulsive

$$V_R(r_{ij}) = Ae^{-\lambda_1 r_{ij}} \tag{3.62}$$

and attractive

$$V_A(r_{ij}) = Be^{-\lambda_2 r_{ij}} \tag{3.63}$$

interactions, thus being way more computationally efficient than an conventional 3-body potential. However, pure pair potentials are intrinsically isotropic in bond angle variation and therefore cannot reproduce the crystallisation of silicon in its characteristic diamond structure. The T3 now introduces an environment-dependent coefficient

$$b_{ij} = (1 + (\zeta_{ij})^{\eta})^{-\delta} \tag{3.64}$$

containing

$$\zeta_{ij} = \sum_{k(\neq i,j)} f_c(r_{ik}) \cdot g\left(\cos(\theta)\right) \cdot e^{p(r_{ij}-r_{ik})^q} \tag{3.65}$$

to include bond angle information. Here, the summation over k involves all neighbor atoms of the respective atom pair i and j. θ is the bond angle spanned between r_{ij} and r_{ik}. ζ_{ij} therefore implicitly includes 3-body interactions and allows to reproduce 3-body effects like bond strengthening at surfaces of covalent materials, while still retaining the computational cost of a pair potential. The bond angle term reads

$$g\left(\cos(\theta)\right) = a\left(1 + \frac{c^2}{d^2} - \frac{c^2}{d^2 + (h - \cos(\theta))^2}\right) \tag{3.66}$$

and the cut-off radius is defined as

$$f_c(r_{ij}) = \begin{cases} 1, & r_{ij} \leq R_1 \\ \frac{1}{2}\left[1 + \cos\left(\pi \frac{r_{ij}-R_1}{R_2-R_1}\right)\right], & R_1 < r_{ij} < R_2 \\ 0, & r_{ij} \geq R_2. \end{cases}$$

The Modified Tersoff Potential The modified Tersoff potential (MOD) was modified by [194] to further improve melting temperature and elastic properties of the material. This was achieved by altering the angular-dependent term to

$$g\left(\cos\theta\right) = c_1 + \frac{c_2(h - \cos\theta)^2}{c_3 + (h - \cos\theta)^2}\left[1 + c_4 \exp\left(-c_5(h - \cos\theta)^2\right)\right]$$

and the cut-off radius to

$$f_c(r_{ij}) = \begin{cases} 1, & r_{ij} \leq R_1 \\ \frac{1}{2} + \frac{9}{16}\cos(\pi\frac{r_{ij}-R_1}{R_2-R_1}) - \frac{1}{16}\cos(3\pi\frac{r_{ij}-R_1}{R_2-R_1}), & R_1 < r_{ij} < R_2 \\ 0, & r_{ij} \geq R_2. \end{cases}$$

The potential parameters for silicon are shown in table 3.3.

The temperature-dependent Modified Tersoff Potential Each empirical interatomic interaction potential reproduces the effects it was tailored to reproduce. This renders specific potentials appropriate for specific tasks. In the last decades, the interest in femtosecond laser ablation strongly increased due to its advantages in material processing, and so did the desire for interatomic interaction potentials to reproduce the occurring non-thermal phenomena. While the MOD was optimized to reproduce thermodynamic phase transitions at correct temperatures while keeping mechanical properties as close to experimental data as possible, the MOD still lacks the inclusion of non-thermal effects. Although the inclusion of electronic structure and bond manipulation effects into MD simulations was already possible within the Car-Parinello MD approach (CPMD) [89], the CPMD is unsuitable for the task of laser ablation simulations. The idea of the CPMD approach is basically to perform an MD simulation where the forces acting on each particle are calculated within ab initio DFT calculations. However, such approaches are computationally very costly when compared to empirical interatomic interaction potentials and limit feasible sample sizes to a few thousand atoms only [86, 198]. Consequently, alternative methods had to be developed.

To tackle this problem, our institute developed the MOD* interatomic interaction potential, which is a parametrization of the MOD by electronic temperature. Explicitly, the MOD* was developed by Kiselev [93, 94, 199] by expressing the attraction and repulsion coefficients A and B, as well as the attraction length λ_2 and angular modification c_2 of the MOD as a Taylor series

$$P(T_c) = \sum_{n=0}^{8} a_n (k_\mathrm{b} T_c)^n \tag{3.67}$$

in carrier temperature T_c. The finite temperature coefficients a_n for each parameter P where obtained by generating a data set of atomic configurations calculating the resulting temperature-dependent energy surface. The energy hyperplane in configurational space was calculated by finite temperature density functional theory (FTDFT) calculations for varying electronic temperatures T_c applying the Vienna Ab initio Simulation Package (VASP) [200–202]. The MOD* was then fitted to the energy hyperplane by variation of the parameters a_n using the force matching program potfit [203–205]. A thorough documentation of the implemented algorithms and fitting procedures, as well as the chosen weighting factors, can be found elsewhere [93]. To conclude, the MOD* is designed to incorporate the effects of carrier excitation into a classical interatomic interaction potential without significantly increasing the computational cost. The potential parameters for unexcited silicon $a_0 = P(T_c = 0)$ are displayed in table 3.3 in comparison to the corresponding MOD parameters. The derived finite temperature coefficients a_n are given in table 3.2.

a_n	A	B	λ_2	c_4
a_0	3337.89405000	117.25000000	1.3447680	6798.70936900
a_1	0.00000000	-6.65214929	0.0000000	715.81319624
a_2	749.86315013	177.79082685	0.4421857	-41431.42426030
a_3	1184.11723007	38.82600406	1.3098913	101066.85464000
a_4	-7259.53969859	-504.81962703	-4.7575282	-125153.26353800
a_5	9649.37058037	534.54870394	5.8346456	90001.64049490
a_6	-6277.88799086	-287.55739878	-3.6474661	-37529.94507610
a_7	2056.02229389	88.10934104	1.1531319	8363.22100809
a_8	-269.31466346	-11.80471283	-0.1472813	-764.39215505

Table 3.2: Temperature-dependent MOD* parameters P [94].

	MOD	MOD*
$A[eV]$	3281.5905	3337.89405
$B[eV]$	121.00047	117.25
$\lambda_1[1/\mathring{A}]$	3.2300135	3.24
$\lambda_2[1/\mathring{A}]$	1.3457970	1.344768
η	1.0	1.0
δ	0.53298909	0.54935
α	2.3890327	2.22
β	1	1
c_1	0.20173476	0.1695
c_2	730418.72	6798.709369
c_3	1000000.0	10000.0
c_4	1.0	1.0
c_5	26.0	26.0
h	-0.365	-0.365
$R_1[\mathring{A}]$	2.7	2.8
$R_2[\mathring{A}]$	3.3	3.2

Table 3.3: Comparison of MOD and MOD* parameters at zero temperature [94].

3.5 Analysis Tools

3.5.1 Cluster and Void Analysis

Depending on the inciting laser fluence, a variety of ablation effects compete for being the dominating ablation mechanism, each resulting in a different distribution of ejected droplets, chunks or plates. Consequently, we are interested in the exact composition of the ejected material at every time step. For this task, it would be best to be able to save the atomic configuration at every MD step and extract the information of interest in post-production. Unfortunately, due to memory restrictions, this approach is far from being feasible in our large scale massively parallel MD simulations. For example, a single run of a typical simulation would generate 5 PB of atomic configurations for a simulation time of 100 ps if written out on every time step. This way, the data accumulated within the simulations of chapter 7 would add up to 552 PB alone. This amount of data is enough to declare this approach as unfeasible in the year 2022 without even considering the resulting slow-down due to the immense I/O cost. However, in the end we are not interested in the properties of each single atom, but in the properties of each connected volume of material. To bypass the shown restriction, we implemented our own dynamic cluster analysis algorithm into IMD and extract the relevant data on the fly.

The main idea of the on-the-fly cluster analysis algorithm is that the workload of analysis is shared equally among the CPU grid. Each CPU loops through local atoms and assigns a tuple (id_{CPU},id_C) to each atom. We call id_{CPU} the CPU ID and id_C the cluster ID. The loop is set up as a recursion that assigns neighboring atoms within the potential cut-off radius an identical id_C. Note that this intrinsically includes effects of bond manipulation depicted by the MOD*. In pseudo code this algorithm reads:

```
### simplified pseudo code of the cluster analysis

## define recursive functions

def loop_neighbors(atom):
    for neighbor in get_neighbors(atom):     ## loop over neighboring atoms
        if (   ( neighbor.id_c   > id_c    ) ## if neighbor has lower CPU
```

```
            or ( neighbor.id_cpu > id_cpu) ):## or cluster ID
            assign_IDs(atom)                 ## assign tuple with lowest CPU ID
            CHANGED_TAG = yes                ## tag if changes occur
            loop_neighbors(neigbour)         ## loop again

def loop_local_cells():
   for FD_cell in local_FD_cells:            ## loop through all local FD Cells
    for MD_cell in FD_cell:                  ## loop through all MD Cells
        for atom in MD_cell:                 ## loop through every atom
            loop_neighbors(atom)             ## start recursion


## main program

# initialize analysis

for FD_cell in local_FD_cells:               ## loop through all local FD Cells
    for MD_cell in FD_cell:                  ## loop through all MD Cells
        for atom in MD_cell:                 ## loop through every atom
            initialize(atom)                 ## assign start value to each atom

# main loop

while ( CHANGED_TAG == yes ):                ## if previous loop changed IDs
    MD_comunication()                        ## Communicate MD Cells
    loop_local_cells()                       ## start loop
```

We visualize the core concept in figure 3.7. On the left side we see a CPU grid of four CPUs divided by thick lines. Each CPU encompasses FD cells and some green material. The indices on the upper left denote $\mathrm{id}_{\mathrm{CPU}}$ and on the lower right id_{C}. In practice, every atom gets assigned its own tuple, but for this overview we write it on the FD cells. The concept remains the same. First every CPU assigns the local CPU-ID to each atom and loops recursively through all local atoms. Connected atoms get the identical id_{C}. Then we use the MD communication to communicate surface MD Cells with the assigned tuples. With the now communicated atoms, we repeat the recursion and favour lower CPU IDs. The result is a CPU grid sketched on the right.

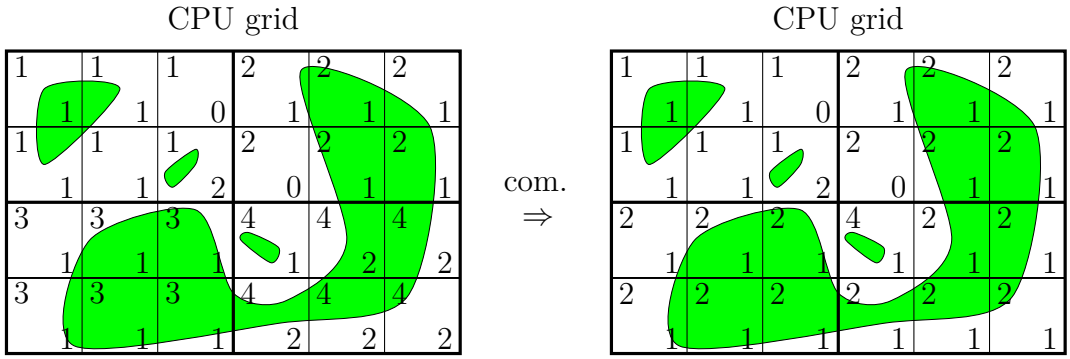

Figure 3.7: Illustration of the cluster and void analysis algorithm at an arbitrary time step in two dimensions. Green areas indicate a cluster. Left shows the state after local CPU ID and cluster ID assignment. Right shows the state after communication and global CPU ID and cluster ID assignment.

Now, while all atoms remain on the respective original CPUs, the tuple ($\mathrm{id_{CPU}}$,$\mathrm{id_C}$) assigns each atom to a unique cluster. For the evaluation of cluster statistics we set up an MPI array of size $\max(\mathrm{id_{CPU}}) \times \max(\mathrm{id_C})$. Now, every relevant property like cluster size, momentum, center of mass, CSP or temperature can be communicated and computed on this array with effective standard MPI communication schemes like `MPI_Reduce`. The algorithm to detect voids is set up analogously but assigns the tuple to empty MD cells.

3.5.2 Analysing the Atomic Structure

In this work, we simulate crystalline materials under extreme thermodynamical conditions which ultimately lead to phase transitions or non-equilibrium pathways of multiple kinds. In all cases, we are interested in the dynamical behavior of the material. Under extreme non-equilibrium conditions, we expect heterogeneous melting propagating into the sample, the generation of melting nuclei in overheated crystals, the ejection of molten or crystalline material or the generation of crystal defects. For the description of all these effects, the local thermodynamical phase or the specific crystal structure is of interest.

In the past, many computational analysis methods to evaluate this have been developed. Each shows different emphasis on accuracy, robustness or computational

efficiency. Other methods were designed for more specific purposes, like reliably differentiating between fcc and bcc structures. However, in this work, we specifically use the centrosymmetry parameter (CSP) and the modified common neighbor analysis (mod-CNA) to analyze atomic structures and quantify melting processes. In the following, we want to define these methods and motivate their use by short comparison to other analysis methods. Table 3.4 gives a short comparative overview over common structural analysis methods and their computational cost.

common abbreviation, analysis method	dimensionality	computational cost
atomic energy	1	-
CSP, centrosymmetric parameter	1	1
CNA, common neighbor analysis	$3N$	3
mod-CNA, adaptive common neighbor analysis	$3N$	4
BAA, bond angle analysis	8	4
BOA, bond order analysis	2	100
Voronoi analysis	4	50
NDA, neighbor distance analysis	$N(N-1)/2$	20

Table 3.4: Comparison of common structure identification methods. N represents the number of nearest neighbors around the probe atom. The cost factors are expressed relative to the CSP with neglect of cost of generating neighbor lists. For more details and analysis methods see [206].

CSP The CSP was developed by Kelchner et al [207] and quantifies the symmetry of bonds from a probe atom i to its N neighboring atoms. We choose atom i as the origin of coordinates, define the distance vector towards its neighbor atom j as $\mathbf{r}_j$ and index the opposing neighbor atom as $j + N/2$. In its original formulation by Kelchner, the

$$\mathrm{CSP}_i = \sum_{j=1}^{N/2} \left| \mathbf{r}_j - \mathbf{r}_{j+N/2} \right|^2 \tag{3.68}$$

of atom i is then calculated as the sum over the squared difference between opposing neighbor atom positions. In this definition, the CSP is zero for a perfect centrosymmetric crystal and non-zero for atoms contributing to defects. However, this definition comes with a set of crucial drawbacks. First, it leads to the computational burden of first having to identify and sort out opposite bond sites. Second, simple elastic deformation or changes in temperature will scale the CSP, making it hard to compare to different thermodynamic conditions. And third, structures with a different number of nearest neighbors lead to completely different CSP values, making it hard to compare different materials. However, a modified definition of the CSP, namely

$$\mathrm{CSP}_i = 1 - \frac{\left(\sum_{j=1}^{N} \mathbf{r}_j\right)^2}{N \sum_{j=1}^{N} \mathbf{r}_j^2} \tag{3.69}$$

was proposed [206]. This definition scales the CSP $\in [0 : 1]$ and conserves the idea of distance vectors canceling out pairwise for centrosymmetric crystals, while removing the necessity of explicitly sorting them pairwise. Plus, standardisation makes it applicable and comparable between different lattice structures and pressure conditions. In fact, this new attribute is the great advantage of the CSP. Elastic, or any affine deformation will not change the CSP, making it very robust in non-equilibrium conditions.

Of course, in the context of laser ablation, we encounter sample surfaces where surface atoms have only one-sided neighbors. Consequently, surface atoms will show a low CSP despite being part of a perfect crystal structure. The CSP has to be understood only as a parameter representing local symmetry rather than a parameter representing thermodynamical phases or crystal structures. These downsides are easy to cope with, when we consider that the CSP is computationally extremely cheap, as its calculation can be done on the fly within the MD force calculation, thus induce minimal overhead.

BOA Bond order analysis (BOA) is based on the idea of mapping the N nearest neighbors around a probe atom i to a unit sphere and evaluating a set of local bond

order parameters

$$Q_l = \sqrt{\frac{4\pi}{2l+1} \sum_{m=-l}^{l} |q_{lm}|} \tag{3.70}$$

$$\text{with} \qquad q_{lm} = \frac{1}{N} \sum_{j=1}^{N} Y_l^m \left(\theta_j, \phi_j\right). \tag{3.71}$$

These parameters are also-called Steinhardt order parameters [208]. The Steinardt order parameters are constructed of sets of rotationally invariant combinations of spherical harmonics Y_l^m, making them independent of crystal orientation. Each parameter shows characteristic values for specific lattice structures. For example all parameters for $l \leq 3$ vanish for cubic symmetry. The parameters Q_4 and Q_6 are often utilized to distinguish fcc, hcp and bcc phases. Table 3.5 shows example values for Q_4 and Q_6 for some perfect crystal structures. However, thermal fluctuations broaden the distribution of the Steinhardt order parameters, making it necessary to define arbitrary regions in the Q_4-Q_6-plane to identify said structures [209, 210]. Still, the BOA is a robust tool to identify different lattice structures with a high computational cost due to the evaluation of spherical harmonics.

Q_l	fcc	bcc	hcp
Q_4	0.191	0.036	0.097
Q_6	0.575	0.511	0.485

Table 3.5: Values of Q_l in the bond order analysis method defined in equation (3.70) for different perfect crystal structures.

BAA Bond angle analysis (BAA) was developed by Ackland and Jones [211] specially to differentiate between fcc, hpc and bcc structures. For N neighbors, $N(N-1)/2$ eight-bin histograms over all possible combinations of neighboring atoms j and k of $\cos(\theta_{jk})$ are generated. The angle θ_{jk} denotes the angle spanned between the probe atom i and neighboring atoms j and k. All generated histograms are then reduced to one histogram. From this histogram and by a set of heuristic rules, the

lattice type can be evaluated. This rule set has been optimized towards a stable differentiation between fcc, bcc and hcp structures. It is not applicable to diamond structures.

CNA The common neighbor analysis (CNA) takes a different approach than calculating floating-point numbers from spatial vectors. In contrast to the CSP and BOA, for N neighbors within a cut-off distance, the CNA computes N characteristic triples (n_{cn},n_{b},n_{lcb}) from the topology of bonds surrounding a probe atom. These triples can then be compared to reference structures. The triples consists of the number of neighbor atoms n_{cn} the probe atom and its neighbors have in common, the total number of bonds between these atoms n_{b} and the number of bonds n_{lcb} in the longest chain of connected common neighbors. For example, for the computation of the CNA in a fcc lattice we get

$$\mathrm{CNA}_{\mathrm{fcc}} = 12 \times (4,2,1) \tag{3.72}$$

by taking into account the second neighbor shell. This gives $N = 12$. Note that the N triples do not necessarily have to be identical. The CNA is a very robust tool to identify different crystal structures and does not bring any requirements to the probed lattice structure as does e.g. centrosymmetry. It is a more complex high dimensional method than a scalar method. On the other hand, the assignment of lattice structure is a binary choice and the comparing of triples to a data base is very precise. However, identification and recursive calculation of bonding topology renders this method computationally very costly, thus unsuitable for on the fly calculations. Also, in its first published formulation it is not able to classify diamond structures.

mod-CNA The adaptive or modified version of the CNA proposed by Maras [212] and implemented in the open vizualization tool OVITO [213]. The basic idea is the same as within the CNA approach, but extended to identify diamond structures more robustly. Conventional CNA fails at classifying diamond structures because in the diamond lattice, nearest neighbors do not have common neighbors and the second and third neighbor shells are not well separated. To tackle this problem, the

nearest neighbors of the probe atom are identified. For each of these neighbor atoms a second list of neighbors is identified. The union of these atoms gives a list of first and second nearest neighbors.

4 Summary of Used Model Parametrization and Parameters

4.1 Roadmap

The structure of this work follows the idea to stepwise increase the number of spatial dimensions of the simulation setup. With each added dimension, more effects contribute to the outcome of the simulation, allowing us to separate effects clearly from each other.

Simulation Parameters In this chapter 4 we give a compact synopsys of the parametrization details, studied samples and performed sample preparations. We also display all parameters from literature, as well as their references in a compact format.

Ultra-thin Films In chapter 5, we refine the optical parametrization of our simulation model. For this, we put our attention to ultra-thin films. Here, ultra-thin films are defined as structures with a lateral expansion smaller than the laser beam diameter and sample depths shorter than absorption length. As a result, transport phenomena are non-relevant in this geometry, allowing us to directly compare the predictions of electronic excitation of the derived models. We will construct and justify a transition from the currently established parametrization based on fitting-laws towards our optical parametrization, which is solely derived from theory. Finally, we will extend the model by the MOD* and compare homogeneous laser heated material to ab initio MD simulations.

Bulk Material In chapter 6, we shift our attention from ultra-thin films towards bulk samples. Bulk samples show a lateral expansion smaller than the beam diameter and a sample depth deeper than the absorption length. As a vivid image, under homogeneous irradiation, this geometry represents the material along the optical axis exactly in the center of the laser spot. By doing this, we allow for excitation gradients and one-dimensional energy transportation effects. We compare the derived transport models and extend them by our refined optical parametrization. As a result, we obtain a combined continuum-atomistic model, capable of correct prediction of transport phenomena under varying electronic excitations. Based on this model, we perform laser ablation simulations and investigate the ablation depth and categorize novel non-thermal ablation mechanics.

The Ablation Crater In chapter 7, we perform huge MD simulations on samples with lateral extensions of several micrometers, thus being greater than the laser spot diameter. We irradiate the sample with Gaussian pulse shapes and investigate the complex mechanics involved in the formation of the ablation crater for varying fluences. Finally, we show and isolate effects based on the lateral energy and material transport.

4.2 Summary of Model Parameterization and Parameters

In the chapter 2, we gave an overview on the physical processes during ultra-fast laser ablation and how they can be modelled and implemented. However, some scalar physical properties like e.g. the parametrization of the semiconductor band gap E_g are still missing. Furthermore, we have not specified which parametrization combination we are explicitly applying. Unfortunately, we observed that this is a state which many publications in the laser ablation community can be found in. It is not uncommon that crucial parametrization choices are unclear or relevant details of the studied sample are missing. Without a specific parametrization given, it is unclear which effects are taken into account implicitly.

If we stay with our example of the semiconductor band gap E_g, the choice of

parametrization often is the Varshini equation [214]

$$E_g = E_0 - \alpha \frac{T_l^2}{T_l + \beta} \tag{4.1}$$

or the extended Varshini equation [109]

$$E_g = E_0 - \alpha \frac{T_l^2}{T_l + \beta} - \gamma\, n_c^{1/3}, \tag{4.2}$$

both most often cited only as the Varshini equation. The first equation describes the band gap narrowing in semiconductors with increasing lattice temperature T_l. The latter includes the band gap narrowing effects caused by the density of excited CB carriers n_c. For continuous wave irradiation, this extension plays a minor role. However, when considered as a parametrization of transport effects in semiconductors with e.g. the TSM, it suddenly alters the qualitative behavior of the carrier density wave. By including this extension to the internal energy of CB carriers,

$$U_c = n_c \left(E_g(n_c) + 3k_b T_c\right) \tag{4.3}$$

scales with band gap narrowing and gives rise to altered energy

$$\mathbf{W} = \left(E_\mathrm{g} + 3n_c k_\mathrm{B} T_\mathrm{c}\right) \mathbf{J} - \kappa_\mathrm{c} \nabla T_\mathrm{c}. \tag{4.4}$$

and carrier fluxes

$$\mathbf{J} = -D_0 \left[\nabla n_c + \frac{2n_c}{k_\mathrm{b} T_\mathrm{c}} \nabla E_\mathrm{g} + \frac{n_c}{2T_\mathrm{c}} \nabla T_\mathrm{c}\right] \tag{4.5}$$

which now implicitly include carrier confinement effects due to gradients in the band gap. Now by the choice of which Varshini equation we use, we implicitly decide wether or not to include ultra-fast excitation gradients in the carrier-particle dynamic.

The practice of unclear parametrizations does not only hinder interpretation of the presented data sets in literature, but also prevents the reproducibility of simulation data, thus undermining the scientific process itself. This is the reason why we

want to devote this chapter to the rigorous listing of all material parametrizations and adopted numeric values, as well as to show our applied sample preparation method. Furthermore, one key element of this work is to incrementally improve and compare different model parametrizations. During this process, this section should serve as an anchor point for the reader to fall back to and to get an overview over the parametrization combinations. For convenience, if no index is provided, the parameters α, β and γ are to be understood as the degrees of freedom for each parametrization.

4.3 Optical Properties

Reflectivity The reflectivity R at vacuum-solid interfaces is modelled by the well-known Fresnel equations. In this work only normal incidence is considered, therefore the reflectivity coefficient can be written as

$$R = \frac{|\bar{n} - 1|^2}{|\bar{n} + 1|^2} \tag{4.6}$$

with the complex refractive index $\bar{n}$. The Fresnel reflectivity will be compared to a widely used fitting-law, which reads [110, 215]

$$R = \alpha + \beta\,(T_l - \gamma). \tag{4.7}$$

Laser Absorption The absorbed laser intensity is modelled with the absorption rate equation for semiconductors presented in equation (2.10). We consider the most important optical absorption processes. These are one-photon SPA and FCA as well as TPA processes. In this case, the rate equation reads

$$\frac{dI}{dx} = -\left(\alpha_{\mathrm{SPA}} + \alpha_{\mathrm{FCA}}\right) I - \beta_{\mathrm{TPA}}\, I^2 \tag{4.8}$$

with α_{FCA} being the intraband absorption coefficient, most commonly denoted as free carrier absorption coefficient, α_{SPA} the interband absorption coefficient and β_{TPA} the two-photon absorption coefficient. Note that due to the crystal symmetry of silicon, three-photon absorption processes are intrinsically forbidden.

Single Photon Absorption Coefficient α_{SPA} The SPA coefficient α_{SPA} describes the interband absorption rate caused by SPA. Laser irradiation of semiconductors inevitably leads to lattice heating and therefore band gap narrowing. In turn, band gap narrowing increases the number of excitable VB states at a given wavelength. The increase of excitable states obviously leads to an increase of excitation rate and therefore an increase of the SPA coefficient. To model this complex interplay, we apply the fitting-law

$$\alpha_{\mathrm{SPA}} = \alpha \cdot \exp\left(\frac{T_l}{\beta}\right) \tag{4.9}$$

proposed by [215].

Free Carrier Absorption Coefficient α_{FCA} The free carrier absorption coefficient α_{FCA} describes the SPA rate by CB electrons. In this work, different descriptions of the free carrier absorption coefficient will be compared with regard to their impact on laser ablation simulation. First, a widely adopted fitting-law [216]

$$\alpha_{\mathrm{FCA}} = n_c \cdot \Theta_{\mathrm{FCA}} \tag{4.10}$$

$$= n_c \cdot \alpha \frac{T_l}{T_0}, \tag{4.11}$$

which implicitly takes band gap narrowing into account is implemented. This fitting-law explicitly includes the temperature dependence of the free carrier absorption cross section Θ_{FCA}. Secondly,

$$\alpha_{\mathrm{FCA}} = \frac{2\,\mathrm{Im}\,\bar{n}}{c_0} \tag{4.12}$$

is directly modelled by the well-known Drude model presented in equation (2.5).

Two Photon Absorption Coefficient β_{TPA} The two-photon absorption coefficient β_{TPA} describes the increase of general laser light absorption α in the first order of intensity, so that $\alpha = \alpha_0 + \beta_{\mathrm{TPA}} I$ holds. Here α should be understood as a summation of all linear absorption effects. For band gap materials, this first order

contribution is strongly dominated by the simultaneous absorption of two photons involving a virtual state within the band gap [103, 104], hence the naming two-photon absorption coefficient. Rigorous treatment of the origin of contributing non-linear effects lie outside the scope of the present work. In short, theoretical solid state band calculations [105–107] have shown that the two-photon absorption coefficient can be expressed as a general equation. This holds for most parabolic and non-parabolic semiconductors [81]. This general form can be simplified by band structure assumptions in Hartree-Fock approximation [217]. And finally, taking the angular average of the interband matrix elements, we arrive at the expression by [108] which reads

$$\beta = K \frac{\sqrt{E_p}}{n_0^2 E_g^3} \cdot \psi(2\hbar\omega / E_g) \tag{4.13}$$

$$\text{with} \qquad \psi(2x) = \frac{(2x-1)^{3/2}}{(2x)^5} \qquad \text{for} \qquad 2x > 1. \tag{4.14}$$

E_p is a result of the listed approximations and is given by $E_p \approx 21\,\text{eV}$ for most semiconductors [108]. K can be interpreted as a reasonable material fitting parameter [81].

4.4 Semiconductor Parametrization

Band Gap E_g The temperature dependence of the semiconductor band gap arises from different bond lengths at different lattice temperatures. Consequently, lattice temperature variations change the relative position of conduction and valence bands due to dilatation of the lattice. The most popular experimentally determined fit equation for semiconductors that reproduces this fact is the in equation (4.2) introduced extended Varshini equation [109, 214]

$$E_g = E_0 - \alpha \frac{T_l^2}{T_l + \beta} - \gamma\, n_c^{1/3}. \tag{4.15}$$

The last term is a correction to take band gap narrowing by excitation into account. Note that a more complex fitting-law was proposed by [219] to fine tune the temper-

name	symbol	value	λ [nm]	reference
reflectivity, T-expression	R	$R = \alpha + \beta\,(T_l - \gamma)$	-	[218]
	α	0.329	800	[216]
	β	$5 \cdot 10^{-5}\,/\mathrm{K}$	800	[216]
	γ	$300\,\mathrm{K}$	800	[216]
reflectivity, Drude	R	See (4.6)	-	
single photon	α_{SPA}	$\alpha_{\mathrm{SPA}} = \alpha \cdot \exp(T_l/\beta)$	-	[215]
absorption coefficient,	α	$1.34 \cdot 10^3\,/\mathrm{cm}$	694	[215]
T-expression	α	$1.12 \cdot 10^3\,/\mathrm{cm}$	800	[216]
	β	$427\,\mathrm{K}$	694	[215]
	β	$430\,\mathrm{K}$	800	[216]
free carrier absorption	α_{FCA}	$\alpha_{\mathrm{FCA}} = n_c \cdot \alpha\,\frac{T_l}{\beta}$	-	[216]
coefficient,	α	$6.4 \cdot 10^3\,/\mathrm{cm}$	800	[216]
T-expression	β	$300\,\mathrm{K}$	800	[216]
free carrier absorption	α_{FCA}	See (2.5)		
coefficient, Drude				
two-photon absorption	β_{TPA}	$2\,\mathrm{cm/GW}$	800	See sect. 5.2.4
coefficient, const.				
two-photon absorption	β_{TPA}	See (4.13)	-	
coefficient, Drude				

Table 4.1: Short summary of the optical parameters for silicon.

ature dependency of the band gap. However, it lacks the charge carrier contribution to band gap narrowing and thus is not useful for our purposes.

Rate Equation for Excited Carriers The local free carrier generation is modelled by the rate equation discussed in (2.11) and supplemented with the absorption

coefficients. The rate equation reads

$$\frac{dn_c}{dt} = \frac{\alpha_{\mathrm{SPA}}}{\hbar\omega_{\mathrm{L}}} I + \frac{\beta_{\mathrm{TPA}}}{2\hbar\omega_{\mathrm{L}}} I^2 + \delta_{\mathrm{imp}} n_c - \gamma_{\mathrm{Aug}} n_c^3 \tag{4.16}$$

with the impact ionization coefficient δ_{imp} and the Auger recombination coefficient γ_{Aug}.

Impact Ionization Coefficient δ_{imp} The impact ionization coefficient δ_{imp} for semiconductors can be expressed by Chynoweth's Law [220]

$$\delta_{\mathrm{imp}} = \alpha \cdot \exp\left(-\frac{\beta}{E}\right) \tag{4.17}$$

which suggests that the impact ionization rate δ_{imp} scales exponentially with the local electric field component E in current flow-direction. For silicon, the parametrization can be extended to [109]

$$\delta_{\mathrm{imp}} = \alpha \cdot \exp\left(-\beta \frac{E_g}{T_c}\right), \tag{4.18}$$

to include band gap effects and carrier temperature-dependence.

Carrier Thermal Conductivity κ_c We use Fourier's law in the derivation of the general heat equation. Fourier's law states that heat flux is proportional to the thermal gradient with the proportionality constant κ_c. This constant is called the carrier thermal conductivity. This implies that heat transfer is a diffusion-like phenomena based on carrier-carrier scattering. Obviously, we expect carrier-carrier scattering rates to increase with increasing carrier temperature. To take this phenomenon into account, a first order Taylor series fitting-law [110, 221]

$$\kappa_c = \alpha + \beta\, T_c \tag{4.19}$$

is applied.

Carrier-Phonon Energy Relaxation Time τ_c In theory and experiments on silicon, a drastic increase of τ_c with increasing carrier density is observable [221–225]. This effect is included in the parametrization by Yoffa [225], which reads

$$\tau_c = \alpha \left[1 + \left(\frac{n_c}{\beta} \right)^2 \right]. \tag{4.20}$$

Here α can be interpreted as the carrier-phonon energy relaxation time at room temperature. The term $\left(\frac{n_c}{\beta}\right)^2$ accounts for screening effects occurring above a critical carrier density β.

Carrier Diffusivity D For the carrier diffusivity, different parametrizations are available. Based on the well-known Einstein relation, the diffusion coefficient can be expressed in ambipolar approximation as

$$D = \frac{1}{q} k_\mathrm{b} T_c \frac{\sigma_e \sigma_h}{\sigma_e + \sigma_h} \tag{4.21}$$

with the electron σ_e and hole σ_h mobility respectively. The downside of this approach is that this expression is only valid for low lattice temperatures. In the context of laser ablation, high lattice temperatures occur, thus we use the fitting-law

$$D = \alpha \cdot \left(\frac{\beta}{T_\mathrm{l}} \right) \tag{4.22}$$

suggested in [109].

name	symbol	value	reference
electron DOS effective mass	$m^*_{e,\mathrm{DOS}}$	$0.33\, m_e$	[110]
hole DOS effective mass	$m^*_{h,\mathrm{DOS}}$	$0.81\, m_e$	[226]
electron conductivity effective mass	m^*_e	$0.26\, m_e$	[109]
hole conductivity effective mass	m^*_h	$0.37\, m_e$	[109]

Table 4.2: Summary of effective masses for silicon. m_e is the electron mass.

name	symbol	value	λ [nm]	reference
Auger recombination coefficient	γ_{Aug}	$3.8 \cdot 10^{-31}\,\mathrm{cm}^6/\mathrm{s}$	-	[227]
impact ionization coefficient	δ	$\delta = \alpha \cdot \exp(-\beta\, E_g/T_c)$	-	[227]
	α	$3.6 \cdot 10^{10}\,/\mathrm{s}$	-	[227]
	β	$1.5/k_b$	-	[227]
carrier thermal conductivity	κ_c	$\kappa_c = \alpha + \beta\, T_c$	-	[221]
	α	$-3.47\,\mathrm{eV}/(\mathrm{s\,cm\,K}^2)$	-	[228]
	β	$4.45 \cdot 10^{14}\,\mathrm{eV}/(\mathrm{s\,cm\,K}^2)$	-	[228]
ambipolar carrier diffusivity	D	$D = \alpha \cdot \left(\frac{\beta}{T_\mathrm{l}}\right)$	-	[109]
	α	$18\,\mathrm{cm}^2/\mathrm{s}$	-	[109]
	β	$300\,\mathrm{K}$	-	[109]
band gap	E_g	$E_g = E_0 - \alpha \frac{T_l^2}{T_l+\beta} - \gamma\, n_c^{1/3}$	-	[214]
	E_0	$1.170\,\mathrm{eV}$	-	[214]
	α	$4.73 \cdot 10^{-4}\,\mathrm{eV/K}$	-	[214]
	β	$636\,\mathrm{K}$	-	[214]
	γ	$1.5 \cdot 10^{-10}\,\mathrm{eV} \cdot \mathrm{m}^3$	-	[109]
carrier-phonon energy relaxation time	τ_c	$\tau_c = \alpha\,[1 + (n_c/\beta)^2]$	-	[225]
	α	$240\,\mathrm{fs}$	-	[127]
	β	$6.0 \cdot 10^{20}\,/\mathrm{cm}^3$	-	[127]

Table 4.3: Short summary of the semiconductor parameters for silicon adopted in this work.

4.5 Sample Equilibration

Within this work, we want to start production runs of laser ablation on silicon in thermal equilibrium at room temperature i.e. $T_l = T_c = 300\,\mathrm{K}$ and zero pressure. For each interaction potential, the atomic configurations fulfilling theses criteria are different, due to different pair potential minima positions.

Each sample is generated by

1. placing silicon atoms on a face-centered diamond lattice with a lattice constant of $a = 5.5\,\text{Å}$. For aluminium, we construct a face centered cubic lattice with a lattice constant of $a = 4.0\,\text{Å}$.

2. Initializing velocities by assigning random velocities according to a Maxwell-Boltzmann distribution

$$B(\mathbf{v}) = \sqrt{\frac{m}{2\pi k_\mathrm{b} T_l}} \exp\left(\frac{-m\mathbf{v}^2}{2k_\mathrm{b} T_l}\right) \tag{4.23}$$

   for a temperature of $T_l = T_c = 300\,\mathrm{K}$.

3. Setting up an NPT simulation with PBCs in all directions. The temperature is kept constant, while the simulation box size is scaled according to the pressure requirements. We perform 50000 MD steps at a time step $\Delta t_\mathrm{MD} = 0.1\,\mathrm{fs}$. This is equivalent to a simulation time of $t = 5\,\mathrm{ps}$. The box size is scaled by a factor of

$$\mu = 1 - 1.2\,\Delta t_\mathrm{MD}(p_\mathrm{end} - p) \tag{4.24}$$

   for each MD step.

4. Setting up an NVT simulation with PBCs in all directions. The box volume is kept constant while the temperature is increased by $\Delta T_l = 5\,\mathrm{K}$ by the Nosé-Hoover thermostat. We perform 50000 MD steps at a time step $\Delta t_\mathrm{md} = 0.1\,\mathrm{fs}$.

5. Repeat step 3 and 4 until $p = 0$ and $T_l = T_c = 300\,\mathrm{K}$ is reached.

6. Repeat step 3 and 4 for open PBCs in x-direction. This is necessary because we want to simulate open surfaces in laser incitation-direction and opening boundary conditions suddenly changes coordination number of surface atoms, thus changing their corresponding potential energy.

7. Setting up an NVE simulation with open PBCs in x-direction. Generally, we assume a sample is equilibrated when it fulfills the equi-partition theorem demanding

$$\sum_i^N \frac{1}{2} m \mathbf{v}_i^2 = U(\{\mathbf{r}\}) = \frac{3}{2} k_b T_l, \tag{4.25}$$

thus demanding equal distribution of energy in kinetic and potential energy. However, this definition does not prevent the sample from showing spatial gradients in energy distribution. We perform an additional simulation for 50000 MD steps at a time step $\Delta t_{\mathrm{md}} = 1\,\mathrm{fs}$.

material	atomic mass m [u]	lattice constant a [Å]
silicon	28.085	5.5
aluminium	26.981	4.0

Table 4.4: Material parameters for sample construction at $T_l = 0$.

name	symbol	value	note
initial carrier density	n_{eq}	$10^{14}\,/\mathrm{cm}^3$	Until section 5.3
initial carrier density	n_{eq}	$10^{19}\,/\mathrm{cm}^3$	After section 5.3
initial lattice temperature	T_l	300 K	
initial carrier temperature	T_c	300 K	
hydrostatic pressure	p	0 hPa	

Table 4.5: Initial conditions for production run simulations.

name	n_x	n_y	n_z	Cell	N_A	T_l [K]	Potential
`surface`	150	20	20	diamond	$4.8 \cdot 10^5$	300	MOD
`depth`	$4 \cdot 10^4$	40	40	diamond	$5.12 \cdot 10^7$	300	MOD
`depth_alu`	$4 \cdot 10^4$	40	40	fcc	$2.5 \cdot 10^7$	300	EAM
`depthT`	$1 \cdot 10^3$	10	10	diamond	$8 \cdot 10^5$	300	MOD
`block`	150	150	150	diamond	$2.7 \cdot 10^7$	300	MOD
`plate`	1024	32	2048	diamond	$5.3 \cdot 10^8$	300	MOD

Table 4.6: Summarized parameters for the studied samples. n_i is the number of unit cells in i-direction. N_A is the total number of atoms and x_i is the length of the sample in i-direction. The sample is in thermal equilibrium at temperature T_l.

name	x_x [nm]	x_y [nm]	x_z [nm]	offset [nm]
`surface`	82	10	10	44
`depth`	2225	22	22	1736
`depth_alu`	1616	16	16	1736
`depthT`	5500	5.5	5.5	550
`block`	82	82	82	0
`plate`	556	17	1113	556

Table 4.7: Summary of the spatial dimensions of the studied samples. x_i is the material length in i-direction. The offset corresponds to the length of material free area in laser-direction within the simulation box.

5 Simulations and Results - Ultra-thin Films

5.1 Characteristic Single Pulse Excitation

First, we want to compare the nTTM, TSM and the BETE model in respect to excitation of the carrier subsystem and show its characteristic time evolution after single pulse irradiation. We will start with the simplest optical parametrization available and use the T-expressions of table 4.1 for all optical parameters, namely the reflectivity, SPA and FCA. Also, we set the TPA coefficient to zero.

Simulations are performed on the ultra-thin silicon film sample `surface` under homogeneous laser irradiation with a sub-damage threshold fluence. The nTTM and TSM are solved with the semi-implicit Crank-Nicolson algorithm and the BETE with FTCS Euler integration. `surface` shows a depth of 82 nm, which is roughly a tenth of the characteristic absorption length of unexcited silicon for the inciding wavelength of $\lambda = 800\,\mathrm{nm}$. In this simplified case, the sample gets homogeneously excited, thus transport phenomena, as well as spatial carrier density gradients can be neglected. The resulting temporal evolution of spatially averaged observables of the nTTM, TSM and BETE is displayed in figure 5.1.

It is observable that the nTTM, TSM and BETE show qualitatively and quantitatively the same excitation mechanisms, confirming the assumption of invariance of excitation mechanics under varying transport mechanics. All models show a carrier temperature plateau at low laser intensities, followed by rapid CB electron generation and carrier laser heating. Post-pulse mechanisms are also identical, featuring carrier and lattice temperature equilibration due to electron-phonon coupling, as well as Auger heating. Auger heating originates from CB electron recombinations

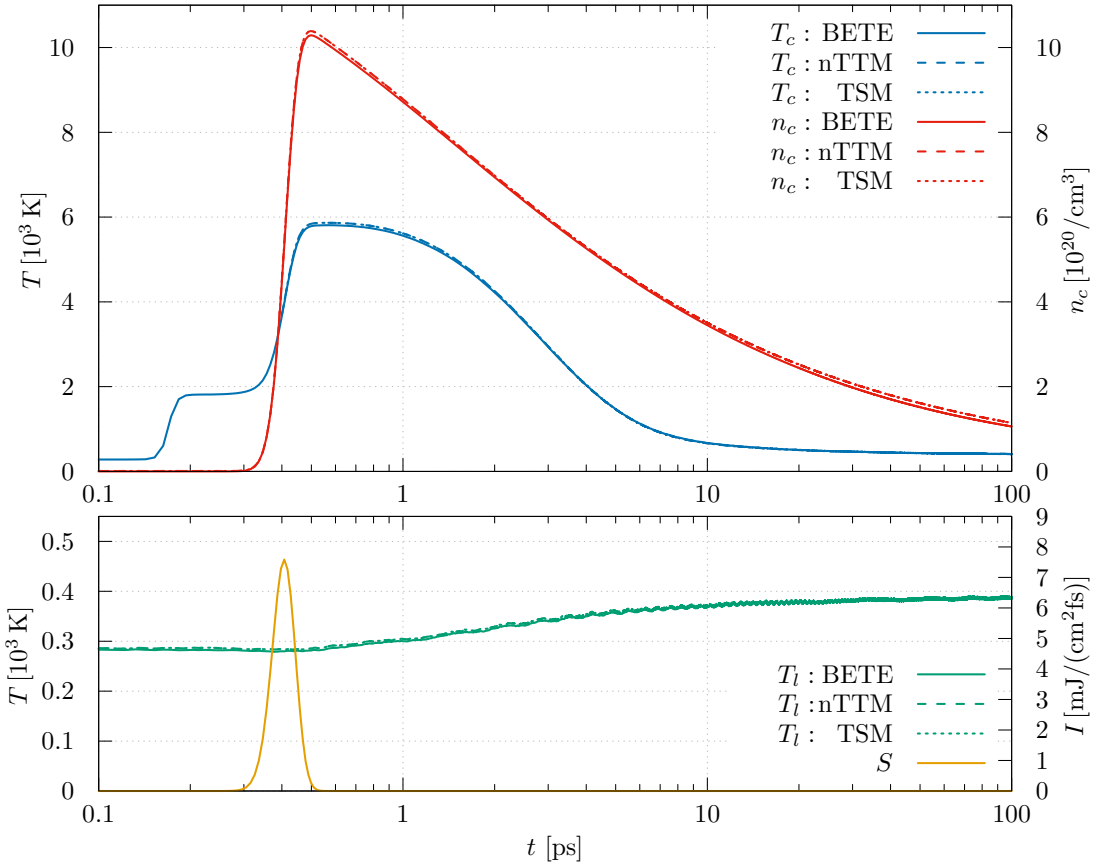

Figure 5.1: Time evolution of spatially averaged observables of the nTTM, TSM and BETE on sample `surface` under homogeneous laser irradiation with a sub-damage threshold fluence of $\sigma = 0.16\,\mathrm{J/cm^2}$ and a FWHM pulse duration of $\tau_p = 100\,\mathrm{fs}$. The free carrier absorption coefficient is modelled with the T-expression and the two-photon absorption coefficient β_{TPA} is set to zero.

leading to lowering of the specific heat capacity and therefore heating the carrier subsystem. Because of identical parametrization in absorption mechanics the carrier density dynamics is identical for all models.

The low Heat Capacity Plateau The occurrence of the initial carrier temperature plateau in all models, can be phenomenologically described by the identification of

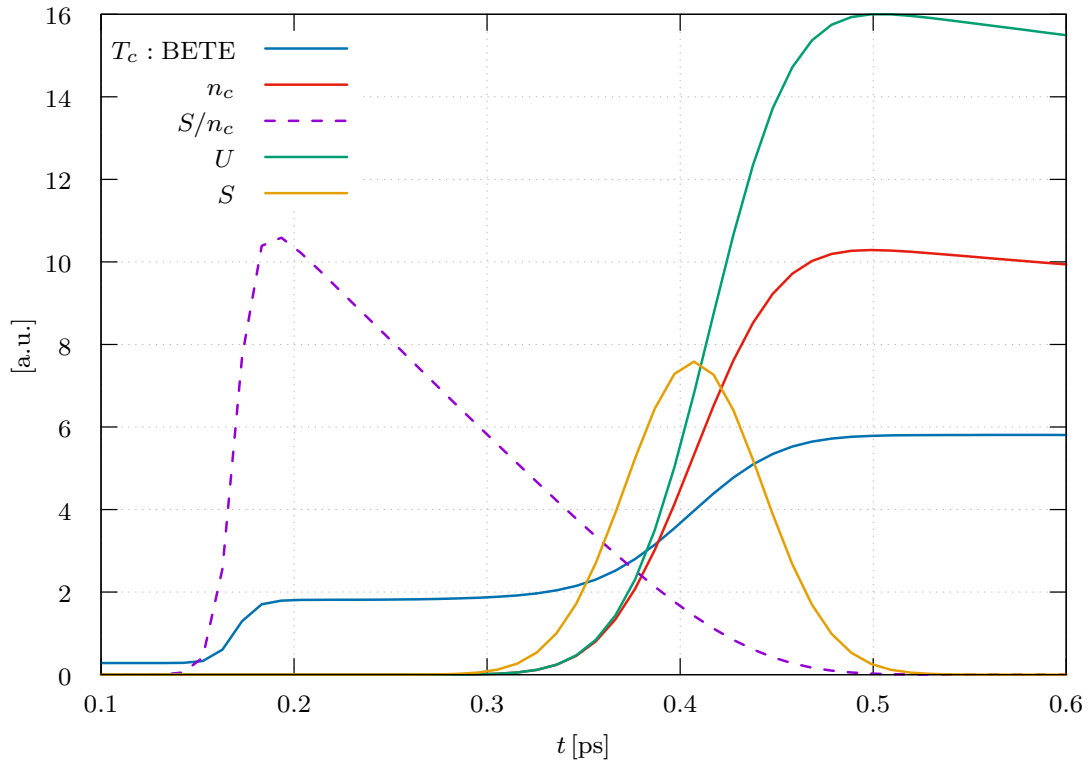

Figure 5.2: Time evolution of BETE observables of sample `surface` under laser irradiation with a fluence of $\sigma = 0.16\,\mathrm{J/cm^2}$ in arbitrary units. S/n_c marks the laser intensity per carrier density.

the specific heat capacity c_p of the electron gas, namely

$$c_p = \frac{\partial U}{\partial T_c} = \partial_{T_c} n_c \left(3 k_b T_c + E_g\right). \tag{5.1}$$

In all models, the specific heat capacity is proportional to the CB charge carrier density n_c. In semiconductors, equilibrium CB charge carrier density n_c is typically very small compared to post-irradiation CB charge carrier density. In the case of silicon, equilibrium CB charge carrier density n_c takes a value of $n_c \approx 10^{10}\,/\mathrm{cm}^3$ at a lattice temperature of $T_l = 300\,\mathrm{K}$. In contrast to the equilibrium case, laser excited CB carrier densities are typically in the order of $n_c \approx 10^{20}$ to $10^{22}\,/\mathrm{cm}^3$. In other words, during laser irradiation, the specific heat capacity of the CB carrier system typically increases by a factor of $\sim 10^{10}$ to $\sim 10^{12}$. As a result, silicon shows

a vanishing specific heat capacity in equilibrium conditions compared to its excited state. Apart from generating very high carrier temperatures at low excitation energies, this also gives rise to a number of numerical problems, which will be discussed in section 5.3.

The time evolution of BETE observables as well as the ratio of inciding laser intensity per CB carrier density S/n_c is shown in figure 5.2. It is observable that the carrier temperature plateau occurs when both the laser intensity and the carrier densities are small. Therefore, we can assume effects of order n_c^1 and I^1 to be dominant. Therefore interband absorption is the only contributing excitation mechanism. Interband absorption leads to CB charge carrier generation as well as CB charge carrier excitation. Both effects increase the heat capacity of the carrier system but work against each other in terms of carrier temperature increase. In detail, charge carrier generation cools the electron gas by increasing the heat capacity while carrier excitation directly increases carrier temperature proportional to c_p. With increasing time, the inciding energy per photon remains constant while the carrier temperature increment per absorbed photon decreases with increasing specific heat capacity. This leads to a saturated carrier temperature. As a result, in the regime of effects of order n_c^1 and I^1 a carrier temperature plateau originates.

For a more quantitative explanation, we start with the introduced low temperature/density assumptions. From Sommerfeld theory we know the time derivative of the internal energy U can be written as

$$\frac{\partial U}{\partial t} = \frac{\partial U}{\partial T_c}\frac{\partial T_c}{\partial t} + \frac{\partial U}{\partial n_c}\frac{\partial n_c}{\partial t} + \frac{\partial U}{\partial E_g}\left[\frac{\partial E_g}{\partial n_c}\frac{\partial n_c}{\partial t} + \frac{\partial E_g}{\partial T_l}\frac{\partial T_l}{\partial t}\right]. \tag{5.2}$$

Heat and carrier diffusion as well as lattice interactions occur on longer timescales after peak laser pulse intensity, thus will be ignored for this explanation. Inserting

the parametrization of local laser field intensity into (5.2) leads to

$$\begin{aligned}\partial_t T_c = &\left(\frac{\alpha_{\mathrm{SPA}}}{3k_b n_c} + \frac{\alpha_{\mathrm{FCA}}}{3k_b n_c}\right) I + \frac{\beta_{\mathrm{TPA}}}{3k_b n_c} I^2 \\ &- T_c \left[\frac{\alpha_{\mathrm{SPA}}}{n_c \hbar\omega_L} I + \frac{\beta_{\mathrm{TPA}}}{2n_c \hbar\omega_L} I^2 + \frac{\delta}{3k_b} - \frac{\gamma_{\mathrm{Auger}}}{3k_b} n_c^2\right] \\ &- \frac{1}{3k_b}\left[E_g + \frac{1}{3}\gamma_{\mathrm{Egap}} n_c^{\frac{1}{3}} + \frac{\partial E_g}{\partial T_l}\frac{\partial T_l}{\partial t}\right] \\ &\quad \times \left[\frac{\alpha_{\mathrm{SPA}}}{n_c \hbar\omega_L} I + \frac{\beta_{\mathrm{TPA}}}{2n_c \hbar\omega_L} I^2 + \frac{\delta}{3k_b} - \frac{\gamma_{\mathrm{Auger}}}{3k_b} n_c^2\right].\end{aligned} \tag{5.3}$$

In the limit of small n_c and small I and under the assumption that n_c varies sufficiently slower than T_c, the above differential equation simplifies to

$$\partial_t T_c(t) = \left(\frac{\hbar\omega_L}{3k_b} - T_c - \frac{\gamma_{\mathrm{Egap}} n_c^{\frac{1}{3}}}{9k_b}\right) \frac{\alpha_{\mathrm{SPA}}}{n_c} I(t). \tag{5.4}$$

Since we investigate an effect occurring ~ 4 FWHM times before laser peak intensity, it is appropriate to linearize the differential equation in $I \approx \kappa t$. The resulting differential equation is solvable with standard techniques giving

$$\begin{aligned}T_c(t) = &\left(\frac{\hbar\omega_L}{3k_b} - \frac{\gamma_{\mathrm{Egap}} n_c^{\frac{1}{3}}}{9k_b}\right) \\ &+ \left[T(0) - \left(\frac{\hbar\omega_L}{3k_b} - \frac{\gamma_{\mathrm{Egap}} n_c^{\frac{1}{3}}}{9k_b}\right)\right] \exp\left(-\frac{1}{2}\frac{1}{\hbar\omega_L}\frac{\alpha_{\mathrm{SPA}}}{n_c}\kappa t^2\right).\end{aligned} \tag{5.5}$$

This solution is coherent with our phenomenological explanation. Note that the term $\gamma_{\mathrm{Egap}} n_c^{\frac{1}{3}}$ originates from the extended Varshini equation (4.15) and describes band gap narrowing due to excited CB electrons. Band gap narrowing leads to an increased interband absorption and therefore to a lower saturation temperature. Also, this solution suggests that the value of the plateau only depends on the inciding laser wavelength and band gap parameters, while the temporal width of the plateau decreases with higher initial CB charge carrier density or photon energy. Furthermore, it increases with a higher SPA coefficient. For the parametrizedation

applied in figure 5.1 the steady state of the solution (5.6) reads

$$k_b T_c^{\text{Plateau}} = \frac{1}{3}\hbar\omega_L - \frac{1}{9}\gamma_{\text{Egap}} n_c^{\frac{1}{3}} \tag{5.6}$$

and gives a plateau temperature of $T_c^{\text{Plateau}} = 1889\,\text{K}$. This matches very well with the simulation data.

However, it is necessary to mention that the low heat capacity plateau reflects a pre-pulse state of the charge carrier subsystemm and shows a lifespan of roughly 200 fs. A characteristic of this pre-pulse state is that while carrier temperature varies drastically, the total energy deposited into the system is neglectably small. As discussed in section 2.2, thermalization of the charge carrier subsystem takes place on a timescale of around 100 fs after laser irradiation. Within this time frame, the assumption of Maxwell-Boltzmann or Fermi-Dirac distributed electrons does not hold and the concept of temperature is not applicable. So, strong varying pre-pulse charge carrier temperature has to be viewed with caution, since artificial lattice heating could occur in simulations. Fortunately, this effect does appear to be a problem, due to the proportionality

$$c_{\text{p}} \propto G \tag{5.7}$$

which leads to a vanishing electron-phonon coupling G and therefore to no artificial heating of the lattice at low carrier densities. However, effects like non-thermal melting lead to the desire to use interatomic potentials parametrizeded by charge carrier temperature. The low heat capacity plateau is an effect to bear in mind when interatomic potentials parametrized on charge carrier temperature are considered. A high temperature state is induced before bond breaking energy is deposited and could lead to unphysical behavior when only CB carrier temperature is considered. Also, application of parametrization by temperature during a time where the concept of temperature does not hold is prone to failure.

5.2 Parametrization of Optical Properties

5.2.1 The Problem

In the previous simulations we parametrized optical properties based on temperature fitting-laws. Analogously to other groups [80], we called these fitting-laws T-expressions. T-expressions are widely adopted in the context of laser ablation simulation to empirically model the complex, often highly non-linear, interplay between chosen observables. Computational physics has an intrinsic ambivalent relation towards such fitting-laws. On the one hand, fitting-laws allow for simplification of a connection of two or more observables and therefore greatly reduce computational cost while maintaining validity. On the other hand, the physical validity depends on the context in which this empirical connection has been measured or calculated. The T-expressions applied in recent ultra-fast laser ablation simulation publications [80, 91] all originate from experiments performed in the mid 80's. For example the T-expression for the SPA coefficient α_{SPA} and the reflectivity R were determined by the group of Modine [215, 218] by ellipsometry experiments. For this, a substrate was heated at the back of the sample, irradiated with lasers of different wavelengths in CW mode and the results were averaged over time. This measurement setup assumes, that the electronic and lattice subsystem were in equilibrium during the whole measurement, meaning $T_l = T_c$. This justifies a parametrization solely by lattice temperature T_l , hence the name T-expression. In these experiments, changes in α_{SPA} based on the current excitation status were not investigated. Consequently, this parametrization loses its validity for sub-picosecond laser pulses, where the assumption of carrier-lattice equilibrium no longer holds. Figure 5.3 shows the predictions of some T-expressions and the Drude model on the reflectivity R under variation of CB charge carrier density for silicon. Needless to say, the T-expressions fail horribly at a task they were not designed for. Other well adopted parametrization like the parametrization of the free carrier cross section and interband absorption coefficients by the group of Svantesson [229, 230] or the Auger recombination coefficient [231] suffer the same conceptual problems. All in all, the simulations of laser irradiated covalent materials are in desperate need of new optical parametrization which include the generated carrier-lattice non-equilibrium. In this section we want to

construct a carrier excitation-dependent parametrization of optical properties and close this gap.

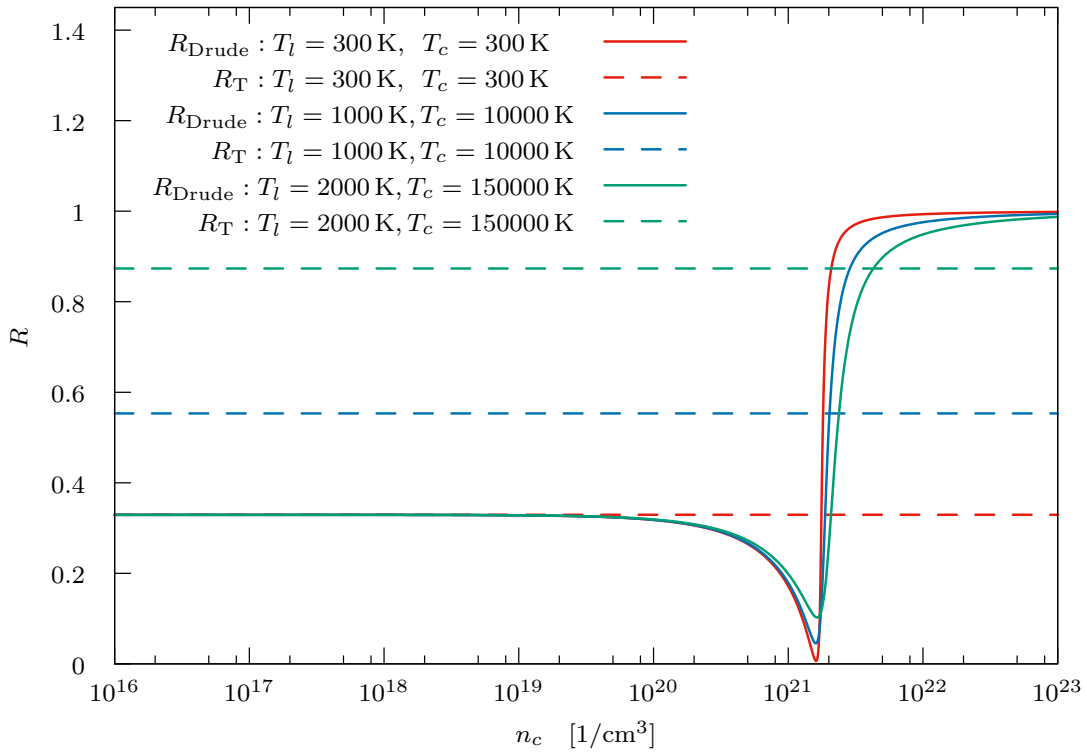

Figure 5.3: Calculated reflectivity at normal incidence for a laser wavelength of 800 nm for different lattice T_l and charge carrier temperatures T_c depending on the charge carrier density n_c of the excited electron-hole plasma. The dashed line is calculated by the T-expression while the solid line is calculated by the Drude model considering electron-phonon and electron-hole collisions parametrized by equation (5.12) and equation (5.14).

5.2.2 Drude FCA parametrization

The rising interest in ultra-fast phase transitions in silicon during laser irradiation lead to a series of ultra-fast pump probe experiments [100, 152, 153, 232], measuring the reflectivity response of silicon in the sub-picosecond regime. In these experiments, pulse duration, wavelength and fluence-dependent reflectivity changes within hundreds of femtoseconds were observed. It was pointed out, that these changes are due to the dominating optical response from the electron-hole plasma

in its excited state [92, 100] and can be modelled within the Drude model. In section 5.1 we have shown sub-damage threshold fluences can lead to a carrier density of $n_c > 10^{21}\,1/\mathrm{cm}^3$ which will result in a drastic reflectivity change according to the Drude model. In the following, we want to discuss possible parametrization of scattering mechanisms entering the Drude model. We swap the FCA fitting-law parametrization

$$\alpha_{\mathrm{FCA}} = n_c \cdot \alpha \exp\left(\frac{T_l}{\beta}\right) \tag{5.8}$$

by expressing the free carrier absorption coefficient according to the Drude expression

$$\begin{aligned}
\alpha_{\mathrm{FCA}} =& \frac{2\,\mathrm{Im}\,\bar{n}}{c_0} && (5.9)\\
=& \frac{2}{c_0}\sqrt{\frac{\varepsilon_r}{2}}\Bigg\{ && (5.10)\\
& \pm \sqrt{\left(\frac{1}{\omega_L\tau_{\mathrm{D}}}\frac{\omega_{\mathrm{p}}^2\tau_{\mathrm{D}}^2}{1+\omega_L^2\tau_{\mathrm{D}}^2}\right)^2 - \left(1-\frac{\omega_{\mathrm{p}}^2\tau_{\mathrm{D}}^2}{1+\omega_L^2\tau_{\mathrm{D}}^2}\right)^2}\\
& - \left(1-\frac{\omega_{\mathrm{p}}^2\tau_{\mathrm{D}}^2}{1+\omega_L^2\tau_{\mathrm{D}}^2}\right)\\
\Bigg\}^{\frac{1}{2}}&.
\end{aligned}$$

This now significantly depends on the plasma frequency ω_p and mean carrier scattering time τ_D. Note that τ_D now non-linearly depends on the ultra-fast changing charge carrier density n_c. However, an expression for the carrier scattering time τ_D is still missing. Unfortunately, there is a great disagreement in literature which scattering mechanisms contribute to τ_D within the Drude framework. Many authors assume constant scattering frequencies [92, 100–102, 233–236], while others emphasize on the importance of temperature-dependent electron-electron an electron-phonon collision frequencies [63, 64, 237, 238]. Third parties argue that electron-electron and hole-hole collisions cannot contribute to the collision frequency due to an identical effective mass leading to conservation of momentum and therefore leading to

an invariant macroscopic current [83, 239, 240]. Electron-hole collisions on the other hand are reported to contribute to τ_D and even dominate [240, 241] under certain conditions. Anyway, literature provides us with different explanations of scattering times resulting from theory.

Electron-Electron Scattering e-e Although it is argued whether electron-electron scattering enters the Drude scattering frequency, it is an important phenomenon for carrier thermalization. Christensen and Balling [64] derived an expression for the electron-electron scattering rate $(\tau_D^{\text{e-e}})^{-1}$ based on kinetic gas theory. Combined with the Debye screening length as effective radius it reads

$$(\tau_D^{\text{e-e}})^{-1} = \frac{4\pi\varepsilon_0}{e^2}\sqrt{\frac{6}{m_0}}\,[k_b T_c]^{\frac{3}{2}}\,. \tag{5.11}$$

Note that this expression is invariant towards charge carrier density changes, even tough charge carrier density effects are taken into account. This is because the Debye screening length decreases in the same order as the classical collision rate increases with rising electron density. As a result, the charge carrier density dependence vanishes.

Electron-Hole Scattering e-h An expression for the electron-hole scattering rate $\left(\tau_D^{\text{e-h}}\right)^{-1}$ in degenerate and non-degenerate electron gases was derived by Rämer [80]. The concept of the derivation is assigning mean internal energy to a mean relative velocity in a semi-classical way. The mean free path of electrons and holes was calculated assuming a screened Coulomb potential [242] and the mean internal energy was calculated in Sommerfeld theory. The result in the non-degenerate formulation reads

$$\left(\tau_D^{\text{e-h}}\right)^{-1} = \frac{\sqrt{3}\varepsilon_0\pi(k_b T_c)^{\frac{3}{2}}}{2e^2}\left[\frac{1}{m^*_{\text{e,DOS}}} + \frac{1}{m^*_{\text{h,DOS}}}\right]^{\frac{1}{2}}. \tag{5.12}$$

Electron-Phonon Scattering e-p The electron-phonon scattering rate $(\tau_D^{\text{e-p}})^{-1}$ is mostly parametrized by the assumption of a direct proportionality between the

scattering rate

$$(\tau_D^{\text{e-p}})^{-1} = A\,T_l \tag{5.13}$$

and the lattice temperature T_l. Unfortunately, this assumption does not take the changes in charge carrier density into account. In this work, we use a formula originally derived for astrophysical objects and then simplified to cold solid matter by Eidmann [135], which takes into account the electron density indirectly via the Fermi-velocity $v_f = \hbar\left(3\pi^2 n_e\right)^{1/3}/m_0$. The simplified expression reads

$$(\tau_D^{\text{e-p}})^{-1} = 2k_s \frac{e^2 k_b}{4\pi\varepsilon_0 \hbar^2 v_f} T_l. \tag{5.14}$$

Where k_s is a material-dependent fitting parameter. It is important to note that this law assumes a linear behavior, thus holds for small charge carrier temperatures. However, more advanced calculations for SiO_2 support the assumption of linear behavior up to an electron kinetic energy of $U_{\text{kin}} \approx 6\,\text{eV}$ followed by a constant plateau for higher energies. On a side note: This non-linear behavior at high carrier temperatures should be modelled in a parametrization. However, in later combinations with the MOD*, charge carrier energies above $U_{\text{kin}} \approx 2.14\,\text{eV}$ will lead to non-thermal melting and therefore dissolution of the lattice, leading to loss of band structure and optical properties anyway.

Electron-Ion Scattering e-i Electron-ion scattering is not taken into account in this work. For completeness, electron-ion scattering frequencies could be parametrized via the Spitzer expression [243], but are not expected to show any significant contribution to optical properties.

Combination of Scattering Rates The effective scattering rate $\frac{1}{\tau_D}$ is obtained by applying Matthiessien's rule [244] and reads

$$\frac{1}{\tau_D} = \frac{1}{\tau_D^{\text{e-e}}} + \frac{1}{\tau_D^{\text{e-p}}} + \frac{1}{\tau_D^{\text{e-h}}}. \tag{5.15}$$

In addition, we need to take into account the dissolution of the lattice and the consequent ultra-fast change of the phonon spectrum. This is done by applying an upper limit of

$$\left(\frac{1}{\tau_D^{\text{e-p}}}\right)_{\max} = \sqrt{\frac{3k_{\text{B}}T_c}{m_0}}\left(\frac{4\pi}{3}n_a\right)^{\frac{1}{3}} \tag{5.16}$$

to electron-phonon scattering mechanisms. This was proposed by [135] under the assumption that the collision rates can never exceed $\left(\frac{1}{\tau_D^{\text{e-l}}}\right)_{\max} = v_e/a$ for a mean electron velocity v_e, a lattice spacing a and a mean ion density of n_a. We emphasize on this, because electron-phonon scattering time will also play an important role in carrier-lattice equilibration and will directly alter our MD-FD coupling coefficient ξ. This is especially relevant since this scattering frequency limit scales with $\propto \sqrt{T_c}$. In laser ablation simulations, typical carrier temperatures can easily range from $T_c = 300\,\text{K}$ to $T_c = 10^5\,\text{K}$ within the same simulation. Needless to say, this dominates the energy transfer towards the lattice and will alter the lattice dynamics and therefore ablation dynamic.

5.2.3 Simulations under Varying Scattering Mechanisms

Now we perform comparative laser ablation simulations with an ultra-fast changing FCA coefficient according to (5.11). For this, we construct all possible combinations of scattering mechanisms presented in section 5.2.2 and empirically check for their relevance in laser ablation simulation.

Simulation Setup The simulations were performed on sample `surface` under homogeneous laser irradiation with a sub-damage threshold fluence of $\sigma = 0.16\,\text{J/cm}^2$ and a FWHM pulse duration of $\tau_p = 100\,\text{fs}$ applying the BETE. The parametrization of the carrier subsystem is identical to the simulations presented in section 5.1 with the exception of the free carrier absorption coefficient α_{FCA}, which is taken from the Drude model. The results of each simulation, as well as a comparison to the solely T-expression-parametrized simulation data from section 5.1 are shown in figure 5.4 in terms of the carrier and lattice temperature dynamics and in figure 5.5 in terms of the dynamics of the resulting optical properties.

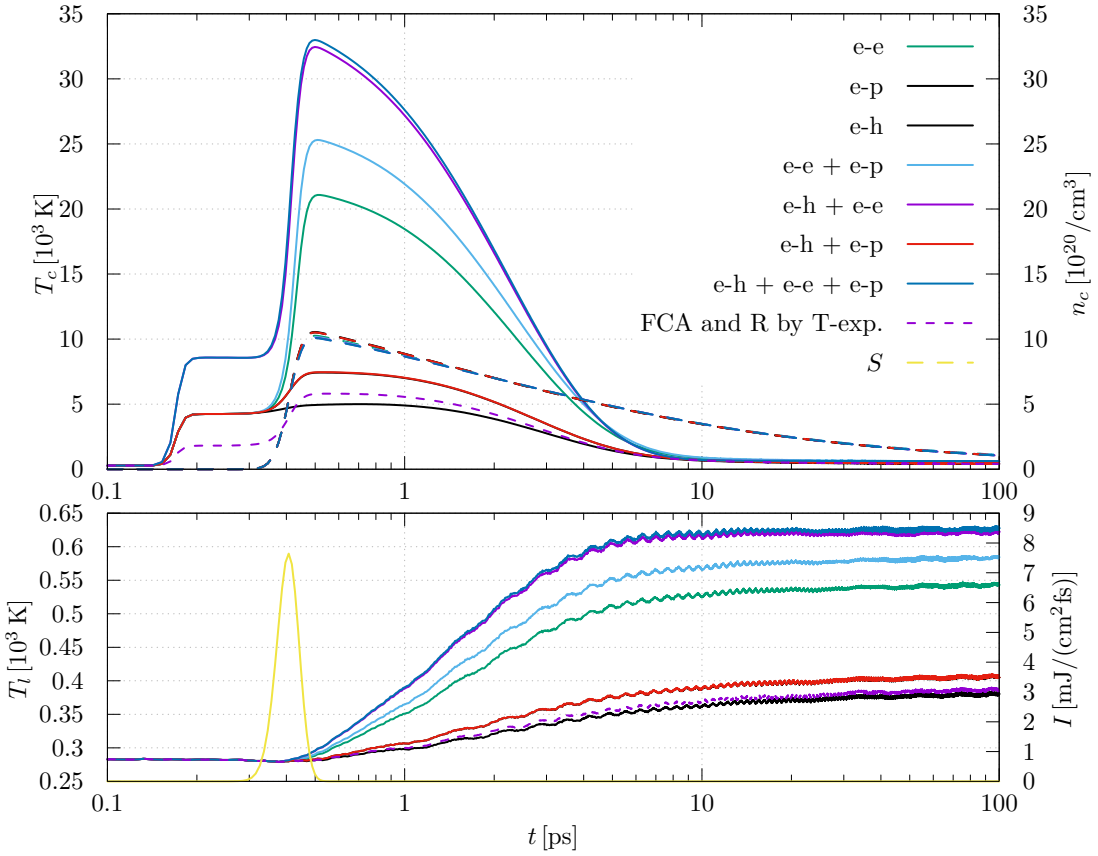

Figure 5.4: Time evolution of spatially averaged observables of the BETE on sample `surface` under homogeneous laser irradiation with sub-damage threshold fluence of $\sigma = 0.16\,\mathrm{J/cm^2}$ and a FWHM pulse duration of $\tau_p = 100\,\mathrm{fs}$. The free carrier absorption coefficient is modelled with the Drude model under various carrier collision frequencies defined in section 5.2.2. The two-photon absorption coefficient β_{TPA} is set to zero.

Lattice End Temperature Interpretation and validation of the presented data appears to be a complex task, as no experimental data on charge carrier temperature as well as lattice end temperature is available. However, the T-expressions were fitted to reproduce the damage threshold and attempt to predict ablation depth. As a result, the T-expressions were designed to roughly predict the correct lattice end temperature after irradiation. In the post-pulse temperature dynamics, presented in figure 5.4, we observe that all lattice end temperatures exceed the melting temperature of silicon when electron-electron scattering is considered. For a sub-damage

laser fluence, this is obviously wrong and in accordance with the observation by [80] that inclusion of electron-electron collisions for picosecond and longer pulses lead to a great overestimation of lattice end temperature due to overestimation of α_{FCA}. We consequently have to rule out electron-electron scattering entering α_{FCA} as well as all scattering combinations including electron-electron scattering.

Direct Comparison of Absorption Dynamics Information on the validity of the remaining scattering mechanisms has to be obtained by comparison of optical parameters. Unfortunately, the dependence of α_{FCA} on charge carrier density is not separately measurable at $\lambda = 800\,\mathrm{nm}$, since electron-hole plasma generation by TPA and SPA also contributes to the absorption properties of the material. Also, charge carrier density-dependent reflectivity as well as defocusation effects make time resolved ultra-fast transmission measurements extremely difficult.

Nevertheless, in contrast to α_{SPA} and β_{TPA}, free carrier absorption α_{FCA} intrinsically shows no contribution to CB carrier generation. Therefore, energy absorbed via FCA shows solely in the heating of the charge carrier temperature and consequently in lattice end temperature. The lattice end temperatures shown in figure 5.4 suggest that only the isolated use of electron-hole and electron-phonon scattering, as well as a combination of both, lead to an estimation of lattice end temperature comparable to the T-expression, while not exceeding melting temperature.

Considering the explicit value of α_{FCA}, we refer to the data reported by Jellison [245], who meassured the refraction index under sub-damage threshold CW mode laser irradiation at a laser wavelength of $\lambda = 780\,\mathrm{nm}$. Inserting the corresponding data from Jellison into our definition (5.11) leads to a free carrier absorption coefficient of $\alpha_{\mathrm{FCA}} = 0.36\,1/\mu\mathrm{m}$. In figure 5.5 we present the dynamic and T-expression parametrized value of α_{FCA} within our simulation and find that the value given by Jellison matches only with the choice of the combination of electron-hole and electron-phonon collisions as Drude scattering mechanisms, while sole electron-hole scattering shows significant underestimation of α_{FCA}.

Reflectivity The choice of the combination of e-h and e-p collisions as Drude scattering mechanisms is confirmed further when we consider the resulting reflectivity R shown in figure 5.5. According to pump probe experiments [100, 128, 153, 218],

ultra-fast carrier excitation is expected to induce an ultra-fast drop in reflectivity for small laser fluences. Again, the qualitative and quantitative behavior of reflectivity drop only matches experiments when solely e-h and e-p collisions are considered.

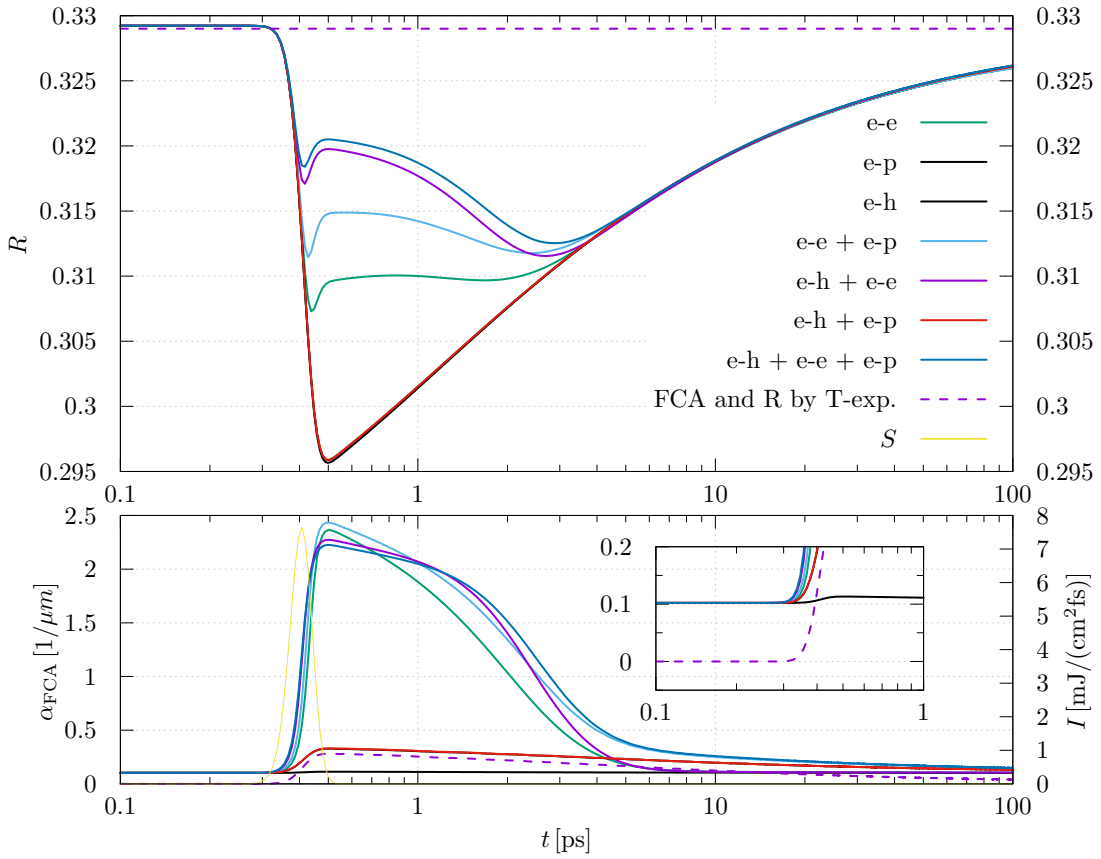

Figure 5.5: Time evolution of spatially averaged observables of the BETE on sample `surface` under homogeneous laser irradiation with sub-damage threshold fluence of $\sigma = 0.16\,\mathrm{J/cm^2}$ and a FWHM pulse duration of $\tau_p = 100\,\mathrm{fs}$. The free carrier absorption coefficient is modelled with the Drude model under various carrier collision frequencies defined in section 5.2.2. The two-photon absorption coefficient β_{TPA} is set to zero.

In the case of reflectiviy, the drawbacks of the T-expression become most obvious. In figure 5.5 we observe the reflectivity parametrized by T-expression to stay constant, since the lattice system remains at a cold state within pulse duration. This worsens when higher fluences are considered. At a critical excitation the dense electron-hole plasma will induce a purely reflective plasma state due to plasma

screening. This phenomenon is well-known as the so-called plasma reflection edge. For silicon irradiated with a wavelength of $\lambda = 800\,\mathrm{nm}$, this is often reported to be at carrier density of about $n_c \approx 10^{22}\,\mathrm{cm}^{-3}$ [100, 239, 240, 246, 247]. In figure 5.6 we present a map of reflectivity predicted by our parametrization, solely to show that the plasma screening effect is also included within our proposed parametrization.

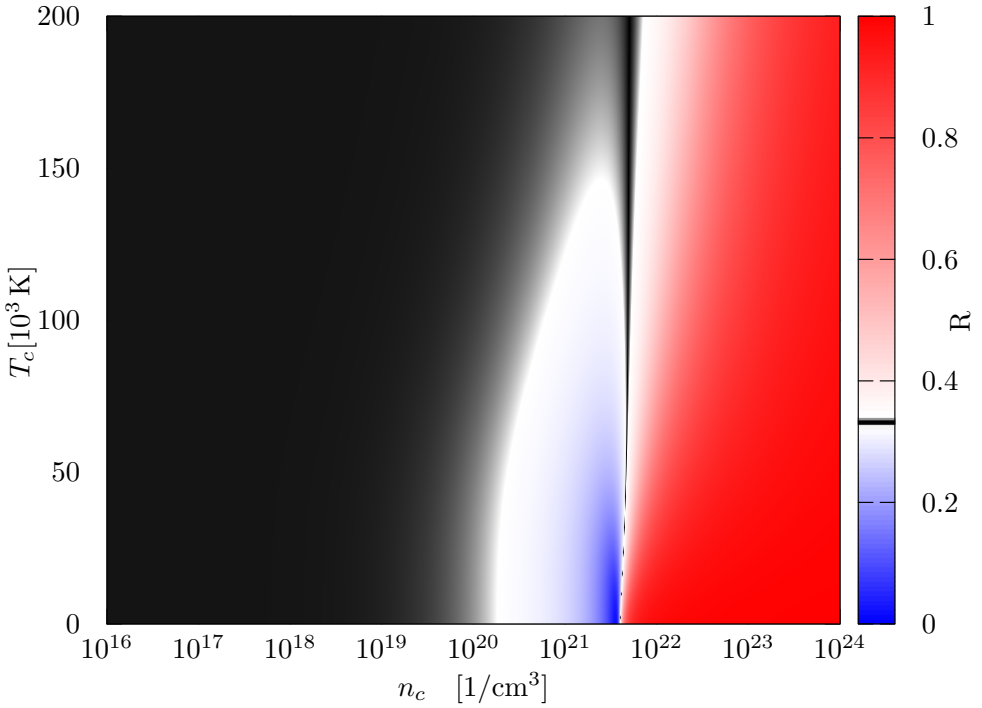

Figure 5.6: Reflectivity calculated by the Drude model in dependence on carrier temperature T_c and carrier density n_c. Carrier collision frequencies are modelled under consideration of electron-hole and electron-phonon collisions at a laser wavelength of $\lambda = 800\,\mathrm{nm}$ and a lattice temperature of $T_l = 300\,\mathrm{K}$. The black color code refers to the reported reflectivity at equilibrium conditions of $R = 0.329$ [218].

Conclusion Following our explanation, we choose e-h and e-p scattering mechanisms for our Drude parametrization of α_{FCA}. At this point we have to admit, that the T-expression parametrization manages to continuously produce lattice end temperatures relatively close to our dynamic Drude parametrization for low fluence single pulses. However, we have to emphasize that the Drude parametrization is solely derived from theory and valid for any wavelength, while the T-expression is

a result of many experiments for a single wavelength and thus lacks universality. In addition, as shown in figure 5.5, the T-expression fails on short timescales where carrier-phonon relaxation has not significantly heated the lattice yet. Consequently, the T-expression will fail when pulse durations are scaled down or multi-pulses are studied. Another important problem will occur when we add a charge carrier temperature-dependent interatomic interaction potential to our model. This will be discussed in section 5.4. As a leap ahead, non-thermal melting will artificially increase lattice temperature by sudden bond weakening followed by particle acceleration within a time frame of $\sim 100\,\mathrm{fs}$. As we discussed just now, the T-expression fails when fast changing parameters are considered. On top of that, sudden bond weakening will lead to a collapse of lattice structure and induce a state the T-expression was simply not designed to be used in.

5.2.4 Drude TPA Parameterization

The Problem and the Solution We know that bulk[†] silicon is an indirect band gap semiconductor, meaning the lowest unoccupied CB state lies at a different crystal momentum than the highest VB state. Consequently, single photon interband excitations with photon energies near the direct band gap energy are in need of phonon assistance. This directly translates to an increasing interband absorption probability with increasing lattice temperature. TPA, however, allows for interband excitation without phonon assistance and therefore can occur at lower temperatures. This is most relevant, because in section 5.2.3 we have demonstrated that lattice heating occurs on post-pulse timescales, which implies that the sample can be viewed as cold during first-pulse absorption. Consequently, for first-pulse absorption, we expect TPA contribution to surpass SPA and FCA contribution due to the unexcited state of CB carriers. This is also the reason why TPA is argued to play the major

[†]Note that in this section we emphasize on the optical parameters of bulk silicon, although we perform simulations of ultra-thin silicon films. This is due to the fact that this work is thematically settled at an intersection of scientific sub-communities. For the laser physicist community ultra-thin films are defined as sub-absorption length thick films, while in the viewpoint of theoretical solid state physics ultra-thin films are films of typically ≤ 10 monolayers. Band gap and optical parametrization typically originate from theoretical solid state physics. In the case of several monolayers, optical properties and band structure vary drastically with increasing number of layers [248] while our $\sim 100\,\mathrm{nm}$ thick film shows the optical properties of bulk silicon.

role in the generation of the dense electron-hole plasma, with increasing importance towards lower fluences [81, 100, 109]. This again emphasizes the importance of a robust carrier excitation-dependent TPA coefficient when realistic spatially inhomogeneous pulse shapes are considered. On top of that, TPA plays the major role for laser ablation simulations with sub-band gap laser wavelengths, which will be part of our future work.

However, to this date β_{TPA} remains the most uncertain parameter within established laser ablation publications. Although complex dynamical models exist, β_{TPA} is most often treated as a constant. This observation, combined with the fact that reported TPA coefficients for bulk silicon at $\lambda = 800\,\mathrm{nm}$ range from neglectable [109] over 2 cm/GW [81], 9 cm/GW [216], 15 cm/GW [91] or 50 cm/GW [74] up to 55 cm/GW [246] leads to the problem that most authors of continuum-atomistic laser simulations choose the two-photon absorption coefficient according to the resulting ablation depths or damage thresholds within the studied model. The great downside of this approach is that other non-sharply defined factors, like the freedom of choice of interatomic potential or energy transport parametrization also show a great impact on the macroscopic dynamic, rendering the chosen TPA coefficient a self-fulfilling prophecy. When this is done, the inclusion of theoretical restrictions like the dynamic behavior of the TPA coefficient are thrown away for the sake of matching data. Unfortunately this imposes a disadvantage to the discovery of correct parameters for other non-sharply defined macroscopic observables. On top of that, the parametrization of β_{TPA} as a constant comes with the identical conceptual flaws as T-expressions parametrizations.

We improve on this by applying the density-dependent TPA coefficient

$$\beta = \begin{cases} fK\frac{\sqrt{E_p}}{\bar{n}^2 E_g^3} \cdot \frac{(2\hbar\omega_{\mathrm{L}}/E_g - 1)^{3/2}}{(2\hbar\omega_{\mathrm{L}}/E_g)^5}, & \text{for} \quad 2\hbar\omega_{\mathrm{L}}/E_g > 1 \\ 0, & \text{for} \quad 2\hbar\omega_{\mathrm{L}}/E_g \leq 1 \end{cases} \tag{5.17}$$

discussed in section 2.1.2. $\bar{n}$ is the linear part of the refraction index and is calculated by the Drude formula. Therefore, β_{TPA} also includes information about the ultrafast changing properties of the carrier subsystem. f is a numerical factor that depends on the angular averages of interband matrix elements and can be utilized

as a reasonable fitting parameter for different materials as long as $0 \leq f \leq 1$ holds [217]. Note that in contrast to a parametrization by a constant TPA, equation (5.17) is a universal function for most semiconductors [108] and for all laser frequencies [81, 249]. The choice of $f = 1$ yields $\beta_{\mathrm{TPA}} = 10.68\,\mathrm{cm/GW}$ at our equilibrium conditions and thus matches with the reported experimental values. Note that by parametrization in $E_g(n_c,T_l)$ we also include the enhancement of TPA by band gap shrinkage [81].

Now we compare the absorption predictions of the dynamic β_{TPA} against the commonly assumed static β_{TPA} values and determine the most suitable material parameter f for bulk silicon.

Simulation Setup Simulations on sample `surface` under homogeneous laser irradiation with a sub-damage threshold fluence of $\sigma = 0.16\,\mathrm{J/cm^2}$ and a FWHM pulse duration of $\tau_p = 100\,\mathrm{fs}$ were performed applying the BETE. α_{FCA} is modelled with the Drude model under contribution of electron-phonon and electron-hole collisions. Different choices of non-zero TPA coefficients β_{TPA} were taken into account. For the variation of β_{TPA} in the dynamical description, the parameter f was adjusted to reproduce the respective stated value at room temperature in equilibrium. The equilibrium β_{TPA} was varied in the interval $\beta_{\mathrm{TPA}} = 0\,\mathrm{cm/GW}$ to $\beta_{\mathrm{TPA}} = 600\,\mathrm{cm/GW}$. The simulation results for selected β_{TPA} are shown in figure 5.7 and figure 5.8.

Carrier System Observations In contrast to FCA, TPA is an interband absorption mechanism, thus contributes to CB charge carrier generation. CB charge carrier generation increases the carrier heat capacity, thus cools the carrier system. The inverse effect of consequent electron-hole recombination decreases carrier heat capacity and thus increases carrier temperature and is known as the effect of Auger heating. Figure 5.7 shows the time evolution of carrier and lattice temperatures, as well as the generated carrier densities. For an equilibrium $\beta_{\mathrm{TPA}} > 2\,\mathrm{cm/GW}$ we observe an over-generation of carrier density, which reflects in post-pulse Auger heating, leading to a lattice end temperature above the melting temperature. This, of course, contradicts experimental data, since we have chosen a sub-damage threshold fluence. At this point, we have to mention that our simulations on ultra-thin films neglect energy dissipation into the bulk and therefore are prone to underestimate

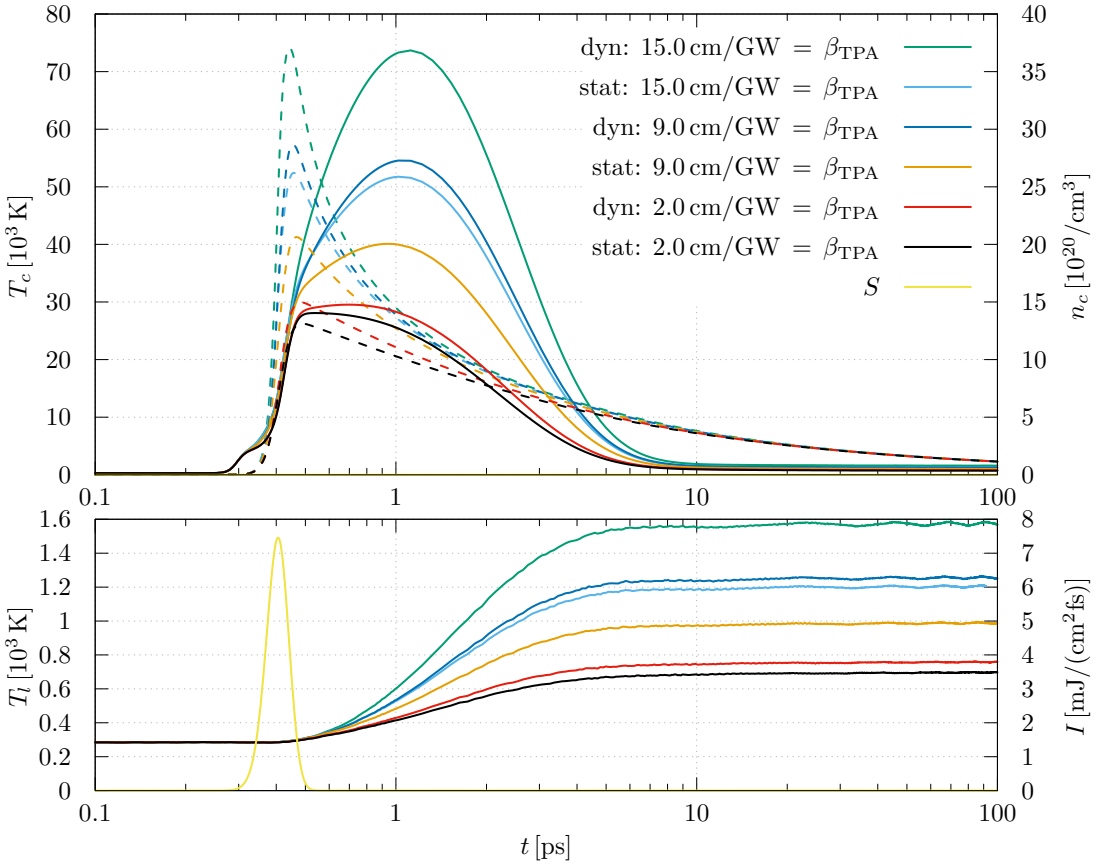

Figure 5.7: Time evolution of spatially averaged observables of the BETE on sample `surface` under homogeneous laser irradiation with sub-damage threshold fluence of $\sigma = 0.16\,\mathrm{J/cm^2}$ and a FWHM pulse duration of $\tau_p = 100\,\mathrm{fs}$. In the top picture the solid lines correspond to the carrier temperature and the dashed line corresponds to carrier density. The free carrier absorption coefficient is modelled with the Drude model under electron-phonon and electron-hole collisions. The two-photon absorption coefficient β_{TPA} is modelled dynamically by equation (4.13) or set to a constant value.

the damage threshold of a bulk sample. For this reason we cross checked the shown results with the future simulations of bulk silicon of section 6.1. There, a dynamic TPA coefficient of equilibrium $\beta_{\mathrm{TPA}} = 2\,\mathrm{cm/GW}$ accurately reproduces a damage threshold of $\sigma = 0.16\,\mathrm{J/cm^2}$.

Additionally, the value of $\beta_{\mathrm{TPA}} = 2\,\mathrm{cm/GW}$ for $\lambda = 800\,\mathrm{nm}$ matches with the most recent z-scan measurements on bulk silicon by Bristow [81]. These measurements do

not only support our phenomenological deduction of β_{TPA}, but are also supported by theoretical work, recently done by the group of Garcia [249] by a perturbation theory approach. Therefore, we propose the dynamic parametrization of TPA with an equilibrium value of $\beta_{\mathrm{TPA}} = 2\,\mathrm{cm/GW}$.

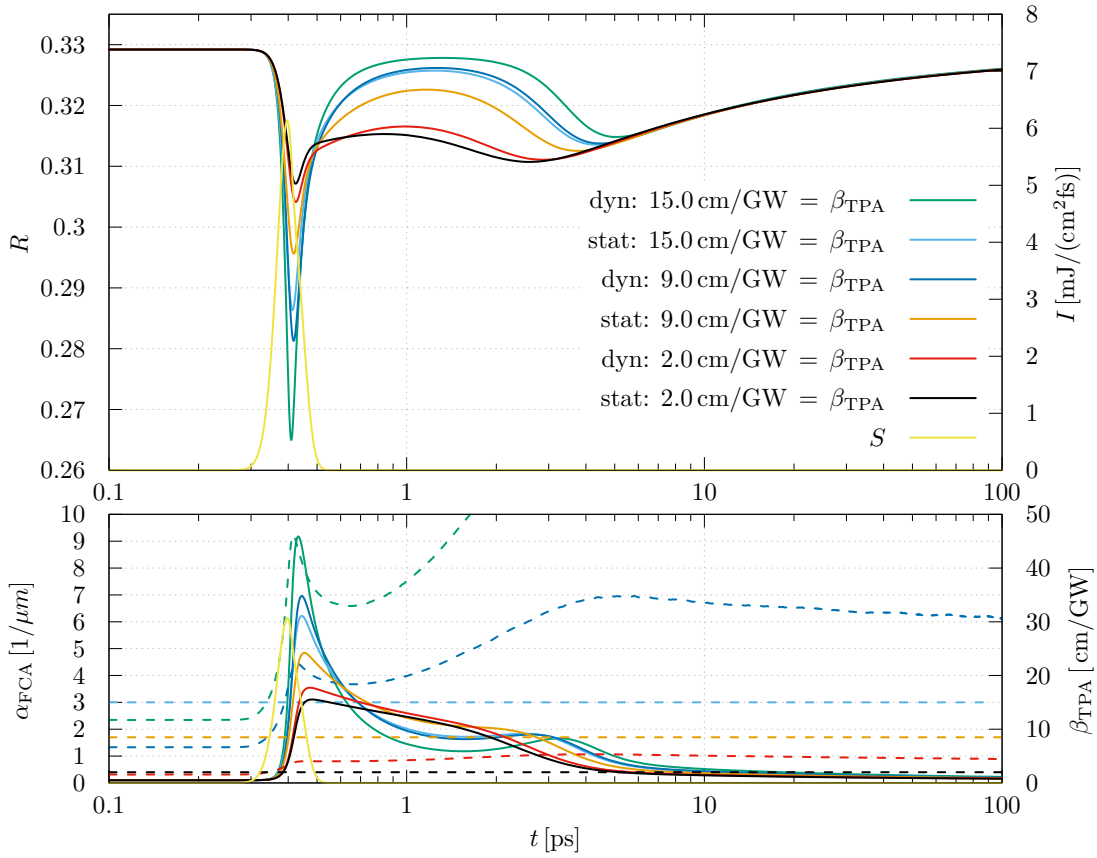

Figure 5.8: Time evolution of spatially averaged observables of the BETE on sample `surface` under homogeneous laser irradiation with sub-damage threshold fluence of $\sigma = 0.16\,\mathrm{J/cm^2}$ and a FWHM pulse duration of $\tau_p = 100\,\mathrm{fs}$. In the bottom picture the solid lines correspond to α_{FCA} and the dashed lines correspond to β_{TPA}. The free carrier absorption coefficient is modelled within the Drude model under electron-phonon and electron-hole collisions. The two-photon absorption coefficient β_{TPA} is modelled dynamically by equation (4.13) or set to a constant value.

Self-consistency Figure 5.8 shows that TPA coefficients of $\beta_{\mathrm{TPA}} > 2\,\mathrm{cm/GW}$ induce a behavior in α_{FCA} by charge carrier generation, which contradicts our previous

examination of FCA parametrization for both static and dynamic parametrizations.

Reflectivity Although the proposed parametrization of β_{TPA} already yields convincing results, we want to address the dynamics of the reflectivity in figure 5.8. In contrast to the simulations on FCA in section 5.2.3, the reflectivity shows two recoveries. When compared to the reflectivity map of figure 5.6, this can be identified as the n_c-T_c-trajectory crossing the valley between $n_c = 10^{21}\,1/\mathrm{cm}^3$ and $n_c = 10^{22}\,1/\mathrm{cm}^3$. The first recovery, therefore, is a result from CB carrier generation, and the second is a result from CB carrier recombination. The first recovery is not observed in comparable pump-probe experiments, where $\lambda = 800\,\mathrm{nm}$ and $\tau = 28\,\mathrm{fs}$ [128] and $\lambda = 625\,\mathrm{nm}$ and $\tau = 100\,\mathrm{fs}$ [100] were considered. However, the reason for this is that in pump-probe experiments with short delay times, the pump and probe pulse temporally overlap, yielding a virtual reflectivity increase. As a result, we do not expect the first reflectivity drop and recovery of our data to be measured in the cited experiments.

The Spread of β_{TPA} In figure 5.8 it is observable that the TPA coefficient in dynamical formulation varies drastically with initial β_{TPA} and time. This extreme variation is due to band gap shrinkage, combined with CB carrier generation and offers a possible explanation for the broad spread of experimentally determinated β_{TPA}. Due to the sensitive dependency on charge carrier density, variation of pump fluence as well as probe-delay, will immensely alter the measured data. In our simulations the dynamic parametrization of β_{TPA} results with a chosen equilibrium value of

$$\begin{aligned}
&\beta_{\mathrm{TPA}} = 2\,\mathrm{cm/GW} \quad \text{in a peak value of } \beta_{\mathrm{TPA}} \approx 6\,\mathrm{cm/GW}, \quad \text{with}\\
&\beta_{\mathrm{TPA}} = 9\,\mathrm{cm/GW} \quad \text{in a peak value of } \beta_{\mathrm{TPA}} \approx 35\,\mathrm{cm/GW}, \quad \text{and with}\\
&\beta_{\mathrm{TPA}} = 15\,\mathrm{cm/GW} \text{ in a peak value of } \beta_{\mathrm{TPA}} \approx 72\,\mathrm{cm/GW}.
\end{aligned}$$

Note that the variation of f in equation (5.17) leads to roughly the same spread of TPA coefficients as the spread in experimental data.

Conclusion We proposed and validated ultra-fast changing optical parametrizations for the FCA and TPA coefficients of silicon. FCA and TPA were adjusted not to overestimate the generation of CB carriers, thus altering the plasma frequency of the material and therefore overestimate lattice heating by laser light absorption. Simultaneously, we found that the FCA in Drude formulation under consideration of electron-hole and electron-phonon scattering is suitable to reproduce the ultra-fast changing reflectivity observed in pump-probe experiments. Although we have previously criticized the effect of fallacy of incomplete evidence, it is still relevant to point out existing data. One of the most recent measurements of TPA on bulk silicon measured a $\beta_{\mathrm{TPA}} = 2\,\mathrm{cm/GW}$ for $\lambda = 800\,\mathrm{nm}$ in accordance with theoretical predictions [249] by a perturbation theory approach. These results, combined with our observation of reasonable lattice end temperature, as well as consistency with reflectivity measurements, lead us to the choice of the dynamical paramtrization of TPA with an equilibrium value of $\beta_{\mathrm{TPA}} = 2\,\mathrm{cm/GW}$ for our future simulations. We now arrive at the excitation-dependent parametrization summerized in table 5.1. In future sections we will abbreviate this parametrization set simply as D. We want to point out, that this definition is derived purely from theory and depends on the ultra-fast changing refractive index parametrized in the previous section. The usage of the presented TPA parametrization is not only necessary to model carrier dynamics induced by sub-picosecond laser irradiation, but brings no downsides besides added complexity and neglectable increase in computational cost.

subsystem	excitation mechanism
coupling	$\mathbf{F}_i^{\mathrm{fric}} = -\xi m_i \dot{\mathbf{x}}_i$
energy	$\frac{dI}{dx} = -(\alpha_{\mathrm{SPA}} + \alpha_{\mathrm{FCA}})I - \beta_{\mathrm{TPA}} I^2$
carriers	$\frac{dn_c}{dt} = \frac{\alpha_{\mathrm{SPA}} I}{h\omega_L} + \frac{\beta_{\mathrm{TPA}} I^2}{2h\omega_L} - \gamma_{\mathrm{Aug}} n_c^3 + \delta_{\mathrm{imp}} n_c$

Table 5.1: Excitation parametrization table for each subsystem as a colourful guide to the eye. The colours are read as follows: Orange, the parameter is set to an constant value. red, the parameter is set to a T-expression fitting-law. Teal, the parameter is set to excitation-dependent expression.

5.3 Tweaking of Initial Conditions

The Problem In most band gap materials, only excited CB electron-hole pairs contribute to energy transport. Therefore, electronic heat conduction is highly sensitive towards the CB carrier density which inevitably enters the charge carrier heat transport equations. This gives rise to a set of numerical problems. In the case of explicit numerical solution schemes, the stability of the applied scheme can be determined with the well-known von Neumann stability analysis. The von Neumann stability analysis results in the condition CFL ≤ 1 with CFL being the Courant-number. The CFLs for the homogeneous part of both, the nTTM and TSM transport equations, are given in table 5.2. We find that the contribution of charge carrier density to the specific heat capacity leads to the inverse proportionality

$$\text{CFL} \propto 1/n_c \tag{5.18}$$

between the CFL number and charge carrier density. The BETE model does not show this proportionality and was our approach to bypass this constraint. In order to achieve numerical stability for the nTTM and TSM within a reasonable FD grid spacing of $\Delta x = 11$ nm, a FD time step of $\Delta t = 4.78 \cdot 10^{-27}$ seconds would be necessary. This translates to the requirement of roughly $2.2 \cdot 10^{12}$ FD steps per MD step to achieve numerical stability. Due to the immense computational cost, this is not suitable for a combined continuum-atomistic approach on today's supercomputers.

	nTTM	TSM
n_c	$\frac{\Delta t}{\Delta x^2}\left(\frac{D_0}{n_c}\right)$	$\frac{\Delta t}{\Delta x^2}\left(\frac{D_0}{n_c} + \frac{2}{T_c}\partial_{n_c} E_g\right)$
T_c	$\frac{\Delta t}{\Delta x^2}\left(\frac{\kappa}{n_c}\right)$	$\frac{\Delta t}{\Delta x^2}\left(\frac{\kappa}{n_c} + \frac{1}{2}E_g + \frac{3}{2}k_B\right)$

Table 5.2: Courant numbers (CFL) for the time integration step of the homogeneous transport equations of the nTTM and TSM for the carrier density n_c and the carrier temperature T_c.

Other groups suggested to use semi-implicit solution techniques like the Crank-Nicolson algorithm, which is unconditionally stable for varying n_c and arbitrary Δt.

This approach was shown to be fruitful to predict charge carrier dynamics in laser excited silicon for small timescales [91, 92] and is the reason why all previous sub-damage threshold simulations were performed with the semi-implicit Crank-Nicolson algorithm.

However, while a semi-implicit solution scheme is not only considerably more difficult to implement, it also requires considerably more computational resources, when compared to explicit solution schemes. Additionally, the semi-implicit solution scheme shows an extreme downside for longer simulation times, especially when combined with MD. At fluences greater than the ablation threshold, we want to investigate effects like evaporation, phase explosions, melting and general material removal. This results in the necessity of an FD cell being deactivated when the corresponding material within the FD cell is removed. In the context of a semi-implicit solution scheme, this directly leads to an under-determined system of equations, where convergence of the respective solutions is not given anymore.

The Solution When silicon is excited by laser light with a suitable wavelength, the carrier density increases suddenly by many orders of magnitude, thus rendering explicit solution schemes applicable again. Note that from a numerical model perspective, this is the same as assuming doped silicon.

We now want to investigate the implications of an artificially increased initial carrier density n_{eq} on simulation results and report the existence of a critical carrier density $n_{\mathrm{eq}}^{\mathrm{crit}}$ which forms a threshold under which numerical stabilization occurs without altering the simulation outcome.

Simulation Setup and Observations Now we use the nTTM in semi-implicit formulation and examine observables relevant to laser ablation simulation for their dependence on initial carrier density. The nTTM is chosen, because it is the most simple and most accepted of the presented models and leads to identical results as the TSM when transport effects are neglected. Analogously to the previous section 5.2.4 simulations, we use the ultra-thin film sample `surface` under homogeneous laser irradiation with a sub-damage threshold fluence of $\sigma = 0.16\,\mathrm{J/cm^2}$ and the parametrization D. The resulting time evolution of characteristic laser ablation observables is shown in figure 5.9. The dynamics of the resulting optical properties

is shown in figure 5.10. In the presented simulation data, we observe four main features.

1. We observe that on long post-pulse timescales, the results of the nTTM observables (T_c,T_l,n_c), as well as the optical properties show no noteworthy dependency on the initial carrier density below a critical carrier density of $n_{\mathrm{eq}}^{\mathrm{crit}} = 10^{19}\,/\mathrm{cm}^3$. A more tangible determination of $n_{\mathrm{eq}}^{\mathrm{crit}}$ will be done in section 5.3.

2. For $n_{\mathrm{eq}} > n_{\mathrm{eq}}^{\mathrm{crit}}$, an artificial carrier temperature surplus is generated by Auger heating on post-pulse timescales, as well as a drastic Auger heating induced overheating on pre-pulse scales in some cases.

3. In addition to Auger-overheating the high initial charge carrier density of $n_{\mathrm{eq}} > n_{\mathrm{eq}}^{\mathrm{crit}}$ implicitly overestimates the FCA coefficient α_{FCA} leading to cascade of mutually overestimated carrier temperature, carrier density and absorption properties. This obviously leads to unphysical behavior. Also it is noteworthy that it can be assumed, that the influence of surplus charge carrier generation on the FCA coefficient will decrease absorption length on simulations of bulk systems and therefore manipulate spatial energy deposition.

4. Apart from the post-pulse dynamics, it can be observed that the width of the low heat capacity plateau decreases with increasing initial carrier density. Due to the identical temporal profile of S and increased n_c, the critical value of S/n_c is reached later in the simulation. Strictly speaking, this gives a non-physical pre-pulse temperature dynamics. On the other hand, this eliminates the discussed problem of artificial bond breaking in carrier temperature-dependent interatomic potentials at sub-bond breaking energy depositions where the usage of temperature parametrization was questionable.

The combination of post-pulse invariance of nTTM observables and resulting optical properties for an initial carrier density $n_{\mathrm{eq}} < n_{\mathrm{eq}}^{\mathrm{crit}}$ suggests that MD simulations of single-pulse ablation on ultra-thin films will yield the same result. This, in turn, legitimizes the usage of initial carrier densities of $n_{\mathrm{eq}}^{\mathrm{CFL}} < n_{\mathrm{eq}} < n_{\mathrm{eq}}^{\mathrm{crit}}$ which allows for

the usage of explicit solution schemes for the carrier subsystem, greatly decreasing computational cost and implementation complexity.

Determination of the Critical Carrier Density In this section we want to present a more rigorous determination of $n_{\mathrm{eq}}^{\mathrm{crit}}$ for the data presented in figure 5.9. For MD simulations of laser ablation within the nTTM framework, the dynamics of the lattice temperature T_l is the core observable which reflects the macroscopic dynamics of the ablation process. Consequently and conveniently, T_l is a result of all parameters and models entering the simulation. Therefore, it is adequate to characterize the implications of variation of n_{eq} by the lattice end temperature T_l. For this task, we first need to define a suitable tool set. Due to the discrete nature of computer simulations, all observables are burdened with fluctuations. We smooth out these fluctuations by a running average defined over corresponding lattice temperatures at time $t = i\Delta t$ as

$$T_l^{\mathrm{avg}}(i\Delta t) = \frac{1}{N+1} \sum_{k=i-N/2}^{i+N/2} T_l(k\Delta t) \tag{5.19}$$

over $N+1$ data points in the time interval $\Delta T = \Delta t(N+1)$. However, the magnitude of said fluctuations is still a relevant quantity. We characterize the temperature fluctuations by the root mean square deviation

$$\mathrm{RMSD}(T_l,T_l^{\mathrm{avg}}) = \sqrt{\frac{1}{j} \sum_{k=0}^{j} \left[T_l(k\Delta t) - T_l^{\mathrm{avg}}(k\Delta t)\right]^2} \tag{5.20}$$

between the raw T_l and averaged temperature T_l^{avg} from beginning until the end of the simulation $t^{\mathrm{end}} = j\Delta t$. Since we want to compare resulting T_l differences under variation of initial equilibrium carrier density n_{eq}, we need a baseline to compare to. We carry out the natural choice with the literature value $n_{\mathrm{eq}} = 10^{10}\,/\mathrm{cm}^3$ and denote the resulting averaged lattice end temperature as

$$T_l^{\mathrm{avg}}(\mathrm{end},\mathrm{min}(n_{\mathrm{eq}})) \tag{5.21}$$

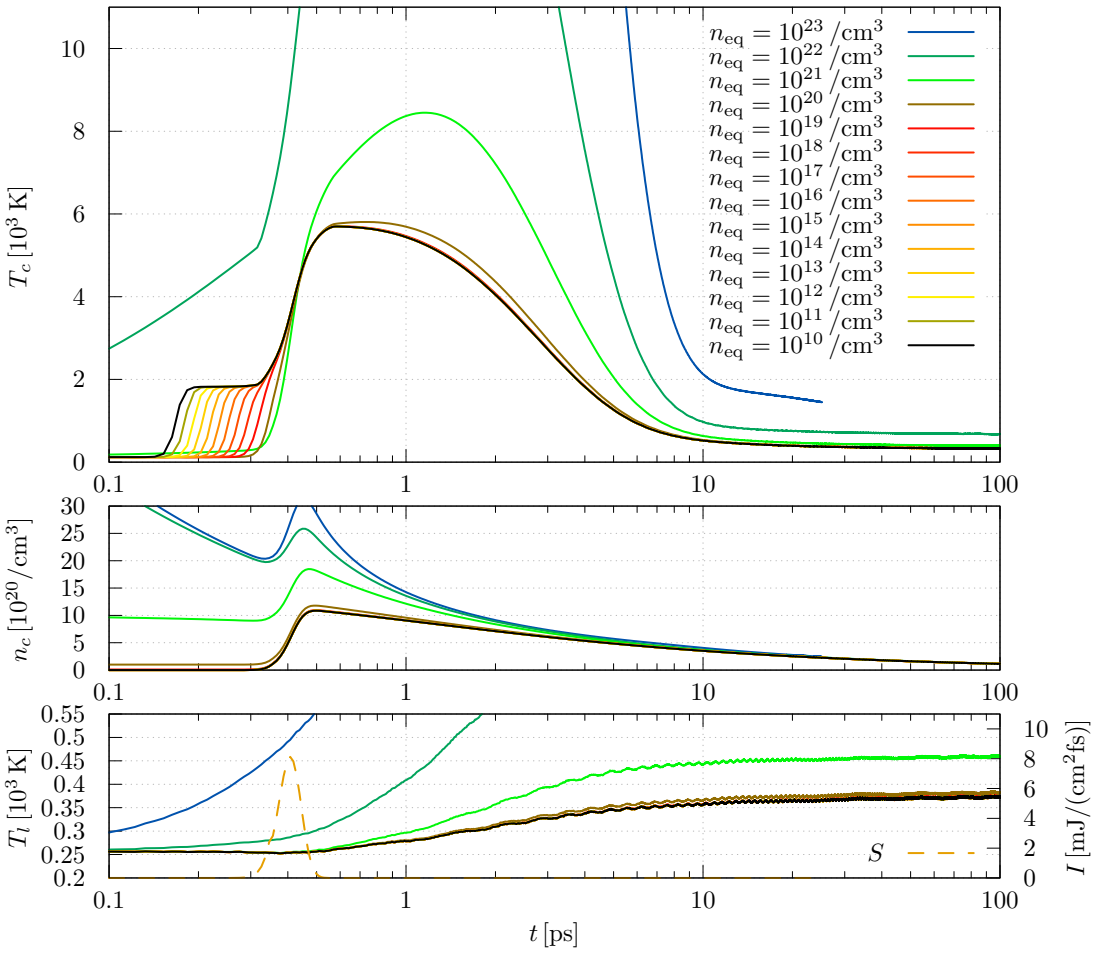

Figure 5.9: Time evolution of spatially averaged observables of the nTTM on sample `surface` under homogeneous laser irradiation with sub-damage threshold fluence of $\sigma = 0.16\,\mathrm{J/cm}^2$ and a FWHM pulse duration of $\tau_p = 100\,\mathrm{fs}$, depending on the initial carrier densities n_{eq}. The equilibrium carrier density at room temperature is of the order $n_{\mathrm{eq}} = 10^{10}\,/\mathrm{cm}^3$. The dashed line indicated the infused laser intensity S.

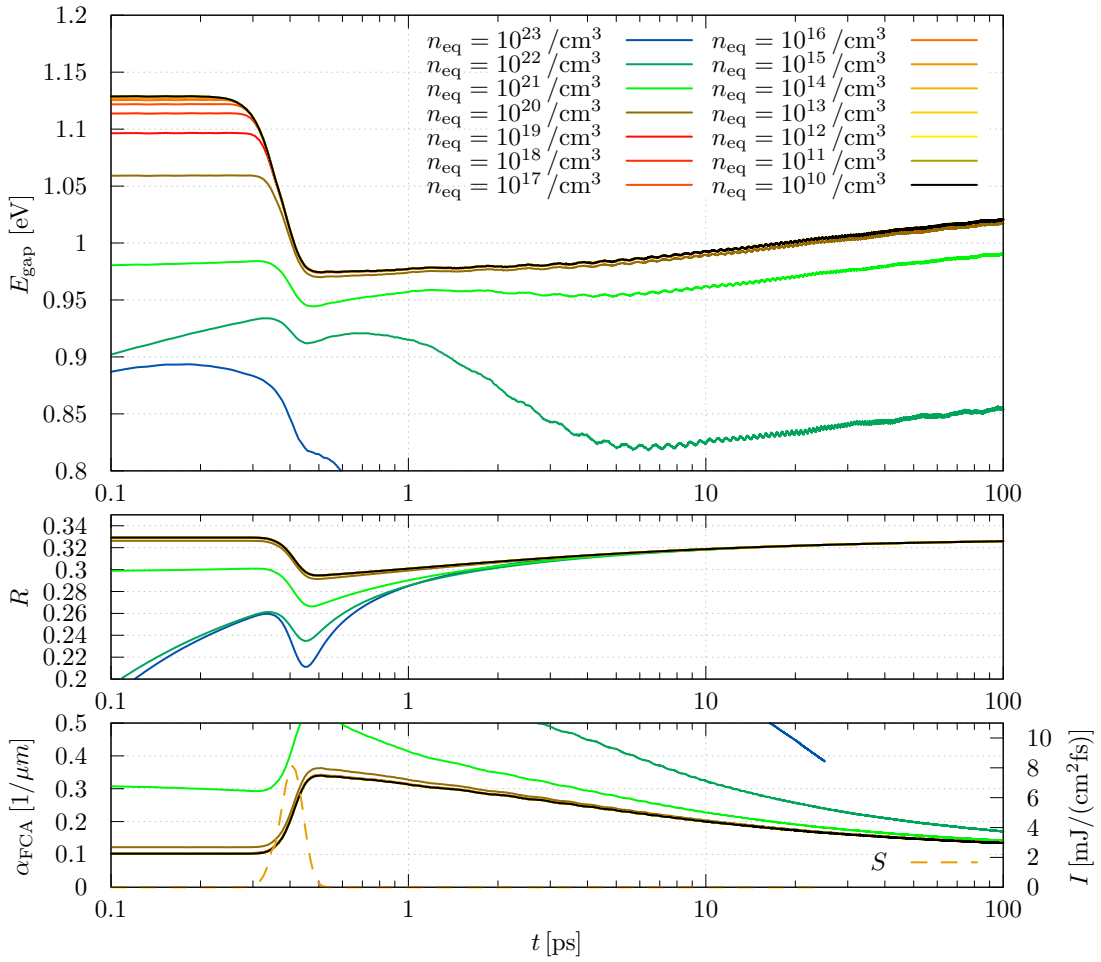

Figure 5.10: Time evolution of spatially averaged optical properties of the nTTM on sample `surface` under homogeneous laser irradiation with sub-damage threshold fluence of $\sigma = 0.16\,\mathrm{J/cm^2}$ and a FWHM pulse duration of $\tau_p = 100\,\mathrm{fs}$. The dashed line indicated the infused laser intensity S.

since it will be the lowest relevant carrier density we investigate. This definition allows us to define a function

$$\Delta^{n_{\mathrm{eq}}} = |T_l^{\mathrm{avg}}(\mathrm{end}) - T_l^{\mathrm{avg}}(\mathrm{end},\min(n_{\mathrm{eq}}))| \tag{5.22}$$

of n_{eq}, which shows the deviation of the lattice end temperature for a chosen n_{eq} from our baseline. Now we want to find the critical initial carrier density $n_{\mathrm{eq}}^{\mathrm{crit}}$, which is the highest possible carrier density which also leads to a lattice end temperature that differs from our baseline less than the occuring noise occurring. Within our tool set this condition simply reads

$$\Delta^{n_{\mathrm{eq}}} < \mathrm{RMSD}(T_l,T_l^{\mathrm{avg}}). \tag{5.23}$$

Now we apply these definitions to our data set. Fast Fourier transformation of the lattice temperatures yields relevant fluctuations up to a periodic length of $\lambda_T = 18\,\mathrm{ps}$ with the most dominant fluctuations at about $\lambda_T = 2.7\,\mathrm{ps}$. Consequently, an averaging time interval of $\Delta T = 20.36\,\mathrm{ps}$ was chosen. The results are shown in figure 5.11. For $n_{\mathrm{eq}} \leq 10^{20}\,/\mathrm{cm}^3$, all end temperatures are within $T_l^{\mathrm{avg}} = 372.3 \pm 0.05\,\mathrm{K}$. The RMSD was calculated over the complete time series and is of order $10^0\,\mathrm{K}$ for all initial carrier densities $n_{\mathrm{eq}} \leq 10^{22}\,/\mathrm{cm}^3$ and defines the threshold for possible accuracy. We observe, that for all $n_{\mathrm{eq}} \leq 10^{19}\,/\mathrm{cm}^3$, lattice end temperature differs less than RMSD from the simulation results obtained by setting $n_{\mathrm{eq}} = 10^{10}\,/\mathrm{cm}^3$. Optical parameters, already shown in figure 5.10, show the same behavior. Consequently, we chose $n_{\mathrm{eq}}^{\mathrm{crit}} = 10^{19}\,/\mathrm{cm}^3$ as the highest initial carrier density fulfilling our criterion (5.23).

For practical application, this means we are able to increase the initial carrier density by a factor of 10^9 without changing simulation results. Following the stability criterion (5.18), this decreases the CFL by a factor of 10^{-9}. As a result, our previous example of $2.2 \cdot 10^{12}$ required FD steps per MD step lowers to merely 2200 FD steps, which is not only suitable for today's supercomputers but for today's home desktop computers, too. This enormous reduction of computational cost does not only reduce resource requirements but also opens up the possibility of applying FTCS integration schemes rather than their semi-implicit counterparts. When do-

ing this, we are lowering computational cost and implementation complexity even further, while simultaneously eliminating all downsides coming with semi-implicit implementations.

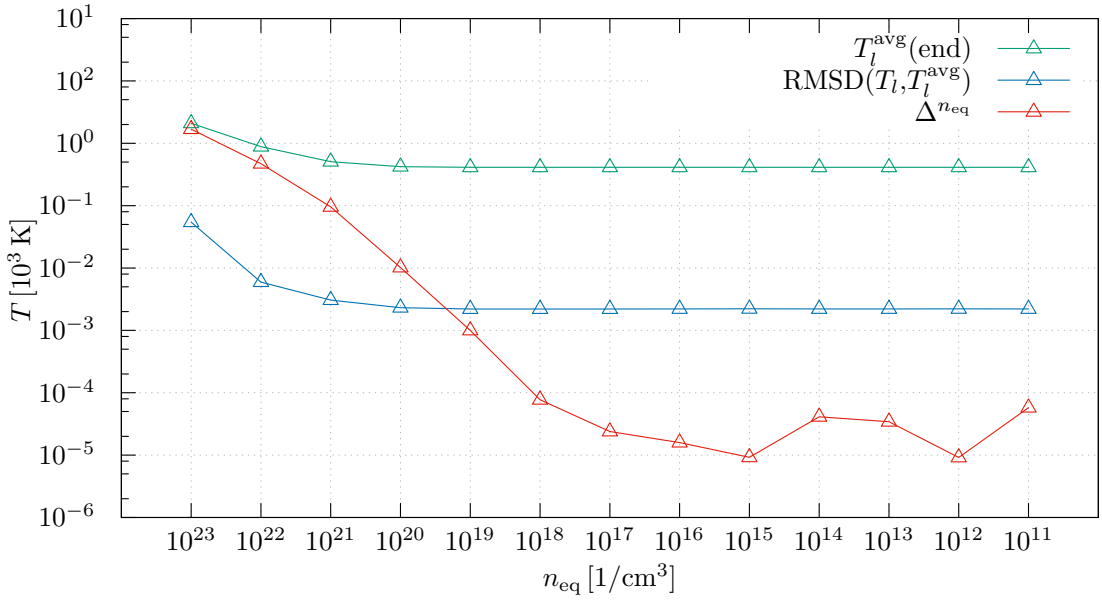

Figure 5.11: Comparison of averaged lattice temperatures T_l^{avg}(end) reached in the end of the simulation under variation of initial carrier density n_{eq}. In addition, the respective root mean square deviation RMSD(T_l,T_l^{avg}) between the averaged and non-averaged end temperature is shown, as well as the deviation $\Delta^{n_{\text{eq}}}$ from the expected lattice temperature.

Conclusion We showed that an explicit FTCS scheme with an artificially high n_{eq} will give the same results in the TSM and nTTM framework as semi-implicit Crank-Nicolson scheme with the correctly chosen n_{eq}. This allows for the usage of explicit FTCS integration schemes by decreasing computational cost by a factor of 10^{-9}. In addition, explicit schemes are usually easier to implement and are also computationally cheaper, especially in the context of large-scale HPC when inter-CPU communication is crucial for performance. This renders an explicit FTCS scheme with an artificially high n_{eq} the way to go. We want to emphasize that this allows for solving the transport equations on a three-dimensional FD lattice. This opens the new opportunity to perform large-scale laser ablation simulations

on covalently bonded semiconductors with spatially non-uniform laser profiles and the investigation of the ablation crater within realistic spatial dimensions. To our knowledge, this was not possible for covalently bonded semiconductors before.

5.4 Considering Non-thermal Effects

As the last step in the process of simulation model improvement in terms of excitation mechanics, we want to consider non-thermal effects.

The Problem The periodic length of optical phonons in silicon ranges from 70 fs to 90 fs. We mention this because one of the most often considered criteria for melting of crystalline solids in classical melting theory is the Lindemann criterion. The Lindemann criterion states that melting takes place when the lattice vibrations show a root mean square displacement of a certain fraction of the edge length of a unit cell. As a result, this criterion intrinsically demands a lower boundary on melting times, set by the highest occurring phonon frequency. However, ultra-fast melting phenomena conflicting with this boundary were observed in bulk silicon during laser excitation decades ago [153]. These ultra-fast structural changes take place in the order of several femtoseconds, thus cannot be explained by classical melting theories. A decade later, Parinello and Frenkel investigated these melting phenomena with a combination of DFT and MD calculations [89]. They showed that laser induced charge carrier excitation leads to excitation into anti-bonding CB states and thus induces instantaneous bond weakening followed by the ultra-fast collapse of lattice structure. This collapse of structure is called non-thermal melting. Of course, this process is expected to play a key role in the material dynamics and has to be taken into account in our simulations. Unfortunately, the usage of DFT calculations within each MD step is computationally very costly. At its time, the approach of Parinello and Frenkel was performed on a CRAY-C98 supercomputer which allowed for the processing of a maximum of 64 atoms per simulation [89]. Even with the extreme rise in computational power in the early 2000s to this day, 20 years later the DFT-MD approach is only able to handle super cells of up to 2000 atoms for several hundreds of femtoseconds and is restricted to closed periodic boundary conditions

[87, 91, 250]. Needless to say, this renders the DFT-MD approach insufficient for laser ablation simulation, where multi million particle simulations are needed to render macroscopic effects of interest. On the other hand, the microscopic excitation and bond weakening dynamics on the single particle level is desperately needed to correctly depict phase behavior and thus material dynamics on the macroscopic scale. As a result, we are in an area of conflict between the lengthscales which cause the material behavior we want to model and the lengthscale of material behavior we want to investigate.

The Solution To greatly reduce computational cost, our institute developed the MOD* [93]. The MOD* is based on the MOD and is a classical interatomic potential parametrized on electronic excitation to reproduce ab initio simulations of laser excited silicon. We implement the MOD* into our in-house MD code IMD [183] and compare the resulting material dynamics to theory and check for its applicability in massive MD simulations.

Simulation Setup We apply our implementation of the MOD* on our laser ablation simulations of ultra-thin films. Simulations on sample `surface` under homogeneous laser irradiation with a fluence of $\sigma = 0.8\,\mathrm{J/cm^2}$ and a FWHM pulse duration of $\tau_p = 100\,\mathrm{fs}$ were performed applying the MOD*. The chosen fluence is roughly five times the damage threshold of silicon. Carrier transport phenomena are modelled with the TSM and absorption is modelled by D with an initial $\beta_{\mathrm{TPA}} = 2.0\,\mathrm{cm/GW}$. The resulting absorption length is greater than the sample length.

Simulation Observations Although DFT calculations underline the necessity of excitation-parametrized interatomic potentials, the vast majority of publications on atomistic modelling of laser ablation still employ excitation-independent interatomic potentials [65]. Most often, this follows the argumentation that excitation-dependent material dynamics plays a key role in the short time dynamics of the material but shows no significant difference when long term macroscopic material behavior is studied. Obviously, this is not the case and the reason why we first want to underline the massive differences in material dynamics predictions between MOD and MOD*. In figure 5.12 and figure 5.13, we show snapshots of the simulation box for

a simulation under the use of the MOD and MOD* at identical simulation times. In figure 5.14 we show additional snapshots within a narrower time frame for the simulation applying the MOD*. Although we observe a complete melting of the silicon film in both cases, we observe a fundamentally different ablation and melting kinematics in each case. The MOD shows a heterogeneous melting process, which is the expected behavior for picosecond and longer pulse durations. After excitation, the carrier subsystem thermalizes and relaxes with the lattice system. Local energy deposition into the lattice system is proportional to difference in carrier and lattice temperature, leading to a characteristic spatial gradient in melting speed. On the microscopic scale, melting takes place by homogeneous nucleation with a spatially varying nucleation rate. For the parameters considered, melting starts roughly at $t_{\mathrm{start}} = 1\,\mathrm{ps}$ after laser peak intensity and is completed at $t_{\mathrm{stop}} = 1.75\,\mathrm{ps}$ after laser peak intensity. This is expected because, at identical fluences, longer pulse durations show a lower laser peak intensity, thus generating a less strongly excited electron-hole plasma. Simultaneously, lattice-carrier equilibration takes place on pulse timescales, which further decreases peak excitation. As a result, the fluence threshold for non-thermal melting monotonously increases with pulse duration for super-picosecond laser pulses [216].

In direct comparison, the melting kinematics predicted by the MOD* shows homogeneous non-thermal melting, completed within $t_{\mathrm{stop}} = 0.108\,\mathrm{ps}$ after laser peak intensity. At $t = -25.7\,\mathrm{fs}$, carrier temperature exceeds 24834 K which corresponds to 2.14 eV where the silicon bonds are reported to be purely repulsive and anti-bonding states are occupied. With the sudden drop in angular potential energy, the diamond structure collapses into an amorphous state, allowing for a more dense packing. However, the repulsive nature of anti-bonding states also results in rapid evaporation into a mono-atomic gas. In addition to that, within this timescale no significant carrier-lattice energy relaxation has taken place. The ablation mechanism observed in figure 5.13 is purely driven by bond energy manipulation and not by increase of thermal energy. In fact, T_{l} drops from $T_{\mathrm{l}}(-150\,\mathrm{fs}) = 300\,\mathrm{K}$ to $T_{\mathrm{l}}(-9.8\,\mathrm{fs}) = 198\,\mathrm{K}$ during pulse duration. This behavior is in accordance with ab initio simulations by [89], was confirmed by [87] and is reproduced by our MOD*.

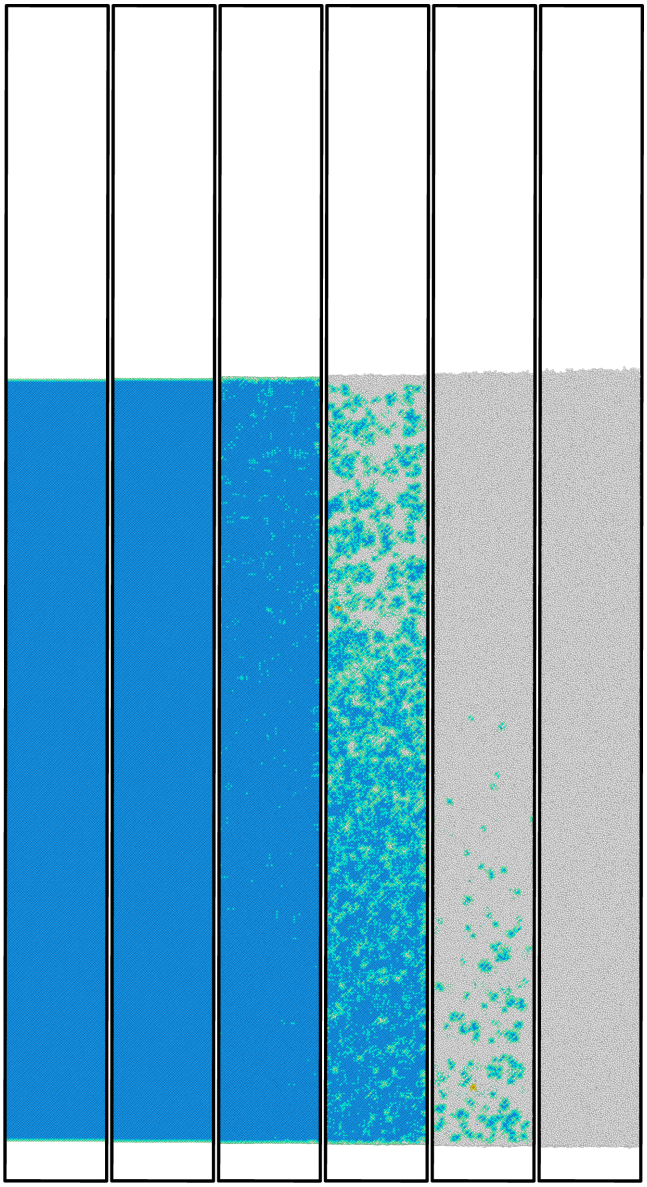

$t = -0.40\,\text{ps}$ $0.10\,\text{ps}$ $0.62\,\text{ps}$ $1.13\,\text{ps}$ $1.63\,\text{ps}$ $2.14\,\text{ps}$

Figure 5.12: Snapshots of the simulation box at different times t. The inciting laser shows a fluence of $\sigma = 0.80\,\text{J/cm}^2$ with a FWHM pulse duration of $\tau_p = 100\,\text{fs}$ and peak intensity at $t = 0$. The parametrization combination MOD+D is applied. The color coding is calculated with the mod-CNA method. Blue atoms show a cubic diamond structure in first and second shell, while turquoise atoms show a cubic diamond structure only in the first shell. White atoms show no lattice structure.

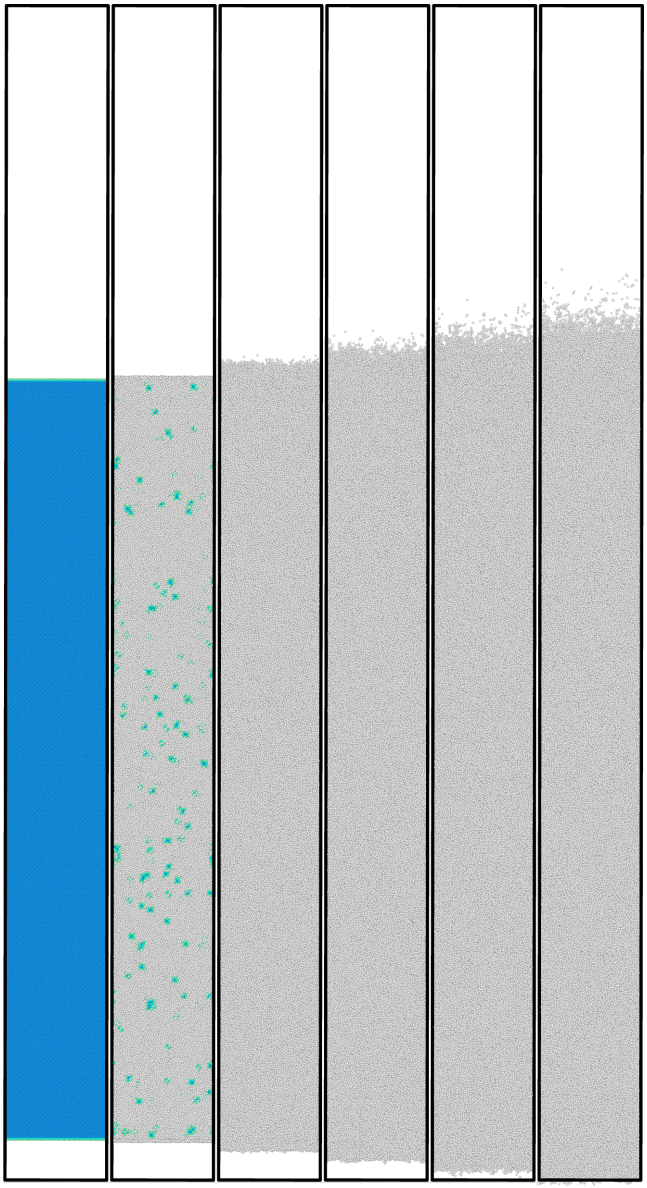

Figure 5.13: Snapshots of the simulation box at different times t. The inciting laser shows a fluence of $\sigma = 0.8\,\mathrm{J/cm^2}$ with a FWHM pulse duration of $\tau_p = 100\,\mathrm{fs}$ and peak intensity at $t = 0$. The parametrization combination MOD*+D is applied. The color coding is calculated with the mod-CNA method. Blue atoms show a cubic diamond structure in first and second shell, while turquoise atoms show a cubic diamond structure only in the first shell. White atoms show no lattice structure.

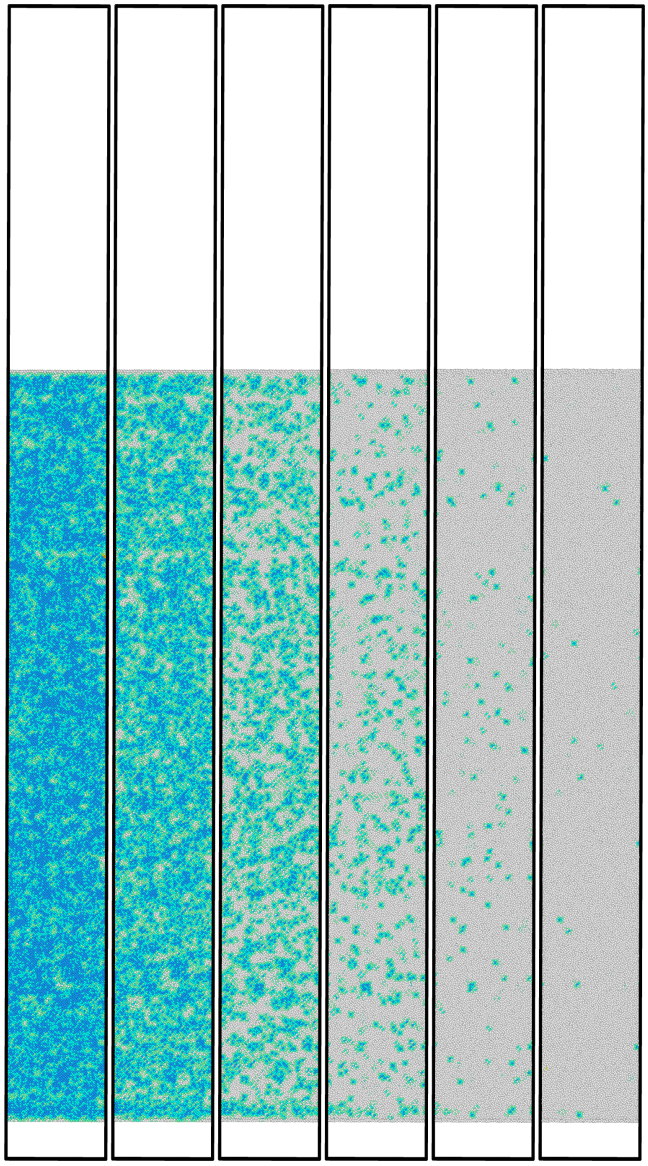

$t =$ 57.1 fs 67.2 fs 77.5 fs 87.6 fs 97.8 fs 108.0 fs

Figure 5.14: Snapshots of the simulation box at different times t. The inciting laser shows a fluence of $\sigma = 0.8\,\mathrm{J/cm^2}$ with a FWHM pulse duration of $\tau_p = 100\,\mathrm{fs}$ and peak intensity at $t = 0$. The parametrization combination MOD*+D is applied. The color coding is calculated with the mod-CNA method. Blue atoms show a cubic diamond structure in first and second shell, while turquoise atoms show a cubic diamond structure only in the first shell. White atoms show no lattice structure.

Obviously, the MOD* manages to reproduce the effect of non-thermal melting and the MOD does not. Having in mind that the MOD is historically designed for super-picosecond ablation and the MOD* was specifically designed to reproduce the effect of non-thermal melting during sub-picosecond excitation, this statement sounds like a tautology. However, due to the wide application of non-excitation-dependent interaction potentials in the context of sub-picosecond laser ablation simulation of covalent materials, we feel the need to address this.

Current State of Quantitative Characterization of Non-thermal Melting Although non-thermal melting is experimentally observed and the underlying qualitative mechanics are widely agreed upon, quantitative classification still scatters widely depending considered method of interpretation. In both scenarios, experimental and theoretical treatment, sample preparation plays a major role on the obtained data, as well as laser frequency, crystal orientation and evaluation method. As an example, Shank [153] measured time resolved reflectivity changes in pump-probe experiments at different wavelengths. His conclusion was that the observed sub-picosecond changes in reflectivity correspond to a metallic-liquid silicon phase induced by non-thermal melting. In his interpretation, melting takes place explicitly after and not during the excitation pulse of $\tau_{\mathrm{FWHM}} = 90\,\mathrm{fs}$. Comparable work by Kudryashov [90] reports a complete band gap collapse due to generation of a dense electron-hole plasma followed by formation of a liquid phase explicitly during the excitation pulse. In his work, ultra-fast reflectivity changes were evaluated by a $\tau_{\mathrm{FWHM}} = 100\,\mathrm{fs}$ pump-probe setup. Though, as discussed in section 5.2, the ultra-fast laser generated electron-hole plasma can induce a metallic state of optical properties. This makes it difficult to distinguish between metallic reflectivity induced by complete band gap collapse and lattice restructuring [100, 232] and optical metallic states induced due to plasma generation. To distinguish these effects more clearly, decay times of electron diffraction patterns after laser incitation where measured by Harb [73]. In these electron diffraction experiments, a $\tau_{\mathrm{FWHM}} = 150\,\mathrm{fs}$ optical pump pulse and a $\tau_{\mathrm{FWHM}} = 200\,\mathrm{fs}$ electron probe pulse was used, claiming a total response time of $t_{\mathrm{resp}} = 300\,\mathrm{fs}$. For the (001)-direction, an exponential decay in refraction intensity with a decay time of $320 \pm 50\,\mathrm{fs}$ was measured. In this particular

experiment, the fluence of the pump pulse was not stated. More importantly, in all presented cases a clear classification of the state 'molten' was not given. Unfortunately, all experimental approaches suffer from the conceptual problem that the excitation pulse will interact with the measurement technique, due to the restriction on available laser pulse durations. On the other hand, theoretical approaches allow for the direct tracking of atomic positions but suffer from the fact that all models are only as valid as the experimental data they are matched to. Fortunately, within the last five years, this problem was rigorously tackled by the group of Garcia within the framework of ab-initio simulations [86–88, 250]. In their simulations, the term 'molten' is defined via the structure factor, thus can be directly compared to diffraction experiments, and predicts non-thermal melting of silicon within $t = 100\,\mathrm{fs}$ after laser peak intensity with a $\tau_{\mathrm{FWHM}} = 100\,\mathrm{fs}$ pulse. This matches the collapse times of diffraction patterns by Harb [73]. For reasons of comparability, we chose this melting time as our baseline to benchmark the melting behavior predicted by our MOD*.

Evaluation Methods As mentioned before, the choice of evaluation technique alters the quantitative characterization of a thermodynamical process such as melting. For this reason, we define our criterion for a molten phase in this section. We apply the CSP and mod-CNA presented in section 3.5.2 on our simulation data. The CSP and mod-CNA parameter are calculated for each atom separately. For the mod-CNA, all non-cubic diamond assignments were counted as molten, while in case of the CSP a threshold of

$$\mathrm{CSP}_{\mathrm{th}} = 0.968 \tag{5.24}$$

is chosen following the analysis in [91]. All atoms with $\mathrm{CSP} < \mathrm{CSP}_{\mathrm{th}}$ are counted as molten. The results of this assignment as the fraction of the number of molten atoms N_{molt} per total number of atoms N_{total} are presented in figure 5.15(a). There we observe three features following from this definition. First, mod-CNA shows a melting time of $t = 108\,\mathrm{fs}$ after laser peak intensity for a complete melting of the lattice. This matches the mentioned ab-initio calculations and experimental data as precisely as it can be taken from the listed publications. Second, the CSP shows a

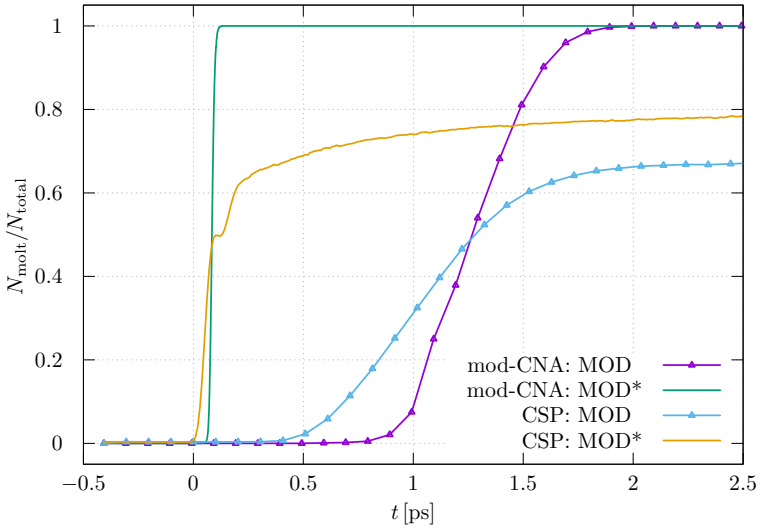

(a) overview

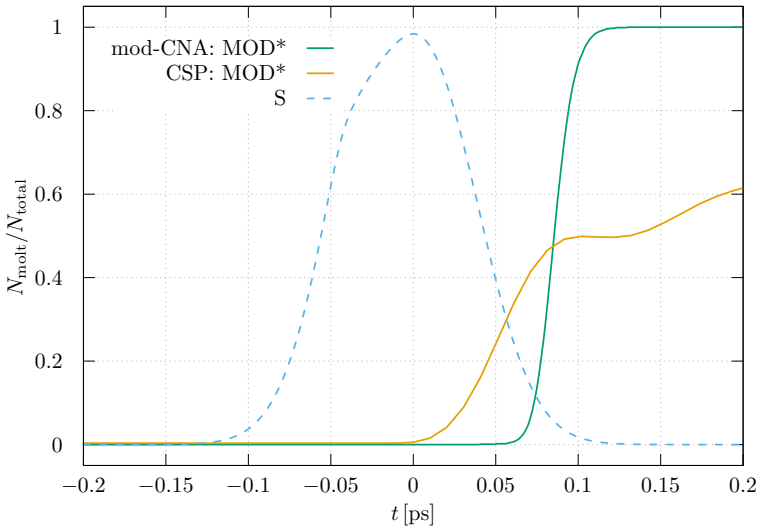

(b) enlarged view

Figure 5.15: Time evolution of the number of molten atoms N_{molten} per total atoms N_{total} for simulations under MOD+D and MOD*+D parametrization combination. The MOD data sets are shown with triangles and the MOD* data sets with solid lines. The assignment of the state molten is done with the mod-CNA method or the CSP falling below the threshold of $\mathrm{CSP_{th}} = 0.968$. The laser parameters are $\sigma = 0.80\,\mathrm{J/cm^2}$ with a FWHM pulse duration of $\tau_p = 100\,\mathrm{fs}$. The t-axis is shifted for $t = 0$ being the time of laser peak intensity. In addition, the spatially averaged effective laser intensity S is indicated by dashed lines as guide to the eye.

5 fs wide plateau while melting. The center of this plateau matches precisely with the time step where mod-CNA reaches a 100% molten sample. This is because, while the mod-CNA analyzes lattice structures, the CSP measures centrosymmetry per atom, thus staying constant during homogeneous lattice restructuring. The reason this plateau happens at a 50% molten fraction is that amorphous phases still show a certain fraction of centrosymmetry. Consequently, we choose the middle of this plateau as the melting time defined by CSP. With increasing time, the CSP shows a monotonic increase after complete melting took place. This is not an unphysical behavior but follows from the definition of the CSP. While the molten phase still shows a reduced centrosymmetry, the rapid expansion of the sample drives the material into a mono-atomic gas. By expansion, atoms dislodge further from their neighbors leaving the cut-off radius and ultimately increasing the CSP. This is expected since single atoms intrinsically show perfect centrosymmetry. Thirdly, the MOD data produces the expected unphysical thermal melting dynamics and is insufficient for sub-picosecond laser pulses.

Simulation Predictions of Melting Times If we look closely at the DFT data cited, we notice that [87] reports an excitation threshold of 1.46 eV for non-thermal melting at zero pressure. Our simulations show a non-thermal melting threshold at an excitation temperature of 1.40 eV. This translates to a peak excitation carrier temperature difference of roughly 700 K between our simulation model and DFT calculations. Although this seems like a noteworthy discrepancy, these differences can be explained by the applied boundary conditions. For our continuum-atomistic simulation of nanosecond laser ablation, we use periodic boundary conditions in y- and z-direction and open boundaries in laser beam-direction (PBC 011), while DFT simulations intrinsically are bound to use completely closed boundaries (PBC 111). This influences the dynamics of the melting procedure. As pointed out by [91], due to the contracting nature of the diamond lattice collapse, both non-thermal and thermal melting are promoted by high pressure and repressed by vacuum vice versa. We repeat the simulation of the last section on the cubic sample `block`, containing $200 \times 200 \times 200$ unit cells with overall $6.4 \cdot 10^7$ silicon atoms at the pressures $p = 0$ and $p = \pm 1.6$ GPa at $T_l = 300$ K for different PBCs and varying laser fluence. We

apply the presented characterization of melting times via the mod-CNA criterion. The resulting melting times are shown in figure 5.16.

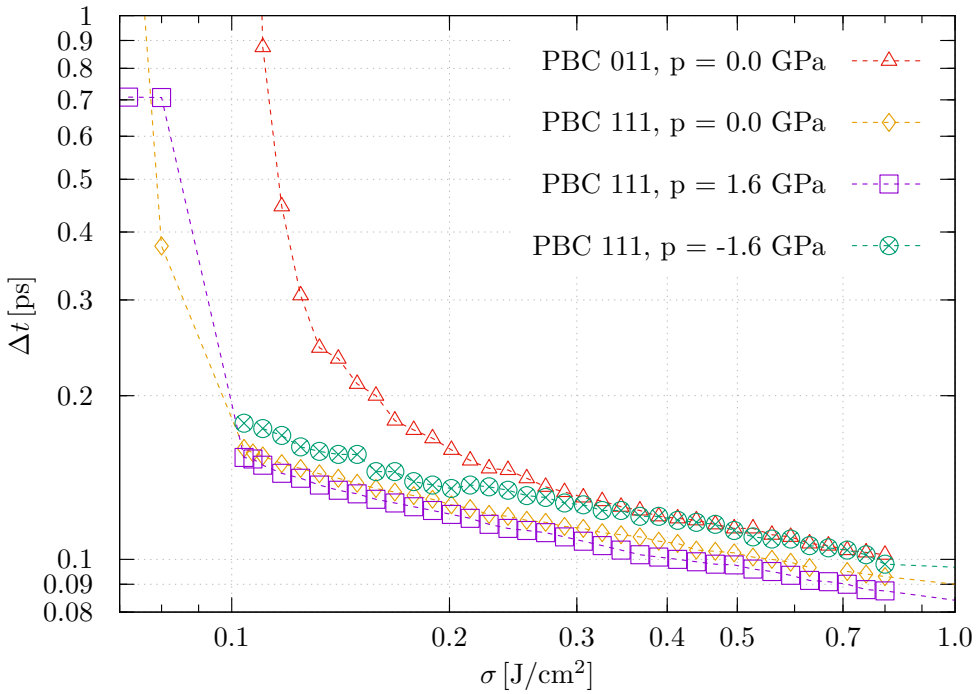

Figure 5.16: Melting times $\Delta t = t - t_0$ as the difference between time of laser peak intensity t_0 and simulation time t when a 100% molten state was reached according to the mod-CNA, for varying laser fluences σ at a FWHM pulse duration of $\tau_p = 100\,\text{fs}$ and different initial pressures p.

Our simulations predict an interesting behavior of open boundary simulations. All PBC 111 simulations show a decrease in melting time with increasing laser fluence which follows a power-law. This is expected, since the collapse of lattice structure is expected to be pressure assisted, thus assisted by an increase in lattice temperature. In contrast, the PBC 011 opens up the laser-direction border, generating an open surface of the sample. This allows the system to compensate the ultra-fast changing pressure conditions by contracting, thus prolong the melting process and raising the excitation threshold. However, the PBC 011 melting times converge towards the data set corresponding to low pressure dataset of PBC 111 for internal fluences $\sigma > 0.30\,\text{J/cm}^2$. At this point, the system reaches an excitation so intense, that the melting procedure is only dominated by local microscopic conditions and

macroscopic material response can no longer counteract the melting process. This means at internal fluences of $\sigma > 0.3\,\mathrm{J/cm^2}$, bond softening and lattice heating are dominatingly fast compared to the response time of the macroscopic dynamics of contraction and lead to locally identical behavior to PBC 111 simulations. The accordance to low pressures, of course, arises from a collective contraction of the sample due to the density anomaly of silicon. Note that we emphasize the term internal fluence, since in bulk samples internal fluence will vary with depth and thus create pressure gradients and follow-up effects. Consequently this means that the non-thermal melting kinematics is strongly influenced by local pressure and macroscopic material response.

p	PBC	$\sigma_{\mathrm{th}}^{\mathrm{melt}}$	Δt_{melt}	$\sigma_{\mathrm{th}}^{\mathrm{melt}}$	Δt_{melt}
1.6 GPa	111	$0.072\,\mathrm{J/cm^2}$	0.708 ps	$0.106\,\mathrm{J/cm^2}$	0.154 ps
0.0 GPa	111	$0.081\,\mathrm{J/cm^2}$	0.377 ps	$0.106\,\mathrm{J/cm^2}$	0.165 ps
0.0 GPa	011	-	-	$0.110\,\mathrm{J/cm^2}$	0.875 ps
−1.6 GPa	111	$0.106\,\mathrm{J/cm^2}$	0.178 ps	$0.106\,\mathrm{J/cm^2}$	0.178 ps

Table 5.3: Fluence thresholds $\sigma_{\mathrm{th}}^{\mathrm{melt}}$ and melting times Δt_{melt} for non-thermal melting of silicon obtained by our simulations for varying periodic boundary conditions PBC and initial pressures p. The left column shows the data by strict application of our criterion and the right column shows the data we classify as true non-thermal melting.

Interpretation Artifacts On the lower side of the studied fluence spectrum of figure 5.16, we can identify the excitation thresholds and resulting maximal melting times due to thermal melting. Unfortunately, the data shows a non-analytical deviation from our claim of $\Delta t(\sigma)$ following a power-law. However, these data points arise from the strict application of our melting criteria. We believe this is caused by long time carrier-lattice equilibration. The bonds are not excited enough for non-thermal melting, but a sufficient amount of energy is infused into the carrier system to slowly melt the sample by carrier-phonon equilibration anyway. This is not non-melting but an artifact due to the lack of cooling by heat transport effects into the

bulk. Anyway, we want to display both, the data obtained by strict mod-CNA and the data points we claim to be true non-thermal melting. The resulting fluence thresholds $\sigma_{\mathrm{th}}^{\mathrm{melt}}$ and melting times Δt_{melt} for non-thermal melting are displayed in table 5.3. In this more quantitative view, we see that all PBC 111 simulations show an identical $\sigma_{\mathrm{th}}^{\mathrm{melt}}$ with melting times decreasing with pressure. This underlines our statement that non-thermal melting is generated by the local microscopic electronic conditions and non-thermal melting speed is dominated by macroscopic conditions.

Conclusion In this section we finalized the process of tweaking and verification of our simulation model by inclusion of non-thermal effects. We showed the necessity of such a potential due to two major reasons:

1. The MOD cannot reproduce non-thermal melting and will depict an unphysical macroscopic material dynamics when applied to sub-picosecond laser ablation simulations.

2. Other simulation techniques, such as DFT-MD are capable of reproducing non-thermal melting but are bound to simulation samples of roughly 2000 atoms and periodic boundary conditions in all directions. These simulation techniques are not applicable to reproduce macroscopic material dynamics induced by laser ablation.

The addition of the MOD* to our present model allows us to surpass all of these restrictions. We showed that the present model is able reproduce non-thermal melting times in silicon predicted by experiments and DFT calculations, all at a comparatively low computational cost, which allows us to tackle macroscopic samples. Also, we utilized the capability of the mod-CNA to identify lattice structures to define our criterion of a molten amorphous phase within the framework of the CSP. In conclusion, the two presented evaluation techniques are capable of characterizing our melting procedure. The mod-CNA is more suitable to detect the explicit lattice structures, while the CSP allows for a more detailed insight into the ultra-fast material dynamics during melting. Additionally, the CSP shows a comparatively low computational cost and can be evaluated on the fly within our implementation. Both techniques show the accordance of our MD approach to ab-initio methods and experiments. This renders our MD approach suitable for future work.

6 Simulations and Results - Bulk Material

6.1 Comparison of Transport Models

Idea Within the last chapter, we improved and verified our simulation model by isolation of excitation effects. Now we expand our sample in laser-direction. With homogeneous laser irradiation, this is equivalent to the paraxial approximation and allows us to enable one-dimensional transport effects. Based on this information, we are able to make statements about the quality of the predictions of the TSM, nTTM and BETE transport model.

Simulation Setup We perform laser ablation simulations on bulk silicon sample `depth` under homogeneous laser irradiation. Sample `depth` shows a depth of 2225 nm and a quadratic cross-section of 475 nm^2 containing 51.2 million atoms. The sample is chosen to be longer than the expected effective absorption length. For reasons explained later, the optical parametrization is done with both, the fully dynamical optical parametrization D and the full T-expression parametrization. We will use both the MOD and MOD*. The laser pulse fluence is varied in search of the ablation threshold. Also a simulation with a fluence set to a supra-damage threshold fluence of $\sigma = 0.32\,\mathrm{J/cm^2}$ and a FWHM pulse duration of $\tau_\mathrm{p} = 100\,\mathrm{fs}$ is performed.

Results First we focus on the sample surface. Figure 6.1 shows a snapshot of the transport observables along laser-direction x at a simulation time of $\Delta t = 2.5\,\mathrm{ps}$ after peak laser intensity. We observe that the BETE and nTTM show an identical carrier excitation dynamics in terms of generated carrier density and temperature.

Despite identical carrier excitation at the time of laser peak intensity, a distinct difference in magnitude of transport effects and consequent surface properties can be observed. The nTTM shows the least pronounced energy transport within the models. The main transport contribution in the BETE is not directly visible by comparing the PDEs, while for the nTTM and TSM the impact of the definition of energy flux

$$\mathbf{W} = \underbrace{(E_\mathrm{g} + 3n_c k_\mathrm{B} T_\mathrm{c})\,\mathbf{J} - \overbrace{\kappa_\mathrm{c} \nabla T_\mathrm{c}}^{\mathrm{nTTM}}}_{\mathrm{TSM}} \tag{6.1}$$

is directly evident. The nTTM transport phenomena are purely driven by temperature gradients while, in case of the TSM, additional carrier density gradients contribute to energy transport. On top of that, carrier temperature gradients enhance the particle flux **J** which in turn enhances energy flux into the sample. This carrier temperature-driven carrier flux leads to a slightly pronounced carrier wave propagating into the sample, again enhancing energy transport into the sample. Again, this leads to both, reduced surface carrier density and therefore reduced local electron-phonon coupling. This results in reduced surface temperature but a deeper laser-affected region when compared to BETE or nTTM. Of course, the surface peak temperatures and carrier densities vary non-linearly with varying laser parameters, but for the chosen parameter set the nTTM yields a $\sim 28\%$ higher surface peak carrier temperature than the TSM. This is a significant difference which reflects in a drastic difference in lattice end temperature and therefore ablation threshold for each model.

On top of this discrepancy, energy transport and carrier excitation is also highly dependent on the local crystal structure and resulting band gap. As a result, the differences in the usage of MOD or MOD* also contribute to this complex interplay of phenomena. Now we want to generate a quick overview of simulation outcomes, when different transport models are combined with each simulation parametrization. We average the transport quantities over the first layer of activated FD cells at $x = 0$, this represents the excitation at the sample surface. For the old parametrization combination MOD+T, we show the time evolution of transport quantities in figure

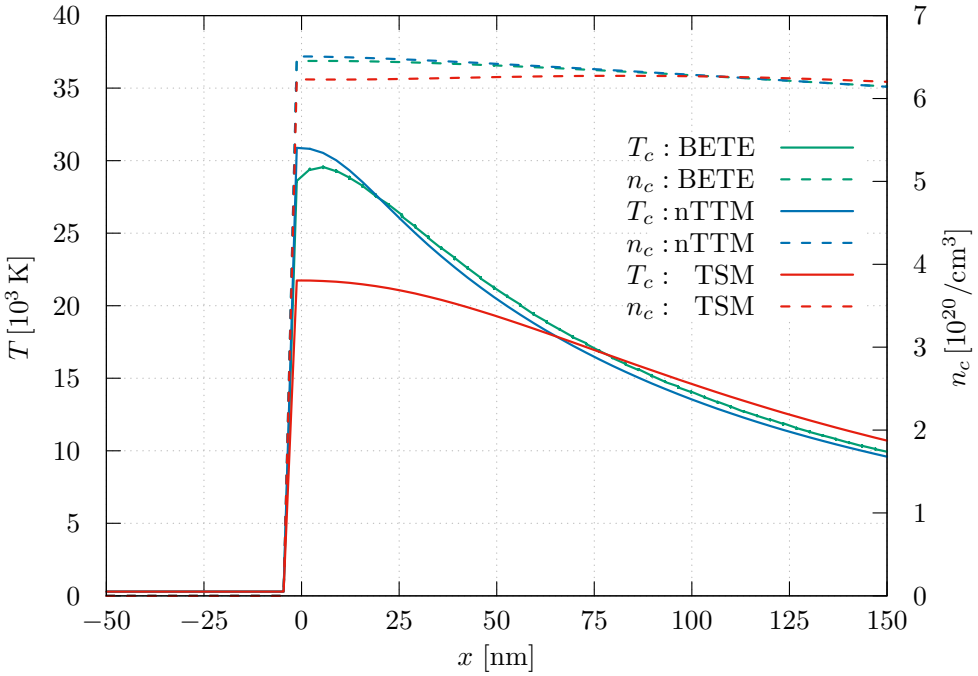

Figure 6.1: Snapshot of the spatial distribution of carrier temperature T_c and carrier density n_c at simulation time $t = 3.5\,\text{ps}$. This corresponds to be at $\Delta t = 2.5\,\text{ps}$ after laser peak intensity. The sample surface is positioned at $x = 0$, with x being the axis of the incident laser beam.

6.2 and the temporal evolution of the number density along the laser axis in figure 6.4. For the MOD*+D parametrization we show identical quantities under otherwise identical parametrization in figure 6.3 and figure 6.5. Although this side by side comparison provides us with a variety of features we could elaborate on, we want to concentrate on the features we didn't expect:

- In figure 6.4 the BETE+MOD+T shows a far less pronounced lattice melting, despite showing comparable excitation to the nTTM. We speculate that this is due to differences in electron-phonon coupling.
- For unclear reasons, the BETE+MOD+T also does not lead to discontinuities in T_l like nTTM+MOD+T and TSM+MOD+T. We expect these, as the discontinuities in T_l indicate the expected phase transition.
- The BETE+MOD*+D shows features in T_l for $t > 3\,\text{ps}$ we cannot explain.

Although a possible explanation could be that the sudden rise in temperature occurs simultaneously with discontinuities in T_c, indicating evaporation by non-thermal melting. The following cooling can be explained by gas expansion. However, nTTM and TSM do not show this feature even though the temperature is calculated by identical MD subroutines. This discrepancy remains unclear.

On the bright side, the remaining features surpass our expectations. For the chosen fluence of $\sigma = 0.320\,\mathrm{J/cm^2}$, we expect an ablation depth of $x_{\mathrm{abl}} = 71.5 \pm 10.0\,\mathrm{nm}$ [96]. When we compare the predictions of all possible parametrization combinations in terms of damage threshold and ablation depth, we obtain table 6.1. The behavior of models shows consistency with our expectations in the sense that enhanced transport capabilities enhance energy dissipation into the sample and therefore increase the damage and ablation threshold. The other way round, increased absorption capabilities lead to a more spatially confined energy imprint and therefore lower ablation depths and thresholds. This effect gets enhanced when excitation-dependent laser light absorption parametrization is considered. Here, the additionally generated carrier-hole plasma further decreases the laser absorption length. In addition, the transition from MOD to MOD* significantly lowers the ablation threshold and changes the occurring ablation mechanism. Due to non-thermal effects, ablation takes place on a much shorter timescale than heat conduction, so energy dissipation into the sample is suppressed and lowers ablation depth when compared to the MOD.

model	MOD+T	MOD+D	MOD*+T	MOD*+D
BETE	✓	$\uparrow_{\mathrm{th}}\downarrow_{\mathrm{d}}$	$\downarrow_{\mathrm{th}}\downarrow_{\mathrm{d}}$	$\downarrow_{\mathrm{th}}\downarrow_{\mathrm{d}}$
nTTM	✓	$\downarrow_{\mathrm{th}}\downarrow_{\mathrm{d}}$	$\uparrow_{\mathrm{th}}\downarrow_{\mathrm{d}}$	$\downarrow_{\mathrm{th}}\downarrow_{\mathrm{d}}$
TSM	$\uparrow_{\mathrm{th}}\downarrow_{\mathrm{d}}$	$\uparrow_{\mathrm{th}}\downarrow_{\mathrm{d}}$	$\uparrow_{\mathrm{th}}\downarrow_{\mathrm{d}}$	✓

Table 6.1: Qualitative classification of prediction quality by model combination. A checkmark indicates a correct prediction of both ablation threshold th and ablation depth d. Arrows indicate an over-(↑) or under-(↓) estimation of the respective.

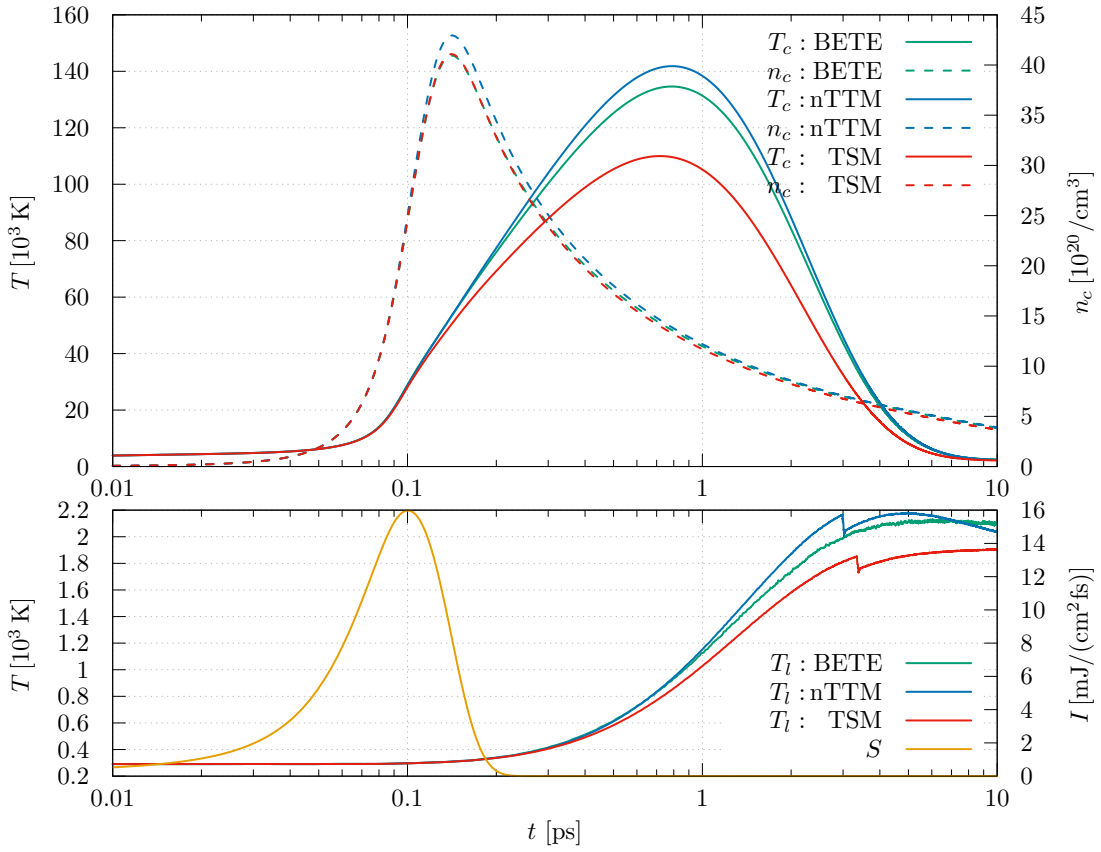

Figure 6.2: Time evolution of observables of the nTTM, TSM and BETE at the surface of sample `depth` under homogeneous laser irradiation with fluence of $\sigma = 0.32\,\mathrm{J/cm^2}$ and a FWHM pulse duration of $\tau_p = 100\,\mathrm{fs}$. The remaining parameters are chosen to be MOD+D.

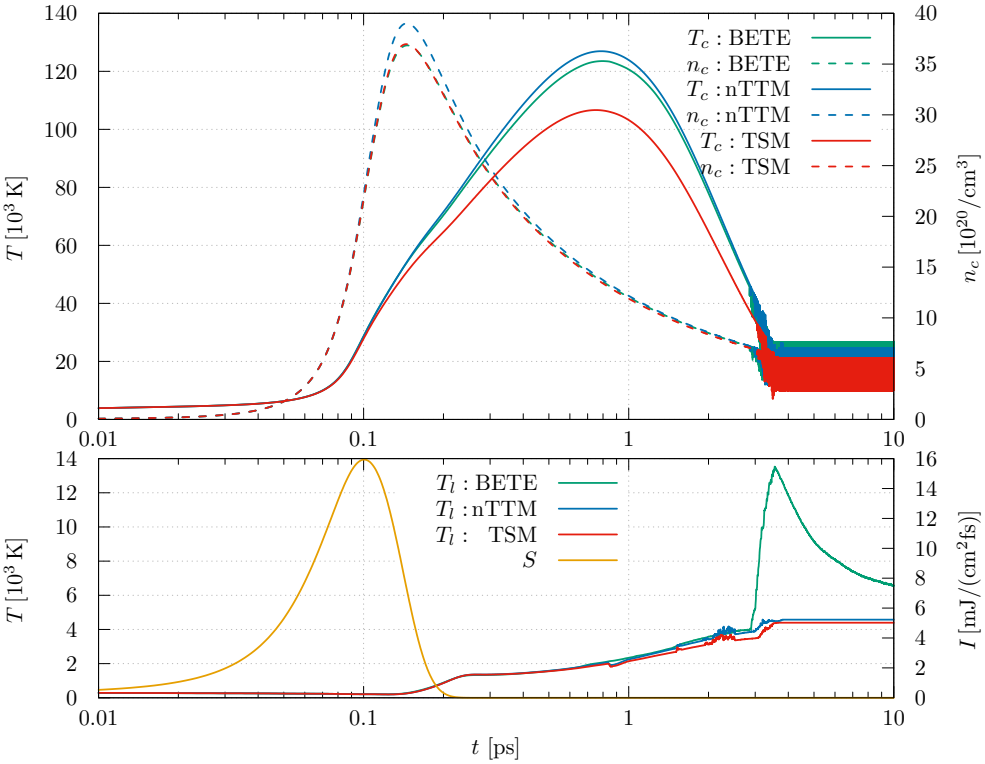

Figure 6.3: Time evolution of observables of the nTTM, TSM and BETE at the surface of sample `depth` under homogeneous laser irradiation with fluence of $\sigma = 0.32\,\mathrm{J/cm^2}$ and a FWHM pulse duration of $\tau_p = 100\,\mathrm{fs}$. The remaining parameters are chosen to be MOD*+D.

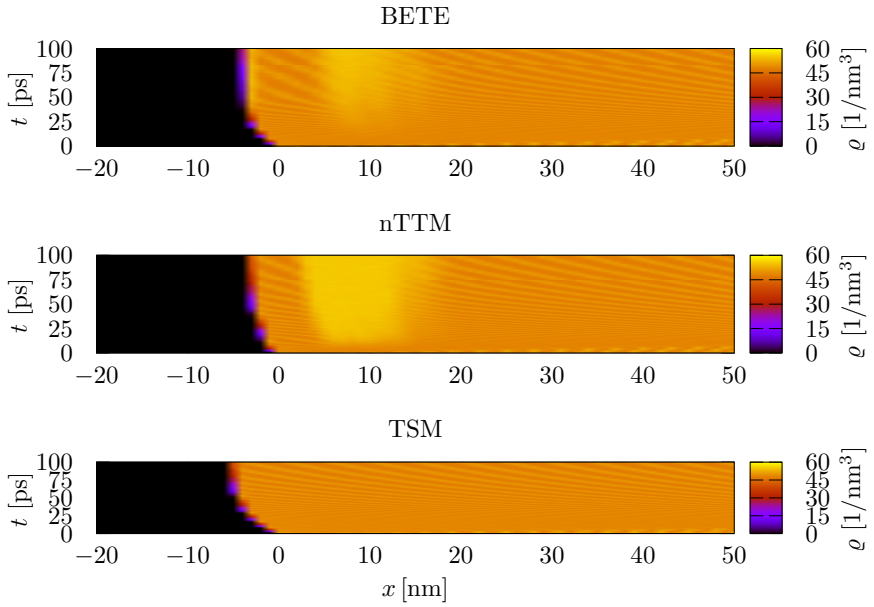

Figure 6.4: Time evolution of the number density along the axis of the incident laser beam by model. The remaining parameters are chosen to be MOD+D.

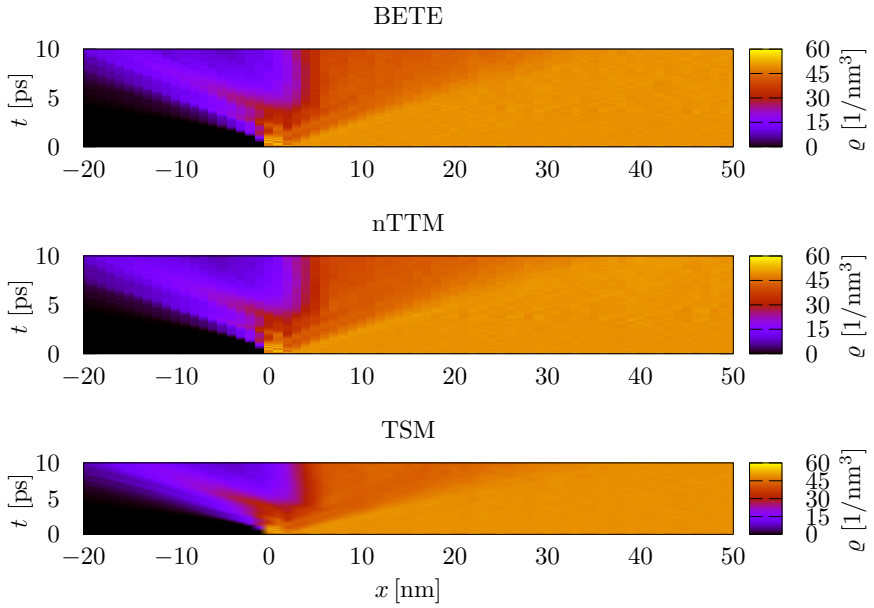

Figure 6.5: Time evolution of the number density along the axis of the incident laser beam model. The remaining parameters are chosen to be MOD*+D.

Conclusion All presented effects are working against each other and, in combination, lead to a new observation. The quality of models within laser ablation simulations is most often judged by the capability to reproduce the occurring laser ablation depth and threshold. Now we see that the established combination of the nTTM+MOD+T [80] leads to the correct ablation depth but with unphysical ablation mechanics for sub-picosecond laser pulses. When the MOD* is added to the model, we obtain a correct ablation mechanism but a massively underestimated damage threshold. By every gradual step of improvement, the model predictions deviate from experimental data. We assume that this is the main reason why the nTTM+MOD+T stayed the most established parametrization combination for MD laser ablation simulation in semiconductors [80, 91, 93–95, 199], altough the TSM was proposed and applied for continuum calculations much earlier [83, 109]. However, additional model improvements, namely the increased energy transport by carrier flux advection of the TSM counters the lowered ablation threshold of the MOD*. As a result, we obtain the TSM+MOD*+D as a model which correctly predicts ablation depth as well as ablation mechanics. For our following simulations, this will be our obvious choice.

Unfortunately, the BETE model is disappointing in its predictions. The goal of the BETE was to parametrize transport effects by energy instead of temperature because of the vanishing heat capacity of CB carriers within equilibrium conditions. In combination with semi-implicit integration algorithms, it enabled us to verify the existence of a critical carrier density at which the TSM is stable and results in identical predictions. However, it fails on its main task of energy transport predictions.

6.2 Empirical Stability Observations on the TSM and nTTM

Idea At this point, a purely numerical advantage of the TSM is noteworthy.

Simulation Setup We perform laser ablation simulations on bulk silicon sample `depthT` under homogeneous laser irradiation. Sample `depthT` shows a depth of 5500 nm and a quadratic cross-section of $30.25\,\mathrm{nm}^2$ containing $8 \cdot 10^7$ atoms. We use the TSM+MOD+D and nTTM+MOD+D parametrization at varying supra-damage threshold fluences and a FWHM pulse duration of $\tau_\mathrm{p} = 100\,\mathrm{fs}$.

Simulation Observations Snapshots of carrier density and carrier temperature after laser irradiation with a single pulse of 100 fs FWHM pulse duration and fluences of $\sigma = 0.75\ \mathrm{J/cm}^2$ are shown in figures 6.6 and 6.7. It can be seen that in the case of the nTTM, numerical instabilities occur at the back of the sample. These instabilities emerge as self-amplifying numerical oscillations, visible as a noise-like structure, propagating towards the sample surface, causing the simulation to crash. In contrast, the TSM behaves numerically stable for the same parameter set. The coupling of the transport equations to MD fluctuations makes it appropriate to view the problem as a system of stochastic non-linear partial differential equations. Since a rigorous and precise mathematical stability analysis for such a system is a very complex and protracted task, we want to give a phenomenological reasoning for the increase in stability.

In table 5.2, we already demonstrated that the CFL numbers for the nTTM and TSM are inversely proportional to the carrier density. Now in the case of bulk material, excitation occurs most pronouncedly at the sample surface and decreases into the bulk. Following from this, instabilities occur at the back of the sample where laser excitation and therefore charge carrier excitation shows the smallest impact. In case of the TSM, we observe that drift terms contribute to the CFL number in a carrier density-independent way, greatly increasing stability in regions of small carrier densities. Moreover, in both models the band gap E_g is dependent on the MD temperature and therefore shows statistical fluctuations. The local laser field

absorption shows MD temperature dependencies which lead to the post-excitation carrier and temperature distributions reflect these fluctuations. The nTTM only uses a rate equation for carrier dynamics, allowing no diffusion of charge carriers, thus leading to an accumulation of noise. This noise enters the computation of heat propagation favoring numerical instabilities. The TSM on the other hand includes diffusion terms for carrier dynamics as well as drift terms for heat propagation which lead to smoothing of temperature and carrier distributions.

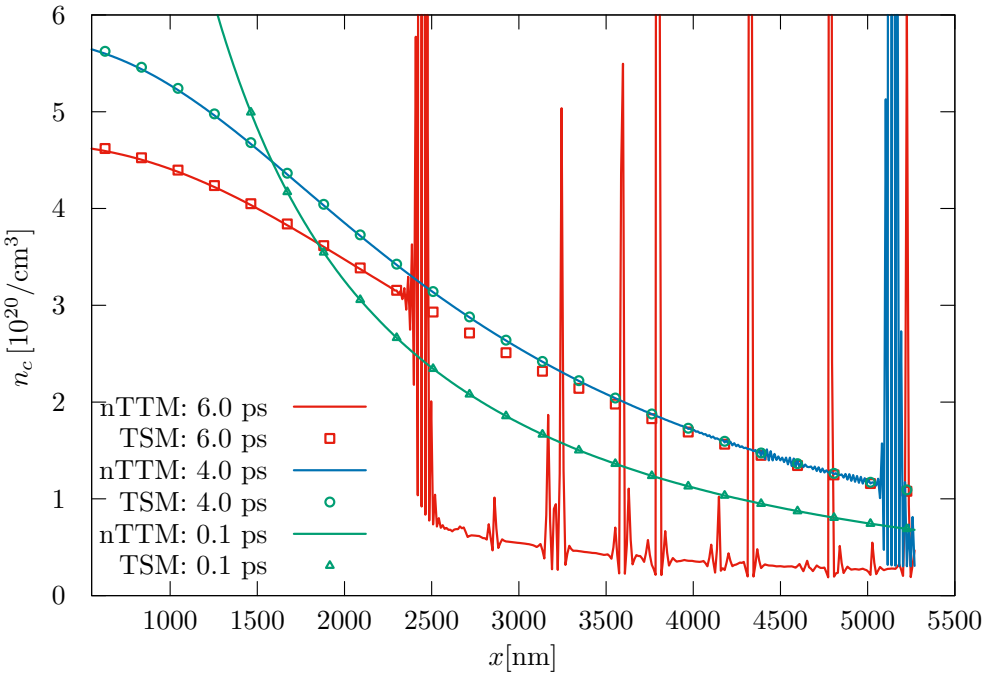

Figure 6.6: Snapshots of carrier density n_c depending on sample depth at different simulation times for both the nTTM and the TSM after laser irradiation with a fluence of $\sigma = 0.75$ J/cm^2. The data corresponding to the nTTM is shown as a solid line while data corresponding to the TSM is shown as squares. The numerical instabilities of the nTTM are visible as oscillations, while the TSM shows a smooth behavior.

Conclusion We observed the numerical advantage in stability increase of the TSM compared to the nTTM due to carrier diffusivity and the corresponding smoothing of observables. Combined with the artificial increase of equilibrium carrier density, this

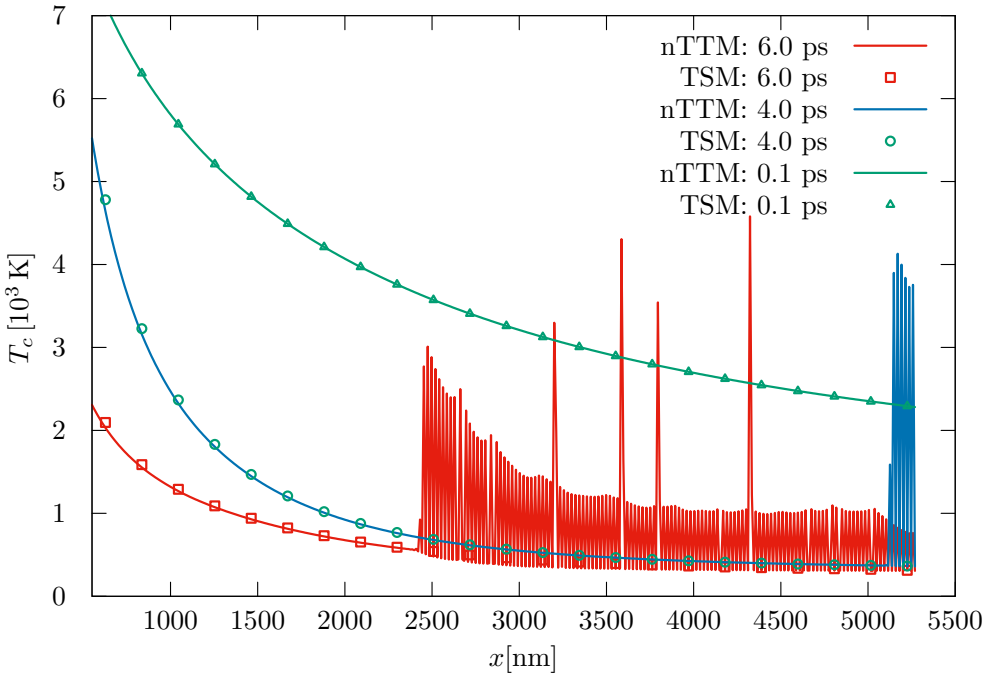

Figure 6.7: Snapshots of carrier temperature T_c depending on sample depth at different simulation times for both the nTTM and the TSM after laser irradiation with a fluence of $\sigma = 0.75$ J/cm^2. The data corresponding to the nTTM is shown as a solid line while data corresponding to the TSM is shown as squares. The numerical instabilities of the nTTM are visible as oscillations, while the TSM shows a smooth behavior.

makes the TSM suitable for large scale HPC and allows for long time, self-stabilizing continuum-atomistic simulations under extreme conditions.

6.3 Ablation Depth and Threshold

Idea To this point, the objective of this work was to refine our simulation model. In the last section, we finally arrived at the TSM+MOD*+D and claimed that the developed model is able to correctly predict the ablation threshold, as well as ablation depth under extreme simulation conditions. In this section, we want to verify this claim by sampling through a wide range of fluences and compare the predicted macroscopic material dynamics to experimental results.

Simulation Setup We perform laser ablation simulations on bulk silicon sample `depth` under homogeneous laser irradiation within the TSM+MOD*+D framework. The laser parameters are set to a pulse duration of $\tau_\mathrm{p} = 100\,\mathrm{fs}$ and a wavelength of $\lambda = 800\,\mathrm{nm}$. Laser fluence is varied the range of $0.072\,\mathrm{J/cm^2} < \sigma < 0.627\,\mathrm{J/cm^2}$. Each simulation was performed threefold.

Results From a physical point of view, the primary observable of interest in laser ablation experiments is the ablation depth x_abl per laser pulse. In industrial applications on the other hand, where material processing is usually done by a series of laser pulses, the observable of interest is most often the efficiency of material removal. We introduce the ablation efficiency

$$\varepsilon = \frac{x_\mathrm{abl}}{\sigma}, \tag{6.2}$$

which indicates the ratio of volume of the ablated material to infused laser energy. In figure 6.8, the simulated ablation depth x_abl and ablation efficiency ε of the TSM+MOD*+D, as well as experimental data obtained by Zhang [96] is shown. Since experimental data is scarce or distributed over a range of varying laser parameters, we want to emphasize on the fact that this experimental data is obtained by single shot experiments with a wavelength of $\lambda = 800\,\mathrm{nm}$ and a pulse duration of $\tau_\mathrm{FWHM} = 100\,\mathrm{fs}$. The laser spot size is stated to be set to $b_{1/e^2} = 1.2\,\mu\mathrm{m}$ full $1/e^2$-width and therefore corresponds to a spatial FWHM of $b_\mathrm{FWHM} \approx 0.71\,\mu\mathrm{m}$. Our simulation is set up with identical parameters. Consequently, the work by Zhang is one of the few experimental data sets that can be directly compared to our simulation data. Although, one difference remains, namely the experiment was carried out in ambient air, while our simulations correspond to laser ablation in a perfect vacuum. Also, it is not specified whether polycrystalline or monocrystalline samples were prepared. In both cases, we would expect differing direction-dependent heat conduction due to the local crystal orientation. However, MD-TTM simulations on quasi-crystalline aluminum–cobalt alloy showed that the anisotropy in the thermal properties of the system are of neglectable importance, when the infused energy greatly surpasses interatomic binding energies [251].

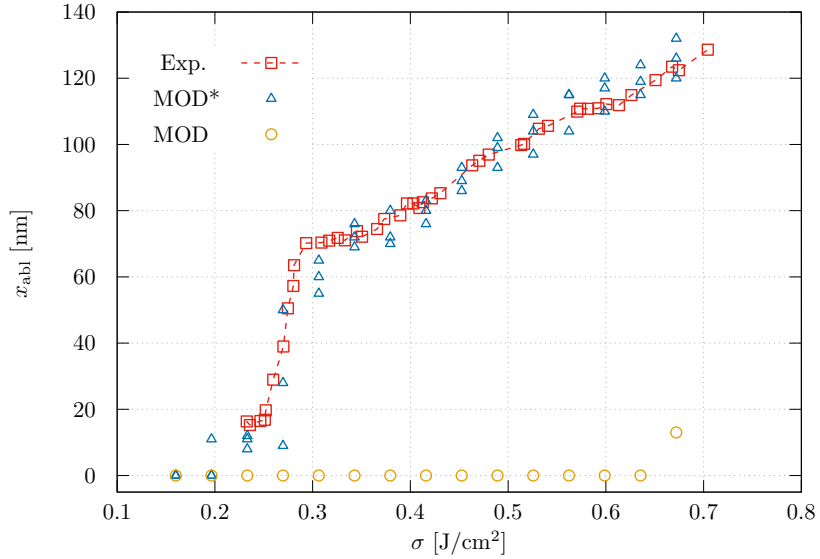

(a) ablation depth x_{abl}

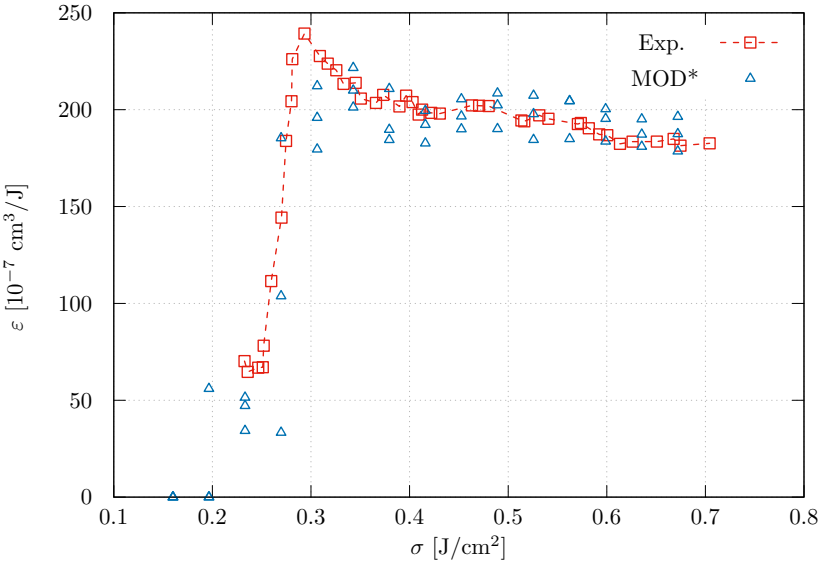

(b) ablation efficiency ε

Figure 6.8: Ablation depth x_{abl} or ablation efficiency ε depending on laser fluence σ. Blue triangles represent data predicted by TSM+MOD*+D with fully dynamical parametrization of optical properties. Yellow circles represent the predictions by TSM+MOD+D with fully dynamical parametrization of optical properties. Red squares are experimentally measured ablation depths by Zhang [96] in single shot laser ablation experiments with $\lambda = 800\,\mathrm{nm}$ and $\tau_{\mathrm{FWHM}} = 100\,\mathrm{fs}$.

First, we want to explain the spread of our simulation data in figure 6.8. This spread is due to finite size effects of the quasi-1D simulation. By limiting our simulation cell in non-laser-directions, no stabilizing effects from surrounding non-damaged material will occur and allow our sample to break in places where otherwise redeposition would have occurred. These artificial sample fractures arise randomly due to the non-linear nature of the fluid dynamics of the molten material. However, at this point, only the existence of these effects is necessary to understand the spread of the simulation data. The precise impact of these effects will be discussed in chapter 7.

Nevertheless, the simulated ablation depths are in surprisingly good agreement with the experimental data and reproduce scaling of x_{abl} with σ for fluences $\sigma > 0.35\,\mathrm{J/cm^2}$. For fluences $\sigma < 0.35\,\mathrm{J/cm^2}$, the results are not only in good agreement, but also reproduce characteristic features. First, the ablation threshold σ_{th}. Our simulations reproduce the ablation threshold of $\sigma_{\mathrm{th}} = 0.22 \pm 0.03\,\mathrm{J/cm^2}$. Isolated simulations show a lowered σ_{th}, however a close look at the simulation data revealed that this is due to the mentioned finite size effects. Here, non-thermal melting and the accompanying sudden negative pressure within the laser-affected zone cause the sample to snap in an unphysical position. Additionally, the simulated ablation threshold is in agreement with the ablation threshold measurement of Bonse [97]. In these experiments, the pulse duration dependence of ablation depth in the sub-picosecond regime was measured. Bonse reported a damage threshold of $\sigma_{\mathrm{th}}^{\mathrm{dmg}} = 0.20 \pm 0.05\,\mathrm{J/cm^2}$ for all $\tau_p \in [5\,\mathrm{fs} : 500\,\mathrm{fs}]$ and a laser wavelength of $\lambda = 800\,\mathrm{nm}$. Second, our simulations reproduce a step in ablation depth in the frame of fluence $\sigma \in [0.25\,\mathrm{J/cm^2} : 0.3\,\mathrm{J/cm^2}]$.

In literature, this sudden jump is often explained by the sudden dominance of TPA when increasing laser intensity. We see the reproduction of this TPA step in ablation depth as further confirmation of the quality of our dynamical absorption model.

As a single downside, our simulations on a quasi-1D sample do not reproduce the peak in ablation efficiency ε we see in the experimental data. However, this is not a failure of our model but a restriction of the quasi-1D sample. In reality we see that at this fluence regime the dominating ablation mechanism is the so-called phase explosion. A sub-surface solid to gas phase transition will cause the surrounding

material to be ejected in the form of partially molten droplets. In contrast to higher fluences where ablation is dominated by evaporation, less energy is converted by phase transition. As a result, the ratio of ejected atom per laser energy increases and results in the ablation efficiency peak. However, the removal of partially molten material occurs on the rim of the ablation crater and is therefore not pictured in the paraxial approximation of the quasi-1D simulation. This effect will be discussed in chapter 7.

Limitations Although the simulation results are in promising accordance to the presented experimental data, it is obligatory to discuss the limitations of the presented simulation setup. During our production runs, we observed limitations in our parameter space due to the interplay of computational resources and simulation setup. Within the presented framework, we are able to simulate fluences of up to $\sigma \approx 1\,\mathrm{J/cm^2}$. For fluences above that threshold, the simulations show unphysical behavior or crash due to extreme conditions. These extreme conditions are due to a high energy deposition into the MD system and result in an unphysical acceleration of atoms. In these extreme conditions, ultra-short particle distances occur and result in an infinite force acting on particles. Needless to say, our used second order integrator loses validity in this scenario. However, this is a well-known problem in MD simulations and is often countered by decreasing the MD time step Δt_{MD}. In pure MD simulations, computation time t_c scales with

$$t_c \propto \frac{1}{\Delta t_{\mathrm{MD}}} \tag{6.3}$$

for identical simulation times. We chose an MD step of $\Delta t_{\mathrm{MD}} = 1.018\,\mathrm{fs}$. For the simulations we used 16384 CPUs on a grid of $1024 \times 4 \times 4$ AMD EPYC 7742 processors provided by the High Performance Computing Center Stuttgart. Here, we achieve simulation times of up to $t_{\max} = 250\,\mathrm{ps}$ within a walltime of 24 hours. For the evaluation of the ablation threshold, we need the state of the system at $t > 1\,\mathrm{ns}$ and therefore need to continue the simulation for at least four times. With typical queue times, one simulation therefore takes roughly one week. A decrease of Δt_{MD} is therefore not practical. In HPC, when a code is already tuned to maximal efficiency, this problem is often tackled by increase of raw computational power.

However, two reasons prohibit us from just increasing the number of used CPUs.

1. the computational cost. The exponential growth of the cost of communication with increasing number of CPUs drastically slows down the computation time of one MD step. Not only does FD communication increase due to more FD-FD surfaces but also the communication of atoms between MD cells. Our current simulation setup results in a ratio of roughly 3000 atoms per CPU. This is already a third of the MD rule of thumb of 10000 atoms per CPU. Below that number communication cost surpasses computational cost of force calculation.

2. the FD cell decomposition. The chosen CPU grid on sample `depth` results in an maximal FD box size of 36Å $\times$ 36Å $\times$ 36Å, as each CPU must contain at least one FD cell. More CPUs would force a smaller FD grid spacing which in turn would strongly contradict the validity of the used continuum equations.

This means the current simulation setup is already tweaked to its maximum in terms of simulation parameters on the current hardware. Further scaling in number of CPUs will allow us to increase sample size but not the computational cost per MD step.

Conclusion The TSM+MOD*+D replicates experimental data not only by depicting the correct ablation depth but also by reproducing the ablation mechanics observed in experiments. Beyond that, we observe the TPA peak at low fluences in our simulation prediction, which in turn underlines the importance of the dynamical light absorption model. On top of that, ablation takes place at rather long simulation times. In this time fluence regimes, transport effects dominate the energy deposition within the sample. The reproduction of correct ablation depths at high simulation times therefore further increases our confidence in the quality of the TSM transport model.

On the downside, the current implementation of the simulation code is already at the limit of computational efficiency. We expect simulations not to be able to be carried out for significantly longer simulation times on the current state of hardware. However, it is able to tackle bigger sample sizes by increase of computation nodes.

With bigger samples, we will be able to correct the false prediction of peak ablation efficiency.

6.4 Novel Ablation Mechanics

Idea Based on the strong accordance of the TSM+MOD*+D with experimental ablation depths, we view the development of the TSM+MOD*+D as completed. Now we want to shift our focus from model validation towards the unexamined predictions of the TSM+MOD*+D and classify novel ablation mechanics. For this, we take a closer look at the time evolution of the sample irradiated with the highest applied fluence of $\sigma = 0.627\,\mathrm{J/cm^2}$.

Simulation Setup We perform laser ablation simulations on bulk silicon sample `depth` under homogeneous laser irradiation within the TSM+MOD*+D and TSM+MOD+D framework. The laser parameters are set to a pulse duration of $\tau_\mathrm{p} = 100\,\mathrm{fs}$ and a wavelength of $\lambda = 800\,\mathrm{nm}$. Laser fluence is chosen to be $\sigma = 0.627\,\mathrm{J/cm^2}$.

Results In figure 6.9, we show time resolved material density histograms along laser-direction x. We already established that the usage of nTTM+MOD+T leads to identical ablation behavior as the TSM+MOD+D and therefore reflects the current state of observed ablation mechanics within continuum-atomistic laser ablation simulations on silicon. However, as we already discussed, the validity of the observed mechanics for sub-picosecond laser pulses is highly doubted due to the neglect of non-thermal melting and its consequences. When we compare the time resolved density histograms, we observe the expected variety of new effects when comparing the predictions of MOD in figure 6.9(a) to MOD* in figure 6.9(b). We classify the novel ablation mechanics as

- non-thermal surface evaporation,
- pre-shockwave melting,
- non-thermal void formation and

- void-induced liquid spallation

and define them in the following.

Non-thermal Surface Evaporation Non-thermal surface evaporation is an extreme version of non-thermal melting, where anti-bonding states dominate the interatomic energy landscape. A sufficiently high laser excitation first leads to bond weakening and second to an increase in thermal energy. Like in purely classical theories, when the thermal energy exceeds the potential energy, the material evaporates. However, in the case of non-thermal surface evaporation, the evaporation takes place on the sub-picosecond timescale within the laser-affected zone.

Pre-Shockwave Melting Pre-shockwave melting is another non-thermal effect. In laser ablation, we expect the sample surface to rapidly expand due to material heating, thus generating a pressure wave propagating into the sample. With sufficient heating, this results in a heterogeneous melting front. Classically, this shockwave is restricted to propagate with the local speed of sound

$$c_s = \sqrt{\frac{\partial p}{\partial \varrho}}, \tag{6.4}$$

which can be expressed in terms of the local pressure p and density ϱ. However, in figure 6.9(b) we observe a non-thermal melting front, propagating with the local speed of light. This non-thermal melting front melts material before the shockwave develops, hence we call this effect pre-shockwave melting. Pre-shockwave melting is observed to only affect the material to a distinct depth x_{melt}. This depth is defined by laser light absorption processes and the depth where the internal fluence still meets the conditions for non-thermal melting. In our example, we observe the melting depth to be $x_{\mathrm{melt}} = 692\,\mathrm{nm}$.

Non-thermal Void Formation Non-thermal void formation is a direct consequence of pre-shockwave melting. In the laser-affected zone, where pre-shockwave melting

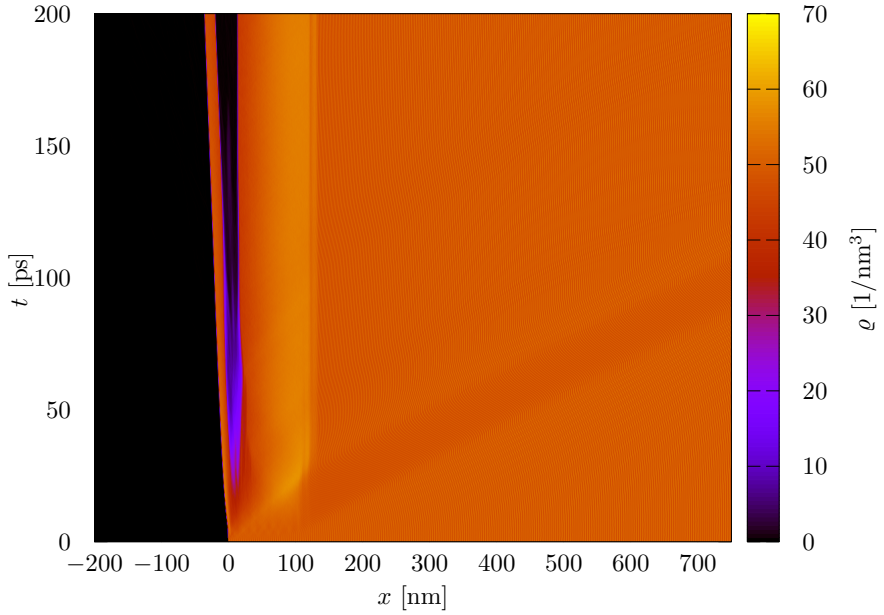

(a) TSM+MOD+D

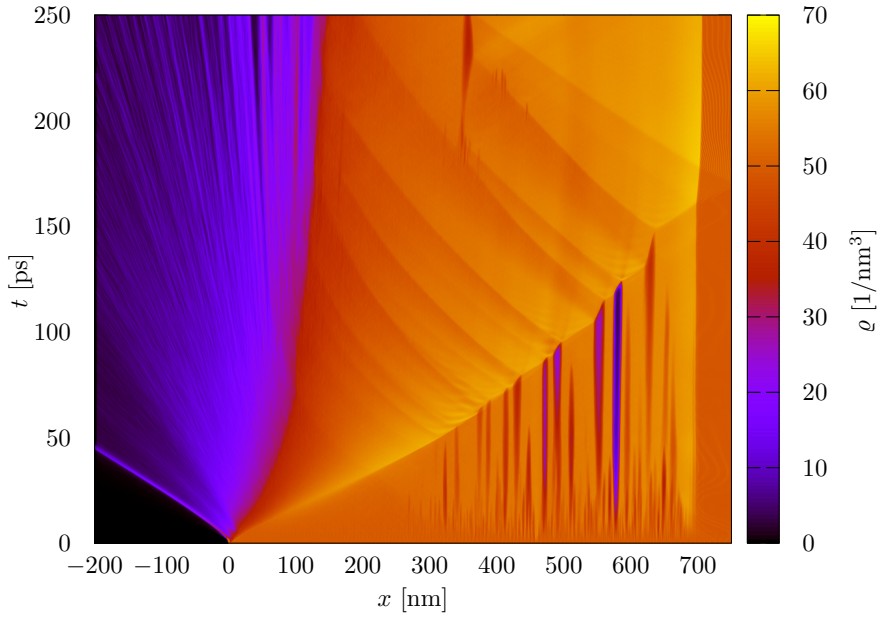

(b) TSM+MOD*+D

Figure 6.9: Comparison of time resolved number density histograms for $\sigma = 0.672$ J/cm^2. 6.9(a) shows the material dynamics under the use of TSM+MOD+D and 6.9(b) shows the material dynamics under the use of TSM+MOD*+D.

takes place, the diamond structure of silicon collapses into a dense amorphous state which is accompanied by an instantaneous drop in local pressure. In section 5.4, we determined the non-thermal melting time to be $\tau_{\text{melt}} = 108\,\text{fs}$. The melting speed $v_{\text{melt}} = x_{\text{melt}}/\tau_{\text{melt}}$ exceeds the reported equilibrium speed of sound $c_s(300\,\text{K}) = 8433\,\text{m/s}$ by three orders of magnitude. As a result, local material flow is too slow to compensate the resulting vacuum and the material relaxes by the formation of voids. At the front of the surface, this phenomenon is counteracted by non-thermal surface evaporation and pressure increase due to thermal expansion.

On a side note, we currently believe that this formation of an instantaneous vacuum is the reason for the convergence of the 'PBC 011, $p = 0$'- and 'PBC 111, $p = -1.6\,\text{GPa}$'-data presented in figure 5.16. A rigorous explanation is currently missing.

Void-induced Liquid Spallation Void-induced liquid spallation is another consequence of non-thermal void formation. In the classical sense, spallation happens when the shockwave gets reflected on the back of the sample and propagates back to the sample surface. On the sample surface, the shockwave gets reflected one more time, interferes with itself and causes crystalline or liquid material to be ejected. In this new mechanism the formation of voids by pre-shockwave melting generates open surfaces at which the pressure wave gets partially reflected. The result is that in this new case, the reflected shockwave is fanned out into multiple shockwaves. Each of the reflected shockwaves is propagating back towards the surface and can lead to the known effect of spallation. Additionally, due to the preceeding pre-shockwave melting, the material in the laser-affected zone is present in liquid or gaseous form, leading to the emission of liquid droplets.

Conclusion The ablation mechanisms predicted by TSM+MOD*+D show novel non-thermal characteristics and vary drastically from the metallic ablation mechanisms predicted by the MOD.

6.5 Pre-Shockwave Melting Depth

Idea In the last section, we introduced pre-shockwave melting as a non-thermal phenomenon due to laser induced bond weakening. In this section, we want to quantify the fluence dependency of the non-thermal melting depth x_{melt}.

Simulation Setup We perform laser ablation simulations on bulk silicon sample `depth` under homogeneous laser irradiation within the TSM+MOD*+D framework. The laser parameters are set to a pulse duration of $\tau_{\mathrm{p}} = 100\,\mathrm{fs}$ and a wavelength of $\lambda = 800\,\mathrm{nm}$. Laser fluence is varied in $\sigma \in [0.032\,\mathrm{J/cm^2} : 0.627\,\mathrm{J/cm^2}]$.

Results We measured the depth of pre-shockwave melting x_{melt} by direct evaluation of density histograms at $\Delta t = 650\,\mathrm{ps}$ after peak laser intensity. The resulting melting depths x_{melt} are shown in figure 6.10, as well as a fitting-law (6.9) we propose for x_{melt}. The presented data suggests that the melting depth follows a logarithmic law. For melting, the thermal energy of atoms needs to exceed the energy provided by the interatomic bonds. The pre-shockwave melting depth x_{melt}, is therefore a direct result of the energy provided by the local effective fluence and the initial thermal energy of the atoms. In the case of simple metals, the same argumentation holds, although no bond weakening occurs. For metals, the melting depth

$$x_{\mathrm{melt}}^{\mathrm{metal}} = \frac{1}{\alpha} \ln\left(\frac{\sigma}{\sigma_{\mathrm{th}}^{\mathrm{melt}}}\right) \tag{6.5}$$

follows [252]. This equation is obtained by assumption of neglectable heat conduction, constant reflectivity and constant SPA during the laser pulse. Under these assumptions, the thermal energy distribution along the laser axis x, follows the instantaneous energy imprint of the solution of the Lambert-Beer law

$$\frac{dI}{dx} = -\alpha I. \tag{6.6}$$

$x_{\mathrm{melt}}^{\mathrm{metal}}$ can then be directly extracted by the condition that the local effective fluence σ must exceed the fluence threshold $\sigma_{\mathrm{th}}^{\mathrm{melt}}$ for melting. However, this functional form of melting depth is not transferable to semiconductors, since the assumptions of

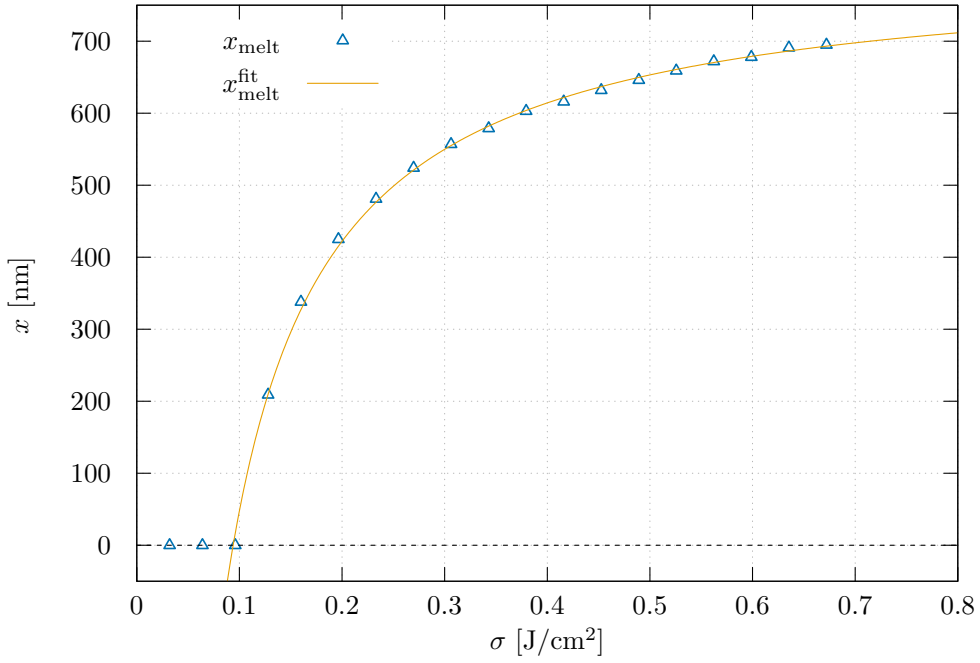

Figure 6.10: Pre-shockwave melting depths x_{melt} by fluence σ and the obtained fitting-law $x_{\text{melt}}^{\text{fit}}$.

constant reflectivity and constant absorption coefficients do not hold. For analogous treatment, we would have to solve the semiconductor absorption equation

$$\frac{dI}{dx} = -\alpha I - \beta I^2 \tag{6.7}$$

analytically. Of course, $\alpha = \alpha_{\text{SPA}} + \alpha_{\text{FCA}}$ and $\beta = \beta_{\text{TPA}}$ are highly dependent on the local lattice temperature, carrier temperature and carrier density, thus position and time. Moreover, we have shown that non-thermal melting leads to complete band gap collapse on laser pulse timescales, which in turn affect reflectivity and laser light absorption. We want to follow Rousse [75] and assume α and β are constant during laser excitation. The resulting constants can then be viewed as time averaged effective parameters $\bar{\alpha} \equiv \bar{\alpha}_{\text{SPA}} + \bar{\alpha}_{\text{FCA}}$ and $\bar{\beta} \equiv \bar{\beta}_{\text{TPA}}$. Although this treatment is technically unphysical, it allows us for analogous treatment as in the case of metals

and leads to

$$x_{\text{melt}}^{\text{sc}} = \frac{1}{\bar{\alpha}} \ln \left[\left(1 + \frac{\bar{\alpha}}{\bar{\beta} I_c} \right) \frac{I_0}{I_0 + \frac{\bar{\alpha}}{\bar{\beta}}} \right], \tag{6.8}$$

with I_c as a free variable. $x_{\text{melt}}^{\text{sc}}$ has to be viewed with caution and can physically be interpreted as the temporally averaged melting depth. However, with this constraint in mind, we use the mean surface laser intensity as $I_c = \sigma_{\text{th}}^{\text{melt}}/\tau_p$ and fit the melting depth x_{melt} according to

$$x_{\text{melt}}^{\text{fit}} = A \cdot \ln \left[B \frac{\sigma/\tau_p}{\sigma/\tau_p + C} \right] \tag{6.9}$$

$$\stackrel{!}{=} \frac{1}{\bar{\alpha}_{\text{SPA}} + \bar{\alpha}_{\text{FCA}}} \cdot \ln \left[\left(1 + \frac{(\bar{\alpha}_{\text{SPA}} + \bar{\alpha}_{\text{FCA}})\tau_p}{\bar{\beta}_{\text{TPA}} \sigma_{\text{th}}^{\text{melt}}} \right) \frac{\sigma/\tau_p}{\sigma/\tau_p + \frac{(\bar{\alpha}_{\text{SPA}} + \bar{\alpha}_{\text{FCA}})}{\bar{\beta}_{\text{TPA}}}} \right] \tag{6.10}$$

to our data. We obtain the parameters shown in table 6.2 and compare them to experimental results. In [75], the identical fitting-law (6.8) is applied. The experimental data was obtained by ultra-fast time-resolved X-ray diffraction experiments where the material gets excited by a laser pulse of wavelength $\lambda = 800\,\text{nm}$ and a pulse duration of $\tau_p = 120\,\text{fs}$. Simultaneously, the sample is probed by a time resolved X-ray diffraction setup. The resulting non-thermal collapse of lattice structure was therefore observed in terms of collapse of the diffraction pattern.

parameter	$(\bar{\alpha}_{\text{SPA}} + \bar{\alpha}_{\text{FCA}})[1/\text{cm}]$	$\sigma_{\text{th}}^{\text{melt}}[\text{J/cm}^2]$	$\bar{\beta}_{\text{TPA}}[\text{cm/GW}]$
result	$4.798 \cdot 10^4$	0.0948	1170.56
exp. [75]	$1.0 \cdot 10^5$	0.095 ± 0.013	780.56 ± 190

Table 6.2: Effective fitting parameters of figure 6.10 compared to experimental results.

At first glance, we notice that the predicted fluence of irreversible melting damage $\sigma_{\text{th}}^{\text{melt}}$ fits the presented experimental data surprisingly well, while the effective optical constants $\bar{\alpha}$ and $\bar{\beta}$ are not within the intervals of error. However, in the experiment the presented $\bar{\alpha}$ was taken from [253] to reduce the degrees of freedom within the fitting procedure. Unfortunately, this constant, again, was measured via

ellipsometry in the mid 80's. While our argumentation against the transferability of ellipsometry experiments to the sub-picosecond regime from section 5.1 still holds, an error in the assumption of $\bar{\alpha}$ influences the obtained $\bar{\beta}$ linearly, as $C = \bar{\alpha}/\bar{\beta}$ is the degree of freedom within the fitting procedure. With an already assumed $\bar{\alpha}$, the error in assumption is therefore shifted into $\bar{\beta}_{\mathrm{TPA}}$. For comparison of the obtained optical parameters with the presented experimental values, we have to compare the fitting coefficients as

$$C_{\mathrm{exp}} = \gamma \cdot C_{\mathrm{sim}} \tag{6.11}$$

and obtain a deviation by a factor of $\gamma = 3.325 \pm 0.810$.

Conclusion The TSM+MOD*+D is able to predict the fluence of melting damage $\sigma_{\mathrm{th}}^{\mathrm{melt}}$ within the error range of comparable experiments and was determined to $\sigma_{\mathrm{th}}^{\mathrm{melt}} = 0.0948\,\mathrm{J/cm^2}$. The predicted depth of pre-shockwave melting x_{melt} by fluence σ for single pulses follows the expected logarithmic law and can be expressed in terms of time averaged effective optical parameters.

6.6 Ablation Mechanisms by Fluence

Idea The TSM+MOD*+D predicts various new ablation mechanics which were introduced in section 6.4. Analogously to metals, we expect semiconductors to change the dominating ablation mechanism under variation of laser fluence. In this section, we examine the fluence dependency of occurring known and new ablation mechanics using the TSM+MOD*+D.

Simulation Setup We perform laser ablation simulations on bulk silicon sample `depth` under homogeneous laser irradiation within the TSM+MOD*+D framework. The laser parameters are set to a pulse duration of $\tau_{\mathrm{p}} = 100\,\mathrm{fs}$ and a wavelength of $\lambda = 800\,\mathrm{nm}$. Laser fluence is varied in $\sigma \in [0.032\,\mathrm{J/cm^2} : 0.627\,\mathrm{J/cm^2}]$.

Results The time resolved density histograms for selected laser fluences are shown in figure 6.11 and figure 6.12. As expected, we observe that the dominating ablation

mechanisms vary drastically by laser fluence. However, the dominating ablation mechanism does not change on sharply divided fluence regimes, but rather merge into each other. A graphical summary for this section is given in figure 6.13. There, the time resolved density histograms are evaluated at $t = 250\,\mathrm{ps}$ and $t = 650\,\mathrm{ps}$ and lined up by fluence. Below that, we show the results of the following classification.

Generally, the effect of non-thermal void formation and pre-shockwave melting are observable for all studied laser fluences. Both effects were already extensively treated in previous sections. However, as a side note, in section 6.3 we argued that the spread of ablation depth in our simulation data results from limitations of the quasi-1D geometry. This effect is convincingly visualized in figure 6.11(b) and figure 6.11(d). At $x \approx 350\,\mathrm{nm}$ or respectively $x \approx 500\,\mathrm{nm}$, the artefact of sample breakage can be observed in terms of a time evolution where a non-thermal void leads to an artificial fracture of the sample. In a geometry showing more than one dimension, the material surrounding the void would stabilize the sample, thus prevent this artifact.

First we want to focus on effects near the sample surface. With increasing fluence, we enter the regime dominated by phase explosion. This effect is observed to be dominating within $\sigma \in [0.15\,\mathrm{J/cm^2} : 0.42\,\mathrm{J/cm^2}]$ and drives ablation to different extents. During phase explosion, sub surface material gets super heated and sublimates into the gaseous state. Due to the lack of backpressure, the surface layer cools itself by rapid expansion, thus staying in the liquid state. This results in a skin layer of molten material whose surface tension counteracts the expansion of gaseous sub surface material. Now, depending on the energy infused into the sub surface material via laser light absorption two distinct scenarios happen:

1. For lower laser fluences of $\sigma \in [0.15\,\mathrm{J/cm^2} : 0.26\,\mathrm{J/cm^2}]$, the surface tension of the skin layer exceeds the gas pressure of the sublimated material. In this case, the skin layer forms a bent open structure without detaching from the sample known as a nano-bump [40]. This process can be viewed in figure 6.11 and figure 6.12 as a redeposition of the surface layer. The formation of nano-bumps depends on the correct prediction of surface tension. In our quasi-1D approximation, we obviously neglect the areas of the surrounding material where the skin layer is still attached to the sample and thus highly underes-

timate the correct surface tension. However, the process of the formation of nano-bumps is still vividly discussed in literature [45] and thus worth a more rigorous treatment within the quasi-2D approximation.

2. For higher fluences, the phase explosion surpasses the surface tension and bursts open the skin layer resulting in the formation of droplets.

When laser fluence is increased to $\sigma > 0.35\,\mathrm{J/cm^2}$, non-thermal melting occurs in an extreme mode where the interatomic bonds are excited to be purely repulsive and result into direct non-thermal evaporation. This non-thermal surface evaporation is dominating the ablation mechanism for all following laser fluences. In this fluence regime, lattice dissolution occurs on shorter timescales than carrier-lattice equilibration, thus bond manipulation becomes the main driving force for particle acceleration. As a result, we observe the ejection of the surface layer with identical energies, thus identical ejection speeds independent of laser fluences. This effect is visible in figure 6.13 in terms of the identical position of the ejected surface layer at $t = 250\,\mathrm{ps}$ for $\sigma \gtrapprox 0.4\,\mathrm{J/cm^2}$.

The transition from phase explosion to non-thermal surface evaporation as the dominating ablation mechanism shows a drastic impact on the total energy ejected from the system via ablation. In the fluence regime dominated by phase explosion, the formation of the ablation plume by thermal processes allows for heat flow into the sample by heat conduction. In contrast to this, non-thermal evaporation directly ejects material. As a consequence, the ejected energy per particle is much higher in the case of non-thermal surface evaporation compared to the case of phase explosion, where material is also ejected in liquid or solid state. With this realization, we want to refer back to figure 6.8 where we analyzed the ablation efficiency ε and observed peak ablation efficiency at $\sigma \approx 0.29\,\mathrm{J/cm^2}$ with decreasing efficiency for increasing fluences. With our classification of ablation regimes, we can now offer a different view on the presented data. The pronounced peak in ablation efficiency directly corresponds to the regime of phase explosion and the following decrease in ε is a direct result of the transition towards surface evaporation, as non-thermal surface evaporation requires more energy infused per ejected atom. Consequently, the sharp increase in ablation depth x_{abl} and ablation efficiency ε at $\sigma \approx 0.26\,\mathrm{J/cm}$ corresponds to the transition from nano-bump formation towards ejection of the skin layer. Here,

the sudden increase in ablation depth reflects the complete ejection of the skin layer.

Additionally, we observe ablation mechanics and features occurring within the bulk material. For $\sigma \in [0.44\,\mathrm{J/cm^2} : 0.672\,\mathrm{J/cm^2}]$, we observe the shockwave to close all non-thermal voids within the area of pre-shockwave melting. However, non-thermal voids are a direct result of the sudden pressure drop due to the density anomaly of silicon combined with pre-shockwave melting. The non-thermal voids within the melt are observed to not be filled with vapour, thus are expected to close for long timescales. Furthermore, we expect a 2D geometry to enhance void closing due to the inclusion of void surface tension. Thus, complete void closing is expected for all laser fluences. However, non-thermal voids still contribute to the ablation mechanics in the way that we observe the shockwave to be partially reflected by non-thermal voids. The reflected shockwaves propagate back to the sample surface and cause liquid spallation on the molten surface. In our 1D approximation, this is observed as the ejection of additional layers of material, where in higher dimensions this causes the ejection of macroscopic droplets and/or alters the surface morphology of the laser crater.

Conclusion The dominating ablation mechanics for silicon vary drastically with increasing fluences due to the dominance of non-thermal effects towards higher fluences. We classified the occurring ablation mechanics for fluences $\sigma \in [0.032\,\mathrm{J/cm^2} : 0.627\,\mathrm{J/cm^2}]$ and found that for lower fluences, silicon shows an ablation behavior analogous to the ablation mechanics observed in metals. This fluence regime is dominated by ablation by phase explosion, where superheated material sublimates and consequently ejects material in solid, liquid and gaseous states. For higher fluences, this behavior is overshadowed by simultaneously occurring non-thermal evaporation, leading to direct ejection of material in the gaseous state. The direct non-thermal evaporation suppresses the importance of the complex fluid dynamical effects involved in droplet formation. However, we found that the required energy per ejected atom is higher for non-thermal evaporation than for the phase explosion. As a consequence, peak ablation efficiency is achieved in the fluence regime of phase explosion.

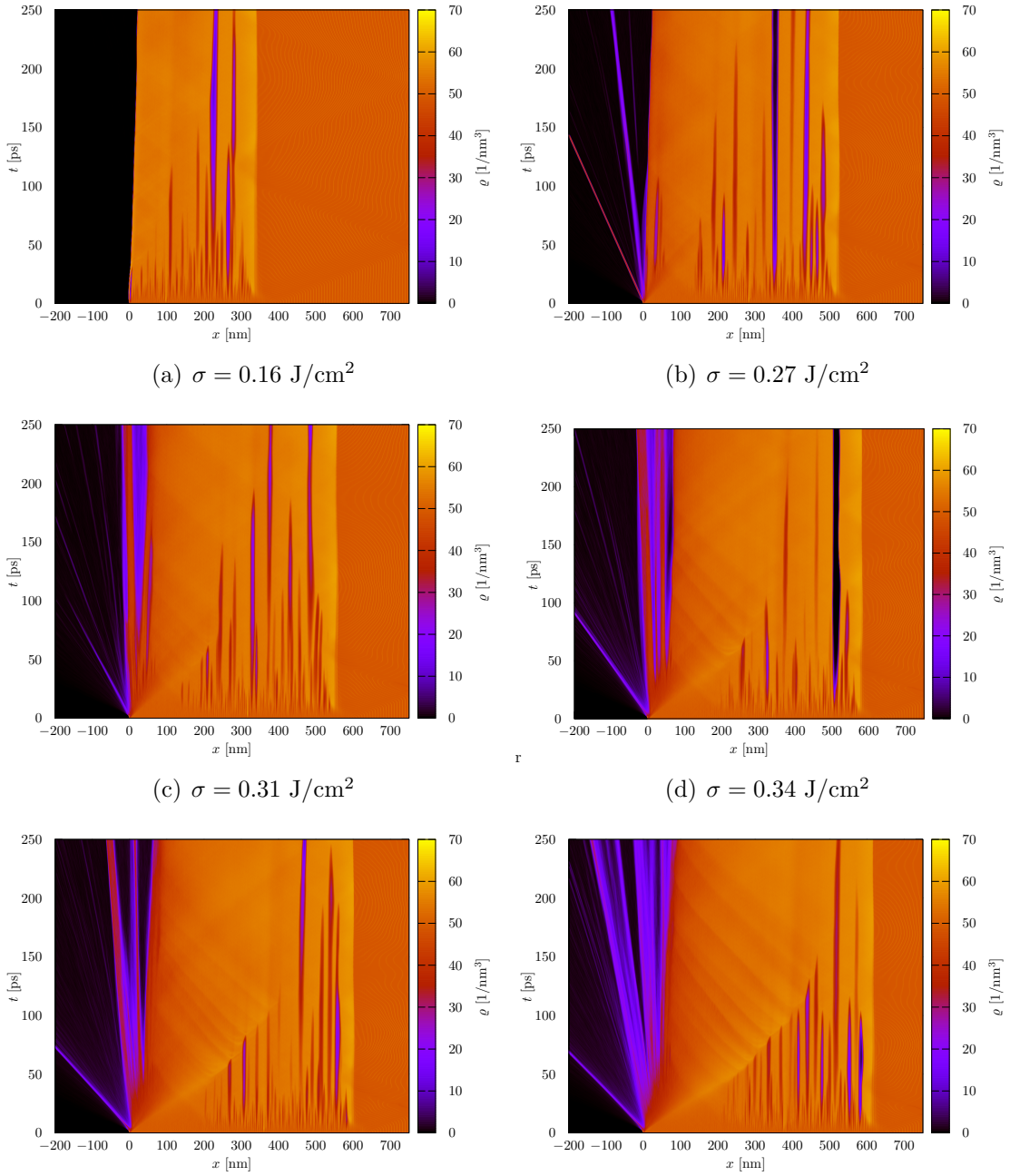

(a) $\sigma = 0.16$ J/cm^2

(b) $\sigma = 0.27$ J/cm^2

(c) $\sigma = 0.31$ J/cm^2

(d) $\sigma = 0.34$ J/cm^2

(e) $\sigma = 0.38$ J/cm^2

(f) $\sigma = 0.42$ J/cm^2

Figure 6.11: Time resolved density histograms along the laser axis of simulations under TSM+MOD*+D parametrization combination for varying laser fluences σ.

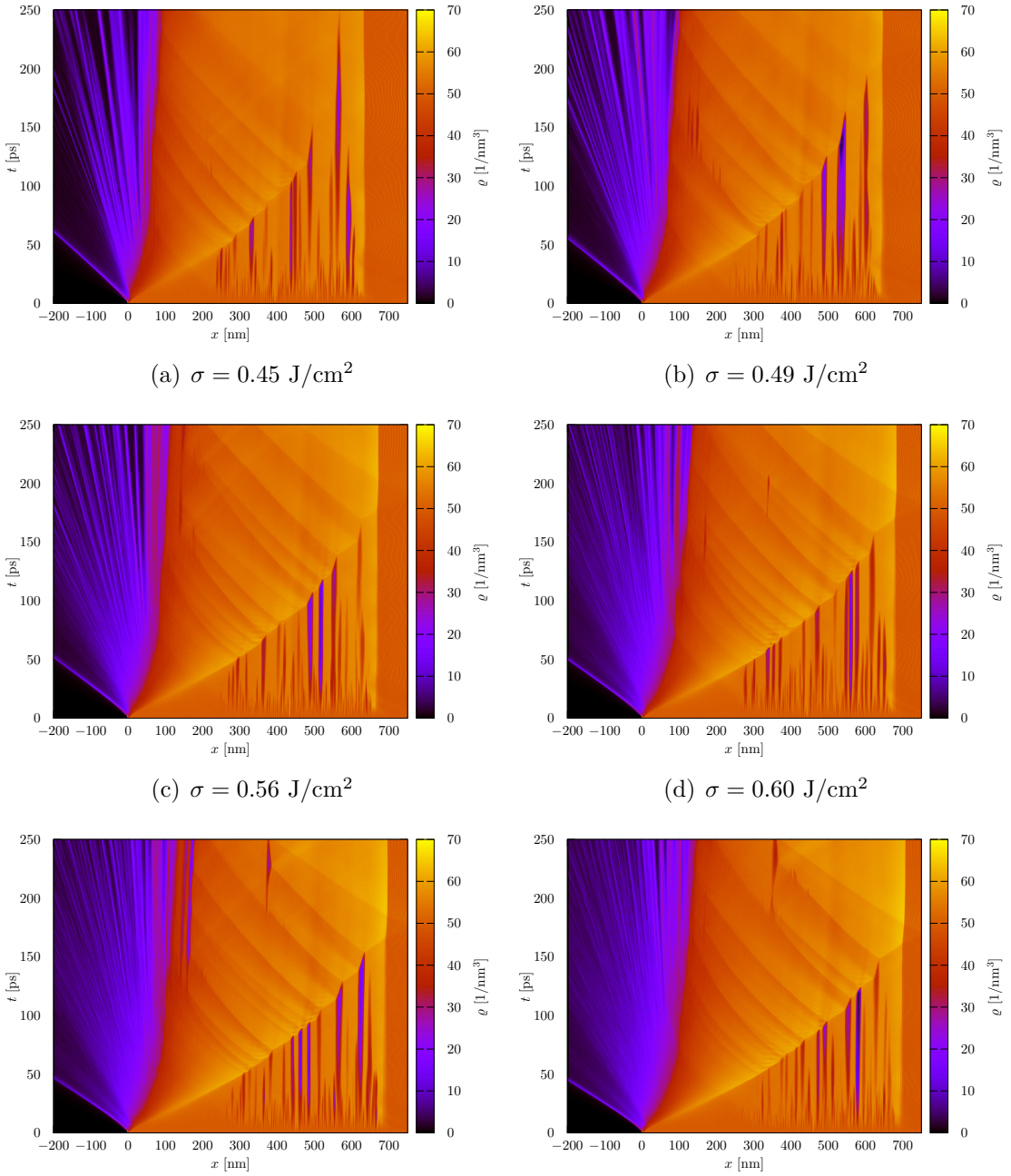

(a) $\sigma = 0.45$ J/cm^2 (b) $\sigma = 0.49$ J/cm^2

(c) $\sigma = 0.56$ J/cm^2 (d) $\sigma = 0.60$ J/cm^2

(e) $\sigma = 0.64$ J/cm^2 (f) $\sigma = 0.67$ J/cm^2

Figure 6.12: Time resolved density histograms along the laser axis of simulations under TSM+MOD*+D parametrization combination for varying laser fluences σ.

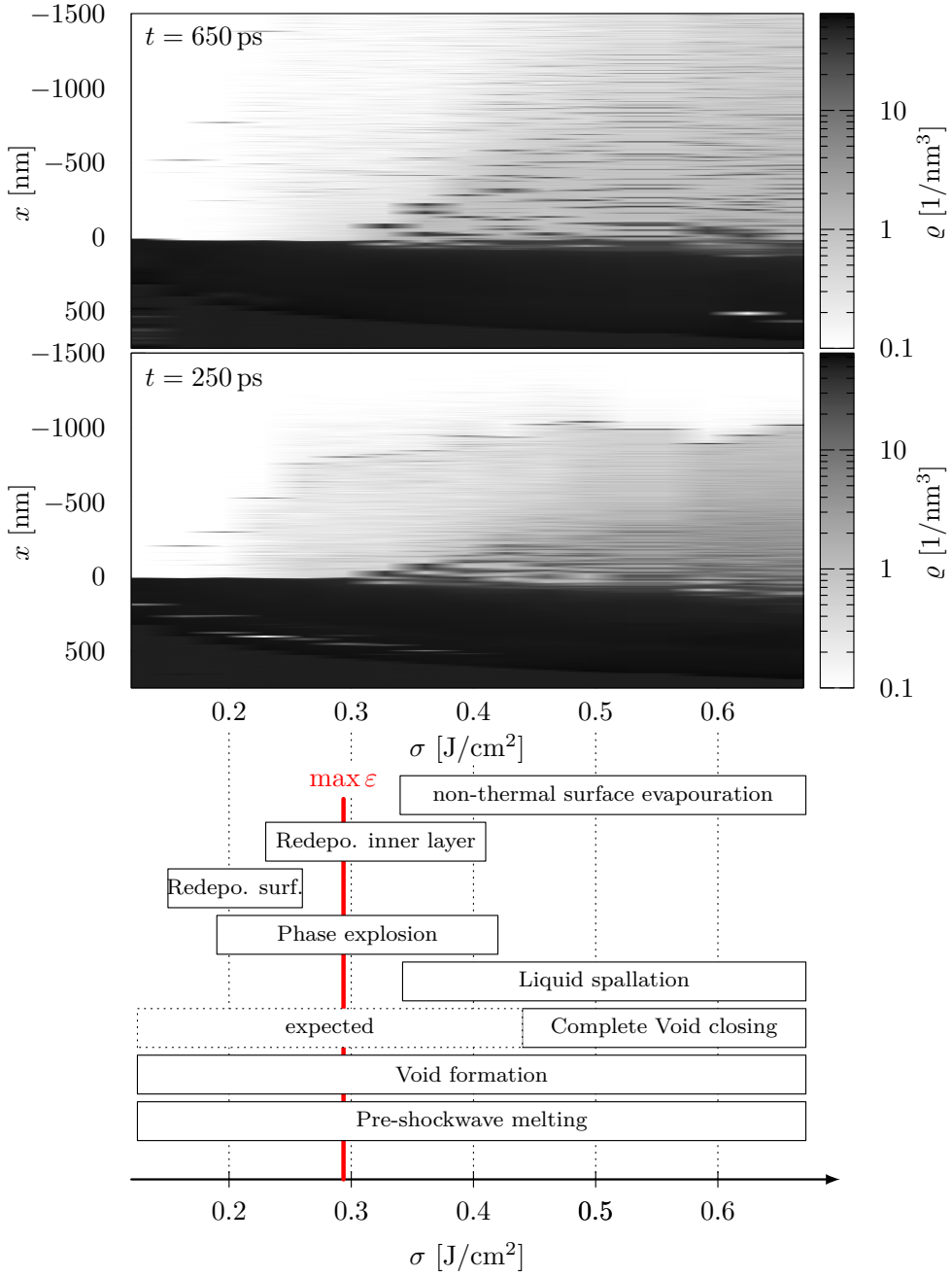

Figure 6.13: Fluence regimes of the occurring laser ablation mechanics assigned to time resolved density histograms. The assigned time resolved density histograms are snapshots at simulation times $t = 250\,\text{ps}$ and $t = 650\,\text{ps}$ respectively. A logarithmic colorbar is chosen to highlight the variation of density of the ejected material. $\max \varepsilon$ marks the peak material removal efficiency in terms of infused energy per material yield.

6.7 Cluster Distribution of the Ejected Material

Idea In the last section, we examined new ablation features of laser irradiated silicon in terms of their dependency on laser fluence. Obviously, varying ablation mechanics result in a varying composition of the ablated material. The composition of ablated material shows a huge impact on typical laser ablation applications, such as laser drilling or laser deposition. For example, in the case of laser drilling it is often observed that ablated material deposits back on the sample surface contaminating the surrounding surface with nano-droplets of varying sizes. In the case of laser deposition, the ablated material is wanted to be deposited on a substrate surface in a controlled way. Most often, a homogeneous surface coating with as little as possible crystal imperfections is desired. Here, the composition of the ablated material i.e. distribution of nano-droplet sizes directly determines the resulting coating roughness and the smallest possible coating layer thickness.

However, despite the demand for a closed theoretical description of plume composition, the highly non-linear dynamics of cluster formation, especially in excitation-dependent directionally bonded covalent materials, is far from being understood. To our knowledge, only few theoretical studies on the cluster distribution of laser irradiated metals exist [57, 254, 255]. Unfortunately, the main reason why this is the case, is a simple lack of experimental studies on this topic. Although, the evaluation of cluster distributions in the context of sputtering experiments on metals was of interest in the 90's [256–259], no relevant measurements in the context of covalent materials were carried out. Anyway, in the past numerous experimental studies were performed measuring time-of-flight signals of laser irradiated silicon and analyzed the monomer ion composition using mass spectrometry [260, 260–263]. Such signals typically show a distinct spectrum. Okano demonstrated that from this spectrum the cluster distribution can be obtained directly [264]. We look forward to the future existence of such data for the ultra-fast laser ablation of silicon, since feasibility seems evident.

Now we want to use the TSM+MOD*+D to examine the composition of the ablated material under variation of the laser fluence in terms of the resulting distribution of occurring nano-droplet sizes.

Simulation Setup We perform laser ablation simulations on bulk silicon sample `depth` under homogeneous laser irradiation within the TSM+MOD*+D framework. The laser parameters are set to a pulse duration of $\tau_\mathrm{p} = 100\,\mathrm{fs}$ and a wavelength of $\lambda = 800\,\mathrm{nm}$. Laser fluence is varied in $\sigma \in [0.032\,\mathrm{J/cm^2} : 0.627\,\mathrm{J/cm^2}]$. The simulations are repeated on the aluminium sample `depth_alu` applying the TTM with optical parameters according to [254].

Method We extend IMD by a recursive on the fly cluster analysis algorithm. The algorithm itself is presented in more detail section 3.5.1. In short, we assign each atom to a cluster. Each atom i is assigned to a cluster c if it interacts with at least one atom j of cluster c. In our context, interaction is defined as being within the potential cut-off radius r_cut such that

$$|\mathbf{r}_i - \mathbf{r}_j| \leq r_\mathrm{cut}(T_\mathrm{c}). \tag{6.12}$$

holds. For the MOD*, the parameter r_cut becomes a function of the local carrier temperature T_c and increases with excitation up to $r_\mathrm{cut}(2.14\,\mathrm{eV}) = 4.0\,\text{Å}$. The number of atoms, center of gravity and mean velocity of each cluster is calculated for each MD step.

Limitations When analyzing droplet distributions on this simulation series, we need to be aware of the limitations by spatial confinement in z- and y-direction within our quasi-1D simulation setup. Possible finite size effects occur due to the simulation box showing a cross section of $A = 21\,\mathrm{nm} \times 21\,\mathrm{nm}$. Under assumption of spherical droplets, the maximal reproducible cluster size is restricted to contain

$$N_\mathrm{max} = \frac{4\pi}{3}\varrho\left(\frac{\sqrt{A}}{2}\right)^3 \tag{6.13}$$

atoms. For a solid spherical chunk of silicon with a typical number density $\varrho^\mathrm{solid} = 35\,/\mathrm{nm^3}$ or a typical liquid droplet with number density of $\varrho^\mathrm{liquid} = 50\,/\mathrm{nm^3}$, the simulation is limited to reproduce maximum cluster sizes of

- $N_\mathrm{max}^\mathrm{solid} \approx 169\,716$ and

- $N_{\max}^{\text{liquid}} \approx 242\,452$.

These cluster sizes correspond to a layer, for example ablated by spallation effects, of $\Delta x^{\text{solid}} \approx 9.5$ nm and $\Delta x^{\text{liquid}} \approx 13.5$ nm thickness. The following analysis is therefore only valid for clusters up to $N_{\text{atoms}} = \mathcal{O}(10^5)$.

Results We introduce the so-called ablation yield per cluster size $Y(N_{\text{atoms}})$, which measures the amount of material within the ablation plume dependent on cluster size. Assuming we find $N_{\text{cluster}}(N_{\text{atoms}})$ clusters containing N_{atoms} atoms, we can write the ablation yield per cluster size as

$$Y(N_{\text{atoms}}) = N_{\text{cluster}}(N_{\text{atoms}}) \cdot N_{\text{atoms}}. \tag{6.14}$$

As said before, a rigorous theory of plume decomposition is missing, but a bimodal power-law of the form

$$Y^{\text{fit}}(N_{\text{atoms}}) \propto N_{\text{atoms}}^{\delta} \tag{6.15}$$

is observed in a variety of experiments for different materials. In all cases, one exponent δ_{lm} is found to describe the distribution for ablation yield consisting of small low-mass clusters and one exponent δ_{hm} describing the distribution of high-mass clusters. For example the bimodal power-law distribution of clusters is found in ion beam sputtering experiments [256–259]. Ion beam sputtering is the process of material being bombarded with high energy ions and leads to a vastly different ablation mechanism than laser ablation. Of course this makes the transfer of findings difficult. However, without deeper understanding, the bimodal power-law is believed to be a general phenomenon, as it is also observed in MD simulations of laser ablation of metals [57, 254], organic solids [255] and polymers [265] and is phenomenologically applied to characterize the ablated material.

In figure 6.14(a), we show the ablation yield per cluster size $Y(N_{\text{atoms}})$ obtained from our simulation data as a snapshot for silicon and aluminium at a selected fluence and simulation time. Additionally, we apply a fit function following the bimodal power-law for all considered laser fluences at selected simulation times $t \in \{50\,\text{ps}, 450\,\text{ps}, 650\,\text{ps}\}$ and display the resulting low- and high-mass exponents δ in

figure 6.14(b). For both materials, silicon an aluminium, we can confirm the ablation yield following the bimodal power-law. However, in literature, for all metals the low mass exponent is observed to be typically in the range of $\delta_{\mathrm{lm}} \in [-5 : -3.2]$ and the high-mass exponent in the range of $\delta_{\mathrm{hm}} \in [-1.4 : -0.9]$ [57]. More distinctively, it is empirically found that

$$|\delta_{\mathrm{lm}}| > |\delta_{\mathrm{hm}}| \tag{6.16}$$

holds and $|\delta_{\mathrm{lm}}|$ decreases while $|\delta_{\mathrm{hm}}|$ increases with fluence [57]. Our simulation data on aluminium reproduces this observation and suggests that the sample dimensions are suitable for the performed evaluation. Silicon on the other hand does not show this metallic behavior but instead

$$|\delta_{\mathrm{lm}}| < |\delta_{\mathrm{hm}}| \tag{6.17}$$

for all considered fluences. So compared to metals, silicon shows an overall broader yield distribution for small sized clusters and a sharp decline for clusters containing $N_{\mathrm{atoms}} > 10$ atoms. As a result, we observe that material removal is mainly driven by ejection of low-mass clusters for all laser fluences. We want to underline this in figure 6.15. In this figure, we show the number of ejected clusters N_{clusters} and ablation yield by cluster size $Y(N_{\mathrm{atoms}})$ by inciding laser fluence. The ablation yield contributes in ascending order of cluster size for all laser fluences. Here, we want to point out that the non-monotonic behavior of clusters of order $N_{\mathrm{atoms}} \geq \mathcal{O}(10^4)$ is most likely an artefact due to the spatial limitations of the quasi-1D-approach and has to be interpreted with caution. However, a monotonic increase in ablation yield is observed for all orders of all other cluster sizes with no significant feature under dominating ablation mechanics. An exception to this is the contribution of $N_{\mathrm{atoms}} = \mathcal{O}(10^3)$ clusters which form on the higher end of the phase explosion ablation regime as a result of the disintegrating surface layer. In contrast to $Y(N_{\mathrm{atoms}})$ as a function of laser fluence, the low- and high-mass exponents do show a significant dependency on the dominating ablation mechanism. In figure 6.14(b), we can clearly assign the regimes of previously introduced ablation mechanics but also observe a time-dependence of the yield exponents.

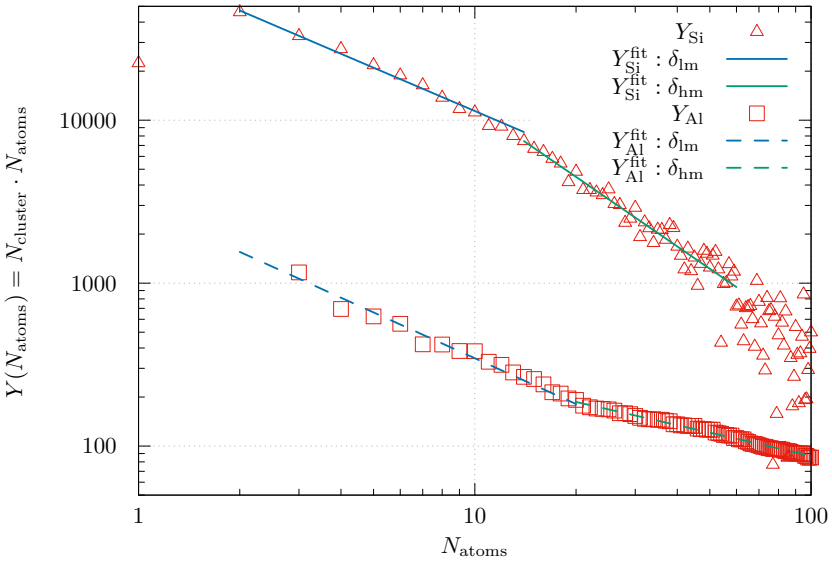

(a) ablation yield distribution

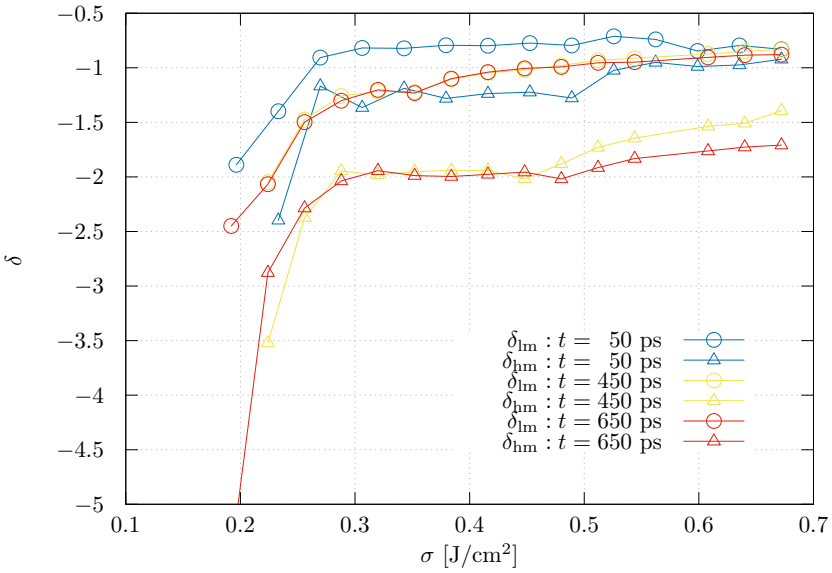

(b) yield exponents δ for Si

Figure 6.14: (a) Snapshot of the bimodal power-law fitted to the data set of Si and Al at $t = 450\,\mathrm{ps}$ for a laser fluence of $\sigma = 0.42\ \mathrm{J/cm^2}$. The ablation yield distribution is fitted with $Y(N_{\mathrm{atoms}}) \propto N_{\mathrm{atoms}}^{\delta}$. (b) The obtained yield exponents δ for silicon for selected fluences at simulation times $t \in \{50\,\mathrm{ps}, 450\,\mathrm{ps}, 650\,\mathrm{ps}\}$. The fitting intervals were chosen separately for a low and high mass regime, denoted with the indices lm and hm respectively.

For a more complete picture, we fit the low- and high-mass exponents to the ablation yield distribution for all considered laser fluences at each MD step. The resulting exponents are shown in figure 6.16 as a heat map and underline and supplement our classification of ablation mechanisms in figure 6.13 of the previous section. We observe that in case of the low-mass exponent δ_{lm}, the ablation regimes are clearly visible. In the fluence regime of

- redeposition of the surface layer, the low-mass clusters are formed under the surface layer by phase explosion and consequently adsorp onto the surface layer or sample surface, due to their difference in ejection speed compared to the surface layer. This is followed by the regime of

- phase explosion without redeposition of the surface layer. Here we observe the low-mass exponent to change from a broad distribution, meaning a small $|\delta_{\mathrm{lm}}|$, towards a distribution favouring monomers within a time frame of $\sim 250\,\mathrm{ps}$ and staying constant in the following. This can be explained with the expansion time of the plume during phase explosion. The main part of the ablated material is trapped in the confinement of the surface layer, driving the ejection and expanding into a dilute gas. With this observation the cluster distribution of the regime of

- non-thermal melting seems contradicting at first. We would expect that extreme irradiation leads to carrier excitation into the often mentioned purely repulsive states, thus a rapid decomposition into monomers. In case of the low-mass exponent, this would mean we expect $|\delta_{\mathrm{lm}}|$ to increase on the transition from phase explosion towards non-thermal surface evaporation. Yet, the opposite is the case. Above a laser fluence of $\sigma \approx 0.4\,\mathrm{J/cm^2}$, the low-mass exponent is favouring broader low-mass distributions, meaning it is more likely to find single atom clusters in the ejected material via phase explosion compared to the ejected material via non-thermal surface evaporation. This is due to the amount of the ablated material. In the case of phase explosion, the super heated material directly relaxes with a sudden burst into the vacuum. In the case of non-thermal surface evaporation, the material evaporates from the surface, with the evaporation surface propagating into the sample,

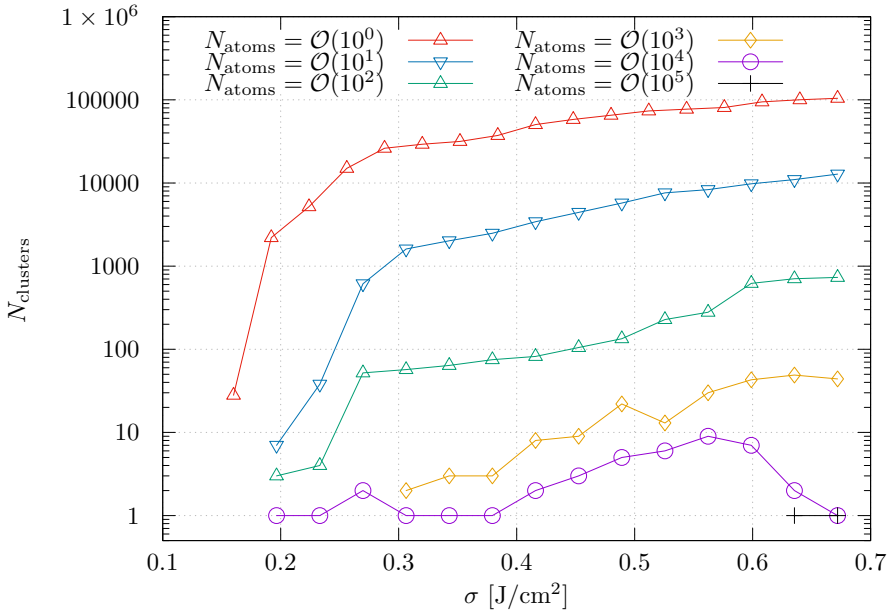

(a) number of clusters

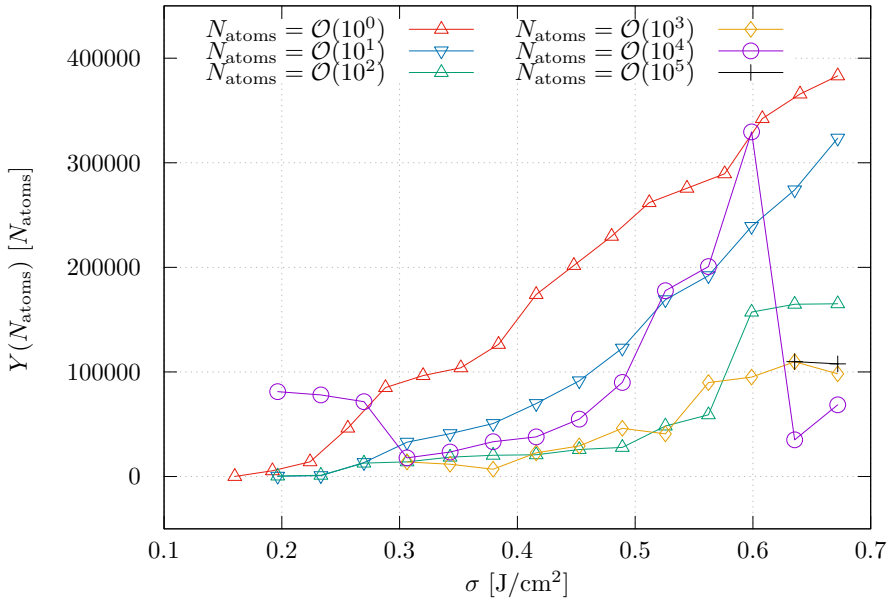

(b) counted ablation yield

Figure 6.15: Number of ejected clusters and ablation yield at $t = 450$ ps simulation time, structured into contribution by order of cluster size.

thus driving the ablated cloud. The result is a dense vapour in front of the sample relaxing on a longer timescale compared to material ejected by phase explosion.

The high-mass exponent, on the other side, does not show a comparable step-like cut between the dominating ablation regimes. However, within the phase explosion regime, we observe a fuzzy transition in δ_{hm} at constant $t \approx 250\,\mathrm{ps}$. This is due to the burst of the skin layer during phase explosion. Here, high-mass clusters are formed from the debris of the surface layer and droplets ejected from the melt. For higher fluences, this effect is gradually suppressed by non-thermal evaporation as both the surface layer itself and the ejected droplets continue vaporising during ejection.

Excursion on Fluence Invariant Characteristics In addition to the presented ablation mechanisms, the material dynamics of laser irradiated silicon also shows features independent of laser fluence. In figure 6.17, we show the temporal dynamics of the number of ejected clusters and the time evolution of the non-thermal voids after laser irradiation with a fluence of $\sigma = 0.64\,\mathrm{J/cm^2}$. Of course, the absolute values of the number of ejected clusters in figure 6.17(a) vary with laser fluence. However, the qualitative dynamics shows to be invariant under laser fluence, in the way that $N_{\mathrm{atoms}} = \mathcal{O}(10^0)$ clusters become the most occurring cluster size for $t \gtrsim 200\,\mathrm{ps}$ as bigger clusters desorb into monomers. For all fluences, we observe a peak in $N_{\mathrm{clusters}}(t)$ for $N_{\mathrm{atoms}} = \mathcal{O}(10^n)$ clusters followed by a peak for $N_{\mathrm{atoms}} = \mathcal{O}(10^{n-1})$ clusters. More interestingly, figure 6.17(b) shows the tie evolution of the non-thermal voids. Here, we observe the direct formation of voids of volume $V \in [1\,\mathrm{nm^3} : 100\,\mathrm{nm^3}]$ due to non-thermal melting within the area of pre-shockwave melting. The formed voids decay into subsequent larger voids until they are closed by the following shockwave and contracting melt. The observed times of void generation, void decay and void closing appear to be universal among the studied laser fluences. The total volume V_{tot} of voids scales linearly with the depth x_{melt} of pre-shockwave melting.

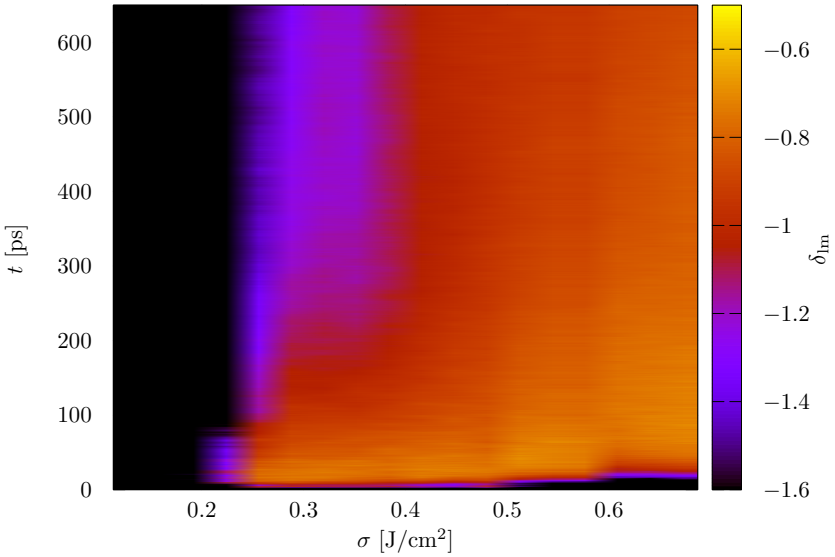

(a) low-mass exponent δ_{lm}

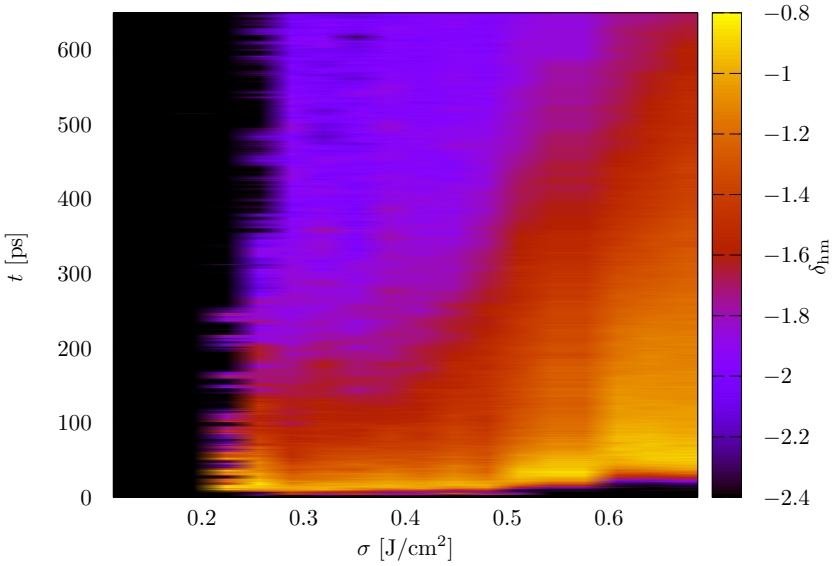

(b) high-mass exponent δ_{hm}

Figure 6.16: Low- and high-mass exponents following $Y^{\mathrm{fit}}(N_{\mathrm{atoms}}) \propto N_{\mathrm{atoms}}^{\delta}$ for all observed laser fluences σ at each simulation time step. Black areas represent non-convergent fits resulting from an insufficient number of clusters within the plume.

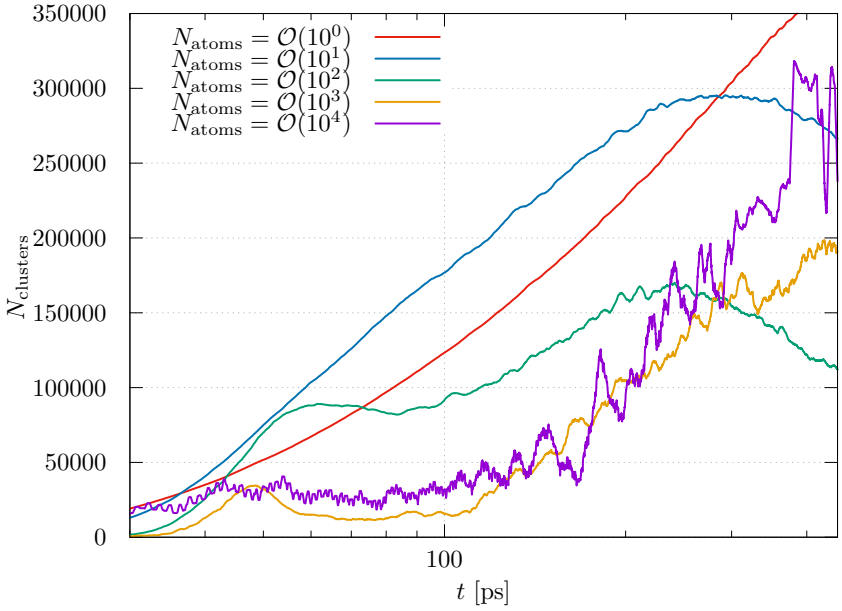

(a) number of ejected clusters

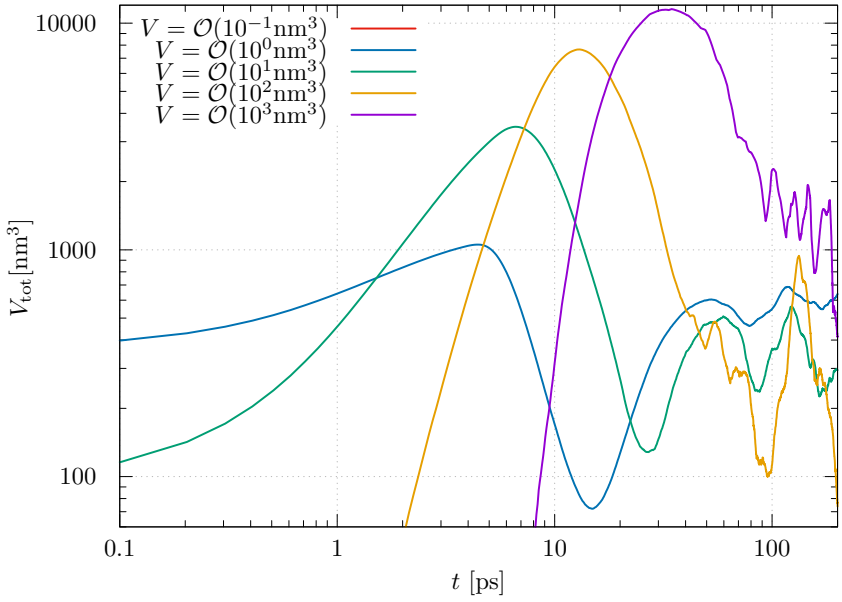

(b) non-thermal void volume

Figure 6.17: Time evolution of the total number of clusters N_{clusters} by order of contributing atoms N_{atoms} and total volume of non-thermal voids V_{tot} by order of contributing void volumes V at an inciding laser fluence of $\sigma = 0.64\,\text{J/cm}^2$.

Conclusion We implemented and performed a cluster analysis algorithm on the ejected material of numerous laser ablation simulations on aluminium and silicon. Our data showed that the ablation process of laser irradiated silicon shows the seemingly universal bimodal power-law of ablation yield. However, silicon clusters are observed to be distributed with $|\delta_{\mathrm{lm}}| > |\delta_{\mathrm{hm}}|$ instead of $|\delta_{\mathrm{lm}}| < |\delta_{\mathrm{hm}}|$. The latter is reported behavior for metals, organic solids and polymers. A comparison to laser ablation simulations on aluminium under comparable conditions suggests that this is not a finite size effect of our quasi-1D geometry, but an intrinsic behavior of silicon. This behavior is not restricted to the regime of non-thermal surface evaporation but a feature for all laser fluences. This is an important observation since we also observe that the total ablated material is mainly composed of monomers for all fluences.

7 Simulations and Results - The Ablation Crater

7.1 Setting the State of the Art of Massive Multi-Parallel High Performance Molecular Dynamic Simulations

Idea Up to now, we restricted our simulation to a quasi-1D geometry. This means, we assumed a homogeneous radial intensity distribution $I_0^r(r) \stackrel{!}{=} 1$ in the spatial and temporal laser pulse profile

$$I_0(t,r) = (1-R)\sigma \cdot \underbrace{\sqrt{\frac{4\ln 2}{\pi t_p^2}} \exp\left(-4\ln 2 \frac{(t-t_0)^2}{t_p^2}\right)}_{\equiv I_0^t(t)} \cdot \underbrace{\frac{4\ln 2}{\pi b^2} \exp\left(-4\ln 2 \frac{r^2}{b^2}\right)}_{\equiv I_0^r(r)} \quad (7.1)$$

and therefore implicitly suppressed all lateral transport processes. In this chapter, we expand the laser description to a spatially Gaussian pulse and investigate the resulting implications of a spatially Gaussian laser profile on the ablation mechanics.

Computational Limitations Now we expand the size of our simulation to realistic lateral sample sizes and include inhomogeneous excitation due to the radial inhomogeneity of a spatially Gaussian laser spot. We assume a perfect beam quality factor $M^2 = 1$, thus laser spot size is essentially limited by the diffraction limit. For our inciting laser wavelength of $\lambda = 800\,\mathrm{nm}$, we assume a focal diameter of $b = 500\,\mathrm{nm}$ at FWHM corresponding to $b_{1/e^2} \approx 850\,\mathrm{nm}$ at full $1/e^2$-width. Consequently, this geometry requires a sample diameter on the micrometer scale. An MD sample of

a $1.0\,\mu\text{m} \times 1.0\,\mu\text{m} \times 1.0\,\mu\text{m}$ block of silicon would contain roughly $5 \cdot 10^{13}$ atoms. Unfortunately, an MD simulation of this size is not feasible with today's technology. We therefore use the rotational isotropy of an Gaussian laser profile and perform quasi-2D simulations on a thin silicon plate within the TSM+MOD*+D framework. The studied sample `plate` shows a size of $0.556\,\mu\text{m} \times 0.032\,\mu\text{m} \times 1.113\,\mu\text{m}$ and contains $5.3 \cdot 10^8$ atoms. The achieved crater size is therefore in the size of experimental lengthscales and shows a lateral extension of over a micrometer. However, such a simulation requires exceptional resources. On the supercomputer Hawk of the High Performance Computing Center Stuttgart we achieve a simulation time of roughly $t = 210\,\text{ps}$ per simulation run with a walltime of 24 hours on 131 072 cores. To put this amount of computational cost into perspective, the stated simulation equals 18.9% of the full capacity of the supercomputer[†]. On the one hand, this can be seen as the absolute limitation of today's MD based laser ablation simulations. But on the other hand, the previously presented tweaks and model optimizations allow for this kind of simulation in the first place. To our knowledge, a laser ablation simulation of this size was not achieved by other research groups to this date. The simulations presented in this chapter are the new state of the art.

7.2 Ablation Mechanics in 2D

Idea In this section, we compare the classification of ablation regimes from the quasi-1D simulations of section 6.6 to the quasi-2D setup under identical parametrization.

Results In figure 7.1 and 7.2, we show the resulting snapshots of the spatial density distribution at $t = 100\,\text{ps}$ simulation time after peak laser intensity for varying laser fluences σ. Here, the observed material dynamics in a quasi-2D geometry strongly underline our previous classification of ablation regimes. Walking through the array of presented fluences, we find

[†]The used Supercomputer Hawk of the High Performance Computing Center Stuttgart consists of a HPE Apollo 9000, AMD EPYC 7742 64C 2.25GHz, Mellanox HDR Infiniband. Hawk achieves a peak 25.16 PFlop/s on total of 698 880 cores and is listed in November 2020 at rank 16 of the 500 most powerful computer systems assembled and released worldwide.

- pre-shockwave melting occurs in all laser fluences with the previously investigated pre-shockwave melting depth x_{melt}. When we consider the 1D pre-shockwave melting depth $x_{\mathrm{melt}}(\sigma_{\mathrm{1D}})$ as a function of fluence σ_{1D}, the resulting amorphous crater intuitively shows the melting profile resulting from the mapping $\sigma_{\mathrm{1D}}(r) = \sigma I_0^r(r)$.

- Phase explosion occurs in the fluence regime $\sigma > 0.35\,\mathrm{J/cm^2}$ before its effect is surpassed by non-thermal surface evaporation. 2D simulations vividly show the sudden sub-surface evaporation of the super-heated fluid and the resulting bent open surface layer counteracting the expansion. For higher fluences, the skin layer can be observed to disintegrate not only by expansion but also by boiling and thereby releasing massive droplets.

- The phase explosion pressure itself seems to show an impact on the resulting surface morphology of the inner crater. This, however, cannot be finally confirmed by our simulations since the shown simulations do not cover the complete ablation duration.

- The transition from a phase explosion dominated ablation mechanism towards a non-thermal surface evaporation dominated mechanism, as well as the consequent cluster distribution shift in favour of small clusters, can directly be observed in the ejected material of the inner crater for fluences $\sigma > 0.45\,\mathrm{J/cm^2}$.

- For fluences in the non-thermal evaporation regime, the local power density $I_0(t,r)$ surpasses the threshold for non-thermal surface evaporation in the center of the sample. However, due to the Gaussian nature of the laser spot, outer areas still meet the criteria for ablation dominated by phase explosion or non-thermal melting. The material dynamics on the edge of the inner crater remains driven by phase explosion. As a result, all craters for fluences above the phase explosion threshold show remains of the skin layer ejection dynamic, thus forming the characteristic ablation crown.

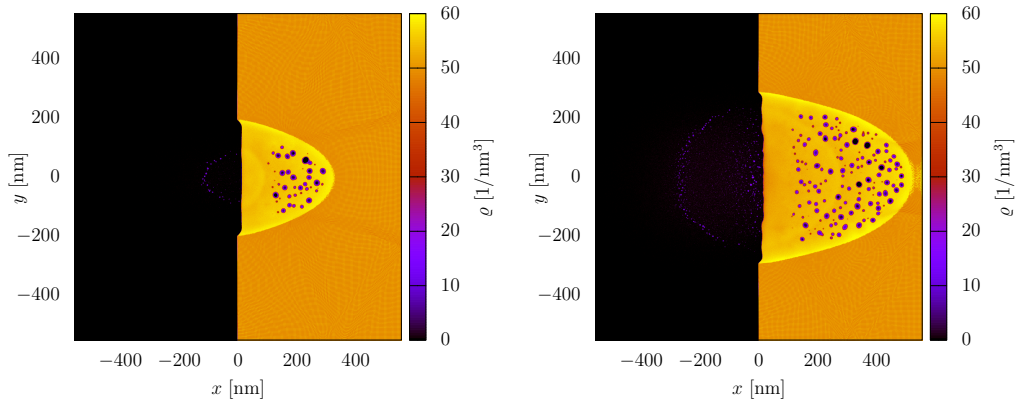

(a) $\sigma = 0.16$ J/cm^2

(b) $\sigma = 0.26$ J/cm^2

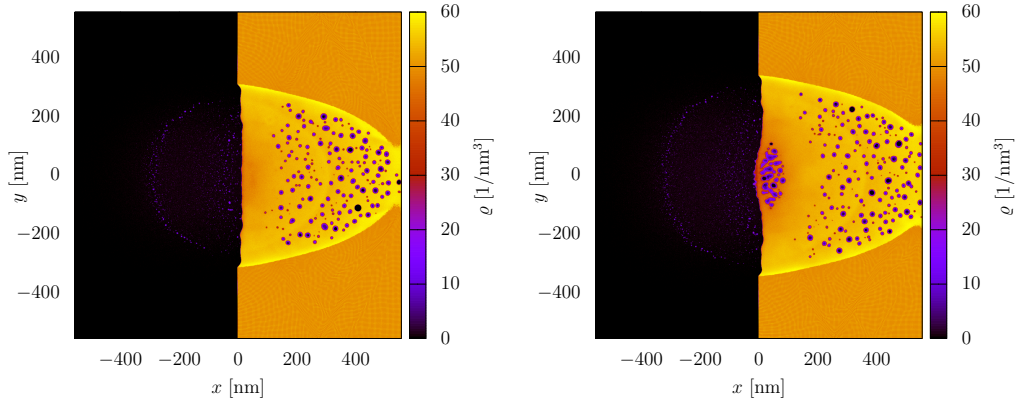

(c) $\sigma = 0.29$ J/cm^2

(d) $\sigma = 0.35$ J/cm^2

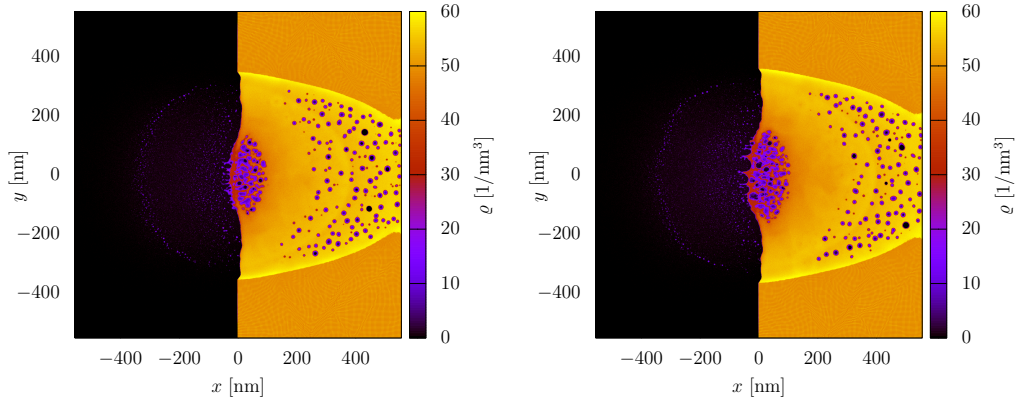

(e) $\sigma = 0.38$ J/cm^2

(f) $\sigma = 0.42$ J/cm^2

Figure 7.1: Snapshots of the spatial density histograms at a simulation time of $t = 100$ ps after peak laser intensity under TSM+MOD*+D parametrization combination for varying laser fluences σ.

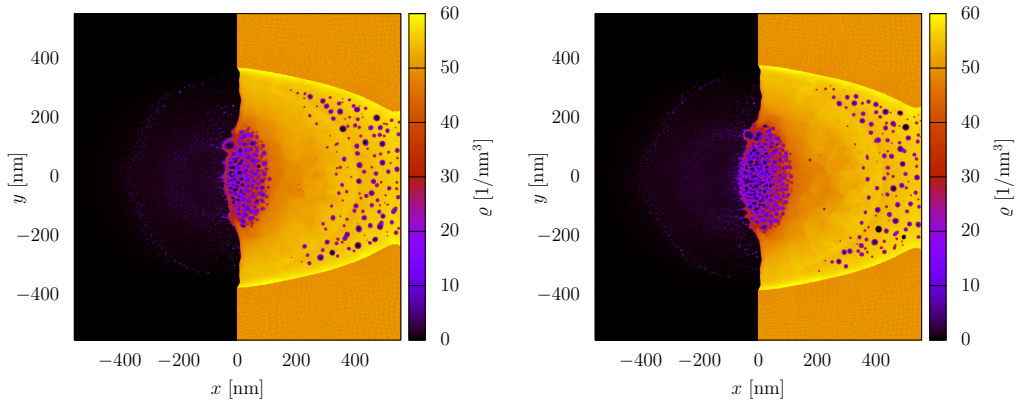

(a) $\sigma = 0.45$ J/cm^2 (b) $\sigma = 0.48$ J/cm^2

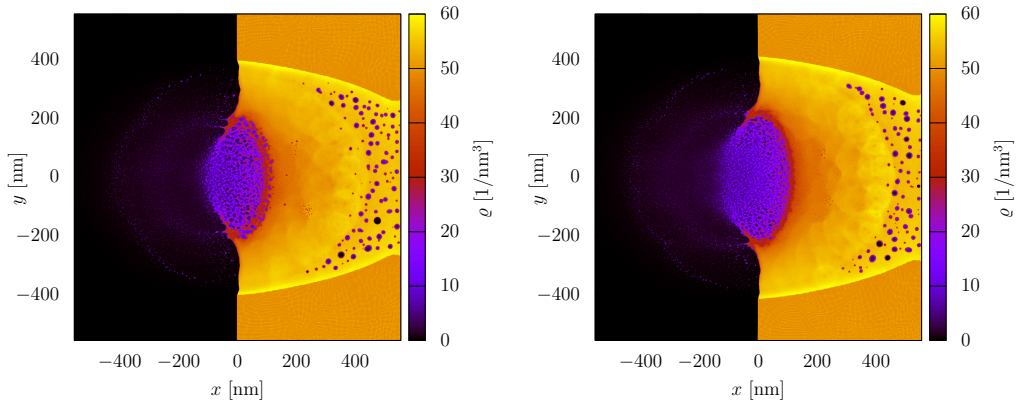

(c) $\sigma = 0.54$ J/cm^2 (d) $\sigma = 0.61$ J/cm^2

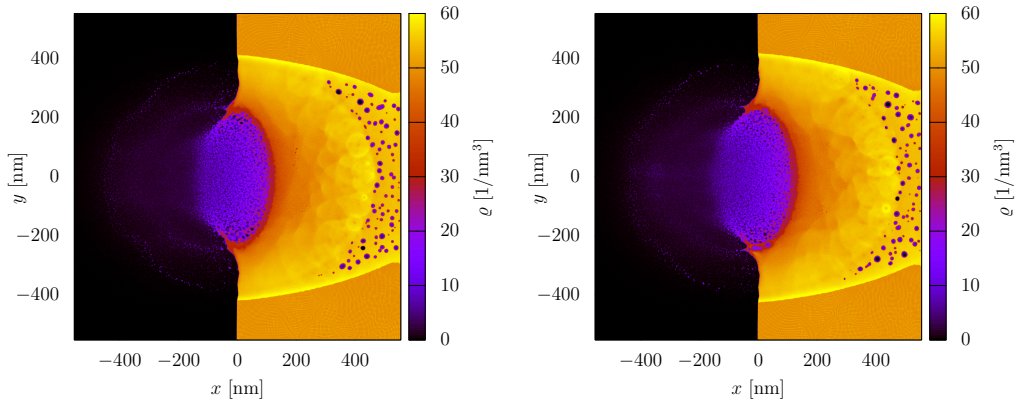

(e) $\sigma = 0.64$ J/cm^2 (f) $\sigma = 0.67$ J/cm^2

Figure 7.2: Snapshots of the spatial density histograms at a simulation time of $t = 100$ ps after peak laser intensity under TSM+MOD*+D parametrization combination for varying laser fluences σ.

Simulation Artifacts It is evident that occurring simulation artifacts have to be addressed and distinguished from physical predictions. In the presented simulations, we can observe minor simulation artifacts which all arise from spatial confinement. We classify them as originating from depth, lateral and 2D confinement.

Depth confinement refers to confinement in x-direction, in our case specifically, by sample truncation at a depth of $x = 550\,\mathrm{nm}$, resulting in an artificial surface at the back of the sample. In many cases, the pre-shockwave melting depth reaches this artificial surface and destabilises crystal structures in the remaining thin crystalline film at the back of the sample. As a result, the non-Gaussian shape of the melting pool on the backside of the sample has to be viewed as a simulation artifact. Moreover, in contrast to the shockwave emitted at the sample surface, the sudden contraction of the melting pool emits a dilution wave. Both propagate through the sample and will be reflected at the back of the sample. These reflected shockwaves reach the crater surface at simulation times $t > 250\,\mathrm{ps}$ and artificially induce spallation and change surface morphology by shaking of droplets.

Analogously, the lateral confinement in y-direction leads to a comparable reflection of shock and dilution waves. However, these pressure waves seem to have only a minor effect on the simulation outcome.

2D confinement originates from the lack of extension in z-direction. This leads to an underestimated surface tension of voids and the skin layer. Analogously to the 1D simulation setup, 2D confinement restricts the maximum observable droplet size.

7.3 The Non-thermal Melting Rim

Idea In section 7.2, we observed the novel ablation mechanics in quasi-2D laser ablation simulations and found that the occurring ablation regimes can be spatially mapped by $\sigma_{1D}(r) = \sigma I_0^r(r)$. Therefore, the concentric crater profile sketched in figure 7.3 follows directly from the demand of a local threshold fluence σ_i^{th} meeting the threshold for ablation mechanism i to dominate the ablation process. In this section, we will discuss this claim and compare it to experimental data.

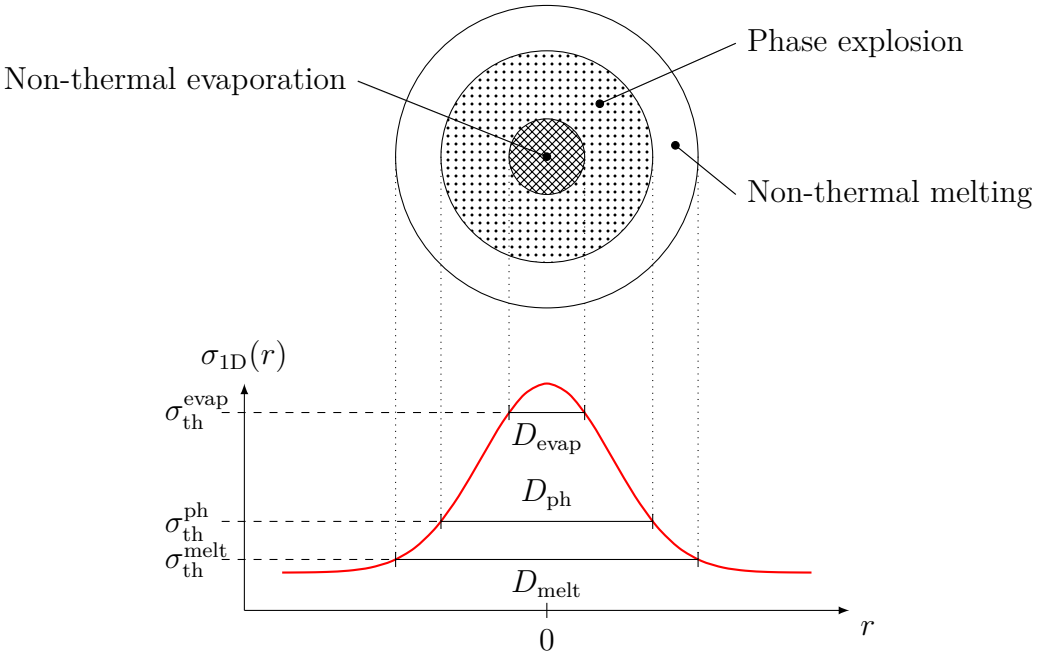

Figure 7.3: Ablation crater profile and corresponding ablation regimes and threshold fluences σ_{th}^i for a Gaussian laser spot. D_i denotes the diameter of the area with dominating ablation mechanism i.

Results As mentioned earlier, comparable experimental data is very sparse due to the wide range of parameters influencing the ablation process. In the case of single shot ablation crater profiles, this worsens as the most commonly applied crater measurement method is atomic force microscopy (AFM). AFM does provide accurate information about crater depth on the micrometer scale but fails to provide information about the crystal structure. As a result, AFM does not recognize the amor-

phous structure generated by non-thermal melting. In figure 7.4, we show recently published single-shot ablation profiles of silicon obtained by different experimental setups. However, both experiments use a spatially Gaussian beam profile. Figure 7.4(a) shows an ex-situ measurement by Bonse [97] after silicon was irradiated with a laser pulse of wavelength $\lambda = 800\,\mathrm{nm}$, a pulse duration of $\tau = 130\,\mathrm{fs}$ and a fluence of $\sigma = 1.5\,\mathrm{J/cm^2}$. The diameter of the outer rim is given to be $D = 45\,\mu\mathrm{m}$. Figure 7.4(b) shows a measurement by Werner [76]. Here, the laser parameters are only given vaguely. Laser wavelength was adjusted to be in the mid-infrared range, namely $\lambda = 2700 - 4200\,\mathrm{nm}$. Pulse duration was given to be $\tau_{\mathrm{FWHM}} = 200\,\mathrm{fs}$ while the fluence was varied between $\sigma = 0.25\,\mathrm{J/cm^2}$ and $2.0\,\mathrm{J/cm^2}$ at a constant focal width of $b_{\mathrm{FWHM}} = 25\,\mu\mathrm{m}$. Although being very different in their respective experimental setup, both authors report the observation of various concentric modification regions.

Bonse reported the ablation modifications to be a centered ablation spot surrounded by a second region dominated by nucleated vaporization and melting followed by recrystallization. The third and outermost structure is reported to be a ring of amorphous structure. Werner on the other hand, classified the ablation spot into four regions, with region 1 being the undamaged silicon. Region 4 corresponds to the ablation crater while region 2 and 3 correspond to an outer rim of amorphous silicon. In contrast to region 2, region 3 shows sub-surface recrystallisation.

On first sight, both experiments cannot be compared directly to each other or to our simulations, since Bonse irradiated a comparatively huge laser spot size and Werner applied a laser wavelength in the mid-infrared range. However, increasing the laser spot size results in a lower local peak fluence with decreased temperature gradients compared to a highly focused laser spot. Vanishing temperature gradients lead to a less sharply defined edge of the ablation spot and a generally less pronounced ablation crown. With this in mind, we propose that the underlying mechanism of the center and middle region in figure 7.4(a) are in fact a non-thermal evaporation spot in the center surrounded by a region of phase explosion. The phase explosion is less pronounced and spread over a huge area. Unfortunately, a more detailed analysis of the crater is missing, since Bonse focused on the morphology induced by multiple laser pulses. The ablation crater measured by Werner on the

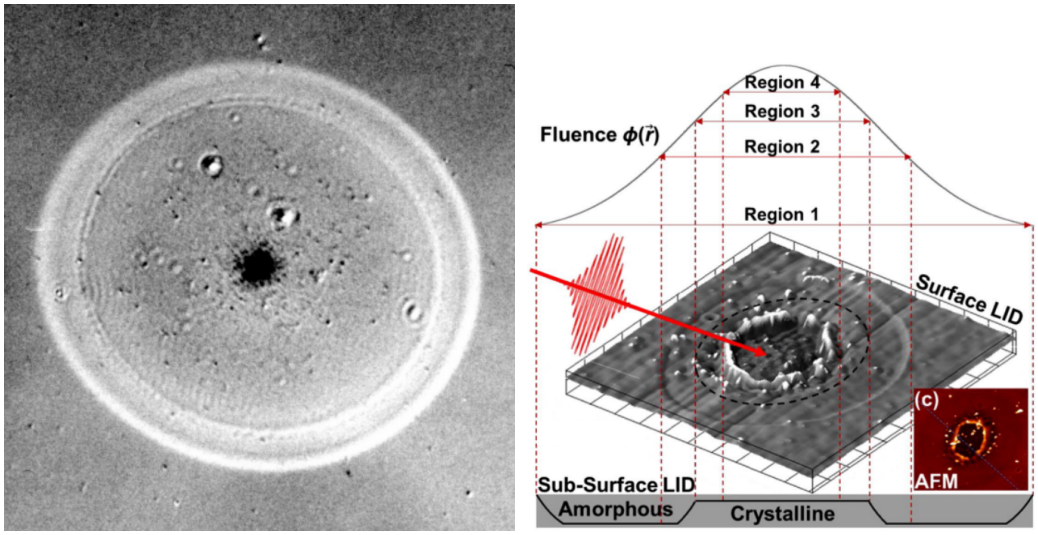

(a) Bonse (b) Werner

Figure 7.4: Ex-situ measurements of single-shot laser ablation of silicon. (a) was measured by Bonse[†][97] and (b) was measured by Werner[‡][76].

other hand shows great qualitative similarities with our simulation data. The inciting laser wavelength of $\lambda = 2700 - 4200\,\mathrm{nm}$ enhances the importance of TPA compared to our considered wavelength of $\lambda = 800\,\mathrm{nm}$. However, recombination processes and the following carrier-lattice equilibration processes remain identical.

Besides the differences, the great similarity between all experiments and simulations presents itself in the formation of an outer rim of amorphous silicon. Werner and Bonse both argue that the formation of amorphous rim is a result of the cooling front exceeding the recrystallisation speed of amorphous in silicon. This explanation goes back to the work of Yen [266] from 1981, where he explained the formation of an amorphous rim extensively by classical thermodynamics. The proposed assumptions hold for the considered scenario of a molten pool of silicon induced by a nanosecond laser pulse but cannot be transferred to ultra-short laser ablation. We want to emphasize that to our belief, the formation of the outmost amorphous rim is a direct result of non-thermal melting induced by a local laser fluence $\sigma_{1\mathrm{D}}(r)$ being below the ablation threshold. Considering that non-thermal melting induces the amorphous

[†]Licensed by Springer Nature and Copyright Clearance Center (License Nr. 5387150855254)
[‡]Licensed under CC-BY-4.0

rim, the argumentation of the cooling front exceeding the recrystallisation speed amorphous silicon remains correct but distracts from the fact that the amorphous structure is already in a cold state and a result of the non-thermal melting process.

7.4 Scaling of the Non-Thermal Melting Rim

Idea The assumption that the non-thermal melting rim is a direct result of the local fluence being $\sigma^{\mathrm{th}}_{\mathrm{melt}} < \sigma_{1\mathrm{D}}(r) < \sigma^{\mathrm{th}}_{\mathrm{ph}}$ raises the condition that rim formation occurs in areas where the corresponding intensity threshold is met. Therefore, the size of the structure scales as

$$I^{i}_{\mathrm{th}} \stackrel{!}{=} I_0(D_i/2) \qquad \Rightarrow \qquad D_i = \sqrt{\ln\left(\frac{\sigma}{\sigma^{\mathrm{i}}_{\mathrm{th}}}\right)} \cdot b. \tag{7.2}$$

In this section, we confirm this claim by investigation of the scaling behavior in our simulation and experimental data.

Results In figure 7.5, we present the scaling behavior of the diameter of the non-thermal melting rim D_{nth} and phase explosion crater D_{ph} obtained from the simulation data presented in section 7.2. The diameters D_i are fitted with the assumed scaling behavior (7.2) using b and the threshold fluence $\sigma^{\mathrm{i}}_{\mathrm{th}}$ as free parameters. Additionally, we show experimental data obtained by Zhang [96] in automated AFM scans of silicon, irradiated by a Gaussian laser pulse with a wavelength of $\lambda = 800\,\mathrm{nm}$ and a pulse duration of $\tau_{\mathrm{FWHM}} = 100\,\mathrm{fs}$. Here, the laser spot was focused to a spatial FWHM of $b_{\mathrm{FWHM}} \approx 710\,\mathrm{nm}$. For better comparison, we choose to give the obtained diameters D_i in units of b as the scaling law (7.2) suggests linear scaling in b anyway.

Two major points can be extracted from this. First, the proposed scaling law for the non-thermal melting rim D_{nth} and the phase explosion crater diameter D_{ph} match the trend of the simulation data reasonably well and yield a non-thermal melting threshold of $\sigma^{\mathrm{th}}_{\mathrm{ntm}} = 0.108\,\mathrm{J/cm^2}$ and a phase explosion threshold of $\sigma^{\mathrm{th}}_{\mathrm{ph}} = 0.304\,\mathrm{J/cm^2}$. The obtained thresholds are in accordance with our quasi-1D simulations, thus strongly implying that lateral energy transport plays no significant role within the ablation process.

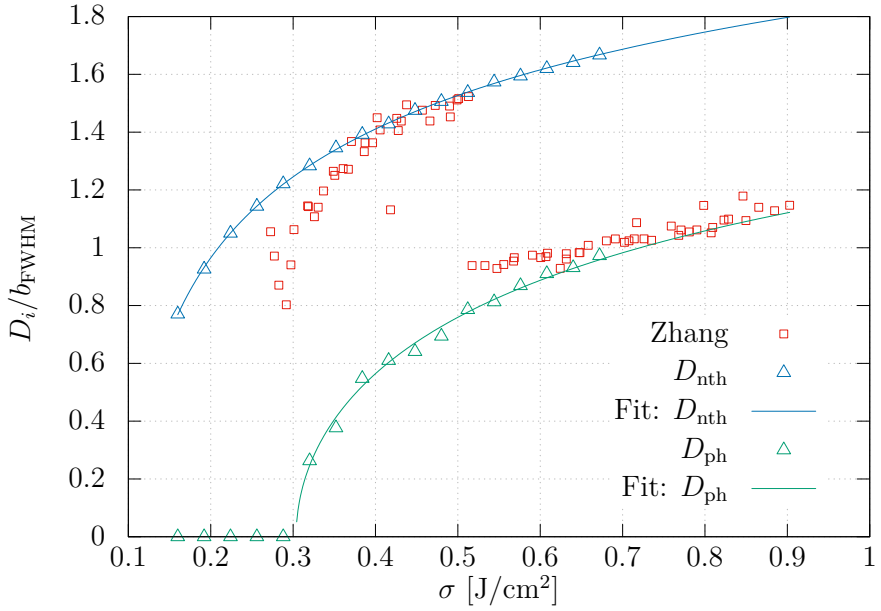

Figure 7.5: Scaling behavior of the diameter of the non-thermal melting rim D_{nth} and phase explosion crater D_{ph} compared to experimental measurements by Zhang [96]. The diameters are given in units of the FWHM focal diameter b_{FWHM}.

Second, the TSM+MOD*+D receives further validation as the presented experimental data matches the simulation outcome. Admittedly, this is not easy to see at first sight as the experimental data shows a discontinuity while matching D_{nth} for small fluences and D_{ph} for higher fluences. This discontinuity is often observed and considered to divide the ablation mechanics into the categories of "soft ablation regime" and "hard ablation regime". In the "soft ablation regime", an amorphous spot is left on the sample surface, while in the "hard ablation regime", a distinct crater, an ablation crown and strong soiling of the sample surface by redeposited droplets is observed. Revisiting figure 7.1 and 7.2 of section 7.2, we find that this observation matches well with our findings. However, if the non-thermal melting rim is not distinguished from the phase explosion region, the complete area of modification is measured until the automated AFM setup locks on the distinct crater generated by phase explosion, hence generating a discontinuity in crater width when switching from primarily measuring D_{nth} to measuring D_{ph}. Analogously, this suggests that the dip in the experimental data is a result of locking into the narrow but deep feature of the less pronounced phase explosion occurring at $\sigma \approx 0.29\,\mathrm{J/cm^2}$.

The classification of ablation into “soft” and “hard” regimes technically still holds as an observation of discontinuity in experimental data but lacks the information that the categorization into non-thermal melting and phase explosion yields.

7.5 Composition of Quasi-1D Simulations Compared to Quasi-2D

Idea The results of the last section strongly suggest that lateral energy transport effects show no significant effect on the crater profile. Therefore, the crater profile becomes a function of the spatial parameters of the pulse shape. If this is correct, a composition of quasi-1D simulations, suppressing lateral effects, should yield identical results as the quasi-2D approach. In this section, we perform such a composition and compare the outcome to our quasi-2D simulations.

Method We explicitly compare the quasi-1D simulations of section 6.6 to the quasi-2D data of section 7.2. For this, we construct an array of identical size as the quasi-2D density histograms. For each pixel $p(x,y)$, we calculate the depth x and radius $r = |y|$ and assign the pixel to the material density obtained from a quasi-1D simulation of fluence $\sigma_{1\mathrm{D}}(r) = \sigma I_0^r(r)$ at position x and identical simulation time t.

Results The so composed quasi-1D and associated quasi-2D density histograms are shown in figure 7.6 for a non-thermal evaporation dominated fluence and again in figure 7.7 for a phase explosion dominated fluence, both at a simulation time of $t = 100\,\mathrm{ps}$. The accuracy of this approach has often been proposed and argued, but not proven since quasi-2D simulations were not feasible in the past. We observe that the composed simulations yield identical results in terms of crater and non-thermal rim diameters, as well as ablation depth. These properties are therefore independent of lateral energy transport. The dominating ablation mechanism of silicon at radius r is only dependent on the local fluence $\sigma_{1\mathrm{D}}(r)$. In direct comparison, the composition of quasi-1D simulations works unexpectedly well in depicting the material dynamic, especially at the ablation crown. Here, the residuals of the skin layer form a lobe that is driven by the sub-surface pressure induced by the phase

explosion region. However, this area especially shows the limitations of the quasi-1D composition. Although lateral energy transport seems to be neglectable, lateral material dynamic is not. For simulation times $t > 100\,\mathrm{ps}$, the lobe will be held back by surface tension and fold outward, elongate and eventually eject big droplets. This cannot be depicted in the composed simulation and the lobe will continue to be ejected parallel to the laser axis. Obviously, this holds for all ejected clusters and the ejection angle distribution is distorted in composed quasi-1D simulations. Next, lateral material dynamics features are lateral shockwaves closing non-thermal voids in areas of $\sigma_{1\mathrm{D}}(r) < \sigma_{\mathrm{th}}^{\mathrm{ph}}$. The shockwaves emitted by the closing of non-thermal voids decay faster in the quasi-2D case, as energy is distributed over a broader and increasing area. The decrease in shockwave intensity further reduces the effect of liquid spallation and therefore alters the resulting surface morphology.

As a result, quasi-2D or higher dimensional simulations are needed to depict effects involving surface tension, such as nano-bump formation or redeposition of larger clusters slung back by the ablation crown. However, for fluences above the non-thermal evaporation threshold, where surface tension becomes neglectable as the major contribution of ejected material is ejected within D_{evap}, quasi-1D compositions yield comparable results to the quasi-2D setup when only the ejected material and macroscopic crater features are of interest.

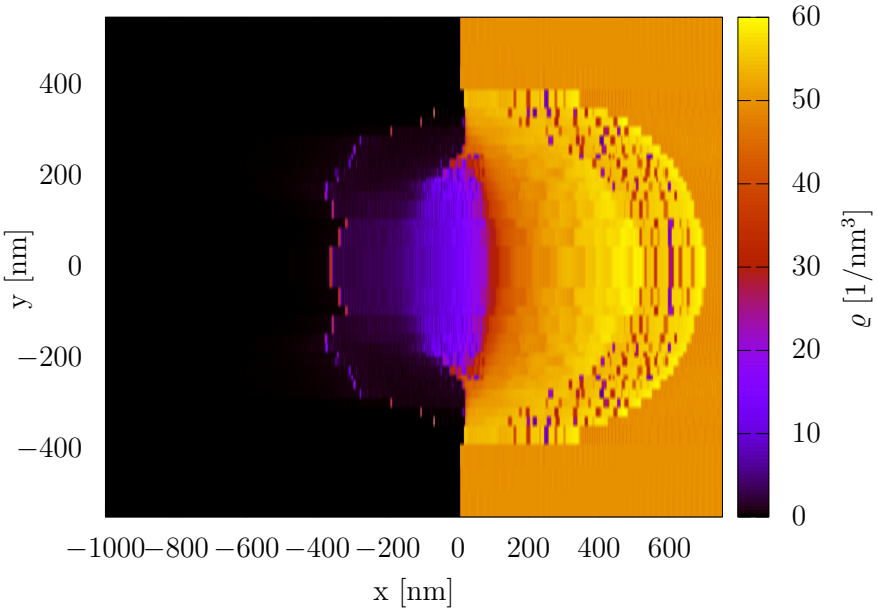

(a) Composed Simulation

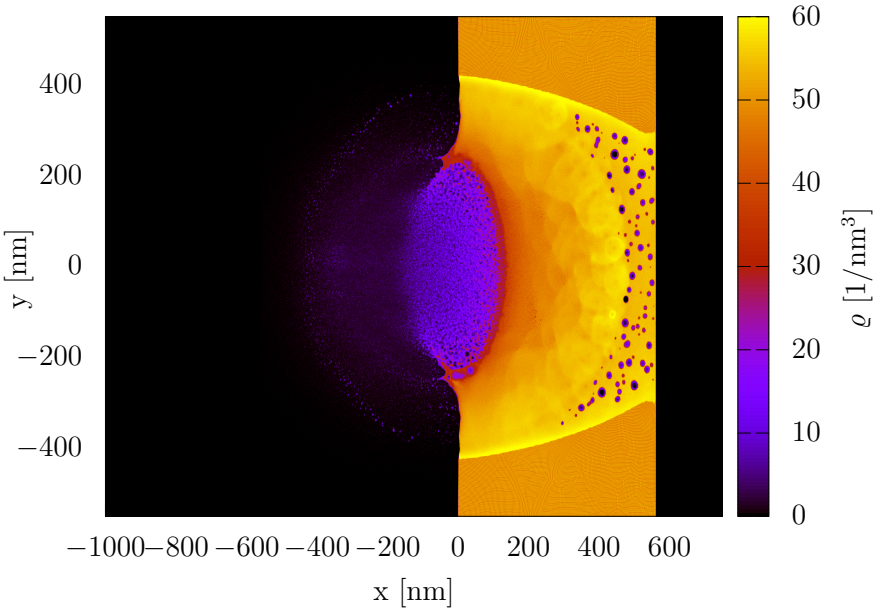

(b) Direct Simulation

Figure 7.6: Composed and direct snapshots of the spatial density histograms at a simulation time of $t = 100\,\mathrm{ps}$ after peak laser intensity under TSM+MOD*+D parametrization combination at a laser fluence of $\sigma = 0.67\,\mathrm{J/cm^2}$ and a Gaussian beam profile of width $b_{\mathrm{FWHM}} = 500\,\mathrm{nm}$.

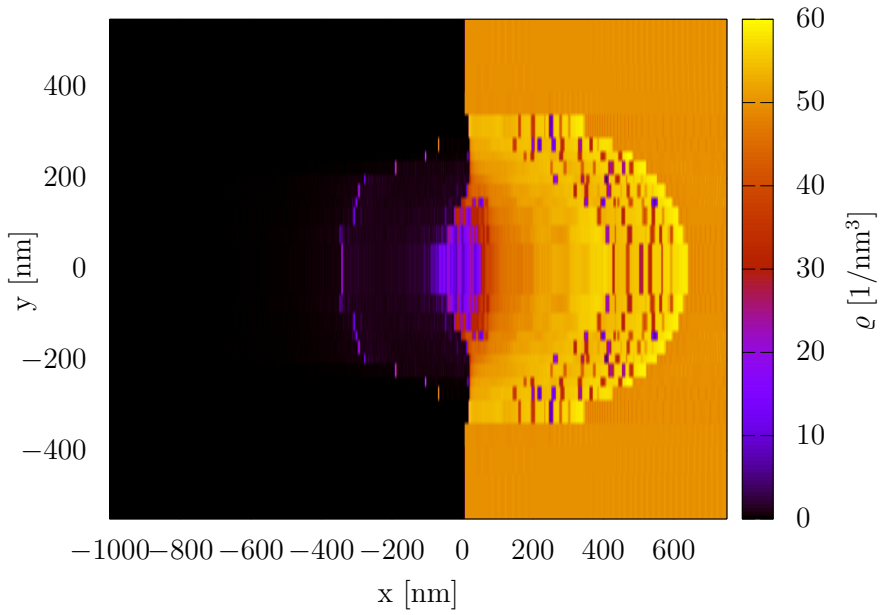

(a) Composed Simulations

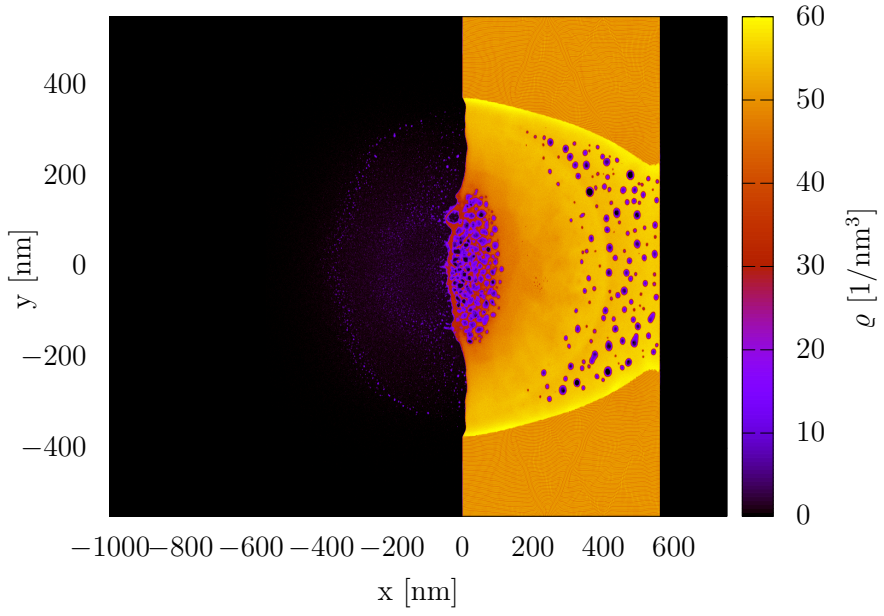

(b) Direct Simulation

Figure 7.7: Composed and direct snapshots of the spatial density histograms at a simulation time of $t = 100\,\mathrm{ps}$ after peak laser intensity under TSM+MOD*+D parametrization combination at a laser fluence of $\sigma = 0.45\,\mathrm{J/cm^2}$ and a Gaussian beam profile of width $b_{\mathrm{FWHM}} = 500\,\mathrm{nm}$.

8 Conclusion

8.1 Summary

The goal of this work was to develop and implement a model for the continuum-atomistic simulation of laser ablation of silicon by ultra-fast laser pulses. The requirement for the model was twofold. On the one hand, the model needed to be as computationally performant as possible in order to achieve realistic time- and lengthscales. On the other hand, the model also needed to cover the implications of extreme and ultra-fast electronic excitations of the irradiated material on the femtosecond timescale. In the case of silicon, ultra-fast excitation results not only in the change of optical parameters but also in the manipulation of the interatomic binding energies, thus leading to novel ablation mechanics.

The isolation of optical excitation effects allowed us to achieve a fully dynamical description of optical properties. These include the ultra-fast changes in charge carrier density and temperature during the laser pulse. Also, the fully dynamical description covers band gap effects and two-photon absorption, while accurately reproducing the ultra-fast reflectivity changes observed in experiments.

The implementation and comparison of three energy transport models, namely the nTTM, BETE and TSM, within an unconditionally stable semi-implicit solution scheme showed the existence of a critical carrier density. The usage of this critical carrier density allows for the use of FTCS solution schemes, thus massively decreasing computational cost without alteration of the simulation outcome.

The MOD* was implemented into our simulation model and proven to accurately reproduce non-thermal melting effects of homogeneously excited silicon in MD simulations. The simulation results are in accordance with ab-initio calculations, whilst not being restricted to closed periodic boundary conditions, allowing for open border

ablation simulations.

While the nTTM and BETE have proven to reproduce unphysical material dynamics when combined with the MOD* and the proposed fully dynamical optical description D, the combination TSM+MOD*+D does generate a 1:1 match with experimental data in terms of ablation depth and allowed for the observation of novel ablation mechanics.

The TSM+MOD*+D suggests that these novel ablation mechanics are the main material modification processes for laser fluences above and below the phase explosion regime. At low laser fluences, laser light absorption induces bond weakening thus instantaneous non-thermal melting within a $\sim 100\,\mathrm{fs}$ time frame. For higher laser fluences, the ablation mechanics is dominated by non-thermal surface evaporation where interatomic bonds are excited into purely repulsive states. The result is an instantaneous evaporation of the non-thermal molten material. For fluences between these two regimes, the material dynamics during the ablation process shows the characteristic phase explosion dynamics which is also observed in non-covalent bonded materials like metals. Hereby, phase explosion stands out as the most efficient ablation mechanism in terms of infused energy per material yield, and is the reason of the often observed ablation efficiency peak at a laser fluence $\sigma = 0.29\,\mathrm{J/cm^2}$.

Cluster analysis of the ablated material yields that the non-thermal evaporation driven ablation produces more dilute gas, resulting in finer droplets and therefore less surface soiling by redepositing material. However, simulations of laser ablation on Gaussian irradiated massive quasi-2D samples revealed that the local material dynamics is mainly a result of the initial local inciding fluence $\sigma(r)$. When irradiated with a Gaussian intensity profile, the laser spot is always a concentric arrangement of a hierarchy of ablation regimes and therefore always contains phase explosion dynamics for fluences above the phase explosion threshold. The circular arrangement of the phase explosion regime is the origin of the formation of the ablation crown. The lowest regime consists of non-thermal melting. Consequently, the experimentally often observed amorphous ring around the area of material removal is the area of non-thermal melting.

8.2 Outlook

Within the course of this work, we built a robust numerical framework for the simulation of laser ablation of silicon.

Application This framework can directly, or with minor modifications, be adopted to investigate the origin of other phenomena observed in laser ablation of silicon. The process of nano-bump formation is far from being understood on a detailed level [39–45]. Here, a more detailed parameter study for longer simulation times in the nano-bump regime presents itself to be fruitful. For this, IMD already comes with suitable tools, like the dynamic hydrostatic pressure analysis. Furthermore, related phenomena like the formation of nano-spikes or nano-jets follow comparable mechanics [39–47] and could also be investigated.

The presented cluster analysis has shown that the non-thermal ablation processes show a great impact on the composition of the ablated material. By simply introducing an artificial surface of a chosen material at the border of the simulation box, it is possible to study the process of pulsed laser deposition (PLD) [58] and investigate the nucleation and growth of a deposition film with regard to the cluster distribution induced by different ablation regimes.

While all simulations in this work represent laser ablation in vacuum, the side project on selective laser melting (see appendix A) has shown that IMD can already treat an unpolar protective gas. The next low-hanging fruit would be to perform laser ablation simulations under an atmosphere of varying pressure and density. During ablation under atmosphere, altered ablation mechanics can be expected [267–272]. For this, the results of an ongoing master thesis [273] on a coarse-graining description of protective gas could be utilized.

Another simple modification of the presented framework would be to investigate the influence of modified pulse shapes [274, 275]. In recent years, the temporal pulse profile 'tophat', a more or less square shaped pulse, has become a topic of interest. Other forms of laser treatment of semiconductors could be simulated in the quasi-2D setup with only the change of the spatial laser profile.

The most promising example in this case would be femtosecond laser-induced periodic surface structuring (LIPSS) [32, 168–172]. LIPSS is a laser ablation based

method to generate functional surfaces by nanostructuring and allows to control optical, mechanical, or chemical surface properties, which then can be utilized for various applications [32, 168–172].

Even though we observed and classified novel ablation dynamics arising from the non-thermal material dynamics of strongly excited silicon, these effects give rise to a series of follow-up questions that yet remain unanswered but could be investigated within the current simulation setup. The most urgent question is that of the implications of the non-thermal melting pool for the long term crystallic structure within the area of the non-thermal melting pool. While the surface is observed to stay amorphous or recrystallize dependent on the ablation regime, the sub-surface dynamics remains unknown. Here, simulations concerning the recrystallisation followed by the classification of emerging stacking faults and crystal delocations as well as the resulting stress would be highly interesting. During this work, the MOD* turned out to show recrystallisation times surpassing the available simulation time when a simple thermostat is used. However, a Monte-Carlo simulation-based cooling of the sample after laser irradiation could be applied. For this, methods like parallel tempering or nested sampling seem to be a promising approach [276].

Improvement A series of research questions can already be investigated with the presented simulation framework. For most scenarios, computational efficiency is the limiting factor in achievable sample size and general feasibility. While the core loop of the presented MD-FD framework offers little to no room for improvement, our simulations show that not every area of the sample undergoes the extreme conditions as the ablation plume, thus can be accurately modelled with less accurate approaches. We highly recommend to swap out the MD based description of the undamaged parts of the sample with hydrodynamic approaches.

During the ablation process, the sample shows a highly non-uniform distribution of atoms over the CPU grid, leading to a non-ideally distributed computational load. An implementation of a dynamical load-balancing for covalent materials would greatly reduce computational cost, as our group already demonstrated this by implementing a dynamical load-balancing for metals into IMD. Also, shockwave absorbing boundary conditions, as our group already implemented for metals [277], would allow

for smaller sample sizes, thus further reducing computational cost.

Expansion The presented TSM+MOD*+D achieves accurate results within the parameter space studied in this work. Small deviations in some specific parameters will result in unphysical behavior due to parametrization assumptions being used outside of their validity. These parametrizations are in need of expansion in future works. For example, it is tempting to simulate multi-pulse irradiation by simply adding additional laser pulses within the laser pulse description. From a physical point of view, this opens up a lot of questions. In the current state, the model includes description of the generated electron-hole plasma, but lacks a description of the generated plasma cloud within the ejected material. In multi-pulse irradiation this plasma cloud is known to absorb the second laser pulse due to screening effects [277–279]. To include such effects, the model could be expanded with the so called wide-range model [280–282].

Non-thermal melting breaks crystal structure within pulse durations and leads to a complete collapse of band structure. The parametrizations in this work assumes crystalline silicon. As a result, the optical properties for post-first-pulse irradiation remain unclear. The same argumentation holds for the parametrization of carrier-phonon coupling as the parametrization utilizes the phononic spectrum found in crystalline silicon. The next step to achieve an accurate description of these two problems would be to perform FT-DFT simulations on smaller samples and feed the obtained relation back into our simulation model by a computationally cost-efficient parametrization.

The inclusion of plasmons [283] would allow for the investigation of single-shot LIPPS [97, 284] or other field-induced self-organized structures like laser-ripples [97].

To the personal believe of the author, the most interesting expansion to the current state of the simulation code would be the description of laser light propagation by a Maxwell solver. This expansion requires rigorous treatment of optical parameters in terms of the carrier density-dependent non-linear dielectric function. While our group has already successfully done this for metals [277, 285], a migration of the solver to treat covalent materials would be on the scale of another PhD thesis. However, this expansion would allow for the study of novel ablation dynamics and

possibly novel manufacturing applications based on non-thermal effects, when combined with NIR to MIR laser wavelengths. In the case of silicon, we know that FCA is comparably small at $T_\mathrm{l} = 300\,\mathrm{K}$ and SPA vanishes for sub-bandgap wavelengths, rendering TPA the main absorption process. Also, silicon shows a positive Kerr coefficient n_2 for wavelengths of $850\,\mathrm{nm} < \lambda < 2200\,\mathrm{nm}$ [81]. As a result, laser light shows self-focusing effects when propagating through silicon, which are covered by the Maxwell solver approach. The self-focusing beam generates sub-surface areas of locally increased laser light intensity which in turn enhance TPA. The thereby absorbed laser light generates CB carriers, which again enhance FCA and also induce band gap shrinkage. If fine-tuned, this effect could be steered towards a scenario where band gap shrinkage also allows for SPA, thus generating a sub-surface area of locally extreme absorption properties. This area is subject to amorphization due to non-thermal phase transitions. It would be most interesting to investigate if this form of laser treatment allows for sub-surface induced dislocations or crystal-structure errors without extreme damaging of the sample surface. A long-shot idea would be to use the induced sub-surface dislocations in the context of silicon wafer manufacturing. If the dislocations were induced in an ordered manner, silicon wafers could be simply sheared off the silicon ingot resulting in clean cuts which are needed for the manufacturing of solar cells. As of today, this is typically done via the use of a wire saw, resulting in huge amounts of waste and maintenance requirements.

Transfer Another take on the data obtained by the TSM+MOD*+D is to view it as a proof of concept on the relevance of non-thermal effects in the laser treatment of silicon. The next step in the development chain of first proving non-thermal effects exist by DFT calculation [88] and then showing the impact on the macroscopic material dynamics of laser treated silicon would be transferring the obtained ablation mechanics into computational fluid dynamics (CFD) simulations. With this approach, realistic sample sizes could be accurately simulated with lower computational cost. The transfer of the non-thermal material dynamics needs an accurate parametrization of the phase diagram of silicon dependent on both lattice temperature T_l and carrier temperature T_c. The construction of this parametrization is part of an ongoing thesis in our group [276, 286].

A Side Project

Introduction to Additive Manufacturing

Within the course of this work, we pursued a side project and a collaboration with another PhD thesis [287] regarding the laser-based additive manufacturing of metals, commonly referred to as 3D-printing or selective laser melting (SLM). We developed and performed atomistic simulations of SLM as another form of laser processing. Here, the highly non-equilibrium material dynamics of melting, splashing and resolidification depicted by the MD approach allows for the investigation of the fundamental mechanics responsible for material defects and processing quality.

In this chapter, we only touch on the idea of modelling SLM by MD, while detailed information is given in the listed publications.

Additive Manufacturing of Metals

Selective laser melting (SLM) is a powder bed fusion technique for the 3D-printing of metals. Here, a high intensity laser scans over a metallic powder to melt and fuse particles into arbitrary shapes and subsequently build parts out of raw material in layers with a predefined thickness. These layers are fused via different techniques based on a wide array of technology. High freedom of design and new possibilities in manufacturing belong to the many opportunities that additive manufacturing brings to the table, like e.g. even replacing the step of assembly in some examples. Although many sectors profit from the advantages, the technology lends itself especially well to industries demanding parts with a low weight to high strength ratio. Along with these opportunities, a new field of challenges emerges. Inconsistent production, repeatability and quality issues put a dent in the high hopes for this new technology. While additive manufacturing is not expected to replace established conventional production processes [288, 289], the demands for quality are rising. In order to make the new technology competitive to traditional methods of manufacturing, requirements concerning productivity, surface quality and mechanical properties of the finished part must be met [290]. These rising demands lead to an optimization process that is known from most fields of manufacturing and production. In order to reach these goals, the modelling of production processes is often viewed as the essential tool. As with any production process, the achieved optimization is the result of an in-depth knowledge and understanding of the process. This knowledge can either be attained by carrying out experiments or by analyzing the underlying phenomena and identifying the main mechanisms [291].

Here, the strong suit of MD simulations comes into play as it intrinsically includes non-equilibrium dynamics of the molten material as it does in the modelling of laser ablation. In contrast to other simulations like continuum-mechanical approaches, this allows us to understand the process of SLM and identifying and understanding the underlying mechanisms and main effects taking place in the process origin, as well as the effects that lead to defects and consequently poor product quality. Such effects, for example, include the generation of pores where gas inclusions are incorporated into the material [292] or the so-called lack-of-fusion. Lack-of-fusion originates from insufficient energy supply during melting. The width of the molten

lane is too small, which causes bonding defects and powder inclusions and the different layers are not fused. Both effects increase roughness and disturb the matter flow for the next layer. They can gradually propagate through several layers and serve as starting points for cracks that can propagate through the material [293]. Also, the extreme temperature gradients during printing and the related strong thermal expansion gradients lead to high stress in the material.

Modelling Additive Manufacturing with IMD

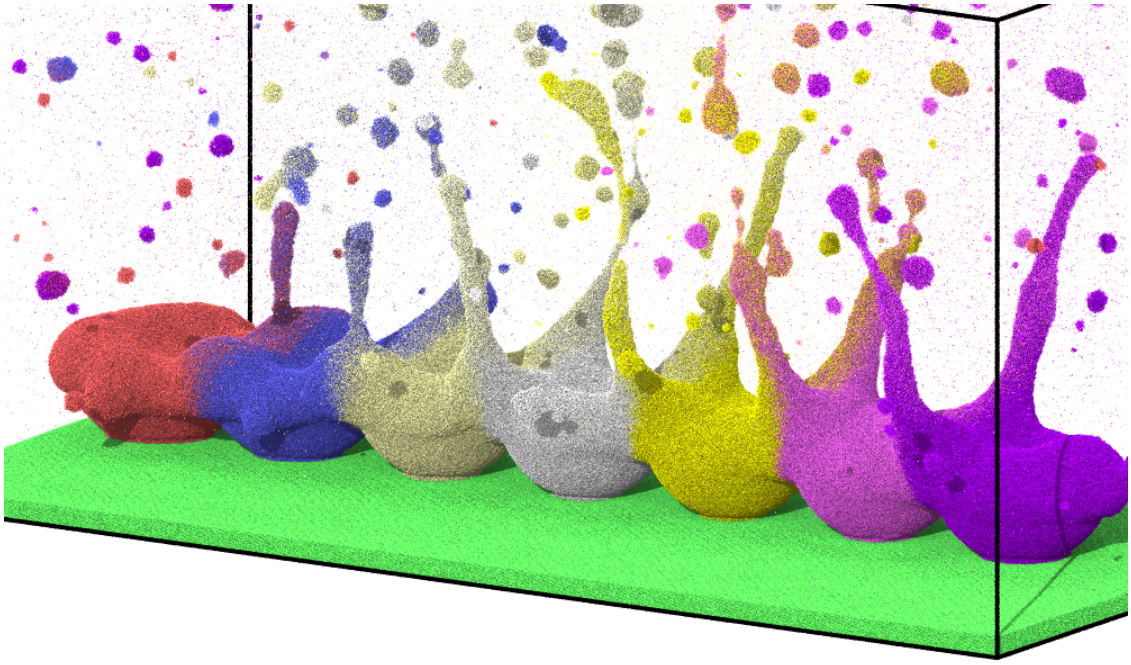

Figure A.1: Current state of our SLM simulation on aluminum powder particles without protective gas. Fusion errors can be observed due to inhomogeneous melting.

The sizes of powder particles in the SLM process are in the range of a micrometers [294] and thus are at the limit of current production simulations. For the intended simulations, the size of the system has been scaled down to a few hundred nanometers, but will be increased subsequently in future simulations. Scaling factors have been introduced to connect simulation and experiment. The procedure can be motivated by the work of Glosli et al. [295]. This group demonstrated that

MD simulations reproduce qualitatively identical macroscopic dynamics, like for example the Kelvin-Helmholtz instability in fluids, even when scaled down multiple orders of magnitude. SLM depends on the behavior of fluids in a similar way.

For the simulation of SLM, adjustments of our in-house MD code IMD were necessary. These changes were implemented, tested and carried out in a series of bachelor and master theses conceptualized and supervised by the author of this work. The works include

- the proof of concept, consisting of implementing gravity and a scanning laser in continuous wave mode for melting a single aluminium sphere [296, 297],
- rigorous parameter studies of the interplay of scanning speed and laser power and implementation of the argon protective gas [298],

as well as currently ongoing works focusing on

- adaptive material density-dependent laser light absorption and coarse gaining of aluminium and the protective gas description [273] and
- fusion of arbitrarily stacked multi-layers of aluminium as well as copper coated aluminium spheres and binary alloys [299].

In addition, simulations like shown in figure A.1 were performed for the PhD thesis of Müller [287] and were able to explain occurring fusion errors due to inhomogeneous melting and the power and scanning-speed dependency of the splashing and balling effect [300].

B Publications and Conference Contributions

Publications

- *In preparation* D. Klein, S. Müller – Modelling 3D-printing with a priori inclusion of phase dynamics
- *In review* A. Gorgis, D. Klein, S. Müller, J. Roth – Selective Laser Annealing of 3d Printed Material
- *In printing* F. Oelschläger, D. Klein, S. Müller, J. Roth Computing in Science and Engineering '21, eds. W.E. Nagel, D.B. Kröner, M.M. Resch, Springer, Molecular Dynamics Simulation of Selective Laser Melting
- E. Eisfeld, D. Förster, D. Klein, J. Roth 2022 J. Phys. D: Appl. Phys. **55** 135301 doi: `https://doi.org/10.1088/1361-6463/ac41f9`
- D. Klein, E. Eisfeld, J. Roth 2021 J. Phys. D: Appl. Phys. **54** 015103 doi: `https://doi.org/10.1088/1361-6463/abb38e`
- E. Eisfeld, D. Klein, J. Roth 2021 arXiv:2107.05937 [cond-mat.mtrl-sci] doi: `https://doi.org/10.48550/arxiv.2107.05937`
- J. Roth, D. Klein, D. et al. 2019 Eur. Phys. J. Spec. Top. **227**, 1831–1836 doi: `https://doi.org/10.1140/epjst/e2019-800147-7`

Conference Contributions

- J. Roth, F. Oelschlager, A. Gorgis, D. Klein, S. Müller, 2023. Molecular Dynamics Simulation of Selective Laser Melting. [Talk]. Verhandlungen der Deutschen Physikalischen Gesellschaft SKM, Dresden.
- S. Kümmel, D. Klein, J. Roth. 2023. Excitation-induced non-thermal melting effects in silicon. [Poster presentation]. Verhandlungen der Deutschen Physikalischen Gesellschaft SKM, Dresden.
- K. Vietz, A. Gorgis, D. Klein, J. Roth. 2023. Molecular dynamics simulation of additive manufacturing: A highly non-equilibrated business. [Poster presentation]. Verhandlungen der Deutschen Physikalischen Gesellschaft SKM, Dresden.
- J. Schmid, K. Vietz, D. Klein, J. Roth. 2023. MD Simulation of 3D Laser Printing. [Poster presentation]. Verhandlungen der Deutschen Physikalischen Gesellschaft SKM, Dresden.
- D. Klein, A. Kiselev, J. Roth. 2018. Molecular Dynamics Simulations of Laser Ablation in Covalent Materials. [Poster presentation]. Verhandlungen der Deutschen Physikalischen Gesellschaft SKM, Berlin.

C Danksagung

Tja, was ist das nun. Jetzt sitze ich hier ausgeglichen und in voller Ruhe und blicke zurück auf grob fünf Jahre Promotion. Das ist schon ein witziges Gefühl, wenn man mal reflektiert, was alles so passiert ist und wie alles passiert ist. Gefühlt ist alles schief gegangen, was nur irgendwie hätte schief laufen können. Angefangen ohne Bezahlung, ohne Aussicht auf eine Stelle, sich mit einem Haufen HiWi-Jobs gerade so über Wasser gehalten - jedes Semester aufs neue, nebenher noch die Hälfte seiner Zeit damit verbracht Antragsgelder rein zu bekommen. Ich habe immer wieder gewitzelt, dass ich eigentlich nur nebenher hobbymäßig promoviere. Und wenn es mal lief, dann lief es auch gleich nicht mehr. Supercomputerhacks, Upgrades auf (dann) nicht mehr funktionierende Maschinen, Instabilitäten aller Art - selbst und fremd verschuldet, und nebenher noch so eine Pandemie. In den letzten fünf Jahren gab es nicht nur einen Moment, in dem ich am liebsten einfach die Uni angezündet hätte und gedacht habe, dass das Projekt hier einfach nicht zu Ende gebracht wird. Aber anscheinend hat es dann wohl doch irgendwie geklappt.

Naja, was heißt “irgendwie”? Das lag eindeutig an den Menschen die mich auf diesem Weg begleitet und unterstützt haben und mich nun dazu bringen hier jetzt doch ungewohnt sentimental zu werden.

Als aller erstes muss ich mich bei meinem Doktorvater Johannes Roth bedanken. Nicht nur für die Annahme als Doktorrand und der durchweg exzellenten fachlichen Unterstützung während meines Promotionsvorhabens, nein, auch menschlich hätte ich mir keine besseren Doktorvater vorstellen können. Egal welches Problem es gab - und davon gab es viele - Johannes war einfach immer da. Zu allem Überfluss war diese Hilfsbereitschaft auch noch stets mit einer kaum beschreibbaren Bodenständigkeit gepaart, wie man sie nur von wenigen Menschen kennt. Wenn ich so

reflektiere was alles noch in diesen Block zu Johannes gehört, muss ich sagen ich muss ihn nun beenden, da ich sonst aufgrund der dadurch entstehenden Druckkosten dieser Dissertation wohl eine Privatinsolvenz anmelden müsste.

Des weiteren möchte ich mich bei Christian Holm für den Mitbericht und Ronny Nawrodt für den Prüfungsausschussvorsitz bedanken.

Auch ein großer Dank geht selbstverständlich an alle Mitglieder der Arbeitsgruppe die mich auf meine Weg begleitet haben. Ihr seid so viele, dass ich wohl mehrere `\itemize`-Umgebungen öffnen muss. Vielen vielen Dank

- Fabio Ölschläger für die mit Abstand produktivsten Prokrastinationsgespräche. Ich bin mir ziemlich sicher, dass ich die Implementation der Fast inverse square root in Quake 3 Arena nie wirklich verstehen werde.
- Kevin Vietz für ständige Bereitschaft mich aus dem Büro zu entführen.
- Simon Kümmel für den vergeblichen aber ausdauernden Versuch mir Fahrrad-Wheelies bei zu bringen.
- Jonas Schmid für 'sein blödes Geschwätz'.
- Eugen Eisfeld für jedes gemütliche Gespräch und der Hilfestellung bei jedem `IMD`-Problem.
- Sarah Müller (ja für mich zählst du zum Institut), für ausgiebigen Gespräche und die Relativierung der PhD-Panic.

Auch vielen Dank an alle Stipendiaten der Hans-Böckler-Stiftung. So ein großer interdisziplinärer Austausch prägt einen wohl fürs Leben und eröffnet einem Blickwinkel und Einstellungen, zu denen man sonst niemals Zugang gefunden hätte.

Natürlich auch einen riesigen Dank an das weitere Institutsumfeld und die Nachbargruppen. Vielen Dank

- Elli, Ines und Michi für die Gründung einer Instituts Dungeons and Dragons Gruppe und den Snacks die ihr mir dann da mitgebracht habt.
- Jan Lotze für .. ohje .. genau genommen gehen wir schon seit dem ersten Semester gemeinsam durchs Studium. Wahrscheinlich wäre ich ohne dich nicht mal durchs Bachelorstudium gekommen.
- Maria Daghofer, für jeden Spruch der mich zum Lachen gebracht hat.
- Friedemann Aust und Pascal Strobel, für die gelegentliche Auffrischung der Grundlagen der Quantenmechanik.
- Sebastian Loth, für die Duldung an seinem Institut und seiner exzellenten Auswahl an Mitarbeiter:innen in seiner Arbeitsgruppe. Jede:r einzelne war durchaus tauglich mit mir mehrere Stunden in der FMQ-Lounge herum zu lungern - eigentlich - Vielen Dank an die gesamte Loth-Group!
- Felix Huber, für das regelmäßige Bereitstellen von Werkzeug aus der Loth-Group sowie
- Stephan Spieker und Michael Schäfer, für wenn das Werkzeug dann doch mal größer sein musste.
- Sabine und Ulrike, für den ausgiebigen "Sekretariats-Talk" und den mentalen Rückhalt durch den kompletten Verlauf der Promotion.

Zu guter letzt gilt natürlich auch ein unbegrenzt großes Dank an die Menschen die mich außerhalb der Universität unterstützt haben. Ganz besonders gilt es hier Leon, Basti, Rémi, Sebbe, Jonas und Karo zu danken für .. ja eigentlich wisst ihr das jeweils selbst. Warum schreib ich das eigentlich überhaupt aus? Wenn ihr das hier lest, dann habt ihr meine Arbeit ohnehin nur gegoogelt um zu sehen, ob ihr hier steht. You got called out. Du bist nun verpflichtet mich zu kontaktieren und mich auf ein Bier ein zu laden!

D Ausführliche Zusammenfassung in deutscher Sprache

Ultraschnelle Laserablation beschreibt den Prozess der Materialabtragung an Festkörpern durch Einstrahlung von Kurzzeitlaserpulsen mit Pulsdauern unterhalb einer Picosekunde. Dabei ist das distinktive Merkmal der ultraschnellen Laserablation, dass die verwendeten Laserpulsdauern sich unterhalb der Zeitskala der Elektron-Phonon-Relaxationsdauer befinden. Laserangeregte Ladungsträger thermalisieren und leiten Wärme durch Wärmediffusion tief in das bestrahlte Material, während sich das Festkörpergitter noch in einem kalten Zustand befindet. Dieser Nichtgleichgewichtszustand relaxiert schließlich durch schnelle Elektron-Gitter-Thermalisation und heizt das Gitter über ein großes Volumen hinweg gleichzeitig auf. Abhängig von der eingestrahlten Laserenergie wird das Material extrem überhitzt und in einen metastabilen Zustand versetzt. Die Folge sind schnelle hochkomplexe Nichtgleichgewichtsmaterialrelaxationsprozesse. Diese umfassen ein breites Spektrum von Effekten, beginnend bei klassischem homogenem Schmelzen, ultraschnellem heterogenem Schmelzen, über hydrodynamische Expansion bis hin zur instantanen Verdampfung. Nicht selten finden all diese Effekte gleichzeitig statt und/oder führen zu Materialauswurf. Hierbei können die Oberflächenschichten simpel verdampfen oder es entsteht eine verdampdungsgetriebene Explosion unterhalb der Oberfläche, welche die Oberfläche aufbricht und Material in Form von Tröpfchen, Stücken oder Dampf ausschleudert.

Einzelne und Kombinationen dieser Prozesse werfen gleich mehrere Fragestellungen auf, die von großer Relevanz für industrielle Anwendungen und Bestandteil der aktuellen Forschung sind. Während eine Vielzahl von wissenschaftlichen Publikationen sich mit den induzierten Materialdynamiken und den zugrunde liegenden

physikalischen Prozessen in Metallen beschäftigt, widmen wir uns in dieser Arbeit der speziellen Materialdynamik kovalenter Materialien im Kontext der Laserablation. Im Gegensatz zu Metallen besitzen kovalente Materialien eine Bandlücke und zeigen damit auch eine anregungsabhängige elektronische Wärmediffusion. Zudem zeigen kovalente Materialien stark anregungsabhängige interatomare Bindungsstärken, die bei Laserbestrahlung nichtthermische Effekte wie nichtthermisches Schmelzen oder Coulombexplosionen induzieren.

Innerhalb dieser Arbeit wählen wir Silizium als unser prototypisches kovalentes Material und verfolgen die Zielsetzung, die während der Laserablation auftretenden Mechanismen auf atomarer Ebene zu verstehen. Hierzu entwickeln wir ein kontinuumatomistisches Simulationsmodell, welches die etablierten Wärmediffusionsmodelle um Advektionsterme ergänzt und die anregungsabhängige interatomare Bindungsenergiemanipulation durch ein elektronentemperaturabhängiges Wechselwirkungspotential miteinbezieht. Dies alles geschieht mit einem besonderen Augenmerk auf die Recheneffizienz und Optimierung des Modells im Hinblick auf die spätere Anwendung auf hochparallelisierten Hochleistungsrechnern.

Die vorliegende Arbeit gliedert sich in drei thematische Bereiche. Im ersten Teil stellen wir den aktuellen Stand der Forschung zur Modellierung von ultraschneller Laserablation an Metallen und Halbleitern dar. Hierbei geben wir einen Überblick über die während der Laserablation auftretenden physikalischen Effekte, ihre typischen Zeitskalen, ihr Zusammenspiel und die Möglichkeiten, diese zu modellieren. Wir präsentieren alternative Energietransportmodelle, explizit die BETE und das TSM, als Verbesserungen zum etablierten nTTM. Schlussendlich kombinieren wir die einzelnen Modelle zu einem neuen kontinuumatomistischen Simulationsmodell, um die Laserablation von Silizium möglichst performant zu simulieren.

Im zweiten Teil evaluieren und präsentieren wir die numerischen Methoden, die in dieser Arbeit angewendet werden. Hierbei wird das Hauptaugenmerk auf die Darstellung von expliziten, impliziten und semi-impliziten Lösungsschemata für die Finite-Differenzen-Methode, sowie deren Stabilitätsdomänen, gelegt.

Im dritten Teil wenden wir das erarbeitete Simulationsmodell für die Simulation der Laserablation an Silizium an. Hierbei erhöhen wir stufenweise die Quasidimensionalität unserer verwendeten Probe. Durch das Reduzieren unserer Probe

auf einen homogen beleuchteten Siliziumfilm mit einer Tiefe weit unter der Absorptionslänge (quasi-0D), erreichen wir eine homogene Anregung der gesamten Probe. Als Resultat verschwinden alle Transporteigenschaften des verwendeten Modells, was uns erlaubt die vorhergesagten optischen Eigenschaften isoliert zu untersuchen. Auf dieser Basis vergleichen wir verschiedene Parametrisierungen der Absorption durch freie Ladungsträger sowie der Zwei-Photonen-Absorption. Hier gelingt es uns, eine auf dem Drude-Modell basierende Formulierung für die Absorptionsmechanismen zu implementieren und zu validieren und somit bisherige Beschreibungen durch eine dynamische ladungsträgertemperatur-, sowie ladungsträgerdichteabhängige Formulierung zu ersetzen. Des weiteren implementieren wir das elektronentemperaturabhänge interatomare Wechselwirkungspotential MOD* und vergleichen es mit Dichtefunktionaltheoriesimulationen hinsichtlich der resultierenden Schmelzkinetik. Hier konnten wir beobachten, dass das MOD* nicht nur die aus der Dichtefunktionaltheorie vorhergesagten Effekte unter deutlich geringerem Rechenaufwand eins zu eins wiedergibt, sondern auch die Simulation mit offenen Randbedingungen ermöglicht, was im Rahmen der Dichtefunktionaltheorie nicht möglich ist.

Durch das Erweitern unserer Simulation auf eine quasi-1D-Geometrie, kombiniert mit unserer validierten Beschreibung optischer Eigenschaften, konnten wir die Vorhersagen der Transportmodelle nTTM, BETE und TSM untersuchen. Hier konnte beobachtet werden, dass nur die Kombination aus TSM+MOD* experimentell beobachtbare nichtthermische Dynamiken bei korrekten Fluenzen wiedergeben konnte. Diese Kombination ist zudem in der Lage, eine nahezu vollständige Übereinstimmung mit experimentell beobachteten Ablationstiefen vorherzusagen. Motiviert durch vielversprechende Validierungen des verwendeten Systems wurde eine fluenzabhängige Analyse des Ablationverhaltens durchgeführt. Hierbei wurde beobachtet, dass Silizium im mittleren Fluenzbereich eine Ablation durch Phasenexplosion analog zu Metallen zeigt. Für niedrige und hohe Fluenzen konnten hingegen neuartige nichtthermische Ablationsmechanismen beobachtet und klassifiziert werden. Zudem konnte durch die Verwendung von bedingungslos stabilen semi-impliziten Lösungsschemata die Existenz einer kritischen initialen Ladungsträgerdichte nachgewiesen werden. Bei dieser kritischen Ladungsträgerdichte setzt eine numerische Stabil-

isierung ein, sodass explizite Lösungsschemata wieder anwendbar werden ohne die Simulationsresultate zu ändern.

Durch die Kombination aller Leistungszugewinne wurde es möglich, die Simulationsdimension weiter zu erweitern, sodass quasi-2D Simulationen durchgeführt werden konnten, in welchen realistische laterale Ausdehnungen der Probe unter Einstrahlung eines Gaussprofils erreicht wurden. Hierdurch konnte die Relevanz lateraler Transportphänomene untersucht werden. Es konnte demonstriert werden, dass diese bei der Ablation eine untergeordnete Rolle spielen, sodass sich der Schadensbereich der Probe aus einer konzentrischen Anordnung der jeweiligen Ablationsregime zusammensetzt, mit einem Ring aus amorphem Silizium als äußerstem Merkmal. Dieser Ring wurde in Publikationen des Öfteren beobachtet, jedoch nie erklärt. Wir klassifizieren die Entstehungsmechanik dieses Rings als nichtthermisches Schmelzen.

E Eidesstattliche Erklärung

Schriftliche Bestätigung der erbrachten Leistung gemäß §6 Absatz 2 der Promotionsordnung 2016 der Universität Stuttgart

Die eingereichte Dissertation zum Thema

Laser Ablation of Covalent Materials

stellt meine eigenständig erbrachte Leistung dar.
Ich habe ausschließlich die angegebenen Quellen und Hilfsmittel benutzt. Wörtlich oder inhaltlich aus anderen Werken übernommene Angaben habe ich als solche kentlich gemacht.
Die Richtigkeit der hier getätigten Angaben bestätige ich und versichere, nach bestem Wissen die Wahrheit erklärt zu haben.

Stuttgart, den .....
(Datum)

.....
(Unterschrift Doktorand:in)

Bibliography

[1] J. Mark, L. Y. Liu, K. L. Hall, H. A. Haus, and E. P. Ippen. Femtosecond pulse generation in a laser with a nonlinear external resonator. *Optics Letters*, 14(1), 1989. ISSN 0146-9592. doi: 10.1364/ol.14.000048.

[2] Zhiyi Wei, Siyuan Xu, Yujiao Jiang, Yitan Gao, Kun Zhao, and Jiangfeng Zhu. Principle and progress of attosecond pulse generation, 2021. ISSN 20959419.

[3] Charles H. Townes. 1964 Nobel lecture: Production of coherent radiation by atoms and molecules. *IEEE Spectrum*, 2(8), 2013. ISSN 0018-9235. doi: 10.1109/mspec.1965.6501319.

[4] Arthur L. Schawlow. Spectroscopy in a new light. *Reviews of Modern Physics*, 54(3), 1982. ISSN 00346861. doi: 10.1103/RevModPhys.54.697.

[5] Claude N. Cohen-Tannoudji. Nobel Lecture: Manipulating atoms with photons. *Reviews of Modern Physics*, 70(3), 1998. ISSN 0034-6861. doi: 10.1103/revmodphys.70.707.

[6] Ahmed H. Zewail. Femtochemistry: Atomic-scale dynamics of the chemical bond. *Journal of Physical Chemistry A*, 104(24), 2000. ISSN 10895639. doi: 10.1021/jp001460h.

[7] David Politzer. Nobel lecture: The dilemma of attribution. *Reviews of Modern Physics*, 77(3), 2005. ISSN 00346861. doi: 10.1103/RevModPhys.77.851.

[8] Michael Schirber. Nobel Prize—Lasers as Tools. *Physics*, 11, 2018. doi: 10.1103/physics.11.100.

[9] Peter Lebedew. Untersuchungen über die Druckkräfte des Lichtes. *Annalen der Physik*, 311(11), 1901. ISSN 15213889. doi: 10.1002/andp.19013111102.

[10] A. Ashkin. Acceleration and Trapping of Particles by Radiation Pressure. *Physical Review Letters*, 24(4), 1970. ISSN 00319007. doi: 10.1103/PhysRevLett.24.156.

[11] Max Tabak, James Hammer, Michael E. Glinsky, William L. Kruer, Scott C. Wilks, John Woodworth, E. Michael Campbell, Michael D. Perry, and Rodney J. Mason. Ignition and high gain with ultrapowerful lasers. *Physics of Plasmas*, 1(5), 1994. ISSN 1070664X. doi: 10.1063/1.870664.

[12] Cang Zhao, Bo Shi, Shuailei Chen, Dong Du, Tao Sun, Brian J Simonds, Kamel Fezzaa, and Anthony D Rollett. Laser melting modes in metal powder bed fusion additive manufacturing. *Rev. Mod. Phys.*, 94(4):45002, 2022. doi: 10.1103/RevModPhys.94.045002. URL `https://link.aps.org/doi/10.1103/RevModPhys.94.045002`.

[13] B. N. Chichkov, C. Momma, S. Nolte, F. Von Alvensleben, and A. Tünnermann. Femtosecond, picosecond and nanosecond laser ablation of solids. *Applied Physics A: Materials Science and Processing*, 63(2):109–115, aug 1996. ISSN 09478396. doi: 10.1007/BF01567637. URL `https://doi.org/10.1007/BF01567637`.

[14] A. Ruiz de la Cruz, R. Lahoz, J. Siegel, G. F. de la Fuente, and J. Solis. High speed inscription of uniform, large-area laser-induced periodic surface structures in Cr films using a high repetition rate fs laser. *Optics Letters*, 39 (8), 2014. ISSN 0146-9592. doi: 10.1364/ol.39.002491.

[15] Yoshiki Tamamura and Godai Miyaji. Structural coloration of a stainless steel surface with homogeneous nanograting formed by femtosecond laser ablation. *Optical Materials Express*, 9(7), 2019. ISSN 21593930. doi: 10.1364/ome.9.002902.

[16] Joerg Schille, Lutz Schneider, Mathias Mueller, Udo Loeschner, Nicholas Goddard, Patricia Scully, and Horst Exner. Highspeed laser micro processing using ultrashort laser pulses. *Journal of Laser Micro Nanoengineering*, 9(2), 2014. ISSN 18800688. doi: 10.2961/jlmn.2014.02.0015.

[17] Tahseen Jwad, Pavel Penchev, Vahid Nasrollahi, and Stefan Dimov. Laser induced ripples' gratings with angular periodicity for fabrication of diffraction holograms. *Applied Surface Science*, 453, 2018. ISSN 01694332. doi: 10.1016/j.apsusc.2018.04.277.

[18] Jean Michel Guay, Antonino Calà Lesina, Guillaume Côté, Martin Charron, Daniel Poitras, Lora Ramunno, Pierre Berini, and Arnaud Weck. Laser-induced plasmonic colours on metals. *Nature Communications*, 8, 2017. ISSN 20411723. doi: 10.1038/ncomms16095.

[19] A. Y. Vorobyev, V. S. Makin, and Chunlei Guo. Brighter light sources from black metal: Significant increase in emission efficiency of incandescent light sources. *Physical Review Letters*, 102(23), 2009. ISSN 00319007. doi: 10.1103/PhysRevLett.102.234301.

[20] Frank A. Müller, Clemens Kunz, and Stephan Gräf. Bio-inspired functional surfaces based on laser-induced periodic surface structures, 2016. ISSN 19961944.

[21] Tobias Knüttel, Stefan Bergfeld, and Stefan Haas. Laser texturing of surfaces in thin-film silicon photovoltaics - A comparison of potential processes. *Journal of Laser Micro Nanoengineering*, 8(3), 2013. ISSN 18800688. doi: 10.2961/jlmn.2013.03.0007.

[22] Camilo Florian, Evangelos Skoulas, Daniel Puerto, Alexandros Mimidis, Emmanuel Stratakis, Javier Solis, and Jan Siegel. Controlling the Wettability of Steel Surfaces Processed with Femtosecond Laser Pulses. *ACS Applied Materials and Interfaces*, 10(42), 2018. ISSN 19448252. doi: 10.1021/acsami.8b13908.

[23] S. Rekštyte, T. Jonavičius, and M. Malinauskas. Direct laser writing of microstructures on optically opaque and reflective surfaces. *Optics and Lasers in Engineering*, 53, 2014. ISSN 01438166. doi: 10.1016/j.optlaseng.2013.08.017.

[24] Gert Willem Römer, Daniel Arnaldo Del Cerro, R. C.J. Sipkema, M. N.W. Groenendijk, and A. J. Huis In 't Veld. Ultra short pulse laser generated surface textures for anti-ice applications in aviation. In *ICALEO 2009 - 28th*

International Congress on Applications of Lasers and Electro-Optics, Congress Proceedings, volume 102, 2009. doi: 10.2351/1.5061570.

[25] Chongji Huang, Ryan Bell, Alfred Tsubaki, Craig A. Zuhlke, and Dennis R. Alexander. Condensation and subsequent freezing delays as a result of using femtosecond laser functionalized surfaces. *Journal of Laser Applications*, 30 (1), 2018. ISSN 1042-346X. doi: 10.2351/1.4986058.

[26] Sabrina V. Kirner, Thomas Wirth, Heinz Sturm, Jörg Krüger, and Jörn Bonse. Nanometer-resolved chemical analyses of femtosecond laser-induced periodic surface structures on titanium. *Journal of Applied Physics*, 122(10), 2017. ISSN 10897550. doi: 10.1063/1.4993128.

[27] U. Hermens, S. V. Kirner, C. Emonts, P. Comanns, E. Skoulas, A. Mimidis, H. Mescheder, K. Winands, J. Krüger, E. Stratakis, and J. Bonse. Mimicking lizard-like surface structures upon ultrashort laser pulse irradiation of inorganic materials. *Applied Surface Science*, 418, 2017. ISSN 01694332. doi: 10.1016/j.apsusc.2016.12.112.

[28] Alexandre Cunha, Anne Marie Elie, Laurent Plawinski, Ana Paula Serro, Ana Maria Botelho Do Rego, Amélia Almeida, Maria C. Urdaci, Marie Christine Durrieu, and Rui Vilar. Femtosecond laser surface texturing of titanium as a method to reduce the adhesion of Staphylococcus aureus and biofilm formation. *Applied Surface Science*, 360, 2016. ISSN 01694332. doi: 10.1016/j.apsusc.2015.10.102.

[29] Nadja Epperlein, Friederike Menzel, Karin Schwibbert, Robert Koter, Jörn Bonse, Janin Sameith, Jörg Krüger, and Jörg Toepel. Influence of femtosecond laser produced nanostructures on biofilm growth on steel. *Applied Surface Science*, 418, 2017. ISSN 01694332. doi: 10.1016/j.apsusc.2017.02.174.

[30] J. J. Yu and Y. F. Lu. Laser-induced ripple structures on Ni-P substrates. *Applied Surface Science*, 148(3), 1999. ISSN 01694332. doi: 10.1016/S0169-4332(98)00900-3.

[31] J. Bonse, R. Koter, M. Hartelt, D. Spaltmann, S. Pentzien, S. Höhm, A. Rosenfeld, and J. Krüger. Femtosecond laser-induced periodic surface structures on steel and titanium alloy for tribological applications. *Applied Physics A: Materials Science and Processing*, 117(1), 2014. ISSN 14320630. doi: 10.1007/s00339-014-8229-2.

[32] Camilo Florian, Sabrina V. Kirner, Jörg Krüger, and Jörn Bonse. Surface functionalization by laser-induced periodic surface structures. *Journal of Laser Applications*, 32(2), 2020. ISSN 1042-346X. doi: 10.2351/7.0000103.

[33] Ablimit Ablez, Kohei Toyoda, Katsuhiko Miyamoto, and Takashige Omatsu. Microneedle structuring of Si(111) by irradiation with picosecond optical vortex pulses. *Applied Physics Express*, 13(6), 2020. ISSN 18820786. doi: 10.35848/1882-0786/ab8d4b.

[34] Alexey N. Volkov and Leonid V. Zhigilei. Hydrodynamic multi-phase model for simulation of laser-induced non-equilibrium phase transformations. *Journal of Physics: Conference Series*, 59(1), 2007. ISSN 17426596. doi: 10.1088/1742-6596/59/1/135.

[35] B. Rethfeld, K. Sokolowski-Tinten, D. von der Linde, and S. I. Anisimov. Ultrafast thermal melting of laser-excited solids by homogeneous nucleation. *Physical Review B - Condensed Matter and Materials Physics*, 65(9):1–4, feb 2002. ISSN 1550235X. doi: 10.1103/PhysRevB.65.092103. URL `https://link.aps.org/doi/10.1103/PhysRevB.65.092103`.

[36] Klaus Sokolowski-Tinten, Christian Blome, Juris Blums, Andrea Cavalleri, Clemens Dietrich, Alexander Tarasevitch, Ingo Uschmann, Eckhard Förster, Martin Kammler, Michael Horn-von Hoegen, and Dietrich Von der Linde. Femtosecond x-ray measurement of coherent lattice vibrations near the lindemann stability limit. *Nature*, 422(6929), 2003. ISSN 00280836. doi: 10.1038/nature01490.

[37] Leonid V. Zhigilei, Zhibin Lin, and Dmitriy S. Ivanov. Atomistic modeling of short pulse laser ablation of metals: Connections between melting, spallation,

and phase explosion. *Journal of Physical Chemistry C*, 113(27), 2009. ISSN 19327447. doi: 10.1021/jp902294m.

[38] K. Sokolowski-Tinten, J. Bialkowski, M. Boing, and A. Cavalleri. Thermal and nonthermal melting of gallium arsenide after femtosecond laser excitation. *Physical Review B - Condensed Matter and Materials Physics*, 58(18), 1998. ISSN 1550235X. doi: 10.1103/PhysRevB.58.R11805.

[39] Yoshiki Nakata, Noriaki Miyanaga, and Tatsuo Okada. Effect of pulse width and fluence of femtosecond laser on the size of nanobump array. *Applied Surface Science*, 253(15):6555–6557, may 2007. ISSN 01694332. doi: 10.1016/j.apsusc.2007.01.080. URL `https://www.sciencedirect.com/science/article/pii/S0169433207001481https://linkinghub.elsevier.com/retrieve/pii/S0169433207001481`.

[40] Dmitriy S. Ivanov, Zhibin Lin, Baerbel Rethfeld, Gerard M. O'Connor, Thomas J. Glynn, and Leonid V. Zhigilei. Nanocrystalline structure of nanobump generated by localized photoexcitation of metal film. *Journal of Applied Physics*, 107(1):13519, 2010. ISSN 00218979. doi: 10.1063/1.3276161. URL `https://doi.org/10.1063/1.3276161`.

[41] F. Korte, J. Koch, and B.N. Chichkov. Formation of microbumps and nanojets on gold targets by femtosecond laser pulses. *Applied Physics A*, 79(4-6): 879–881, sep 2004. ISSN 0947-8396. doi: 10.1007/s00339-004-2590-5. URL `http://link.springer.com/10.1007/s00339-004-2590-5`.

[42] J. Koch, F. Korte, T. Bauer, C. Fallnich, A. Ostendorf, and B. N. Chichkov. Nanotexturing of gold films by femtosecond laser-induced melt dynamics. *Applied Physics A: Materials Science and Processing*, 81(2), 2005. ISSN 09478396. doi: 10.1007/s00339-005-3212-6.

[43] Yoshiki Nakata, Tatsuo Okada, and Mitsuo Maeda. Nano-sized hollow bump array generated by single femtosecond laser pulse, 2003. ISSN 00214922.

[44] Y. P. Meshcheryakov and N. M. Bulgakova. Thermoelastic modeling of microbump and nanojet formation on nanosize gold films under femtosecond

laser irradiation. *Applied Physics A: Materials Science and Processing*, 82(2), 2006. ISSN 09478396. doi: 10.1007/s00339-005-3319-9.

[45] Dmitriy S. Ivanov, Baerbel Rethfeld, Gerard M. O'Connor, Thomas J. Glynn, Alexey N. Volkov, and Leonid V. Zhigilei. The mechanism of nanobump formation in femtosecond pulse laser nanostructuring of thin metal films. *Applied Physics A: Materials Science and Processing*, 92(4):791–796, 2008. ISSN 09478396. doi: 10.1007/s00339-008-4712-y. URL `https://doi.org/10.1007/s00339-008-4712-y`.

[46] N. A. Inogamov, V. V. Zhakhovskii, and V. A. Khokhlov. Jet formation in spallation of metal film from substrate under action of femtosecond laser pulse. *Journal of Experimental and Theoretical Physics*, 120(1), 2015. ISSN 10637761. doi: 10.1134/S1063776115010136.

[47] A. I. Kuznetsov, J. Koch, and B. N. Chichkov. Nanostructuring of thin gold films by femtosecond lasers. *Applied Physics A: Materials Science and Processing*, 94(2):221–230, feb 2009. ISSN 09478396. doi: 10.1007/s00339-008-4859-6. URL `https://doi.org/10.1007/s00339-008-4859-6http://link.springer.com/10.1007/s00339-008-4859-6`.

[48] Takashige Omatsu, Katsuhiko Miyamoto, Kohei Toyoda, Ryuji Morita, Yoshihiko Arita, and Kishan Dholakia. A New Twist for Materials Science: The Formation of Chiral Structures Using the Angular Momentum of Light, 2019. ISSN 21951071.

[49] S. Syubaev, A. Porfirev, A. Zhizhchenko, O. Vitrik, S. Kudryashov, S. Fomchenkov, S. Khonina, and A. Kuchmizhak. Zero-orbital-angular-momentum laser printing of chiral nanoneedles. *Optics Letters*, 42(23), 2017. ISSN 0146-9592. doi: 10.1364/ol.42.005022.

[50] S. Syubaev, A. Zhizhchenko, O. Vitrik, S. Kudryashov, A. Porfirev, S. Fomchenkov, S. Khonina, and A. Kuchmizhak. Zero-OAM laser printing of chiral nanoneedles. *arXiv*, 42(23), 2017. ISSN 23318422.

[51] Yoshiki Nakata, Masataka Yoshida, and Noriaki Miyanaga. Parallel fabrication of spiral surface structures by interference pattern of circularly polarized beams. *Scientific Reports*, 8(1), 2018. ISSN 20452322. doi: 10.1038/s41598-018-31834-3.

[52] Tatiana E. Itina, Jörg Hermann, Philippe Delaporte, and Marc Sentis. Laser-generated plasma plume expansion: Combined continuous-microscopic modeling. *Physical Review E - Statistical Physics, Plasmas, Fluids, and Related Interdisciplinary Topics*, 66(6), 2002. ISSN 1063651X. doi: 10.1103/PhysRevE.66.066406.

[53] S.I. Anisimov, B.L. Kapeliovich, and T.L. Perel'man. Electron emission from the metal surfaces induced by ultrashort lasers pulses. *Zhurnal Ehksperimental'noj i Teoreticheskoj Fiziki*, 66(2), 1974. ISSN 0044-4510.

[54] John Penczak, Rotem Kupfer, Ilana Bar, and Robert J. Gordon. The role of plasma shielding in collinear double-pulse femtosecond laser-induced breakdown spectroscopy. *Spectrochimica Acta - Part B Atomic Spectroscopy*, 97, 2014. ISSN 05848547. doi: 10.1016/j.sab.2014.04.007.

[55] S. S. Harilal, P. K. Diwakar, M. P. Polek, and M. C. Phillips. Morphological changes in ultrafast laser ablation plumes with varying spot size. *Optics Express*, 23(12), 2015. ISSN 10944087. doi: 10.1364/oe.23.015608.

[56] W. T. Ashurst and Brad Lee Holian. Droplet formation by rapid expansion of a liquid. *Physical Review E - Statistical Physics, Plasmas, Fluids, and Related Interdisciplinary Topics*, 59(6), 1999. ISSN 1063651X. doi: 10.1103/PhysRevE.59.6742.

[57] L. V. Zhigilei. Dynamics of the plume formation and parameters of the ejected clusters in short-pulse laser ablation. *Applied Physics A: Materials Science and Processing*, 76(3):339–350, 2003. ISSN 09478396. doi: 10.1007/s00339-002-1818-5. URL `https://doi.org/10.1007/s00339-002-1818-5`.

[58] Matthew Murray, Gin Jose, Billy Richards, and Animesh Jha. Femtosecond

pulsed laser deposition of silicon thin films. *Nanoscale Research Letters*, 8(1), 2013. ISSN 1556276X. doi: 10.1186/1556-276X-8-272.

[59] W. Schulz, V. Kostrykin, H. Zefferer, D. Petring, and R. Poprawe. A free boundary problem related to laser beam fusion cutting: ODE approximation. *International Journal of Heat and Mass Transfer*, 40(12), 1997. ISSN 00179310. doi: 10.1016/S0017-9310(96)00342-0.

[60] Wolfgang Schulz, Vadim Kostrykin, Markus Nießen, Jan Michel, Dirk Petring, Ernst W. Kreutz, and Reinhart Poprawe. Dynamics of ripple formation and melt flow in laser beam cutting. *Journal of Physics D: Applied Physics*, 32 (11), 1999. ISSN 00223727. doi: 10.1088/0022-3727/32/11/307.

[61] P. P. Pronko, S. K. Dutta, J. Squier, J. V. Rudd, D. Du, and G. Mourou. Machining of sub-micron holes using a femtosecond laser at 800 nm. *Optics Communications*, 114(1-2), 1995. ISSN 00304018. doi: 10.1016/0030-4018(94)00585-I.

[62] P. Balling and J. Schou. Femtosecond-laser ablation dynamics of dielectrics: Basics and applications for thin films. *Reports on Progress in Physics*, 76(3): 36502, 2013. ISSN 00344885. doi: 10.1088/0034-4885/76/3/036502. URL `http://stacks.iop.org/0034-4885/76/i=3/a=036502`.

[63] Kristian Wædegaard, Martin Frislev, and Peter Balling. Femtosecond laser excitation of dielectric materials: Experiments and modeling of optical properties and ablation depths. *Applied Physics A: Materials Science and Processing*, 110(3):601–605, 2013. ISSN 14320630. doi: 10.1007/s00339-012-7136-7. URL `https://doi.org/10.1007/s00339-012-7136-7`.

[64] B. H. Christensen and P. Balling. Modeling ultrashort-pulse laser ablation of dielectric materials. *Physical Review B - Condensed Matter and Materials Physics*, 79(15):155424, apr 2009. ISSN 10980121. doi: 10.1103/PhysRevB.79.155424. URL `https://link.aps.org/doi/10.1103/PhysRevB.79.155424`.

[65] Baerbel Rethfeld, Dmitriy S. Ivanov, Martin E. Garcia, and Sergei I. Anisimov. Modelling ultrafast laser ablation. *Journal of Physics D: Applied Physics*, 50

(19):193001, 2017. ISSN 13616463. doi: 10.1088/1361-6463/50/19/193001. URL http://stacks.iop.org/0022-3727/50/i=19/a=193001.

[66] Nikita Medvedev, Zheng Li, and Beata Ziaja. Thermal and nonthermal melting of silicon under femtosecond x-ray irradiation. *Physical Review B - Condensed Matter and Materials Physics*, 91(5), 2015. ISSN 1550235X. doi: 10.1103/PhysRevB.91.054113.

[67] Nikita Medvedev, Harald O. Jeschke, and Beata Ziaja. Nonthermal phase transitions in semiconductors induced by a femtosecond extreme ultraviolet laser pulse. *New Journal of Physics*, 15(1):15016, jan 2013. ISSN 13672630. doi: 10.1088/1367-2630/15/1/015016. URL http://dx.doi.org/10.1088/1367-2630/15/1/015016.

[68] P. Stampfli and K. H. Bennemann. Theory for the instability of the diamond structure of Si, Ge, and C induced by a dense electron-hole plasma. *Physical Review B*, 42(11):7163–7173, 1990. ISSN 01631829. doi: 10.1103/PhysRevB.42.7163. URL https://link.aps.org/doi/10.1103/PhysRevB.42.7163.

[69] V. Recoules, J. Clérouin, G. Zérah, P. M. Anglade, and S. Mazevet. Effect of intense laser irradiation on the lattice stability of semiconductors and metals. *Physical Review Letters*, 96(5), feb 2006. ISSN 10797114. doi: 10.1103/PhysRevLett.96.055503. URL http://dx.doi.org/10.1103/PhysRevLett.96.055503.

[70] Lalit Shokeen and Patrick K. Schelling. Role of electronic-excitation effects in the melting and ablation of laser-excited silicon. *Computational Materials Science*, 67:316–328, feb 2013. ISSN 09270256. doi: 10.1016/j.commatsci.2012.07.042. URL http://dx.doi.org/10.1016/j.commatsci.2012.07.042https://linkinghub.elsevier.com/retrieve/pii/S0927025612004910.

[71] Eeuwe S. Zijlstra, Tobias Zier, Bernd Bauerhenne, Sergej Krylow, Philipp M. Geiger, and Martin E. Garcia. Femtosecond-laser-induced bond breaking and structural modifications in silicon, TiO2, and defective graphene: An ab initio molecular dynamics study. *Applied Physics A: Materials Science and Processing*, 114(1), 2014. ISSN 09478396. doi: 10.1007/s00339-013-8080-x.

[72] N. M. Bulgakova, R. Stoian, A. Rosenfeld, I. V. Hertel, and E. E.B. Campbell. Electronic transport and consequences for material removal in ultrafast pulsed laser ablation of materials. *Physical Review B - Condensed Matter and Materials Physics*, 69(5), 2004. ISSN 1550235X. doi: 10.1103/PhysRevB.69.054102.

[73] Maher Harb, Ralph Ernstorfer, Christoph T. Hebeisen, Germán Sciaini, Weina Peng, Thibault Dartigalongue, Mark A. Eriksson, Max G. Lagally, Sergei G. Kruglik, and R. J.Dwayne Miller. Electronically driven structure changes of Si captured by femtosecond electron diffraction. *Physical Review Letters*, 100 (15):155504, apr 2008. ISSN 00319007. doi: 10.1103/PhysRevLett.100.155504. URL https://link.aps.org/doi/10.1103/PhysRevLett.100.155504.

[74] A. A. Ionin, S. I. Kudryashov, L. V. Seleznev, D. V. Sinitsyn, A. F. Bunkin, V. N. Lednev, and S. M. Pershin. Thermal melting and ablation of silicon by femtosecond laser radiation. *Journal of Experimental and Theoretical Physics*, 116(3):347–362, mar 2013. ISSN 10637761. doi: 10.1134/S106377611302012X. URL https://doi.org/10.1134/S106377611302012Xhttp://link.springer.com/10.1134/S106377611302012X.

[75] A. Rousse, C. Rischel, S. Fourmaux, I. Uschmann, S. Sebban, G. Grillon, Ph Balcou, E. Förster, J. P. Geindre, P. Audebert, J. C. Gauthier, and D. Hulin. Non-thermal melting in semiconductors measured at femtosecond resolution. *Nature*, 410(6824):65–67, mar 2001. ISSN 00280836. doi: 10.1038/35065045. URL http://www.nature.com/articles/35065045.

[76] Kevin Werner, Vitaly Gruzdev, Noah Talisa, Kyle Kafka, Drake Austin, Carl M. Liebig, and Enam Chowdhury. Single-Shot Multi-Stage Damage and Ablation of Silicon by Femtosecond Mid-infrared Laser Pulses. *Scientific Reports*, 9(1):19993, 2019. ISSN 20452322. doi: 10.1038/s41598-019-56384-0. URL https://doi.org/10.1038/s41598-019-56384-0.

[77] R. F.W. Herrmann, J. Gerlach, and E. E.B. Campbell. Ultrashort pulse laser ablation of silicon: An MD simulation study. *Applied Physics A: Materials Science and Processing*, 66(1), 1998. ISSN 09478396. doi: 10.1007/s003390050634.

[78] Roman Holenstein, Sean E. Kirkwood, Robert Fedosejevs, and Ying Y. Tsui. Simulation of femtosecond laser ablation of silicon. In John C. Armitage, Roger A. Lessard, and George A. Lampropoulos, editors, *Photonics North 2004: Photonic Applications in Telecommunications, Sensors, Software, and Lasers*, volume 5579, page 688, nov 2004. doi: 10.1117/12.567675. URL http://proceedings.spiedigitallibrary.org/proceeding.aspx?doi=10.1117/12.567675.

[79] Dominic Klein. Klassische Molekulardynamiksimulation der Laserablation von Silizium unter Verwendung von Tersoff-Potentialen. Bachelorarbeit, Universität Stuttgart, 2013.

[80] A. Rämer, O. Osmani, and B. Rethfeld. Laser damage in silicon: Energy absorption, relaxation, and transport. *Journal of Applied Physics*, 116(5):053508, aug 2014. ISSN 10897550. doi: 10.1063/1.4891633. URL http://dx.doi.org/10.1063/1.4891633http://aip.scitation.org/doi/10.1063/1.4891633.

[81] Alan D. Bristow, Nir Rotenberg, and Henry M. Van Driel. Two-photon absorption and Kerr coefficients of silicon for 850-2200 nm. *Applied Physics Letters*, 90(19):191104, 2007. ISSN 00036951. doi: 10.1063/1.2737359. URL https://doi.org/10.1063/1.2737359.

[82] H. M. Van Driel, J. S. Preston, and M. I. Gallant. Confinement of laser-generated carriers in semiconductors by induced lattice temperature gradients. *Applied Physics Letters*, 40(5):385–387, mar 1982. ISSN 00036951. doi: 10.1063/1.93111. URL https://doi.org/10.1063/1.93111http://aip.scitation.org/doi/10.1063/1.93111.

[83] J. S. Preston and H. M. Van Driel. Kinetics of plasmas and melting induced in silicon and germanium by nanosecond laser pulses. *Physical Review B*, 30 (4):1950–1956, aug 1984. ISSN 01631829. doi: 10.1103/PhysRevB.30.1950. URL https://link.aps.org/doi/10.1103/PhysRevB.30.1950.

[84] D. Arnold, E. Cartier, and D. J. DiMaria. Theory of high-field electron transport and impact ionization in silicon dioxide. *Physical Review B*, 49(15):

10278–10297, apr 1994. ISSN 01631829. doi: 10.1103/PhysRevB.49.10278. URL https://link.aps.org/doi/10.1103/PhysRevB.49.10278.

[85] V. P. Lipp, B. Rethfeld, M. E. Garcia, and D. S. Ivanov. Semi-implicit finite-difference method with predictor-corrector algorithm for solution of diffusion equation with nonlinear terms. nov 2015. URL http://arxiv.org/abs/1511.08389.

[86] Eeuwe S. Zijlstra, Tobias Zier, and Martin E. Garcia. Simulations of Highly-Excited Silicon. *Silicon*, 10(2):567–568, mar 2018. ISSN 18769918. doi: 10.1007/s12633-016-9491-z. URL https://doi.org/10.1007/s12633-016-9491-zhttp://link.springer.com/10.1007/s12633-016-9491-z.

[87] Tobias Zier, Eeuwe S. Zijlstra, and Martin E. Garcia. Silicon before the bonds break. *Applied Physics A: Materials Science and Processing*, 117 (1):1–5, oct 2014. ISSN 14320630. doi: 10.1007/s00339-014-8316-4. URL https://doi.org/10.1007/s00339-014-8316-4http://link.springer.com/10.1007/s00339-014-8316-4.

[88] Tobias Zier, Eeuwe S. Zijlstra, Alan Kalitsov, Ioannis Theodonis, and Martin E. Garcia. Signatures of nonthermal melting. *Structural Dynamics*, 2(5):54101, sep 2015. ISSN 23297778. doi: 10.1063/1.4928686. URL https://doi.org/10.1063/1.4928686http://aip.scitation.org/doi/10.1063/1.4928686.

[89] Pier Luigi Silvestrelli, Ali Alavi, Michele Parrinello, and Daan Frenkel. Ab initio molecular dynamics simulation of laser melting of silicon. *Physical Review Letters*, 77(15):3149–3152, 1996. ISSN 10797114. doi: 10.1103/PhysRevLett.77.3149. URL https://link.aps.org/doi/10.1103/PhysRevLett.77.3149.

[90] S. I. Kudryashov and V. I. Emel'yanov. Band gap collapse and ultrafast "cold" melting of silicon during femtosecond laser pulse. *JETP Letters*, 73(5):228–231, mar 2001. ISSN 00213640. doi: 10.

1134/1.1371059. URL https://doi.org/10.1134/1.1371059http://link.springer.com/10.1134/1.1371059.

[91] V. P. Lipp, B. Rethfeld, M. E. Garcia, and D. S. Ivanov. Atomistic-continuum modeling of short laser pulse melting of Si targets. *Physical Review B - Condensed Matter and Materials Physics*, 90(24):245306, dec 2014. ISSN 1550235X. doi: 10.1103/PhysRevB.90.245306. URL https://link.aps.org/doi/10.1103/PhysRevB.90.245306.

[92] Yong Gan and J. K. Chen. Combined continuum-atomistic modeling of ultrashort-pulsed laser irradiation of silicon. *Applied Physics A: Materials Science and Processing*, 105(2):427–437, nov 2011. ISSN 09478396. doi: 10.1007/s00339-011-6573-z. URL http://dx.doi.org/10.1007/s00339-011-6573-zhttp://link.springer.com/10.1007/s00339-011-6573-z.

[93] Alexander Kiselev. *Molecular dynamics simulations of laser ablation in covalent materials*. Phd-thesis, Universität Stuttgart, 2017.

[94] Carolina Trichet Paredes. *Molecular Dynamics Simulations of Laser Ablation*. PhD thesis, University of Stuttgart, 2010. URL http://dx.doi.org/.

[95] Alexander Kiselev, Johannes Roth, and Hans Rainer Trebin. Molecular dynamics simulations of silicon:The influence of electron-temperature dependent interactions. In *High Performance Computing in Science and Engineering '16: Transactions of the High Performance Computing Center Stuttgart (HLRS) 2016*, pages 189–202. Springer International Publishing, Cham, 2017. ISBN 9783319470665. doi: 10.1007/978-3-319-47066-5_14. URL http://link.springer.com/10.1007/978-3-319-47066-5_14.

[96] Hao Zhang. *Single-shot femtosecond laser ablation on the nanoscale*. PhD thesis, Utrecht University, 2013.

[97] J. Bonse, S. Baudach, J. Krüger, W. Kautek, and M. Lenzner. Femtosecond laser ablation of silicon-modification thresholds and morphology. *Applied Physics A: Materials Science and Processing*, 74(1):19–25, jan 2002. ISSN

14320630. doi: 10.1007/s003390100893. URL https://doi.org/10.1007/s003390100893http://link.springer.com/10.1007/s003390100893.

[98] Robert W. Boyd. *Nonlinear Optics*. Elsevier Science, 2008. ISBN 9780123694706. doi: 10.1201/9781420004694.ch5. URL https://books.google.de/books?id=3vHb7WGXmSQC.

[99] H. Ehrenreich, H. R. Philipp, and B. Segall. Optical properties of aluminum. *Physical Review*, 132(5):1918–1928, 1963. ISSN 0031899X. doi: 10.1103/PhysRev.132.1918. URL https://link.aps.org/doi/10.1103/PhysRev.132.1918.

[100] K. Sokolowski-Tinten and D. von der Linde. Generation of dense electron-hole plasmas in silicon. *Physical Review B - Condensed Matter and Materials Physics*, 61(4):2643–2650, jan 2000. ISSN 1550235X. doi: 10.1103/PhysRevB.61.2643. URL http://dx.doi.org/10.1103/PhysRevB.61.2643https://link.aps.org/doi/10.1103/PhysRevB.61.2643.

[101] F. Quéré, S. Guizard, and Ph Martin. Time-resolved study of laser-induced breakdown in dielectrics. *Europhysics Letters*, 56(1):138–144, 2001. ISSN 02955075. doi: 10.1209/epl/i2001-00499-9. URL https://doi.org/10.1209%2Fepl%2Fi2001-00499-9.

[102] Tae Y. Choi and Costas P. Grigoropoulos. Plasma and ablation dynamics in ultrafast laser processing of crystalline silicon. *Journal of Applied Physics*, 92 (9):4918–4925, 2002. ISSN 00218979. doi: 10.1063/1.1510565. URL https://doi.org/10.1063/1.1510565.

[103] Rubin Braunstein. Nonlinear optical effects. *Physical Review*, 125(2):475–477, jan 1962. ISSN 0031899X. doi: 10.1103/PhysRev.125.475. URL https://link.aps.org/doi/10.1103/PhysRev.125.475.

[104] R. Braunstein and N. Ockman. Optical double-photon absorption in CdS. *Physical Review*, 134(2A):A499—-A507, apr 1964. ISSN 0031899X. doi: 10.1103/PhysRev.134.A499. URL https://link.aps.org/doi/10.1103/PhysRev.134.A499.

[105] M. H. Weiler. Nonparabolicity and exciton effects in two-photon absorption in zincblende semiconductors. *Solid State Communications*, 39(8):937–940, aug 1981. ISSN 00381098. doi: 10.1016/0038-1098(81)90042-9. URL https://linkinghub.elsevier.com/retrieve/pii/0038109881900429.

[106] C. C. Lee and H. Y. Fan. Two-photon absorption with exciton effect for degenerate valence bands. *Physical Review B*, 9(8):3502–3516, apr 1974. ISSN 01631829. doi: 10.1103/PhysRevB.9.3502. URL https://link.aps.org/doi/10.1103/PhysRevB.9.3502.

[107] C. R. Pidgeon, B. S. Wherrett, A. M. Johnston, J. Dempsey, and A. Miller. Erratum: Two-photon absorption in zinc-blende semiconductors (Physical Review Letters (1979) 43, 24, (1843)). *Physical Review Letters*, 43(24): 1843, 1979. ISSN 00319007. doi: 10.1103/PhysRevLett.43.1843.2. URL https://link.aps.org/doi/10.1103/PhysRevLett.43.1843.2.

[108] Mansoor Sheik-Bahae, David Crichton Hutchings, David J. Hagan, and Eric W. Van Stryland. Dispersion of Bound Electronic Nonlinear Refraction in Solids. *IEEE Journal of Quantum Electronics*, 27(6):1296–1309, jun 1991. ISSN 15581713. doi: 10.1109/3.89946. URL http://ieeexplore.ieee.org/document/89946/.

[109] Henry M. Van Driel. Kinetics of high-density plasmas generated in Si by 1.06- and 0.53- m picosecond laser pulses. *Physical Review B*, 35(15): 8166–8176, may 1987. ISSN 01631829. doi: 10.1103/PhysRevB.35.8166. URL http://dx.doi.org/10.1103/PhysRevB.35.8166https://link.aps.org/doi/10.1103/PhysRevB.35.8166.

[110] J. K. Chen, D. Y. Tzou, and J. E. Beraun. Numerical investigation of ultrashort laser damage in semiconductors. *International Journal of Heat and Mass Transfer*, 48(3-4):501–509, jan 2005. ISSN 00179310. doi: 10.1016/j.ijheatmasstransfer.2004.09.015. URL http://dx.doi.org/10.1016/j.ijheatmasstransfer.2004.09.015.

[111] A. Kaiser and B. Rethfeld. Microscopic processes in dielectrics under irradiation by subpicosecond laser pulses. *Physical Review B - Condensed Mat-*

ter and Materials Physics, 61(17):11437–11450, 2000. ISSN 1550235X. doi: 10.1103/PhysRevB.61.11437. URL https://link.aps.org/doi/10.1103/PhysRevB.61.11437.

[112] B. Rethfeld, A. Kaiser, M. Vicanek, and G. Simon. Ultrafast dynamics of nonequilibrium electrons in metals under femtosecond laser irradiation. *Physical Review B - Condensed Matter and Materials Physics*, 65(21): 2143031–21430311, 2002. ISSN 01631829. doi: 10.1103/PhysRevB.65.214303. URL https://link.aps.org/doi/10.1103/PhysRevB.65.214303.

[113] L. D. Pietanza, G. Colonna, S. Longo, and M. Capitelli. Electron and phonon relaxation in metal films perturbed by a femtosecond laser pulse. *Applied Physics A: Materials Science and Processing*, 79(4-6):1047–1050, sep 2004. ISSN 09478396. doi: 10.1007/s00339-004-2625-y. URL https://doi.org/10.1007/s00339-004-2625-y.

[114] L. D. Pietanza, G. Colonna, S. Longo, and M. Capitelli. Non-equilibrium electron and phonon dynamics in metals under femtosecond laser pulses. *European Physical Journal D*, 45(2):369–389, nov 2007. ISSN 14346060. doi: 10.1140/epjd/e2007-00251-1. URL https://doi.org/10.1140/epjd/e2007-00251-1.

[115] B. Y. Mueller and B. Rethfeld. Relaxation dynamics in laser-excited metals under nonequilibrium conditions. *Physical Review B - Condensed Matter and Materials Physics*, 87(3):35139, jan 2013. ISSN 10980121. doi: 10.1103/PhysRevB.87.035139. URL https://link.aps.org/doi/10.1103/PhysRevB.87.035139.

[116] J. Hohlfeld, J. G. Müller, S. S. Wellershoff, and E. Matthias. Time-resolved thermoreflectivity of thin gold films and its dependence on film thickness. *Applied Physics B: Lasers and Optics*, 64(3):387–390, mar 1997. ISSN 09462171. doi: 10.1007/s003400050189. URL https://doi.org/10.1007/s003400050189http://link.springer.com/10.1007/s003400050189.

[117] L.V. Tanatarov M.I. Kaganov, I.M. Lifshitz. Relaxation between Electrons and the Crystalline Lattice. *Jetp*, 4(9):173, 1955.

[118] S I Anisimov, A M Bonch-Bruevich, M A El'yashevich, Y A Imas, N A Pavlenko, and G S Romanov. Effect of powerful light fluxes on metals. *Sov. Phys.Tech. Phys.*, 11(7):945–952, 1967.

[119] S.I. Anisimov, B.L. Kapeliovich, and T.L. Perel-man. Electron emission from metal surfaces exposed to ultrashort laser pulses. *Journal of Experimental and Theoretical Physics*, 66(2):375–377, 1974. ISSN 1063-7761.

[120] Philip B. Allen. Theory of thermal relaxation of electrons in metals. *Physical Review Letters*, 59(13):1460–1463, sep 1987. ISSN 00319007. doi: 10.1103/PhysRevLett.59.1460. URL `https://link.aps.org/doi/10.1103/PhysRevLett.59.1460`.

[121] Zhibin Lin, Leonid V. Zhigilei, and Vittorio Celli. Electron-phonon coupling and electron heat capacity of metals under conditions of strong electron-phonon nonequilibrium. *Physical Review B - Condensed Matter and Materials Physics*, 77(7):75133, feb 2008. ISSN 10980121. doi: 10.1103/PhysRevB.77.075133. URL `https://link.aps.org/doi/10.1103/PhysRevB.77.075133`.

[122] S. D. Brorson, A. Kazeroonian, J. S. Moodera, D. W. Face, T. K. Cheng, E. P. Ippen, M. S. Dresselhaus, and G. Dresselhaus. Femtosecond room-temperature measurement of the electron-phonon coupling constant in metallic superconductors. *Physical Review Letters*, 64(18):2172–2175, apr 1990. ISSN 00319007. doi: 10.1103/PhysRevLett.64.2172. URL `https://link.aps.org/doi/10.1103/PhysRevLett.64.2172`.

[123] http://www.faculty.virginia.edu/CompMat/electron-phonon-coupling/.

[124] Zhibin Lin and Leonid V. Zhigilei. Temperature dependences of the electron-phonon coupling, electron heat capacity and thermal conductivity in Ni under femtosecond laser irradiation. *Applied Surface Science*, 253(15):6295–6300, 2007. ISSN 01694332. doi: 10.1016/j.apsusc.2007.01.032. URL `https://www.sciencedirect.com/science/article/pii/S0169433207000815`.

[125] Miao He, Chengping Wu, Maxim V. Shugaev, German D. Samolyuk, and Leonid V. Zhigilei. Computational Study of Short-Pulse Laser-Induced Gen-

eration of Crystal Defects in Ni-Based Single-Phase Binary Solid-Solution Alloys. *Journal of Physical Chemistry C*, 123(4):2202–2215, 2019. ISSN 19327455. doi: 10.1021/acs.jpcc.8b09922. URL https://doi.org/10.1021/acs.jpcc.8b09922.

[126] Nils Brouwer and Bärbel Rethfeld. Excitation and relaxation dynamics in dielectrics irradiated by an intense ultrashort laser pulse. *Journal of the Optical Society of America B*, 31(11):C28, nov 2014. ISSN 0740-3224. doi: 10.1364/josab.31.000c28. URL http://josab.osa.org/abstract.cfm?URI=josab-31-11-C28.

[127] Theodore Sjodin, Hrvoje Petek, and Hai Lung Dai. Ultrafast carrier dynamics in silicon: A two-color transient reflection grating study on a (111) surface. *Physical Review Letters*, 81(25):5664–5667, 1998. ISSN 10797114. doi: 10.1103/PhysRevLett.81.5664. URL http://dx.doi.org/10.1103/PhysRevLett.81.5664.

[128] A. J. Sabbah and D. M. Riffe. Femtosecond pump-probe reflectivity study of silicon carrier dynamics. *Physical Review B - Condensed Matter and Materials Physics*, 66(16):1–11, oct 2002. ISSN 1550235X. doi: 10.1103/PhysRevB.66.165217. URL https://link.aps.org/doi/10.1103/PhysRevB.66.165217.

[129] Seongtae Jeong and Jeffrey Bokor. Ultrafast carrier dynamics near the si(100)2×1 surface. *Physical Review B - Condensed Matter and Materials Physics*, 59(7):4943–4951, feb 1999. ISSN 1550235X. doi: 10.1103/PhysRevB.59.4943. URL https://link.aps.org/doi/10.1103/PhysRevB.59.4943.

[130] Mourad El Kharrazi. *Elektronischer Transport über Metall-Isolator-Grenzflächen*. PhD thesis, University of Duisburg-Essen, 2011.

[131] M. P. Lenyuk and K. V. Lakusta. Hyperbolic heat-conduction equation. Mixed boundary-value problem. *Journal of Engineering Physics and Thermophysics*, 82(1):170–175, 2009. ISSN 10620125. doi: 10.1007/s10891-009-0177-x. URL https://doi.org/10.1007/s10891-009-0177-x.

[132] J. Klossika, U. Gratzke, M. Vicanek, and G. Simon. Importance of a finite speed of heat propagation in metals irradiated by femtosecond laser pulses. *Physical Review B - Condensed Matter and Materials Physics*, 54 (15):10277–10279, 1996. ISSN 1550235X. doi: 10.1103/PhysRevB.54.10277. URL https://link.aps.org/doi/10.1103/PhysRevB.54.10277.

[133] N. A. Inogamov and Yu V. Petrov. Thermal conductivity of metals with hot electrons. *Journal of Experimental and Theoretical Physics*, 110(3):446–468, 2010. ISSN 10637761. doi: 10.1134/S1063776110030088. URL https://doi.org/10.1134/S1063776110030088.

[134] S. I. Anisimov and B. Relhfeld. On the theory of ultrashort laser pulse interaction with a metal. *Izvestiya Akademii Nauk. Ser. Fizicheskaya*, 61 (8):1642–1655, apr 1997. ISSN 03676765. doi: 10.1117/12.271674. URL http://dx.doi.org/10.1117/12.271674.

[135] K. Eidmann, J. Meyer-Ter-Vehn, T. Schlegel, and S. Hüller. Hydrodynamic simulation of subpicosecond laser interaction with solid-density matter. *Physical Review E - Statistical Physics, Plasmas, Fluids, and Related Interdisciplinary Topics*, 62(1B):1202–1214, jul 2000. ISSN 1063651X. doi: 10.1103/PhysRevE.62.1202. URL https://link.aps.org/doi/10.1103/PhysRevE.62.1202.

[136] K.-H. Berthel. Thermal Conduction in Semiconductors: Von J. R. Drabble und H. J. Goldsmid. Pergamon Press Ltd. New York/London/Paris 1961. 235 Seiten, zahlr. Bilder, Kld. 60s. net. *Zeitschrift für Chemie*, 3(4):159–160, sep 2010. ISSN 00442402. doi: 10.1002/zfch.19630030421. URL https://onlinelibrary.wiley.com/doi/abs/10.1002/zfch.19630030421https://onlinelibrary.wiley.com/doi/10.1002/zfch.19630030421.

[137] J. G. Fujimoto, J. M. Liu, E. P. Ippen, and N. Bloembergen. Femtosecond laser interaction with metallic tungsten and nonequilibrium electron and lattice temperatures. *Physical Review Letters*, 53(19):1837–1840, nov 1984. ISSN 00319007. doi: 10.1103/PhysRevLett.53.1837. URL https://link.aps.org/doi/10.1103/PhysRevLett.53.1837.

[138] Yong Gan and J. K. Chen. A hybrid method for integrated atomistic-continuum simulation of ultrashort-pulsed laser interaction with semiconductors. *Computer Physics Communications*, 183(2):278–284, feb 2012. ISSN 00104655. doi: 10.1016/j.cpc.2011.10.002.

[139] Patrick Lorazo, Laurent J. Lewis, and Michel Meunier. Thermodynamic pathways to melting, ablation, and solidification in absorbing solids under pulsed laser irradiation. *Physical Review B - Condensed Matter and Materials Physics*, 73(13):134108, apr 2006. ISSN 10980121. doi: 10.1103/PhysRevB.73.134108. URL `https://link.aps.org/doi/10.1103/PhysRevB.73.134108`.

[140] M. J. Stephen. *Transport equations for superconductors*, volume 139 of *Lecture Notes in Physics*. Springer Berlin Heidelberg, Berlin, Heidelberg, 1965. ISBN 978-3-540-89525-1. doi: 10.1103/PhysRev.139.A197. URL `https://doi.org/10.1007/978-3-540-89526-8http://link.springer.com/10.1007/978-3-540-89526-8`.

[141] N. Ben Abdallah and P. Degond. On a hierarchy of macroscopic models for semiconductors. *Journal of Mathematical Physics*, 37(7):3306–3333, 1996. ISSN 00222488. doi: 10.1063/1.531567. URL `https://doi.org/10.1063/1.531567`.

[142] Datong Chen, Edwin C. Kan, Umberto Ravaioli, Chi Wang Shu, and Robert W. Dutton. An Improved Energy Transport Model Including Nonparabolicity and Non-Maxwellian Distribution Effects. *IEEE Electron Device Letters*, 13(1):26–28, jan 1992. ISSN 15580563. doi: 10.1109/55.144940.

[143] Christian Schmeiser and Alexander Zwirchmayr. Elastic and drift-diffusion limits of electron-phonon interaction in semiconductors. *Mathematical Models and Methods in Applied Sciences*, 8(1):37–53, 1998. ISSN 02182025. doi: 10.1142/S0218202598000032. URL `https://doi.org/10.1142/S0218202598000032`.

[144] K. Sokolowski-Tinten, J. Bialkowski, A. Cavalleri, D. Von der Linde, A. Oparin, J. Meyer-Ter-Vehn, and S. I. Anisimov. Transient states of

matter during short pulse laser ablation. *Physical Review Letters*, 81(1): 224–227, jul 1998. ISSN 10797114. doi: 10.1103/PhysRevLett.81.224. URL https://link.aps.org/doi/10.1103/PhysRevLett.81.224.

[145] N. Fabricius, P. Hermes, D. von der Linde, A. Pospieszczyk, and B. Stritzker. Observation of superheating during picosecond laser melting. *Solid State Communications*, 58(4):239–242, 1986. ISSN 00381098. doi: 10.1016/0038-1098(86)90209-7. URL http://www.sciencedirect.com/science/article/pii/0038109886902097.

[146] Bradley J. Siwick, Jason R. Dwyer, Robert E. Jordan, and R. J.Dwayne Miller. An Atomic-Level View of Melting Using Femtosecond Electron Diffraction. *Science*, 302(5649):1382–1385, 2003. ISSN 00368075. doi: 10.1126/science.1090052. URL http://science.sciencemag.org/content/302/5649/1382.

[147] Dmitriy Ivanov and Leonid Zhigilei. Combined atomistic-continuum modeling of short-pulse laser melting and disintegration of metal films. *Physical Review B - Condensed Matter and Materials Physics*, 68(6): 064114, aug 2003. ISSN 1550235X. doi: 10.1103/PhysRevB.68.064114. URL https://doi.org/10.1103/physrevb.68.064114https://link.aps.org/doi/10.1103/PhysRevB.68.064114.

[148] V. I. Motorin and S. L. Musher. Kinetics of the volume melting. Nucleation and superheating of metals. *The Journal of Chemical Physics*, 81(1):465–469, 1984. ISSN 00219606. doi: 10.1063/1.447326. URL https://doi.org/10.1063/1.447326.

[149] Fairoja Cheenicode Kabeer, Eeuwe S. Zijlstra, and Martin E. Garcia. Road of warm dense noble metals to the plasma state: Ab initio theory of the ultrafast structural dynamics in warm dense matter. *Physical Review B - Condensed Matter and Materials Physics*, 89(10):100301, 2014. ISSN 1550235X. doi: 10.1103/PhysRevB.89.100301. URL https://link.aps.org/doi/10.1103/PhysRevB.89.100301.

[150] Szymon L. Daraszewicz, Yvelin Giret, Nobuyasu Naruse, Yoshie Murooka,

Jinfeng Yang, Dorothy M. Duffy, Alexander L. Shluger, and Katsumi Tanimura. Structural dynamics of laser-irradiated gold nanofilms. *Physical Review B - Condensed Matter and Materials Physics*, 88(18):184101, nov 2013. ISSN 10980121. doi: 10.1103/PhysRevB.88.184101. URL https://link.aps.org/doi/10.1103/PhysRevB.88.184101.

[151] P. Stampfli and K. H. Bennemann. Time dependence of the laser-induced femtosecond lattice instability of Si and GaAs: Role of longitudinal optical distortions. *Physical Review B*, 49(11):7299–7305, 1994. ISSN 01631829. doi: 10.1103/PhysRevB.49.7299. URL https://link.aps.org/doi/10.1103/PhysRevB.49.7299.

[152] H. W.K. Tom, G. D. Aumiller, and C. H. Brito-Cruz. Time-resolved study of laser-induced disorder of Si surfaces. *Physical Review Letters*, 60(14): 1438–1441, apr 1988. ISSN 00319007. doi: 10.1103/PhysRevLett.60.1438. URL https://link.aps.org/doi/10.1103/PhysRevLett.60.1438.

[153] C. V. Shank, R. Yen, and C. Hirlimann. Time-resolved reflectivity measurements of femtosecond-optical-pulse- induced phase transitions in silicon. *Physical Review Letters*, 50(6):454–457, feb 1983. ISSN 00319007. doi: 10.1103/PhysRevLett.50.454. URL https://link.aps.org/doi/10.1103/PhysRevLett.50.454.

[154] N. A. Inogamov, V. A. Khokhlov, Yu V. Petrov, and V. V. Zhakhovsky. Hydrodynamic and molecular-dynamics modeling of laser ablation in liquid: from surface melting till bubble formation. *Optical and Quantum Electronics*, 52 (2), 2020. ISSN 1572817X. doi: 10.1007/s11082-019-2168-2.

[155] Lalit Shokeen and Patrick K. Schelling. Thermodynamics and kinetics of silicon under conditions of strong electronic excitation. *Journal of Applied Physics*, 109(7):073503, apr 2011. ISSN 00218979. doi: 10.1063/1.3554410. URL http://aip.scitation.org/doi/10.1063/1.3554410.

[156] K. Lu and Y. Li. Homogeneous Nucleation Catastrophe as a Kinetic Stability Limit for Superheated Crystal. *Physical Review Letters*, 80(20), 1998. ISSN 10797114. doi: 10.1103/PhysRevLett.80.4474.

[157] Sergey Galitskiy, Dmitry S. Ivanov, and Avinash M. Dongare. Dynamic evolution of microstructure during laser shock loading and spall failure of single crystal Al at the atomic scales. *Journal of Applied Physics*, 124(20), 2018. ISSN 10897550. doi: 10.1063/1.5051618.

[158] Leonid V. Zhigilei and Barbara J. Garrison. Pressure waves in microscopic simulations of laser ablation. *Materials Research Society Symposium - Proceedings*, 538:491–496, jan 1999. ISSN 02729172. doi: 10.1557/proc-538-491. URL `http://dx.doi.org/10.1557/PROC-538-491`.

[159] J. P. Colombier, P. Combis, R. Stoian, and E. Audouard. High shock release in ultrafast laser irradiated metals: Scenario for material ejection. *Physical Review B - Condensed Matter and Materials Physics*, 75(10):104105, 2007. ISSN 1550235X. doi: 10.1103/PhysRevB.75.104105. URL `https://link.aps.org/doi/10.1103/PhysRevB.75.104105`.

[160] F. Korte, J. Serbin, J. Koch, A. Egbert, C. Fallnich, A. Ostendorf, and B. N. Chichkov. Towards nanostructuring with femtosecond laser pulses. *Applied Physics A: Materials Science and Processing*, 77(2), 2003. ISSN 09478396. doi: 10.1007/s00339-003-2110-z.

[161] S. M. Huang, M. H. Hong, B. Lukiyanchuk, and T. C. Chong. Nanostructures fabricated on metal surfaces assisted by laser with optical near-field effects. *Applied Physics A: Materials Science and Processing*, 77(2), 2003. ISSN 09478396. doi: 10.1007/s00339-003-2115-7.

[162] Kai Oliver Böker, Frederick Kleinwort, Jan Hendrick Klein-Wiele, Peter Simon, Katharina Jäckle, Shahed Taheri, Wolfgang Lehmann, and Arndt F. Schilling. Laser ablated periodic nanostructures on titanium and steel implants influence adhesion and osteogenic differentiation of mesenchymal stem cells. *Materials*, 13(16), 2020. ISSN 19961944. doi: 10.3390/MA13163526.

[163] A. Chimmalgi, T. Y. Choi, C. P. Grigoropoulos, and K. Komvopoulos. Femtosecond laser aperturless near-field nanomachining of metals assisted by scanning probe microscopy. *Applied Physics Letters*, 82(8), 2003. ISSN 00036951. doi: 10.1063/1.1555693.

[164] J. Jersch, F. Demming, J. Hildenhagen, and K. Dickmann. Nano-material processing with laser radiation in the near field of a scanning probe tip. *Optics and Laser Technology*, 29(8), 1998. ISSN 00303992. doi: 10.1016/s0030-3992(97)00051-0.

[165] J. S. Preston, H. M. Van Driel, and J. E. Sipe. Pattern formation during laser melting of silicon. *Physical Review B*, 40(6):3942–3954, aug 1989. ISSN 01631829. doi: 10.1103/PhysRevB.40.3942. URL `https://link.aps.org/doi/10.1103/PhysRevB.40.3942`.

[166] Juergen Reif, Olga Varlamova, Sebastian Uhlig, Sergej Varlamov, and Michael Bestehorn. On the physics of self-organized nanostructure formation upon femtosecond laser ablation. *Applied Physics A: Materials Science and Processing*, 117(1):179–184, oct 2014. ISSN 14320630. doi: 10.1007/s00339-014-8339-x. URL `https://doi.org/10.1007/s00339-014-8339-xhttp://link.springer.com/10.1007/s00339-014-8339-x`.

[167] Stefan Rung, Kevin Bokan, Frederick Kleinwort, Simon Schwarz, Peter Simon, Jan Hendrik Klein-Wiele, Cemal Esen, and Ralf Hellmann. Possibilities of dry and lubricated friction modification enabled by different ultrashort laser-based surface structuring methods. *Lubricants*, 7(5), 2019. ISSN 20754442. doi: 10.3390/lubricants7050043.

[168] Lewin Rathmann, Lucas Hermann Beste, and Tim Radel. Laser based process chain to use LIPSS on forming tools. *Surface and Coatings Technology*, 426, 2021. ISSN 02578972. doi: 10.1016/j.surfcoat.2021.127761.

[169] Sumit Parvate, Prakhar Dixit, and Sujay Chattopadhyay. Superhydrophobic Surfaces: Insights from Theory and Experiment, 2020. ISSN 15205207.

[170] Hamza Messaoudi, Susanta Kumar Das, Janine Lange, Friedhelm Heinrich, Sigurd Schrader, Marcus Frohme, and Rüdiger Grunwald. Femtosecond-Laser Induced Periodic Surface Structures for Surface Enhanced Raman Spectroscopy of Biomolecules. 2015. doi: 10.1007/978-3-319-12217-5_12.

[171] M. Iqbal, S. A. Khan, D. S. Ivanov, R. A. Ganeev, V. V. Kim, G. S. Boltaev, I. Sapaev, N. A. Abbasi, S. Shaju, M. E. Garcia, B. Rethfeld, and A. S. Alnaser. The mechanism of laser-assisted generation of aluminum nanoparticles, their wettability and nonlinearity properties. *Applied Surface Science*, 527, 2020. ISSN 01694332. doi: 10.1016/j.apsusc.2020.146702.

[172] Md Shamim Ahsan, Yoon Young Kwon, Ik Bu Sohn, Young Chul Noh, and Man Seop Lee. Formation of periodic micro/nano-holes array in boro-aluminosilicate glass by single-pulse femtosecond laser machining. *Journal of Laser Micro Nanoengineering*, 9(1), 2014. ISSN 18800688. doi: 10.2961/jlmn.2014.01.0005.

[173] S. I. Anisimov, N. A. Inogamov, A. M. Oparin, B. Rethfeld, T. Yabe, M. Ogawa, and V. E. Fortov. Pulsed laser evaporation: Equation-of-state effects. *Applied Physics A: Materials Science and Processing*, 69(6):617–620, 1999. ISSN 09478396. doi: 10.1007/s003390051041. URL `https://doi.org/10.1007/s003390051041`.

[174] N. A. Inogamov, S. I. Anisimov, and B. Retfeld. Rarefaction wave and gravitational equilibrium in a two-phase liquid-vapor medium. *Journal of Experimental and Theoretical Physics*, 88(6):1143–1150, jun 1999. ISSN 10637761. doi: 10.1134/1.558903. URL `https://doi.org/10.1134/1.558903`.

[175] J. P. Colombier, P. Combis, F. Bonneau, R. Le Harzic, and E. Audouard. Hydrodynamic simulations of metal ablation by femtosecond laser irradiation. *Physical Review B - Condensed Matter and Materials Physics*, 71(16):165406, apr 2005. ISSN 10980121. doi: 10.1103/PhysRevB.71.165406. URL `https://link.aps.org/doi/10.1103/PhysRevB.71.165406`.

[176] M. E. Povarnitsyn, T. E. Itina, M. Sentis, K. V. Khishchenko, and P. R. Levashov. Material decomposition mechanisms in femtosecond laser interactions with metals. *Physical Review B - Condensed Matter and Materials Physics*, 75(23):235414, jun 2007. ISSN 10980121. doi: 10.1103/PhysRevB.75.235414. URL `https://link.aps.org/doi/10.1103/PhysRevB.75.235414`.

[177] N. A. Inogamov, V. V. Zhakhovskii, S. I. Ashitkov, Yu V. Petrov, M. B. Agranat, S. I. Anisimov, K. Nishihara, and V. E. Fortov. Nanospallation induced by an ultrashort laser pulse. *Journal of Experimental and Theoretical Physics*, 107(1):1–19, aug 2008. ISSN 10637761. doi: 10.1134/S1063776108070017. URL https://doi.org/10.1134/S1063776108070017.

[178] F. Cuadros, I. Cachadiña, and W. Ahumada. Determination of Lennard-Jones interaction parameters using a new procedure. *Molecular Engineering*, 6(3):319–325, sep 1996. ISSN 0925-5125. doi: 10.1007/bf01886380. URL https://doi.org/10.1007/BF01886380.

[179] Arun K. Upadhyay, Nail A. Inogamov, Bärbel Rethfeld, and Herbert M. Urbassek. Ablation by ultrashort laser pulses: Atomistic and thermodynamic analysis of the processes at the ablation threshold. *Physical Review B - Condensed Matter and Materials Physics*, 78(4):45437, jul 2008. ISSN 10980121. doi: 10.1103/PhysRevB.78.045437. URL https://link.aps.org/doi/10.1103/PhysRevB.78.045437.

[180] S. I. Anisimov, V. V. Zhakhovskiĭ, N. A. Inogamov, K. Nishihara, Yu V. Petrov, and V. A. Khokhlov. Ablated matter expansion and crater formation under the action of ultrashort laser pulse. *Journal of Experimental and Theoretical Physics*, 103(2):183–197, aug 2006. ISSN 10637761. doi: 10.1134/S1063776106080024. URL https://doi.org/10.1134/S1063776106080024.

[181] Johannes Roth, Hans Rainer Trebin, Alexander Kiselev, and Dennis Michael Rapp. Laser ablation of Al–Ni alloys and multilayers. *Applied Physics A: Materials Science and Processing*, 122(5):500, may 2016. ISSN 14320630. doi: 10.1007/s00339-016-9754-y. URL http://link.springer.com/10.1007/s00339-016-9754-y.

[182] M. B. Agranat, S. I. Anisimov, S. I. Ashitkov, V. V. Zhakhovskii, N. A. Inogamov, K. Nishihara, Yu V. Petrov, V. E. Fortov, and V. A. Khokhlov. Dynamics of plume and crater formation after action of femtosecond laser pulse. *Applied Surface Science*, 253(15):6276–6282, may 2007. ISSN 01694332. doi: 10.1016/j.apsusc.2007.01.077. URL http://www.

sciencedirect.com/science/article/pii/S0169433207001547https://linkinghub.elsevier.com/retrieve/pii/S0169433207001547.

[183] J. Stadler, R. Mikulla, and H. R. Trebin. IMD: A software package for molecular dynamics studies on parallel computers. *International Journal of Modern Physics C*, 8(5):1131–1140, oct 1997. ISSN 01291831. doi: 10.1142/S0129183197000990. URL https://www.worldscientific.com/doi/abs/10.1142/S0129183197000990.

[184] Johannes Roth, Eugen Eisfeld, Dominic Klein, Stephen Hocker, Hansjörg Lipp, and Hans Rainer Trebin. IMD – the ITAP molecular dynamics simulation package. *European Physical Journal: Special Topics*, 227(14):1831–1836, mar 2019. ISSN 19516401. doi: 10.1140/epjst/e2019-800147-7. URL http://link.springer.com/10.1140/epjst/e2019-800147-7.

[185] Johannes Roth. IMD: A typical massively parallel molecular dynamics code for classical simulations - Structure, applications, latest developments. *Sustained Simulation Performance 2013 - Proceedings of the Joint Workshop on Sustained Simulation Performance*, pages 63–76, 2013. doi: 10.1007/978-3-319-01439-5_5.

[186] Lawrence F. Shampine, W. H. Press, B. P. Flannery, S. A. Teukolsky, and W. T. V. Vetterling. *Numerical Recipes, The Art of Scientific Computing.*, volume 94. Cambridge University Press, New York, NY, USA, 3 edition, 1987. ISBN 9780521880688. doi: 10.2307/2322833. URL http://www.ebook.de/de/product/6504686/william_h_press_saul_a_teukolsky_william_t_vetterling_brian_p_flannery_numerical_recipes.html.

[187] R. Courant, K. Friedrichs, and H. Lewy. Über die partiellen Differenzengleichungen der mathematischen Physik. *Mathematische Annalen*, 100(1):32–74, 1928. ISSN 00255831. doi: 10.1007/BF01448839. URL https://doi.org/10.1007/BF01448839.

[188] J. Crank and P. Nicolson. A practical method for numerical evaluation of solutions of partial differential equations of the heat-conduction type. *Mathe-*

matical Proceedings of the Cambridge Philosophical Society, 43(1):50–67, 1947. ISSN 14698064. doi: 10.1017/S0305004100023197.

[189] Daan Frenkel, Berend Smit, Jan Tobochnik, Susan R. McKay, and Wolfgang Christian. *Understanding Molecular Simulation*, volume 11. Academic Press, Inc., Orlando, FL, USA, 2nd edition, 1997. ISBN 0122673514. doi: 10.1063/1.4822570.

[190] Denis J. Evans and Brad Lee Holian. The Nose-Hoover thermostat. *The Journal of Chemical Physics*, 83(8):4069–4074, aug 1985. ISSN 00219606. doi: 10.1063/1.449071. URL `https://aip.scitation.org/doi/abs/10.1063/1.449071`.

[191] Byeong Joo Lee and M. I. Baskes. Second nearest-neighbor modified embedded-atom-method potential. *Physical Review B - Condensed Matter and Materials Physics*, 62(13):8564–8567, 2000. ISSN 01631829. doi: 10.1103/PhysRevB.62.8564. URL `http://dx.doi.org/10.1103/PhysRevB.62.8564`.

[192] Frank H. Stillinger and Thomas A. Weber. Computer simulation of local order in condensed phases of silicon. *Physical Review B*, 31(8):5262–5271, apr 1985. ISSN 01631829. doi: 10.1103/PhysRevB.31.5262. URL `http://dx.doi.org/10.1103/PhysRevB.31.5262`.

[193] J. Tersoff. New empirical approach for the structure and energy of covalent systems. *Physical Review B*, 37(12):6991–7000, apr 1988. ISSN 01631829. doi: 10.1103/PhysRevB.37.6991. URL `http://dx.doi.org/10.1103/PhysRevB.37.6991`.

[194] T. Kumagai, S. Izumi, S. Hara, and S. Sakai. Development of bond-order potentials that can reproduce the elastic constants and melting point of silicon for classical molecular dynamics simulation. *Computational Materials Science*, 39(2):457–464, apr 2007. ISSN 09270256. doi: 10.1016/j.commatsci.2006.07.013. URL `http://dx.doi.org/10.1016/j.commatsci.2006.07.013`.

[195] João F. Justo, Martin Z. Bazant, and Efthimios Kaxiras. Interatomic potential for silicon defects and disordered phases. *Physical Review B - Condensed Mat-*

ter and Materials Physics, 58(5):2539–2550, aug 1998. ISSN 1550235X. doi: 10.1103/PhysRevB.58.2539. URL http://dx.doi.org/10.1103/PhysRevB.58.2539.

[196] Maria Timonova and Barend J. Thijsse. Thermodynamic properties and phase transitions of silicon using a new MEAM potential. *Computational Materials Science*, 48(3):609–620, 2010. ISSN 09270256. doi: 10.1016/j.commatsci.2010.02.029. URL http://dx.doi.org/10.1016/j.commatsci.2010.02.029.

[197] J. Tersoff. Empirical interatomic potential for silicon with improved elastic properties. *Physical Review B*, 38(14):9902–9905, nov 1988. ISSN 01631829. doi: 10.1103/PhysRevB.38.9902. URL http://dx.doi.org/10.1103/PhysRevB.38.9902.

[198] Bernd Bauerhenne, Eeuwe S. Zijlstra, and Martin E. Garcia. Molecular dynamics simulations of a femtosecond-laser-induced solid-to-solid transition in antimony. *Applied Physics A: Materials Science and Processing*, 123(9):608, sep 2017. ISSN 14320630. doi: 10.1007/s00339-017-1216-7. URL https://doi.org/10.1007/s00339-017-1216-7.

[199] J. Roth, A. Kiselev, and H. R. Trebin. Studying laser ablation with molecular dynamics simulations: From metals to covalent materials. In *2016 Progress In Electromagnetics Research Symposium, PIERS 2016 - Proceedings*, pages 2420–2424, aug 2016. ISBN 9781509060931. doi: 10.1109/PIERS.2016.7734998.

[200] G. Kresse and J. Hafner. Ab initio molecular dynamics for liquid metals. *Physical Review B*, 47(1):558–561, jan 1993. ISSN 01631829. doi: 10.1103/PhysRevB.47.558. URL http://dx.doi.org/10.1103/PhysRevB.47.558.

[201] G. Kresse and J. Furthmüller. Efficiency of ab-initio total energy calculations for metals and semiconductors using a plane-wave basis set. *Computational Materials Science*, 6(1):15–50, jul 1996. ISSN 09270256. doi: 10.1016/0927-0256(96)00008-0. URL http://dx.doi.org/10.1016/0927-0256(96)00008-0.

[202] G. Kresse and J. Furthmüller. Efficient iterative schemes for ab initio total-energy calculations using a plane-wave basis set. *Physical Review B - Condensed Matter and Materials Physics*, 54(16):11169–11186, 1996. ISSN 1550235X. doi: 10.1103/PhysRevB.54.11169. URL http://dx.doi.org/10.1103/PhysRevB.54.11169.

[203] Peter Brommer and Franz Gähler. Potfit: Effective potentials from ab initio data. *Modelling and Simulation in Materials Science and Engineering*, 15 (3):295–304, 2007. ISSN 09650393. doi: 10.1088/0965-0393/15/3/008. URL http://dx.doi.org/10.1088/0965-0393/15/3/008.

[204] P. Brommer and F. Gähler. Effective potentials for quasicrystals from ab-initio data. *Philosophical Magazine*, 86(6-8):753–758, feb 2006. ISSN 14786435. doi: 10.1080/14786430500333349. URL http://dx.doi.org/10.1080/14786430500333349.

[205] Peter Brommer, Alexander Kiselev, Daniel Schopf, Philipp Beck, Johannes Roth, and Hans Rainer Trebin. Classical interaction potentials for diverse materials from ab initio data: A review of potfit. *Modelling and Simulation in Materials Science and Engineering*, 23(7):74002, sep 2015. ISSN 1361651X. doi: 10.1088/0965-0393/23/7/074002. URL http://dx.doi.org/10.1088/0965-0393/23/7/074002.

[206] Alexander Stukowski. Structure identification methods for atomistic simulations of crystalline materials. *Modelling and Simulation in Materials Science and Engineering*, 20(4):45021, 2012. ISSN 09650393. doi: 10.1088/0965-0393/20/4/045021. URL https://doi.org/10.1088%2F0965-0393%2F20%2F4%2F045021.

[207] Cynthia L. Kelchner and S. Plimpton. Dislocation nucleation and defect structure during surface indentation. *Physical Review B - Condensed Matter and Materials Physics*, 58(17):11085–11088, nov 1998. ISSN 1550235X. doi: 10.1103/PhysRevB.58.11085. URL https://link.aps.org/doi/10.1103/PhysRevB.58.11085.

[208] Paul J. Steinhardt, David R. Nelson, and Marco Ronchetti. Bond-orientational order in liquids and glasses. *Physical Review B*, 28(2):784–805, jul 1983. ISSN 01631829. doi: 10.1103/PhysRevB.28.784. URL https://link.aps.org/doi/10.1103/PhysRevB.28.784.

[209] Caroline Desgranges and Jerome Delhommelle. Crystallization mechanisms for supercooled liquid Xe at high pressure and temperature: Hybrid Monte Carlo molecular simulations. *Physical Review B - Condensed Matter and Materials Physics*, 77(5):54201, feb 2008. ISSN 10980121. doi: 10.1103/PhysRevB.77.054201. URL https://link.aps.org/doi/10.1103/PhysRevB.77.054201.

[210] Wolfgang Lechner and Christoph Dellago. Accurate determination of crystal structures based on averaged local bond order parameters. *Journal of Chemical Physics*, 129(11):114707, 2008. ISSN 00219606. doi: 10.1063/1.2977970. URL https://doi.org/10.1063/1.2977970.

[211] G. J. Ackland and A. P. Jones. Applications of local crystal structure measures in experiment and simulation. *Physical Review B - Condensed Matter and Materials Physics*, 73(5):54104, feb 2006. ISSN 10980121. doi: 10.1103/PhysRevB.73.054104. URL https://link.aps.org/doi/10.1103/PhysRevB.73.054104.

[212] E. Maras, O. Trushin, A. Stukowski, T. Ala-Nissila, and H. Jónsson. Global transition path search for dislocation formation in Ge on Si(001). *Computer Physics Communications*, 205:13–21, 2016. ISSN 00104655. doi: 10.1016/j.cpc.2016.04.001. URL http://www.sciencedirect.com/science/article/pii/S0010465516300893.

[213] Alexander Stukowski. Visualization and analysis of atomistic simulation data with OVITO-the Open Visualization Tool. *Modelling and Simulation in Materials Science and Engineering*, 18(1):15012, jan 2010. ISSN 09650393. doi: 10.1088/0965-0393/18/1/015012. URL http://dx.doi.org/10.1088/0965-0393/18/1/015012.

[214] Y. P. Varshni. Temperature dependence of the energy gap in semiconductors. *Physica*, 34(1):149–154, jan 1967. ISSN 00318914. doi: 10.1016/0031-8914(67)

90062-6. URL http://dx.doi.org/10.1016/0031-8914(67)90062-6https://linkinghub.elsevier.com/retrieve/pii/0031891467900626.

[215] G. E. Jellison and F. A. Modine. Optical functions of silicon between 1.7 and 4.7 eV at elevated temperatures. *Physical Review B*, 27(12):7466–7472, jun 1983. ISSN 01631829. doi: 10.1103/PhysRevB.27.7466. URL https://link.aps.org/doi/10.1103/PhysRevB.27.7466.

[216] D. P. Korfiatis, K. A.Th Thoma, and J. C. Vardaxoglou. Conditions for femtosecond laser melting of silicon. *Journal of Physics D: Applied Physics*, 40(21):6803–6808, nov 2007. ISSN 00223727. doi: 10.1088/0022-3727/40/21/047. URL https://doi.org/10.1088%2F0022-3727%2F40%2F21%2F047https://iopscience.iop.org/article/10.1088/0022-3727/40/21/047.

[217] B. S. Wherrett. Scaling rules for multiphoton interband absorption in semiconductors. *Journal of the Optical Society of America B*, 1(1):67, 1984. ISSN 0740-3224. doi: 10.1364/josab.1.000067. URL http://josab.osa.org/abstract.cfm?URI=josab-1-1-67.

[218] G. E. Jellison and F. A. Modine. Optical absorption of silicon between 1.6 and 4.7 eV at elevated temperatures. *Applied Physics Letters*, 41(2):180–182, 1982. ISSN 00036951. doi: 10.1063/1.93454. URL https://doi.org/10.1063/1.93454.

[219] K. P. O'Donnell and X. Chen. Temperature dependence of semiconductor band gaps. *Applied Physics Letters*, 58(25):2924–2926, 1991. ISSN 00036951. doi: 10.1063/1.104723. URL https://doi.org/10.1063/1.104723.

[220] A. G. Chynoweth. Ionization rates for electrons and holes in silicon. *Physical Review*, 109(5):1537–1540, 1958. ISSN 0031899X. doi: 10.1103/PhysRev.109.1537. URL http://dx.doi.org/10.1103/PhysRev.109.1537.

[221] D. Agassi. Phenomenological model for pisosecond-pulse laser annealing of semiconductors. *Journal of Applied Physics*, 55(12):4376–4383, 1984. ISSN 00218979. doi: 10.1063/1.333007. URL http://dx.doi.org/10.1063/1.333007.

[222] J. A. Van Vechten and A. D. Compaan. Plasma annealing state of semiconductors; plasma condensation to a superconductivity- like state at 1000 K? *Solid State Communications*, 39(8):867–873, 1981. ISSN 00381098. doi: 10.1016/0038-1098(81)90027-2. URL http://www.sciencedirect.com/science/article/pii/0038109881900272.

[223] A. Lietoila and J. F. Gibbons. Computer modeling of the temperature rise and carrier concentration induced in silicon by nanosecond laser pulses. *Journal of Applied Physics*, 53(4):3207–3213, 1982. ISSN 00218979. doi: 10.1063/1.331020. URL https://doi.org/10.1063/1.331020.

[224] A. Lietoila and J. F. Gibbons. CALCULATION OF CARRIER AND LATTICE TEMPERATURES INDUCED IN Si AND GaAs BY PICOSECOND LASER PULSES. *Materials Research Society Symposia Proceedings*, 4:163–168, 1982. ISSN 02729172. doi: 10.1557/proc-4-163.

[225] Ellen J. Yoffa. Dynamics of dense laser-induced plasmas. *Physical Review B*, 21(6):2415–2425, 1980. ISSN 01631829. doi: 10.1103/PhysRevB.21.2415. URL http://dx.doi.org/10.1103/PhysRevB.21.2415.

[226] H. D. Barber. Effective mass and intrinsic concentration in silicon. *Solid State Electronics*, 10(11):1039–1051, nov 1967. ISSN 00381101. doi: 10.1016/0038-1101(67)90122-0.

[227] M. Glicksman. Physics of Semiconductor Devices. S. M. Sze. Interscience (Wiley), New York, 1969. xvi + 814 pp. *Science*, 166(3909):1135–1135, nov 1969. ISSN 0036-8075. doi: 10.1126/science.166.3909.1135. URL https://science.sciencemag.org/content/166/3909/1135.1https://www.sciencemag.org/lookup/doi/10.1126/science.166.3909.1135.

[228] R. F. Wood and G. E. Giles. Macroscopic theory of pulsed-laser annealing. I. Thermal transport and melting. *Physical Review B*, 23(6):2923–2942, mar 1981. ISSN 01631829. doi: 10.1103/PhysRevB.23.2923. URL https://link.aps.org/doi/10.1103/PhysRevB.23.2923.

[229] K. G. Svantesson and N. G. Nilsson. Determination of the temperature dependence of the free carrier and interband absorption in silicon at 1.06μm. *Journal of Physics C: Solid State Physics*, 12(18):3837–3842, 1979. ISSN 00223719. doi: 10.1088/0022-3719/12/18/029. URL http://stacks.iop.org/0022-3719/12/i=18/a=029.

[230] K. G. Svantesson. Determination of the interband and the free carrier absorption constants in silicon at high-level photoinjection. *Journal of Physics D: Applied Physics*, 12(3):425–436, 1979. ISSN 00223727. doi: 10.1088/0022-3727/12/3/012. URL https://doi.org/10.1088%2F0022-3727%2F12%2F3%2F012.

[231] K. G. Svantesson and N. G. Nilsson. The temperature dependence of the Auger recombination coefficient of undoped silicon. *Journal of Physics C: Solid State Physics*, 12(23):5111–5120, 1979. ISSN 00223719. doi: 10.1088/0022-3719/12/23/019. URL http://stacks.iop.org/0022-3719/12/i=23/a=019.

[232] K. Sokolowski-Tinten, J. Bialkowski, and D. Von Der Linde. Ultrafast laser-induced order-disorder transitions in semiconductors. *Physical Review B*, 51 (20):14186–14198, 1995. ISSN 01631829. doi: 10.1103/PhysRevB.51.14186. URL https://link.aps.org/doi/10.1103/PhysRevB.51.14186.

[233] B. Rethfeld, H. Krutsch, and D. H.H. Hoffmann. Tracing laser-induced dielectric breakdown in solids. *Contributions to Plasma Physics*, 50(1): 16–20, 2010. ISSN 08631042. doi: 10.1002/ctpp.201010005. URL https://onlinelibrary.wiley.com/doi/abs/10.1002/ctpp.201010005.

[234] E. P. Silaeva, N. S. Shcheblanov, T. E. Itina, A. Vella, J. Houard, N. Sévelin-Radiguet, F. Vurpillot, and B. Deconihout. Numerical study of femtosecond laser-assisted atom probe tomography. *Applied Physics A: Materials Science and Processing*, 110(3):703–707, 2013. ISSN 14320630. doi: 10.1007/s00339-012-7189-7. URL https://doi.org/10.1007/s00339-012-7189-7.

[235] Hao Zhang, D. Van Oosten, D. M. Krol, and J. I. Dijkhuis. Saturation effects in femtosecond laser ablation of silicon-on-insulator. *Applied Physics Letters*, 99(23):231108, 2011. ISSN 00036951. doi: 10.1063/1.3666423. URL https://doi.org/10.1063/1.3666423.

[236] S. Guizard, A. Semerok, J. Gaudin, M. Hashida, P. Martin, and F. Quéré. Femtosecond laser ablation of transparent dielectrics: Measurement and modelisation of crater profiles. *Applied Surface Science*, 186(1-4):364–368, 2002. ISSN 01694332. doi: 10.1016/S0169-4332(01)00681-X. URL http://www.sciencedirect.com/science/article/pii/S016943320100681X.

[237] B. Rethfeld, O. Brenk, N. Medvedev, H. Krutsch, and D. H.H. Hoffmann. Interaction of dielectrics with femtosecond laser pulses: Application of kinetic approach and multiple rate equation. *Applied Physics A: Materials Science and Processing*, 101(1):19–25, 2010. ISSN 09478396. doi: 10.1007/s00339-010-5780-3. URL https://doi.org/10.1007/s00339-010-5780-3.

[238] N. Medvedev, B. Ziaja, M. Cammarata, M. Harmand, and S. Toleikis. Electron kinetics in femtosecond x-ray irradiated SiO2. *Contributions to Plasma Physics*, 53(4-5):347–354, 2013. ISSN 08631042. doi: 10.1002/ctpp.201200095. URL https://onlinelibrary.wiley.com/doi/abs/10.1002/ctpp.201200095.

[239] Monique Combescot and Roland Combescot. Conductivity relaxation time due to electron-hole collisions in optically excited semiconductors. *Physical Review B*, 35(15):7986–7992, 1987. ISSN 01631829. doi: 10.1103/PhysRevB.35.7986. URL https://link.aps.org/doi/10.1103/PhysRevB.35.7986.

[240] D. Hulin, M. Combescot, J. Bok, A. Migus, J. Y. Vinet, and A. Antonetti. Energy transfer during silicon irradiation by femtosecond laser pulse. *Physical Review Letters*, 52(22):1998–2001, 1984. ISSN 00319007. doi: 10.1103/PhysRevLett.52.1998. URL https://link.aps.org/doi/10.1103/PhysRevLett.52.1998.

[241] Bo E. Sernelius. Optical free-carrier absorption of an electron-hole plasma in silicon. *Physical Review B*, 39(15):10825–10830, 1989. ISSN 01631829. doi: 10.1103/PhysRevB.39.10825. URL https://link.aps.org/doi/10.1103/PhysRevB.39.10825.

[242] N. Medvedev and B. Rethfeld. A comprehensive model for the ultrashort visible light irradiation of semiconductors. *Journal of Applied Physics*, 108

(10):103112, 2010. ISSN 00218979. doi: 10.1063/1.3511455. URL https://doi.org/10.1063/1.3511455.

[243] Y. T. Lee and R. M. More. An electron conductivity model for dense plasmas. *Physics of Fluids*, 27(5):1273–1286, 1984. ISSN 10706631. doi: 10.1063/1.864744. URL https://aip.scitation.org/doi/abs/10.1063/1.864744.

[244] Mircea S. Rogalski and Stuart B. Palmer. *Solid state physics*. Cengage Learning, 2014. ISBN 9781482283037. doi: 10.1201/9781482283037. URL https://books.google.de/books?id=x_s_YAAACAAJ.

[245] G. E. Jellison and F. A. Modine. Optical functions of silicon at elevated temperatures. *Journal of Applied Physics*, 76(6):3758–3761, sep 1994. ISSN 00218979. doi: 10.1063/1.357378. URL https://doi.org/10.1063/1.357378http://aip.scitation.org/doi/10.1063/1.357378.

[246] D. H. Reitze, T. R. Zhang, Wm. M. Wood, and M. C. Downer. Two-photon spectroscopy of silicon using femtosecond pulses at above-gap frequencies. *Journal of the Optical Society of America B*, 7 (1):84, jan 1990. ISSN 0740-3224. doi: 10.1364/josab.7.000084. URL http://josab.osa.org/abstract.cfm?URI=josab-7-1-84https://www.osapublishing.org/abstract.cfm?URI=josab-7-1-84.

[247] Waldemar Kuett, Anton Esser, Klaus Seibert, Uli Lemmer, and Heinrich Kurz. <title>Femtosecond studies of plasma formation in crystalline and amorphous silicon</title>. In Andre Antonetti, editor, *Applications of Ultrashort Laser Pulses in Science and Technology*, volume 1268, pages 154–165. International Society for Optics and Photonics, SPIE, aug 1990. doi: 10.1117/12.20333. URL https://doi.org/10.1117/12.20333http://proceedings.spiedigitallibrary.org/proceeding.aspx?articleid=941196.

[248] Linhan Lin, Zhengcao Li, Jiayou Feng, and Zhengjun Zhang. Indirect to direct band gap transition in ultra-thin silicon films. *Physical Chemistry Chemical Physics*, 15(16):6063–6067, 2013. ISSN 14639076. doi: 10.1039/c3cp50429h. URL http://dx.doi.org/10.1039/C3CP50429Hhttp://xlink.rsc.org/?DOI=c3cp50429h.

[249] Hernando Garcia and Ramki Kalyanaraman. Phonon-assisted two-photon absorption in the presence of a dc-field: The nonlinear Franz-Keldysh effect in indirect gap semiconductors. *Journal of Physics B: Atomic, Molecular and Optical Physics*, 39(12):2737–2746, 2006. ISSN 09534075. doi: 10.1088/0953-4075/39/12/009. URL https://doi.org/10.1088%2F0953-4075%2F39%2F12%2F009.

[250] Tobias Zier, Eeuwe S. Zijlstra, Sergej Krylow, and Martin E. Garcia. Simulations of laser-induced dynamics in free-standing thin silicon films. *Applied Physics A: Materials Science and Processing*, 123(10): 625, oct 2017. ISSN 14320630. doi: 10.1007/s00339-017-1230-9. URL https://doi.org/10.1007/s00339-017-1230-9http://link.springer.com/10.1007/s00339-017-1230-9.

[251] S. Sonntag, J. Roth, and H. R. Trebin. Molecular dynamics simulations of laser induced surface melting in orthorhombic Al13Co4. *Applied Physics A: Materials Science and Processing*, 101(1), 2010. ISSN 09478396. doi: 10.1007/s00339-010-5762-5.

[252] S. Preuss, A. Demchuk, and M. Stuke. Sub-picosecond UV laser ablation of metals. *Applied Physics A Materials Science and Processing*, 61(1):33–37, 1995. ISSN 09478396. doi: 10.1007/BF01538207.

[253] D. E. Aspnes and A. A. Studna. Dielectric functions and optical parameters of Si, Ge, GaP, GaAs, GaSb, InP, InAs, and InSb from 1.5 to 6.0 eV. *Physical Review B*, 27(2):985–1009, jan 1983. ISSN 01631829. doi: 10.1103/PhysRevB.27.985. URL https://journals.aps.org/prb/abstract/10.1103/PhysRevB.27.985.

[254] S. Sonntag, C. Trichet Paredes, J. Roth, and H. R. Trebin. Molecular dynamics simulations of cluster distribution from femtosecond laser ablation in aluminum. *Applied Physics A: Materials Science and Processing*, 104 (2):559–565, 2011. ISSN 09478396. doi: 10.1007/s00339-011-6460-7. URL https://doi.org/10.1007/s00339-011-6460-7.

[255] Leonid V. Zhigilei and Barbara J. Garrison. Molecular dynamics simulation study of the fluence dependence of particle yield and plume composition in laser desorption and ablation of organic solids. *Applied Physics Letters*, 74 (9):1341–1343, 1999. ISSN 00036951. doi: 10.1063/1.123544. URL https://doi.org/10.1063/1.123544.

[256] S. R. Coon, W. F. Calaway, M. J. Pellin, and J. M. White. New findings on the sputtering of neutral metal clusters. *Surface Science*, 298(1):161–172, 1993. ISSN 00396028. doi: 10.1016/0039-6028(93)90092-X. URL http://www.sciencedirect.com/science/article/pii/003960289390092X.

[257] A. Wucher and M. Wahl. The formation of clusters during ion induced sputtering of metals. *Nuclear Instruments and Methods in Physics Research, Section B: Beam Interactions with Materials and Atoms*, 115(1-4):581–589, 1996. ISSN 0168583X. doi: 10.1016/0168-583X(96)00153-X. URL http://www.sciencedirect.com/science/article/pii/0168583X9600153X.

[258] S. R. Coon, W. F. Calaway, J. W. Burnett, M. J. Pellin, D. M. Gruen, D. R. Spiegel, and J. M. White. Yields and kinetic energy distributions of sputtered neutral copper clusters. *Surface Science*, 259(3):275–287, 1991. ISSN 00396028. doi: 10.1016/0039-6028(91)90558-A. URL http://www.sciencedirect.com/science/article/pii/003960289190558A.

[259] S. R. Coon, W. F. Calaway, and M. J. Pellin. Neutral copper cluster sputtering yields: Ne+ Ar+ and Xe+ bombardment. *Nuclear Inst. and Methods in Physics Research, B*, 90(1-4):518–522, 1994. ISSN 0168583X. doi: 10.1016/0168-583X(94)95606-5. URL http://www.sciencedirect.com/science/article/pii/0168583X94956065.

[260] A. V. Bulgakov, I. Ozerov, and W. Marine. Silicon clusters produced by femtosecond laser ablation: Non-thermal emission and gas-phase condensation. In *Applied Physics A: Materials Science and Processing*, volume 79, 2004. doi: 10.1007/s00339-004-2856-y.

[261] Andrea Cavalleri, Klaus Sokolowski-Tinten, Joerg Bialkowski, Michaela Schreiner, and Dietrich Von Der Linde. Femtosecond melting and ablation

of semiconductors studied with time of flight mass spectroscopy. *Journal of Applied Physics*, 85(6), 1999. ISSN 00218979. doi: 10.1063/1.369675.

[262] A. Cavalleri, K. Sokolowski-Tinten, J. Bialkowski, and D. Von Der Linde. Time of flight mass spectroscopy of femtosecond laser ablation of solid surfaces. *Springer Series in Chemical Physics*, 63, 1998. ISSN 01726218. doi: 10.1007/978-3-642-72289-9_94.

[263] J. Kanasaki, M. Nakamura, K. Ishikawa, and K. Tanimura. Primary Processes of Laser-Induced Selective Dimer-Layer Removal on [Formula presented]. *Physical Review Letters*, 89(25), 2002. ISSN 10797114. doi: 10.1103/PhysRevLett.89.257601.

[264] Akiko Okano and Kunio Takayanagi. Neutral silicon clusters produced by laser ablation in vacuum. *Applied Surface Science*, 127-129:362–367, may 1998. ISSN 01694332. doi: 10.1016/S0169-4332(97)00656-9. URL `https://linkinghub.elsevier.com/retrieve/pii/S0169433297006569`.

[265] Elodie Leveugle and Leonid V. Zhigilei. Molecular dynamics simulation study of the ejection and transport of polymer molecules in matrix-assisted pulsed laser evaporation. *Journal of Applied Physics*, 102(7):74914, 2007. ISSN 00218979. doi: 10.1063/1.2783898. URL `https://doi.org/10.1063/1.2783898`.

[266] R. Yen, J. M. Liu, H. Kurz, and N. Bloembergen. Space-time resolved reflectivity measurements of picosecond laser-pulse induced phase transitions in (111) silicon surface layers. *Applied Physics A Solids and Surfaces*, 27(3): 153–160, 1982. ISSN 07217250. doi: 10.1007/BF00616666. URL `https://doi.org/10.1007/BF00616666`.

[267] Chaobo Chen and Leonid V Zhigilei. Ultrashort pulse laser ablation in liquids: probing the first nanoseconds of underwater phase explosion. *Light: Science and Applications*, 11(1):111, 2022. ISSN 2047-7538. doi: 10.1038/s41377-022-00800-0. URL `https://doi.org/10.1038/s41377-022-00800-0`.

[268] Wisan Charee, Viboon Tangwarodomnukun, and Chaiya Dumkum. Laser ablation of silicon in water under different flow rates. *International Journal of Advanced Manufacturing Technology*, 78(1-4), 2015. ISSN 14333015. doi: 10.1007/s00170-014-6625-6.

[269] S. van der Linden, R. Hagmeijer, and G. R.B.E. Römer. Picosecond pulsed underwater laser ablation of silicon and stainless steel: Comparing crater analysis methods and analysing dependence of crater characteristics on water layer thickness. *Applied Surface Science*, 540, 2021. ISSN 01694332. doi: 10.1016/j.apsusc.2020.148005.

[270] Dongshi Zhang, Zhuguo Li, and Koji Sugioka. Laser ablation in liquids for nanomaterial synthesis: Diversities of targets and liquids, 2021. ISSN 25157647.

[271] J. Xiao, P. Liu, C. X. Wang, and G. W. Yang. External field-assisted laser ablation in liquid: An efficient strategy for nanocrystal synthesis and nanostructure assembly, 2017. ISSN 00796425.

[272] Peixuan Ouyang, Peijie Li, E. G. Leksina, S. V. Michurin, and Liangju He. Effect of liquid properties on laser ablation of aluminum and titanium alloys. *Applied Surface Science*, 360, 2016. ISSN 01694332. doi: 10.1016/j.apsusc.2015.11.080.

[273] Jonas Schmid. *Molecular dynamic simulation of 3D Laser Printing.* Master thesis, University of Stuttgart, 2023.

[274] J. P. Colombier, P. Combis, A. Rosenfeld, I. V. Hertel, E. Audouard, and R. Stoian. Optimized energy coupling at ultrafast laser-irradiated metal surfaces by tailoring intensity envelopes: Consequences for material removal from Al samples. *Physical Review B - Condensed Matter and Materials Physics*, 74 (22), 2006. ISSN 10980121. doi: 10.1103/PhysRevB.74.224106.

[275] L. Englert, B. Rethfeld, L. Haag, M. Wollenhaupt, Cristian Sarpe-Tudoran, and T. Baumert. Control of ionization processes in high band gap materials

via tailored femtosecond pulses. *Optics Express*, 15(26), 2007. ISSN 10944087. doi: 10.1364/oe.15.017855.

[276] Simon Kümmel. Bestimmung von Phasendiagrammen mit Simulationen anhand von elektronisch angeregtem Silizium, 2021.

[277] Eugen Eisfeld. *Molekulardynamische Simulationen der Laserablation an Aluminium unter Einbeziehung von Plasmaeffekten*. Phd thesis, Universität Stuttgart, 2020. URL `http://elib.uni-stuttgart.de/handle/11682/11293`.

[278] Alexandre Semerok and C Dutouquet. Ultrashort double pulse laser ablation of metals. Thin Solid Films 453-454, 501-505. *Thin Solid Films*, s 453–454: 501–505, 2004. doi: 10.1016/j.tsf.2003.11.115.

[279] Daniel J Förster, Sebastian Faas, Stefan Gröninger, Franziska Bauer, Andreas Michalowski, Rudolf Weber, and Thomas Graf. Shielding effects and re-deposition of material during processing of metals with bursts of ultrashort laser pulses. *Applied Surface Science*, 440:926–931, 2018. ISSN 0169-4332. doi: https://doi.org/10.1016/j.apsusc.2018.01.297. URL `https://www.sciencedirect.com/science/article/pii/S0169433218303192`.

[280] Mikhail E Povarnitsyn, Nikolay E Andreev, Eugeny M Apfelbaum, Tatiana E Itina, Konstatntin V Khishchenko, Oleg F Kostenko, Pavel R Levashov, and Mikhail E Veysman. A wide-range model for simulation of pump-probe experiments with metals. *Applied Surface Science*, 258(23):9480–9483, 2012. ISSN 0169-4332. doi: https://doi.org/10.1016/j.apsusc.2011.07.017. URL `https://www.sciencedirect.com/science/article/pii/S0169433211010725`.

[281] M E Povarnitsyn, N E Andreev, P R Levashov, K V Khishchenko, and O N Rosmej. Dynamics of thin metal foils irradiated by moderate-contrast high-intensity laser beams. *Physics of Plasmas*, 19(2):23110, 2012. doi: 10.1063/1.3683687. URL `https://doi.org/10.1063/1.3683687`.

[282] Mikhail E. Povarnitsyn, Nikolay E. Andreev, Pavel R. Levashov, Konstantin V. Khishchenko, Dmitry A. Kim, Vladimir G. Novikov, and Olga N.

Rosmej. Laser irradiation of thin films: Effect of energy transformation. *Laser and Particle Beams*, 31(4):663–671, dec 2013. ISSN 0263-0346. doi: 10.1017/S0263034613000700. URL `https://www.cambridge.org/core/product/identifier/S0263034613000700/type/journal_article`.

[283] P. N. Terekhin, O. Benhayoun, S. T. Weber, D. S. Ivanov, M. E. Garcia, and B. Rethfeld. Influence of surface plasmon polaritons on laser energy absorption and structuring of surfaces. *Applied Surface Science*, 512, 2020. ISSN 01694332. doi: 10.1016/j.apsusc.2019.144420.

[284] Klaus Czajkowski, Markus Ratzke, Olga Varlamova, and Juergen Reif. Femtosecond-laser-induced periodic surface structures on magnetic layer targets: The roles of femtosecond-laser interaction and of magnetization. *Applied Surface Science*, 417, 2017. ISSN 01694332. doi: 10.1016/j.apsusc.2017.03.148.

[285] Eugen Eisfeld, Daniel Förster, Dominic Klein, and Johannes Roth. Atomistic simulation of ultra-short pulsed laser ablation of Al: An extension for non-thermalized electrons and ballistic transport. *Journal of Physics D: Applied Physics*, 55(13), 2022. ISSN 13616463. doi: 10.1088/1361-6463/ac41f9.

[286] Simon Kümmel. *Lasertreatment of Al-Cu materials*. Master thesis, University of Stuttgart, 2023.

[287] Sarah Müller. *Selektives Laserschmelzen*. Dissertation, Universität Stuttgart, 2022.

[288] Ahmed Arabi Hassen and Michel M. Kirka. Additive manufacturings the rise of a technology and the need for quality control and inspection techniques. *Materials Evaluation*, 76(4):438–453, 2018. ISSN 00255327.

[289] Tanisha Pereira, John V. Kennedy, and Johan Potgieter. A comparison of traditional manufacturing vs additive manufacturing, the best method for the job. *Procedia Manufacturing*, 30:11–18, 2019. ISSN 23519789. doi: 10.1016/j.promfg.2019.02.003.

[290] Tuan D. Ngo, Alireza Kashani, Gabriele Imbalzano, Kate T.Q. Nguyen, and David Hui. Additive manufacturing (3D printing): A review of materials, methods, applications and challenges. *Composites Part B: Engineering*, 143: 172–196, 2018. ISSN 13598368. doi: 10.1016/j.compositesb.2018.02.012.

[291] H. Bikas, P. Stavropoulos, and G. Chryssolouris. Additive manufacturing methods and modeling approaches: A critical review. *International Journal of Advanced Manufacturing Technology*, 83(1-4):389–405, 2016. ISSN 14333015. doi: 10.1007/s00170-015-7576-2.

[292] Bi Zhang, Yongtao Li, and Qian Bai. Defect Formation Mechanisms in Selective Laser Melting: A Review. *Chinese Journal of Mechanical Engineering (English Edition)*, 30(3):515–527, 2017. ISSN 21928258. doi: 10.1007/s10033-017-0121-5. URL `https://cjme.springeropen.com/articles/10.1007/s10033-017-0121-5`.

[293] Cassiopée Galy, Emilie Le Guen, Eric Lacoste, and Corinne Arvieu. Main defects observed in aluminum alloy parts produced by SLM: From causes to consequences. *Additive Manufacturing*, 22:165–175, 2018. ISSN 22148604. doi: 10.1016/j.addma.2018.05.005. URL `https://www.sciencedirect.com/science/article/pii/S2214860417303226`.

[294] J. Hajnys, M. Pagac, J. Mesicek, J. Petru, and F. Spalek. Research of 316L Metallic Powder for Use in SLM 3D Printing. *Advances in Materials Science*, 20(1):5–15, 2020. doi: 10.2478/adms-2020-0001.

[295] J. N. Glosli, D. F. Richards, K. J. Caspersen, R. E. Rudd, J. A. Gunnels, and F. H. Streitz. Extending stability beyond CPU millennium: A micron-scale atomistic simulation of Kelvin-Helmholtz instability. In *Proceedings of the 2007 ACM/IEEE Conference on Supercomputing, SC'07*, pages 1–11, 2007. ISBN 9781595937643. doi: 10.1145/1362622.1362700.

[296] Fabio Oelschläger. Molekulardynamische Simulation von selektivem Laserschmelzen. Bachelorarbeit, Universität Stuttgart, 2021.

[297] F Oelschläger, D Klein, S Müller, and J Roth. Molecular Dynamics Simulation of Selective Laser Melting. In *High Performance Computing in Science and Engineering '21*. Springer Cham, 2022.

[298] Azad Gorgis. *Molecular dynamics simulations of selective laser melting in atmosphere*. Master thesis, University Stuttgart, 2022.

[299] Kevin Vietz. *Manufactoring of binary alloys*. Master thesis, University of Stuttgart, 2023.

[300] Mohd Faizal Sadali, Mohamad Zaki Hassan, Fauzan Ahmad, Hafizal Yahaya, and Zainudin A. Rasid. Influence of selective laser melting scanning speed parameter on the surface morphology, surface roughness, and micropores for manufactured Ti6Al4V parts. *Journal of Materials Research*, 35 (15):2025–2035, 2020. ISSN 20445326. doi: 10.1557/jmr.2020.84. URL `https://doi.org/10.1557/jmr.2020.84`.